



## **Center for Advanced Communications**

**Villanova University**

---

### **FINAL REPORT**

(02/01/2007 – 01/31/2010)

#### **Radar Imaging for Urban Sensing**

Submitted to

#### **Office of Naval Research**

Grant No. N00014-07-1-0043

##### *Principal Investigator*

Moeness G. Amin

##### *Contributors*

Prof. Moeness Amin

Dr. Fauzia Ahmad

Dr. Yeo-Sun Yoon

Mr. Pawan Setlur

---

April 2010

20100504215

## Table of Contents

Executive Summary .....	5
1. Maximum Likelihood and Suboptimal Schemes for Micro-Doppler Estimation using Carrier Diverse Doppler Radars .....	15
1.1 Introduction .....	16
1.2 Signal Model .....	17
1.3 Maximum Likelihood Estimation .....	18
1.3.1 Micro-Doppler.....	21
1.4 Suboptimal Estimators .....	26
1.4.1 Vibrational MD .....	26
1.4.2 Rotational MD.....	28
1.5 Cramér-Rao Bounds.....	31
1.6 Simulations and Experimental Results.....	33
1.6.1 Simulations.....	33
1.6.2 Experimental Results.....	35
1.7 Conclusions .....	36
Appendix-A: Convergence of the IRNLS algorithm .....	37
References.....	40
2. Dual Frequency Doppler Radars for Indoor Range Estimation: Cramér-Rao Bound Analysis .....	51
2.1 Introduction .....	52
2.2 General Signal Model.....	54
2.2.1 Range ambiguity in dual-frequency radar .....	54
2.2.2 Signal model for CRB derivation.....	55
2.3 Cramér-Rao Bounds.....	61
2.3.1 Constant Doppler CRB.....	63
2.3.2 Micro-Doppler CRB.....	65
2.3.3 Accelerating Target CRB .....	68

2.4	Simulations and Quasi-Experimental Results .....	69
2.4.1	Numerical simulations.....	69
2.4.2	Quasi-Experimental results.....	70
2.5	Conclusions .....	73
APPENDIX-A .....		74
APPENDIX-B .....		75
APPENDIX-C .....		78
References .....		80
3.	Optimal Waveform Design for Improved Indoor Target Detection in Sensing Through-the-Wall Applications.....	86
3.1	Introduction .....	87
3.2	Radar Scattering Model and Target Impulse Response.....	89
3.3	Range Resolution Considerations.....	93
3.4	Application of Matched Illumination Technique for Target Identification.....	95
3.5	Target Detection and Classification with Target Orientation Uncertainties ....	95
3.6	Numerical Simulations .....	96
3.6.1	Free-space illumination .....	97
3.6.2	Behind the wall illumination .....	98
3.6.3	Target discrimination.....	99
3.6.4	Target resolution and constrained design .....	99
3.6.5	Target orientation uncertainty .....	100
3.6.6	Effects of clutter .....	101
3.6.7	Human behind wall.....	102
3.6.8	Effect of wall errors .....	102
3.7	Conclusions .....	103
References .....		105
4.	Matched-Illumination Waveform Design for a Multistatic Through-the-Wall Radar System .....	122

4.1	Introduction .....	123
4.2	Problem Statement and Signal Model .....	125
4.2.1	Single Active Transmitter.....	125
4.2.2	A note on range resolution and range gate .....	128
4.2.3	Multiple transmitters.....	129
4.3	Detection Statistic.....	130
4.3.1	Receiver operating characteristic.....	132
4.3.2	Coherent vs. combining.....	133
4.4	Matched Illumination Waveform Design .....	134
4.5	Simulation Results.....	135
4.6	Conclusions .....	138
	References .....	139
5.	High-Resolution Through-the-Wall Radar Imaging Using BeamSpace MUSIC.....	149
5.1	Introduction .....	150
5.2	High-Resolution Imaging .....	151
5.2.1	Signal Modeling .....	151
5.2.2	MUSIC Based Imaging .....	154
5.2.3	Through-the-Wall Radar Data .....	158
5.3	BeamSpace MUSIC for Imaging .....	159
5.3.1	BeamSpace .....	159
5.3.2	Advantages .....	160
5.3.3	Forming BeamSpace .....	164
5.4	Simulations .....	167
5.4.1	Experiment.....	167
5.4.2	Results	168
5.4.3	Conclusions .....	171
	References .....	172



## Executive Summary

This final report presents the results of the research performed under ONR grant number N00014-07-1-0043 over the period of February 1st, 2007 to January 1st, 2010. The research team working on this project consists of Prof. Moeness Amin (PI), Prof. Fauzia Ahmad (Research Professor), Dr. Yeo-Sun Yoon (Postdoctoral Fellow), and Mr. Pawan Setlur (Graduate Student). The research efforts over the life of this grant have evolved around 1) Maximum Likelihood and Suboptimal Schemes for Micro-Doppler Estimation using Carrier Diverse Doppler Radars, 2) Dual Frequency Doppler Radars for Indoor Range Estimation: Cramér-Rao Bound Analysis, 3) Optimal Waveform Design for Improved Indoor Target Detection in Sensing Through-the-Wall Applications, 4) Matched-Illumination Waveform Design for a Multistatic Through-the-Wall Radar System, 5) BS-MUSIC for High Resolution Imaging in Through-the-Wall Radar Imaging Applications.

Each one of the above contributions forms a chapter of this report. Each chapter has its own Abstract, Introduction, Conclusion, and References. It also has its own equation and figure numbers.

### **1. Maximum Likelihood and Suboptimal Schemes for Micro-Doppler Estimation using Carrier Diverse Doppler Radars**

Carrier diverse radars, known as dual frequency radars, employ two different frequencies, and can be effective in determining the moving target range in urban sensing and through-the-wall radar applications. In this report, we derive the maximum likelihood (ML) estimator for the micro-Doppler motion parameters from the dual frequency radar returns. Micro-Doppler signatures, which are commonly associated with vibrating, oscillating, and rotating objects, have emerged to be an important tool in target detection and classification. Unlike linear models, the respective ML estimator does not assume a closed form expression. We solve the ML estimator for dual-frequency radar operations by applying an iteratively reweighted nonlinear least squares algorithm (IRNLS), which is initiated using suboptimal solutions. The

ML-IRNLS algorithm is applied to both simulated and experimental radar returns for estimating the range and the motion parameters of indoor targets.

## **2. Dual Frequency Doppler Radars for Indoor Range Estimation: Cramér-Rao Bound Analysis**

Single frequency Doppler radars are effective in distinguishing moving targets from stationary targets, but suffer from inherent range ambiguity. With a dual-frequency operation, a second carrier frequency is utilized to overcome the range ambiguity problem. In urban sensing applications, the dual-frequency approach offers the benefit of reduced complexity, fast computation time, and real time target tracking. We consider a single moving target with three commonly exhibited indoor motion profiles, namely, constant velocity motion, accelerating target motion, and micro-Doppler motion. RF signatures of indoor inanimate objects, such as fans, vibrating machineries, and clock pendulums, are characterized by micro-Doppler motion, whereas animate translation movements produce linear FM Doppler. In this report, we derive Cramér-Rao bounds (CRB) for the parameters defining indoor target motions under dual-frequency implementations. Experimental data is used to estimate micro-Doppler parameters and to validate the CRBs.

## **3. Optimal Waveform Design for Improved Indoor Target Detection in Sensing Through-the-Wall Applications**

The report also deals with waveform design for improved detection and classification of targets behind walls and enclosed structures. The target impulse response is incorporated in an optimum design of the transmitted waveform which aims at maximizing the signal-to-interference and noise ratio (SINR) at the receiver output. The interference represents signal-dependent clutter which, along with the wall, degrades the receiver performance compared to the free-space and zero-clutter case. Computer simulations show sensitivity of the optimum waveform to target orientation but depict an SINR enhancement over chirped

waveform radar emissions at all aspect angles. Numerical electromagnetic modeling is used to provide the impulse response of typical indoor stationary targets, namely, tables, chairs, and humans.

#### **4. Matched-Illumination Waveform Design for a Multistatic Through-the-Wall Radar System**

We present the matched illumination waveform design for improved target detection in through-the-wall radar imaging and sensing applications. We consider a multistatic radar system for detection of stationary targets with known impulse responses behind walls. The stationary and slowly moving nature of typical indoor targets relaxes the orthogonality requirement on the waveforms, thereby allowing sequential transmissions from each transmitter with simultaneous reception at multiple receivers. The generalization of the matched illumination waveform design concept from a monostatic to a multistatic setting casts the indoor radar sensing problem in terms of multiple-input multiple-output (MIMO) operations and puts in context the offering of MIMO to urban sensing and imaging of targets in enclosed structures. Numerical electromagnetic modeling is used to provide the impulse response of typical behind-the-wall stationary targets, namely tables and humans, for different target orientations and at various incident and reflection angles. Simulation results depict an improvement in the signal-to-clutter-and-noise-ratio (SCNR) at the output of the matched filter receiver for multistatic radar as compared to monostatic operation.

#### **5. BS-MUSIC for High Resolution Imaging in Through-the-Wall Radar Imaging Applications.**

The MUSIC algorithm is a high-resolution direction finding technique which has been successfully applied to enhance radar imaging in inverse synthetic aperture radar (ISAR). Although this signal subspace-based method has proven effective when dealing with point targets and high SNR, it may fail to work when directly applied to extended targets or target returns of low SNR. The Beamspace MUSIC (BS-MUSIC), in which the MUSIC algorithm is applied to multiple beams is capable of locating spatially

extended targets in low SNR environments. We propose BS-MUSIC as an image formation method for indoor radar imaging problems and sensing through-the-wall applications. We compare BS-MUSIC performance to conventional beamforming and element-space MUSIC. Imaging results with both synthesized and real data demonstrate the advantages of the proposed algorithm in depicting targets behind walls.

## List of Publications

(Publications listed in bold font make up the different chapters of this report)

### Journal Papers

- [1] P. Setlur, F. Ahmad, and M. Amin, "Helicopter radar return analysis: estimation and blade number selection," Signal Processing, Submitted.
- [2] C. Debes, J. Riedler, A.M. Zoubir, and M.G. Amin, "Adaptive target detection with application to Through-the-Wall Radar Imaging," IEEE Transactions on Signal Processing (under review).
- [3] **P. Setlur, F. Ahmad, and M. G. Amin, "Maximum likelihood and suboptimal schemes for motion parameter estimation using carrier diverse Doppler radars," IEEE Transactions on Signal Processing (under review).**
- [4] Y.-S. Yoon, M. G. Amin, and F. Ahmad, "MVDR beamforming for imaging robustness of targets behind unknown walls," IEEE Transactions on Aerospace and Electronic Systems (in press).
- [5] **P. Setlur, M. Amin, and F. Ahmad, "Dual frequency doppler radars for indoor range estimation: cramér-rao bound analysis," IET Signal Processing (in press).**
- [6] **F. Ahmad and M. G. Amin, "Matched-illumination waveform design for a multistatic through-the-wall radar system," IEEE Journal on Selected Topics in Signal Processing, December 2009.**
- [7] F. Ahmad, M. G. Amin, and P. D. Zeman, "Dual-frequency radars for target localization in urban sensing," IEEE Transactions on Aerospace and Electronic Systems, October 2009.
- [8] Y.-S. Yoon, and M. G. Amin, "Spatial filtering for wall-clutter mitigation in through-the-wall radar imaging," IEEE Transactions on Geoscience and Remote Sensing, September 2009.
- [9] C. Debes, M. G. Amin, and A. Zoubir, "Target detection in single- and multiple-view through-the-wall radar imaging," IEEE Transactions on Geoscience and Remote Sensing, May 2009.



- [10] Y. Zhang, M. G. Amin, and F. Ahmad, "Time-frequency analysis for the localization of multiple moving targets using dual-frequency radars," IEEE Signal Processing Letters, vol. 15, pp. 777-780, 2008.
- [11] L. Cirillo, A. Zoubir, and M. G. Amin, "Estimation of FM parameters using a time-frequency Hough transform," IEEE Transactions on Signal Processing, September 2008.
- [12] F. Ahmad, M. G. Amin, "Multi-location wideband synthetic aperture imaging for urban sensing applications," Journal of the Franklin Institute, September 2008.
- [13] M. G. Amin, F. Ahmad, "Wideband synthetic aperture beamforming for through-the-wall imaging," IEEE Signal Processing Magazine, July 2008.
- [14] L. Cirillo, A. Zoubir, and M. G. Amin, "Blind source separation in the time-frequency domain based on multiple hypothesis testing," IEEE Transactions on Signal Processing, June 2008.
- [15] **Y. Yoon and M. G. Amin, "High-resolution through-the-wall radar imaging using beamspace MUSIC," IEEE Transactions on Antennas and Propagation, June 2008.**
- [16] F. Ahmad, Y. Zhang, and M. G. Amin, "Three-dimensional wideband beamforming for imaging through a single wall," IEEE Geoscience and Remote Sensing Letters, April 2008.
- [17] F. Ahmad, M. G. Amin, and G. Mandapati, "Autofocusing of through-the-wall radar imagery under unknown wall characteristics," IEEE Transactions on Image Processing, July 2007.

## Conference Publications

- [1] W. Zhang, M. Amin, F. Ahmad, A. Hoorfar, and G. Smith, "Compressive Sensing for Ultra-wideband Radar Through-Wall Imaging," Proceedings of the American Electromagnetics Conference, Ottawa, Canada, July 2010.
- [2] F. Ahmad and M. G. Amin, "Optimal detection waveforms based on signature exploitation techniques for urban sensing," Proceedings of the American Electromagnetics Conference (AMEREM), Ottawa, Canada, July 2010.

- [3] P. Setlur, M. Amin, and F. Ahmad, "Multipath analyses and experiments for moving personnel indoor," Proceedings of the American Electromagnetics Conference (AMEREM), Ottawa, Canada, July 2010.
- [4] P. Setlur, M. G. Amin, and F. Ahmad, "Multipath doppler signatures from targets moving behind walls," Proceedings of the IEEE International Radar Conference, Washington, D.C., May 2010.
- [5] C. Ioana, M. G. Amin, Y. D. Zhang, and F. Ahmad, "Characterization of doppler effects in the context of over-the-horizon radar," Proceedings of the IEEE International Radar Conference, Washington, D.C., May 2010.
- [6] F. Ahmad, M. G. Amin, T. Dogaru, "Waveform design for detection of weapons based on signature exploitation," Proceedings of the SPIE Symposium on Defense, Security, and Sensing, Radar Sensor, Orlando, FL, April 2010.
- [7] P. Setlur, F. Ahmad, and M. G. Amin, "Multipath analyses of moving targets in enclosed structures using doppler radars," Proceedings of the SPIE Symposium on Defense, Security, and Sensing, Radar Sensor, Orlando, FL, April 2010.
- [8] C. Debes, J. Hahn, A. M. Zoubir, and M.G. Amin, "Feature extraction in through-the-wall radar imaging," Proceedings of the IEEE International Conference on Acoustics, Speech and Signal Processing (ICASSP), Dallas, TX, March 2010.
- [9] C. Debes, C. Weiss, A. M. Zoubir, and M.G. Amin "Distributed target detection in through-the-wall radar imaging using the bootstrap", Proceedings of the IEEE International Conference on Acoustics, Speech and Signal Processing (ICASSP), Dallas, TX, March 2010.
- [10] C. Debes, M. Amin and A. Zoubir, "Optimal Decision Fusion In Through-the-Wall Radar Imaging," Proceedings of the IEEE Workshop on Statistical Signal Processing, Cardiff, Wales, UK, September 2009.
- [11] Y. Yoon and M. Amin," Imaging of Behind the Wall Targets Using Wideband Beamforming with Compressive Sensing," Proceedings of the IEEE Workshop on Statistical Signal Processing, Cardiff, Wales, UK, September 2009.
- [12] F. Ahmad and M. Amin, "Multistatic matched-illumination waveform design for detection and identification of indoor targets behind walls," Proceedings of the EUSIPCO 2009, Glasgow, Scotland, August 2009.
- [13] F. Ahmad and M. G. Amin, "Waveform design for multistatic through-the-wall radar," Proceedings of the IEEE Radar Conference, Pasadena, CA, May 2009.



- [14] Y.-S. Yoon, and M. G. Amin, "Behind-the-wall target identification," Proceedings of the SPIE Symposium on Defense, Security, and Sensing, Orlando, FL, April 2009.
- [15] F. Ahmad and M. G. Amin, "Optimal waveform design for through-the-wall radar imaging," Proceedings of the SPIE Symposium on Defense, Security, and Sensing, Orlando, FL, April 2009.
- [16] P. Setlur, M. G. Amin, and A. Zoubir, "Detection and classification of objects using acoustic excitations," Proceedings of the SPIE Symposium on Defense, Security, and Sensing, Orlando, FL, April 2009.
- [17] P. Setlur, M. G. Amin, and F. Ahmad, "Optimal and suboptimal micro-doppler estimation schemes using carrier diverse doppler radars," Proceedings of the IEEE International Conference on Acoustics, Speech, and Signal Processing, Taipei, Taiwan, April 2009.
- [18] C. Debes, J. Riedler, M. G. Amin, and A. M. Zoubir, "Iterative target detection approach in through wall radar imaging," Proceedings of the IEEE International Conference on Acoustics, Speech, and Signal Processing, Taipei, Taiwan, April 2009.
- [19] F. Ahmad, M. G. Amin, and H. Estephan, "Multistatic waveform design for seeing through the wall," Proceedings of the 2009 International Waveform Diversity and Design Conference, Orlando, FL, 8-13 February 2009.
- [20] Y. Zhang, M. G. Amin, and F. Ahmad, "Localization of vibrating targets using dual-frequency synthetic aperture radar and time-frequency analysis," Proceedings of the 2008 IEEE International Geoscience & Remote Sensing Symposium, Boston, MA, July 2008.
- [21] C. Debes, M. G. Amin, and A. Zoubir, "Target detection in multiple-viewing through-the-wall radar imaging," Proceedings of the 2008 IEEE International Geoscience & Remote Sensing Symposium, Boston, MA, July 2008.
- [22] Y. Zhang, P. Setlur, M. G. Amin, and F. Ahmad, "Application of time-frequency analysis and Kalman filter to range estimation of targets in enclosed structures," Proceedings of the 2008 IEEE Radar Conference, Rome, Italy, May 2008.
- [23] S. A. Kassam, F. Ahmad, M. G. Amin, and K. Yemelyanov, "Target and change detection in synthetic aperture radar sensing of urban structures," Proceedings of the IEEE Radar Conference, Rome, Italy, May 2008.

- [24] Y.-S. Yoon, and M. G. Amin, "High resolution through-the-wall radar imaging using extended target model," Proceedings of the 2008 IEEE Radar Conference, Rome, Italy, May 2008.
- [25] Y. Zhang, M. G. Amin, and F. Ahmad, "Moving target localization using dual-frequency radar arrays," Proceedings of the SPIE Symposium on Defense and Security, Radar Sensor Technology XII Conference, Orlando, FL, March 2008.
- [26] Y.-S. Yoon, and M. G. Amin, "High resolution through-the-wall radar image based on beamspace eigenstructure subspace methods," Proceedings of the SPIE Symposium on Defense and Security, Orlando, FL, March 2008.
- [27] F. Ahmad, Y.-S. Yoon, and M. G. Amin, "Through-the-wall polarimetric imaging," Proceedings of the SPIE Symposium on Defense and Security, Orlando, FL, March 2008.
- [28] F. Ahmad and M. G. Amin, "Multi-viewpoint image fusion for urban sensing applications," Proceedings of the SPIE Symposium on Defense and Security, Orlando, FL, March 2008.
- [29] Y.-S. Yoon, and M. G. Amin, "Compressive sensing technique for high-resolution radar imaging," Proceedings of the SPIE Symposium on Defense and Security, Orlando, FL, March 2008.
- [30] Y. Zhang, M. G. Amin, and F. Ahmad, "A novel approach for moving multi-target localization using dual frequency radars and time-frequency distributions," Proceedings of the Annual Asilomar Conference on Signals, Systems, and Computers, Pacific Grove, CA, November 2007.
- [31] Y. Zhang, F. Ahmad, and M. G. Amin, "Application of beamforming for wall detection and localization," Proceedings of the 2007 North American Radio Science Meeting URSI - CNC/USNC, Ottawa, Canada, July 2007.
- [32] P. Setlur, M. G. Amin, F. Ahmad, and H. Estephan "A frequency diverse doppler radar for range-to-motion estimation in urban sensing applications," Proceedings of the 2007 International Waveform Diversity and Design Conference, Pisa, Italy, June 2007.
- [33] F. Ahmad and M. G. Amin, "High-resolution imaging using capon beamformers for urban sensing applications," Proceedings of the IEEE International Conference on Acoustics, Speech, and Signal Processing, Honolulu, HI, April 2007.

- [34] P. Setlur, M. G. Amin, and F. Ahmad, "Cramer-Rao bounds for range and motion parameter estimations using dual frequency radars," Proceedings of the IEEE International Conference on Acoustics, Speech, and Signal Processing, Honolulu, HI, April 2007.
- [35] L. Cirillo, A. Zoubir, and M. G. Amin, "Estimation of near-field parameters using spatial time-frequency distributions," Proceedings of the IEEE International Conference on Acoustics, Speech, and Signal Processing, Honolulu, HI, April 2007.
- [36] F. Ahmad and M. G. Amin, "Performance of autofocus schemes for single target and populated scenes behind unknown walls," Proceedings of the SPIE Symposium on Defense and Security, Orlando, FL, April 2007.
- [37] P. Setlur, M. Amin, F. Ahmad, P.D. Zeman, "Experiments n through-the-wall motion detection and ranging," Proceedings of the SPIE Symposium on Defense and Security, Orlando, FL, April 2007.
- [38] F. Ahmad, M. G. Amin, and P. D. Zeman, "Performance analysis of dual-frequency CW radars for motion detection and ranging in urban sensing applications," Proceedings of the SPIE Symposium on Defense and Security, Orlando, FL, April 2007.
- [39] F. Ahmad and M. G. Amin, "Through-the-wall radar imaging experiments," Proceedings of the IEEE Workshop on Signal Processing Applications for Public Security and Forensics, Washington, D.C., April 2007.
- [40] S. Aviyente, F. Ahmad and M. G. Amin, "Information theoretic measures for change detection in urban sensing applications, Proceedings of the IEEE Workshop on Signal Processing Applications for Public Security and Forensics, Washington, D.C., April 2007.
- [41] P. Setlur, M. G. Amin, and F. Ahmad, "Urban target classifications using time-frequency micro-Doppler signatures," Proceedings of the International Symposium on Signal Processing and its Applications, Sharjah, UAE, February 2007.
- [42] M. Shueb, F. Ahmad, and M. G. Amin, "Source localization in view of urban sensing applications," Proceedings of the International Symposium on Signal Processing and its Applications, Sharjah, UAE, February 2007.

# 1. Maximum Likelihood and Suboptimal Schemes for Micro-Doppler Estimation using Carrier Diverse Doppler Radars

## *Abstract*

Carrier diverse radars, known as dual frequency radars, employ two different frequencies, and can be effective in determining the moving target range in urban sensing and through-the-wall radar applications. In this chapter, we derive the maximum likelihood (ML) estimator for the micro-Doppler motion parameters from the dual frequency radar returns. Micro-Doppler signatures, which are commonly associated with vibrating, oscillating, and rotating objects, have emerged to be an important tool in target detection and classification. Unlike linear models, the respective ML estimator does not assume a closed form expression. We solve the ML estimator for dual-frequency radar operations by applying an iteratively reweighted nonlinear least squares algorithm (IRNLS), which is initiated using suboptimal solutions. The ML-IRNLS algorithm is applied to both simulated and experimental radar returns for estimating the range and the motion parameters of indoor targets.



## 1.1 Introduction

Urban sensing and through-the-wall radar imaging address the desire to detect, locate, and classify both animate and inanimate targets [1]-[4]. Range estimation is typically performed by linear frequency modulated radars, pulse compression radars, or pulse Doppler radars [5]. Such radar systems are wide-band so as to meet the range resolution requirements. However, the operational logistics and system requirements for urban sensing, such as cost, hardware complexity, and portability, may impede or prohibit the use of such radar systems. Further, bandwidth allocation issues may arise since radio frequency (RF) penetration through the walls follows a lowpass filtering model with typical cutoff in the low GHz range, where much of the RF spectrum may be jammed or taken over, in part or fully by adversaries or other emitters. On the other hand, a dual-frequency approach for target range estimation, combined with wide array aperture, can meet the requirements of different system operation modes, and is likely to emerge as the preferred approach in most urban sensing and rescue missions [1],[6]. The dual frequency or carrier diversity is induced by using two different carrier frequencies which are selected to achieve a desirable maximum unambiguous range. The latter is important to allow a unique range estimate of a target, and should be based on the *a priori* knowledge (possible through aerial mapping or ground access) of the spatial extent of the urban structure under surveillance. The technique of employing two frequencies to estimate range has been used in many other radar applications [7], [8].

In this chapter, we apply a dual frequency radar for target range and parameter estimation. We consider the micro-Doppler (MD) target motion profile [9]. Micro-Doppler analysis has been used in many applications for human gait analysis, multistatic radar applications, etc., such works can be seen for example in [10], [11], and references therein. RF signatures of indoor inanimate objects, such as fans, vibrating machineries, and clock pendulums, and animate objects, like the limbs in human gait are characterized by MD motion. Translational motions, producing constant velocity or accelerating velocity, respectively produce complex sinusoids and linear frequency modulation to the incident waveform. The ML techniques for parameter estimation of such returns has been treated in [12], [13], and references therein. However, the ML for micro Doppler, which gives rise to sinusoidal FM signals, has not yet been

examined and is the subject of this chapter. We derive the maximum likelihood optimal estimator for MD motion parameters. The results are compared with the Cramér-Rao lower bounds (CRBs) for MD motion parameters which were recently derived in [14] for dual-frequency operations.

We consider a single moving target whose MD motion profile can be modeled by a finite number of parameters. The MD is further classified as rotational or vibrational MD based on radar cross section (RCS) fluctuations. Maximum likelihood (ML) technique for motion parameter estimation is then formulated and solved using step wise concentration to obtain an iteratively reweighted least squares algorithm. The iterative algorithm is initialized using suboptimal estimates and applied to real radar returns to obtain ML estimates of the MD parameters. It is noted that the focus of this chapter is on single antenna operation. For a multiple target scene, assuming that the targets are separable in cross-range and spatial processing (beamforming) is used in conjunction with the dual-frequency radar, the ML analysis presented in this chapter is applicable to each individual separated target return.

A brief outline of the chapter is as follows. Section 1.2 describes the signal model. In Sections 1.3 and 1.4 we discuss, respectively, the ML and suboptimal estimation schemes for the micro-Doppler motions. Section 1.5 contains the simulation and experimental results, followed by the conclusions in Section 1.6.

## 1.2 Signal Model

The signal returns for the dual frequency Doppler radar after down conversion to baseband and using  $N$  samples are given by,

$$x_i(n) = s_i(n) + v_i(n) = h_i(n; \psi') \exp\left(j \frac{4\pi f_i}{c} R(n; \psi)\right) + v_i(n), \quad i = 1, 2, \text{ and } n = 0, 1, \dots, N-1 \quad (1)$$

$$E\{v_1(n)v_2^*(k)\} = 0 \quad \forall n, k; \quad E\{v_i(n)v_i^*(k)\} = 0 \quad \forall n \neq k, \quad i = 1, 2, \quad E\{v_i(n)v_i^*(k)\} = \sigma_i^2 \quad \forall n = k, \quad i = 1, 2$$

where  $f_i$ ,  $i = 1, 2$  are the carrier frequencies,  $c$  is the speed of light in free space, and the superscript  $^*$  denotes the complex conjugate operation. The target range,  $R(n; \psi)$ , is parameterized by a vector  $\psi \in \mathbb{R}^{P \times 1}$  of  $P$  desired parameters. The amplitude  $h_i(n; \psi')$ , measured at the  $i$ -th frequency, captures the

time variations in the target RCS, and is a function of a subset  $\boldsymbol{\psi}'$  of the parameter vector  $\boldsymbol{\psi}$ . The noise,  $v_1(\cdot)$  and  $v_2(\cdot)$ , at the two carrier frequencies, are assumed to be complex circular AWGN and uncorrelated. Further, the noise sequences are i.i.d for each carrier frequency. Note that the model in (1) corresponds to the discrete-time equivalent of the continuous-time signals, i.e.,  $x_i(n) = x_i(nT_s)$ , where  $T_s$  is the sampling period and has been suppressed in the notations for convenience. The returns in (1) can be statistically characterized by a multivariate complex Gaussian probability density function (pdf),  $p(\mathbf{x}; \mathbf{s})$ ,

$$p(\mathbf{x}; \mathbf{s}) = \frac{1}{\pi^{2N} \det(\mathbf{C})} \exp(-(\mathbf{x} - \boldsymbol{\mu})^H \mathbf{C}^{-1} (\mathbf{x} - \boldsymbol{\mu})) \quad (2)$$

where the received signals at the two frequencies are appended to form a long vector,

$$\begin{aligned} \mathbf{x} &= \mathbf{s} + \mathbf{v} = [x_1(0), x_1(1), \dots, x_1(N-1), x_2(0), x_2(1), \dots, x_2(N-1)]^T = [\mathbf{x}_1 \quad \mathbf{x}_2]^T \\ \mathbf{s} &= [s_1(0), s_1(1), \dots, s_1(N-1), s_2(0), s_2(1), \dots, s_2(N-1)]^T = [\mathbf{s}_1 \quad \mathbf{s}_2]^T \\ \mathbf{v} &= [v_1(0), v_1(1), \dots, v_1(N-1), v_2(0), v_2(1), \dots, v_2(N-1)]^T = [\mathbf{v}_1 \quad \mathbf{v}_2]^T \end{aligned} \quad (3)$$

The mean  $\boldsymbol{\mu} = E\{\mathbf{x}\}$  equals  $[\mathbf{s}_1 \quad \mathbf{s}_2]^T$  and the covariance matrix  $\mathbf{C}$  is Hermitian with the following diagonal structure,

$$\mathbf{C} = E\{(\mathbf{x} - \boldsymbol{\mu})(\mathbf{x} - \boldsymbol{\mu})^H\} = \begin{bmatrix} \sigma_1^2 \mathbf{I} & \mathbf{0}_{N \times N} \\ \mathbf{0}_{N \times N} & \sigma_2^2 \mathbf{I} \end{bmatrix} \quad (4)$$

where  $\mathbf{I}$  is an identity matrix of dimensions  $N \times N$ .

### 1.3 Maximum Likelihood Estimation

We consider the noise free return  $\mathbf{s}$ , which is a function of  $R(n; \boldsymbol{\psi})$ ,  $h_i(n; \boldsymbol{\psi}')$ , and  $f_i$ ,  $i=1,2$ , to be parameterized by the vector  $\boldsymbol{\psi}$  of  $P$  desired parameters. Hereafter, for notational succinctness, we denote  $\mathbf{s} = \mathbf{s}(\boldsymbol{\psi})$ . The ML estimator for  $\boldsymbol{\psi} = [\psi_1, \psi_2, \psi_3, \dots, \psi_P]^T$  is defined as [15],

$$\hat{\boldsymbol{\psi}} = \arg \max_{\boldsymbol{\psi}} p(\mathbf{x}; \mathbf{s}(\boldsymbol{\psi})) = \arg \max_{\boldsymbol{\psi}} \ln(p(\mathbf{x}; \mathbf{s}(\boldsymbol{\psi}))) \quad (5)$$



If the elements of the covariance matrix, i.e.,  $\sigma_i^2$ ,  $i=1, 2$ , are unknown, then using (2) and ignoring the constant terms, the ML estimator of the complete parameter vector,  $\boldsymbol{\theta}=[\boldsymbol{\psi}^T, \sigma_1^2, \sigma_2^2]^T$  can be expressed as,

$$\hat{\boldsymbol{\theta}} = \arg \max_{\boldsymbol{\theta}} \left( -N \ln(\sigma_1^2) - N \ln(\sigma_2^2) - \frac{\|\mathbf{x}_1 - \mathbf{s}_1(\boldsymbol{\psi})\|^2}{\sigma_1^2} - \frac{\|\mathbf{x}_2 - \mathbf{s}_2(\boldsymbol{\psi})\|^2}{\sigma_2^2} \right) \quad (6)$$

Computing the log likelihood (LL) score with respect to the noise nuisance parameters  $\sigma_i^2$ ,  $i=1, 2$ , and equating it to zero, we obtain

$$\sigma_i^2 = \frac{\|\mathbf{x}_i - \mathbf{s}_i(\boldsymbol{\psi})\|^2}{N}, \quad \text{for } i=1, 2 \quad (7)$$

Concentrating the LL with respect to  $\sigma_i^2$ , i.e., substituting (7) in (6), yields

$$\hat{\boldsymbol{\psi}} = \arg \max_{\boldsymbol{\psi}} \left( -N \ln \left( \frac{\|\mathbf{x}_1 - \mathbf{s}_1(\boldsymbol{\psi})\|^2}{N} \times \frac{\|\mathbf{x}_2 - \mathbf{s}_2(\boldsymbol{\psi})\|^2}{N} \right) \right) = \arg \min_{\boldsymbol{\psi}} \ln \left( \prod_{i=1}^2 \frac{\|\mathbf{x}_i - \mathbf{s}_i(\boldsymbol{\psi})\|^2}{N} \right) \quad (8a)$$

$$\hat{\sigma}_i^2 = \frac{\|\mathbf{x}_i - \mathbf{s}_i(\hat{\boldsymbol{\psi}})\|^2}{N} \quad (8b)$$

The ML estimator for the noise nuisance parameters is provided in (8b), and is the same as the expression in (7) with  $\boldsymbol{\psi}$  replaced by  $\hat{\boldsymbol{\psi}}$ . Notice that the noise estimate at one frequency only depends on the data measured at the same frequency. However, it also depends on the ML parameter estimates obtained from the combined frequency information, and as such, the problem cannot be decoupled into two separate ML parts, each corresponding to a single frequency. Equation 8(a, b) constitutes the ML estimator for the dual frequency radar, and due to the involvement of the two terms, it does not have a closed form solution. If the elements of the covariance matrix  $\mathbf{C}$  are known, the ML estimator for  $\boldsymbol{\psi}$  takes the form

$$\hat{\boldsymbol{\psi}} = \arg \min_{\boldsymbol{\psi}} (\mathbf{x} - \mathbf{s}(\boldsymbol{\psi}))^H \mathbf{C}^{-1} (\mathbf{x} - \mathbf{s}(\boldsymbol{\psi})) = \arg \min_{\boldsymbol{\psi}} \left( \frac{\|\mathbf{x}_1 - \mathbf{s}_1(\boldsymbol{\psi})\|^2}{\sigma_1^2} + \frac{\|\mathbf{x}_2 - \mathbf{s}_2(\boldsymbol{\psi})\|^2}{\sigma_2^2} \right) \quad (9)$$

The step wise concentration approach can be applied using (9) to provide an iterative solution to 8(a,b). The iterative ML algorithm is formulated as follows.

1. Initialize with  $\mathbf{C}_0 = \mathbf{I}$ , where  $\mathbf{I}$  is an identity matrix of the same dimension as  $\mathbf{C}_0$ .
2. Using (9), find the estimate  $\hat{\boldsymbol{\psi}}_0$  of  $\boldsymbol{\psi}$ .
3. Use  $\hat{\boldsymbol{\psi}}_0$  in (8b) to obtain the noise variance estimates  $\hat{\sigma}_{i1}^2 = \|\mathbf{x}_i - \mathbf{s}_i(\hat{\boldsymbol{\psi}}_0)\|^2 / N$ , and construct the covariance matrix  $\mathbf{C}_1 = \text{Diag} [\hat{\sigma}_{11}^2 \times \mathbf{1}, \hat{\sigma}_{21}^2 \times \mathbf{1}]$ , where the operator  $\text{Diag}[\cdot]$  transforms a vector into a diagonal matrix and  $\mathbf{1} = [1, 1, \dots, 1]_{1 \times N}$ .
4. Recursively solve at the  $k$ th iteration ( $k > 1$ ),

$$\hat{\boldsymbol{\psi}}_k = \arg \min_{\boldsymbol{\psi}} (\mathbf{x} - \mathbf{s}(\boldsymbol{\psi}))^H \mathbf{C}_k^{-1} (\mathbf{x} - \mathbf{s}(\boldsymbol{\psi})), \text{ initialized with } \hat{\boldsymbol{\psi}}_{k-1}$$

$$\hat{\sigma}_{i(k+1)}^2 = \|\mathbf{x}_i - \mathbf{s}_i(\hat{\boldsymbol{\psi}}_k)\|^2 / N, \forall i = 1, 2; \mathbf{C}_{(k+1)} := \text{Diag}[\hat{\sigma}_{1(k+1)}^2 \times \mathbf{1}, \hat{\sigma}_{2(k+1)}^2 \times \mathbf{1}] \quad (10)$$

5. Stop at convergence, or when an appropriate terminating criterion is satisfied.

The solution of step 4 depends on the underlying motion model, as delineated next. We note that the estimate  $\hat{\boldsymbol{\psi}}_0$  is the non-linear least squares (NLS) estimate. Further, in step 4, the covariance matrix  $\mathbf{C}_k$  is not stressed to be an estimate for reasons to follow shortly. As evident from the above iterative ML implementation, the step-wise concentration approach does not treat the noise variances as of known or estimated values, but rather alternates between the two assumed hypotheses. In other words, for every iteration, a quasi-ML objective is optimized. The step-wise algorithm has been used in generalized linear models in statistical literature [16] and in robust statistics for M-estimation [17]. It is often described as the iteratively reweighted least squares (IRLS). The “reweighting” at each iteration occurs in the estimation of  $\hat{\boldsymbol{\psi}}_k$  through a known  $\mathbf{C}_k$ , as seen in (10). However, for the problem at hand, as shown in the following section,  $\mathbf{s}(\boldsymbol{\psi})$  is nonlinear, and hence a more appropriate name for the algorithm would be the iteratively reweighted nonlinear least squares (IRNLS). Henceforth, we will refer to the iterative ML algorithm as IRNLS. Proof of convergence of the IRNLS estimates is provided in the Appendix.

Three terminating criteria may be considered for the IRNLS algorithm. Denoting the negative LL cost by  $\ell(\boldsymbol{\psi})$ , an appropriate criterion is when  $\ell(\hat{\boldsymbol{\psi}}_k) - \ell(\hat{\boldsymbol{\psi}}_{k-1}) \leq \dot{\epsilon}$ , where  $\dot{\epsilon}$  is an arbitrarily small user-defined positive constant, in which case  $\hat{\boldsymbol{\psi}}_k$  will be the final ML estimate. Another terminating criterion could be  $\|\hat{\boldsymbol{\psi}}_k - \hat{\boldsymbol{\psi}}_{k-1}\| \leq \ddot{\epsilon}$ , where  $\ddot{\epsilon}$  is the available machine precision or can be user-defined. The third terminating criterion is simply constraining the maximum number of iterations, i.e., iterate (10) until  $k = k_{\max}$ . We use this criterion in the simulations. A general flowchart of the ML algorithm is shown in Fig. 1.

In the following, we associate  $\mathbf{s}(\boldsymbol{\psi})$  to different MD motion profiles, and use the IRNLS to derive the respective optimal ML solution.

### 1.3.1 Micro-Doppler

The MD returns can be classified as a) vibrational MD and b) rotational MD. Although the phase of the returns is identical in both cases, a difference between the two exists in terms of the amplitude or RCS fluctuations.

#### 1.3.1.1 Vibrational MD

The vibrational MD arises due to vibrations of the scatterers on the target or of the target itself, example being a target moving back and forth or undergoing a simple harmonic motion (SHM). The vibrational MD is characterized by a sinusoidal instantaneous frequency. It is parameterized by  $\boldsymbol{\psi} = [R_o, d, \omega_o, \phi_o]$ , where  $R_o$  is the range of the target at rest or simply the mean range,  $d$  is the maximum radial displacement,  $\omega_o$  is the vibrational frequency, and  $\phi_o$  is a constant phase. The time-varying range profile for this motion is given by,

$$R(n; \boldsymbol{\psi}) = R_o + d \cos(\omega_o n - \phi_o) \quad (11)$$

Typical indoor vibrating targets have small displacements relative to the target range, especially for longer radar standoff distances from the wall that are normally used for through-the-wall radar operations.

Accordingly, the target aspect angle and hence the RCS is considered constant, thereby yielding a constant amplitude, i.e.,  $h_i(n; \psi') = \rho_i$ ,  $i=1,2$ . Substituting the expressions for  $h_i(n; \psi')$  and  $R(n; \psi)$  in (1), we obtain the signal returns as,

$$x_i(n) = \rho_i \exp \left( j \frac{4\pi f_i (R_o + d \cos(\omega_o n - \varphi_o))}{c} \right) + v_i(n), \quad \forall i=1,2 \quad (12)$$

The radar returns in (12) represent sinusoidal FM signals. Using the data vector  $\mathbf{x}$ , comprised of the returns of (12), in (10) defines the IRNLS-ML estimator for the vibrational MD motion profile. The noise-free signal vector  $\mathbf{s}$  can be decomposed into two multiplicative terms, one containing  $R_o$  and the other being a function of the remaining parameters in  $\psi$ . Accordingly, we express the IRNLS-iterations as

$$\begin{aligned} \hat{\psi}_k &= \arg \min_{\psi'} (\mathbf{x} - \mathbf{A}(\psi') \mathbf{b})^H \mathbf{C}_k^{-1} (\mathbf{x} - \mathbf{A}(\psi') \mathbf{b}), \quad k > 1, \text{ initialized with } \hat{\psi}_{k-1} \\ \mathbf{a}_i(\psi') &:= [1, \exp(j4\pi f_i z(1)/c), \dots, \exp(j4\pi f_i z(N-1)/c)]^T, \quad \psi' := [d, \omega_o, \varphi_o]^T \\ z(n) &:= d \cos(\omega_o n - \varphi_o), \quad b_i := \rho_i \exp(j4\pi f_i R_o / c), \quad \forall i=1,2 \\ \mathbf{A}(\psi') &= \begin{bmatrix} \mathbf{a}_1(\psi') & \mathbf{0} \\ \mathbf{0} & \mathbf{a}_2(\psi') \end{bmatrix}, \quad \mathbf{b} = [b_1, b_2]^T, \quad \mathbf{0} = [0, 0, \dots, 0]_{N \times 1}^T \\ \hat{\sigma}_{i(k+1)}^2 &= \|\mathbf{x}_i - \hat{\mathbf{a}}_i(\hat{\psi}_k) \hat{b}_{ik}\|^2 / N, \quad \text{for } i=1, 2, \end{aligned} \quad (13)$$

In (13),  $\hat{b}_{ik}$  denotes the estimate  $\hat{b}_i$  at the  $k$ -th iteration. We proceed by minimizing (13) with respect to  $\mathbf{b}$ , in which case one obtains the well known weighted least squares solution, substituting this into (13) we obtain the final estimates of the parameters as,

$$\begin{aligned}
(\hat{d}_k, \hat{\omega}_k, \hat{\phi}_{o,k}) &= \arg \max_{d, \omega_o, \phi_o} \left( \frac{\left| \sum_{n=0}^{N-1} x_1(n) \exp(-j4\pi f_1 d \cos(\omega_o n - \phi_o) / c) \right|^2}{\sigma_{1k}^2} + \frac{\left| \sum_{n=0}^{N-1} x_2(n) \exp(-j4\pi f_2 d \cos(\omega_o n - \phi_o) / c) \right|^2}{\sigma_{2k}^2} \right), \quad k > 1 \\
\hat{\mathbf{A}}_k &:= \mathbf{A}(\hat{\psi}'_k), \hat{\mathbf{b}}_k := \mathbf{b}(\hat{\psi}'_k) = (\hat{\mathbf{A}}_k^H \mathbf{C}_k^{-1} \hat{\mathbf{A}}_k)^{-1} \hat{\mathbf{A}}_k^H \mathbf{C}_k^{-1} \mathbf{x}, \quad \hat{R}_{ok} = \frac{\angle(\hat{b}_{2k} \times \hat{b}_{1k}^*)}{4\pi(f_2 - f_1)} c \\
\hat{\rho}_{ik} &= |\hat{b}_{ik}|, \quad \hat{\sigma}_{i(k+1)}^2 = \|\mathbf{x}_i - \hat{\mathbf{a}}_i(\hat{\psi}'_k) \hat{b}_{ik}\|^2 / N, \quad i=1,2
\end{aligned} \tag{14}$$

In (14),  $\hat{\mathbf{A}}_k$  and  $\hat{\mathbf{b}}_k$ , respectively, denote the estimates of  $\mathbf{A}$  and  $\mathbf{b}$  in the  $k$ -th iteration, defined in (13). Similar notational convention follows for the other parameters. The function maximizations in (14) are solved numerically. It is noted in (14) that the range estimate  $\hat{R}_{ok}$  is obtained by subtracting the mean phase estimates at the two carriers and dividing it by the difference of the carrier frequencies. This estimate corresponds to the standard dual-frequency range estimate to avoid the many ambiguous range solutions see [7, pg. 140]. In other words, we are assuming  $R_o \in [0, c / 2(f_2 - f_1)]$ .

### 1.3.1.2 Rotational MD

As the name suggests, targets which are rotating with respect to a fixed location radar follow this model. Unlike the vibration model, the signal returns due to rotation have RCS fluctuations. This is because the radar observes different elevation aspects of the target, thereby inducing a cyclic amplitude modulation in the radar returns. In general, the RCS fluctuations are geometry dependent. For example, the RCS fluctuations are non-existent for a rotating sphere since the sphere is aspect independent, whereas for other complex targets, the RCS fluctuates cyclically. In this chapter, we consider the sinc type fluctuation, which corresponds well to a rotating fan blade [18-20]. It must be noted that most of the typical indoor rotating targets are fans, which may either be ceiling mounted, pedestal or table-top. This is primarily the reason for using the sinc model in the underlying application area. As such, the baseband returns at the two carrier frequencies, for a single blade, can be readily shown to be



$$\begin{aligned}
x_i(n) &= h_i(n; \psi') \exp \left( j \frac{4\pi f_i (R_o + d \cos(\omega_o n - \varphi_o))}{c} \right) + v_i(n), \quad i=1,2 \\
h_i(n; \psi') &:= \rho_i \gamma_i(n; \psi') = \rho_i \text{sinc} \left( \frac{4\pi f_i d \cos(\omega_o n - \varphi_o)}{c} \right), \quad \psi' := [d, \omega_o, \varphi_o]^T
\end{aligned} \tag{15}$$

The sinc function in (15) is defined as  $\text{sinc}(x) := \sin(x) / x$ . From (15), it is noted that the sinc function has a cyclic behavior which depends on the rotational frequency. The rotational frequency, in turn, is also a function of the sampling frequency, and hence the data in (15) must span at least one cycle for any type of processing to be successfully applied to it. Extending the model in (15) to  $Q$  blades, the return at the  $i$ -th frequency is given by,

$$\begin{aligned}
x_i(n) &= \sum_{q=1}^Q h_{iq}(n; \psi') \exp \left( j \frac{4\pi f_i (R_o + d \cos(\omega_o n - \varphi_q))}{c} \right) + v_i(n), \quad i=1,2 \\
h_{iq}(n; \psi') &:= \rho_{iq} \gamma_{iq}(n; \psi') = \rho_{iq} \text{sinc} \left( \frac{4\pi f_i d \cos(\omega_o n - \varphi_q)}{c} \right)
\end{aligned} \tag{16}$$

The model in (16) is general, in the sense that it assumes the  $Q$  blades are different, and thus  $\rho_{iq}$  is indexed by  $q$ . If the blades possess identical geometry, and no have manufacturing defects, then as a special case  $\rho_{iq} = \rho_i, \forall q$ . Further, assuming that the blades are placed symmetrically around the main rotor, we can express  $\varphi_q$  as

$$\varphi_q = \varphi_o + (q-1)2\pi / Q, \quad q=1,2,\dots,Q \tag{17}$$

In this case, the radar return from the rotating object has a harmonic structure with harmonic frequencies at  $mQ\omega_o, m=0,\pm1,\dots,\infty$  [18-20]. We must note that the RCS, which is strictly positive and real, is determined from the magnitude squared of the noise free returns in (15) and (16). The returns in (16) can be rewritten in a compact vector notation as

$$\begin{aligned}
\mathbf{x} &= [\mathbf{x}_1^T, \mathbf{x}_2^T]^T = \mathbf{A}(\psi') \mathbf{b} \\
\mathbf{A}(\psi') &:= \begin{bmatrix} \mathbf{A}_{11}(\psi') & \mathbf{0} \\ \mathbf{0} & \mathbf{A}_{22}(\psi') \end{bmatrix}, \mathbf{b} := [\mathbf{b}_1^T, \mathbf{b}_2^T]^T \\
\mathbf{b}_i &= [b_{i1}, b_{i2}, \dots, b_{iQ}]^T, b_{iq} = \rho_{iq} \exp(j4\pi f_i R_o / c), \mathbf{A}_{ii}(\psi') := [\mathbf{a}_{i1}(\psi'), \mathbf{a}_{i2}(\psi'), \dots, \mathbf{a}_{iQ}(\psi')]^T, i=1,2 \quad (18) \\
\mathbf{a}_{iq}(\psi') &:= \gamma_{iq} \oslash \mathbf{g}_{iq}, \gamma_{iq} := [\gamma_{iq}(0; \psi'), \gamma_{iq}(1; \psi'), \dots, \gamma_{iq}(N-1; \psi')]^T, q=1,2,\dots,Q \\
\mathbf{g}_{iq}(\psi') &:= [e^{j4\pi f_i d \cos(\varphi_q)/c}, e^{j4\pi f_i d \cos(\omega_o - \varphi_q)/c}, \dots, e^{j4\pi f_i d \cos(\omega_o(N-1) - \varphi_q)/c}]^T
\end{aligned}$$

In (18), the symbol ' $\oslash$ ' denotes the Hadamard product or element-wise product. Following the analysis for vibrational MD case, it can be readily shown that the IRNLS ML for rotational MD at the  $k^{th}$  iteration is given by

$$\begin{aligned}
\hat{\psi}'_k &= \arg \max_{\psi'} \mathbf{x}^H \mathbf{P}_k(\psi') \mathbf{C}_k^{-1} \mathbf{x}, \text{ initialized with } \hat{\psi}'_{k-1} \\
\mathbf{P}_k(\psi') &:= \mathbf{A}_k (\mathbf{A}_k^H \mathbf{C}_k^{-1} \mathbf{A}_k)^{-1} \mathbf{A}_k^H \mathbf{C}_k^{-1} \\
\hat{\mathbf{b}}_k &= (\hat{\mathbf{A}}_k^H \mathbf{C}_k^{-1} \hat{\mathbf{A}}_k)^{-1} \hat{\mathbf{A}}_k^H \mathbf{C}_k^{-1} \mathbf{x} = [\hat{\mathbf{b}}_{1k}^T, \hat{\mathbf{b}}_{2k}^T]^T \quad (19) \\
\hat{R}_{ok} &= \mathbf{1}^T \angle (\hat{\mathbf{b}}_{1k}^* \oslash \hat{\mathbf{b}}_{2k}) \times \frac{c}{Q4\pi(f_2 - f_1)} \\
\hat{\sigma}_{i(k+1)}^2 &= \|\mathbf{x}_i - \hat{\mathbf{a}}_i(\hat{\psi}'_k) \hat{\mathbf{b}}_{ik}\|^2 / N, i=1,2, \hat{\rho}_{iq} = |\hat{b}_{iq}|, \forall q
\end{aligned}$$

where  $\mathbf{1}$  is column vector of dimensions  $Q \times 1$  whose elements are comprised of all ones, and  $\mathbf{A}(\psi')$  and  $\mathbf{b}$  are defined in (18). In (19),  $\hat{\mathbf{A}}_k := \mathbf{A}(\hat{\psi}'_k)$  is the estimate of the matrix  $\mathbf{A}_k$ . The function maximizations in (19), as before is carried out numerically. A special arises when the blades are all identical. I.e.,  $\rho_{iq} = \rho_i, \forall q$ , then the IRNLS ML derived thus far still applies, for example in (19), we simply use  $\hat{\rho}_i = \mathbf{1}^T |\hat{\mathbf{b}}_i| / Q$ , where the absolute value is taken element-wise. For a single blade return, we can substitute  $q=1$  in (18-19) and proceed with the analysis.

We use the CRBs to compare the mean squared error (MSE) of the ML estimates for both vibrational and rotational MD motions. The elements of the Fisher Information Matrix (FIM) for rotational MD assuming the sinc model are derived in Section. III. The expressions can then be used to numerically evaluate the inverted FIM. The FIM for vibrational MD, derived in [14], is a special case of the rotational MD FIM.



## 1.4 Suboptimal Estimators

Iterative non-linear schemes, ML or otherwise, require proper initial estimates for achieving convergence. The non-linear cost functions of (8a) and (9) have multiple local extrema. Therefore, in order to obtain  $\hat{\psi}_1$  in step 2 of the IRNLS-ML algorithm, initial estimates, obtained from suboptimal estimators which depend on the noise free returns,  $s_i(\psi)$ ,  $i=1,2$ , can be used. Below, we discuss the suboptimal estimation schemes for both vibrational and rotational MD.

### 1.4.1 Vibrational MD

Ignoring the contribution of noise for the time being, we note that the Fourier spectrum of the return,  $x_i(n)$ ,  $i=1,2$  in (12) is not analytic, and consists of infinitely many harmonics weighted by Bessel functions of the first kind [21],

$$X_i(\omega) = 2\pi\rho_i \exp(j4\pi f_i R_o / c) \sum_{m=-\infty}^{m=\infty} j^m J_m(4\pi f_i d / c) \delta(\omega - m\omega_o) \exp(-jm\phi_o), \quad \forall i=1,2 \quad (20)$$

where  $J_m(\cdot)$  is the  $m^{th}$  order Bessel function of the first kind. Since the Bessel functions rapidly decrease in magnitude for increasing  $m$ , the Fourier transform (20) of the returns in (12) has at the most  $m=K$  significant harmonics. The value of  $K$  is readily inferred from the spectrum. With this in mind, we describe below the suboptimal estimation procedure. Since the noise variances are neither required for estimating the parameters suboptimally nor are they essential to start the IRLS iterations, their suboptimal estimates are omitted.

To obtain initial estimates of  $\omega_o$ , we choose  $2K+1$  peaks of  $X_i(\omega)$ ,  $i=1,2$  and form the vector  $\mathbf{y}_i = [X_i(\omega_{-K}), X_i(\omega_{-K+1}), \dots, X_i(0), \dots, X_i(\omega_{K-1}), X_i(\omega_K)]^T$ . The frequencies corresponding to these peaks are stored in a vector  $\boldsymbol{\omega}_i$ . Since the noise is different for each carrier frequency, different perturbations in the peak frequency locations can occur. Hence, in general,  $\boldsymbol{\omega}_1 \neq \boldsymbol{\omega}_2$ . The DC value in the Fourier transform is important, since it serves a reference for automatic peak-picking, and therefore it must be included in the vector  $\mathbf{y}_i$ . The suboptimal estimates  $\omega_{oi,subopt}$ ,  $i=1,2$ , for  $\omega_o$  can be obtained as,

$$\hat{\omega}_{oi,subopt} = \frac{\mathbf{K}^T \mathbf{w}_i}{(\mathbf{K}^T \mathbf{K})}, \forall i=1, 2, \mathbf{K} := [-K, -K+1, \dots, 0, \dots, K]^T \quad (21)$$

Equation (21) is similar to the least squares estimator proposed in [22, eq. (35)], with subtle differences due to the model choice.

In order to estimate the remaining parameters, albeit suboptimally, one first needs to estimate the amplitude  $\rho_i$ . For this purpose, we employ a computationally efficient technique using higher order statistics which was proposed in [22, eq. (50-52)],

$$\hat{\rho}_{i,subopt} = \sqrt{2 \left( \frac{1}{N} \sum_{n=0}^{N-1} |x_i(n)|^2 \right)^2 - \frac{1}{N} \sum_{n=0}^{N-1} |x_i(n)|^4}, \forall i=1, 2 \quad (22)$$

The above equation relies on the higher order moments of the Gaussian random variable, and may not be valid for other types of distributions. The estimation of  $d_i$  depends on classifying the signal returns as wideband or narrowband. We consider the wideband case<sup>1</sup>. The suboptimal estimator proposed in [23], and also used in, [22, eq. (38), eq. (40)], and [24] can be applied to obtain the estimate of  $d_i$ ,  $i=1, 2$ , as

$$\hat{d}_i = \sqrt{\frac{2(\mathbf{y}_i - \mathbf{y}_i^*)^T (\mathbf{K} - \mathbf{K})}{\rho_i^2 (\mathbf{y}_i^H \mathbf{y}_i)}}, \forall i=1, 2 \quad (23)$$

The estimate for  $R_o$  is given by,

$$\hat{R}_{o,subopt} = (\angle X_2(0) X_1^*(0))c / 4\pi(f_2 - f_1) \quad (24)$$

Indeed, other techniques, based on (20), can be considered for estimating  $R_o$ . However, the suboptimal estimates of (24) were found to perform reasonably well in terms of the mean square error. For  $\varphi_o$ , we use the LS estimator proposed in [22] after appropriately demodulating the phase estimates for  $R_o$ .

$$\hat{\varphi}_{oi,subopt} = \frac{-\mathbf{K}^T \arg(\mathbf{y}_i \exp(-j4\pi f_i \hat{R}_{o,subopt} / c))}{\|\mathbf{K}\|^2}, \forall i=1, 2 \quad (25)$$

---

<sup>1</sup> Narrowband case is treated in [22] and is much simpler than the wideband case.

In (25),  $\arg(\cdot)$  is the unwrapped phase operator, which operates element-wise on a vector. We note that the suboptimal techniques for vibrational MD rely heavily on peak picking in the discrete Fourier transform of the returns and could suffer considerably for low signal-to-noise ratios (SNRs).

It is important to note that there are two sets of suboptimal estimates for  $\omega_o, d$ , and  $\varphi_o$  corresponding to the two carrier frequencies, whereas only one suboptimal estimate for  $R_o$ . In step 2 of the IRNLS, we only need a single suboptimal estimate of  $\omega_o$  for initialization. In the absence of any *a priori* information on the operating conditions, for example, the SNR at the two carriers, one can simply average the suboptimal estimates to obtain a single value as  $\omega_{osubopt} = (\omega_{o1,subopt} + \omega_{o2,subopt}) / 2$ . However, more sophisticated strategies, such as  $\omega_{osubopt} = w_1 \omega_{o1,subopt} + w_2 \omega_{o2,subopt}$ ,  $w_1 + w_2 = 1$  can be used if prior knowledge of the operating conditions is available. Likewise for  $d$  and  $\varphi_o$ . It is further noted that the suboptimal estimates for  $R_o$  and  $\rho_i$  are not required to launch the IRNLS, as these parameters are not involved in step 2 maximizations in the IRNLS.

### 1.4.2 Rotational MD

Consider the single blade returns of (15). Ignoring the noise for the time being, the Fourier transform of (15), denoted as  $X_i(\omega)$ , is given by

$$X_i(\omega) = H_i(\omega, \psi') * e^{j4\pi f_i R_o / c} \sum_{m=-\infty}^{\infty} j^m J_m(d) e^{-jm\varphi_o} \delta(\omega - m\omega_o) \quad (26)$$

where '\*' denotes the convolution operator, and  $H_i(\omega, \psi')$  is the Fourier transform of  $h_i(n; \psi')$ . The sinc fluctuation in  $h_i(n; \psi')$  can be expressed in terms of the spherical Bessel function of zero order, denoted by  $j_o(\cdot)$ , leading to [21]

$$h_i(n; \psi') = \rho_i j_o \left( \frac{4\pi f_i d \cos(\omega_o n - \varphi_o)}{c} \right) \quad (27)$$

Expressing  $j_o(\cdot)$  in terms of the Bessel function of the first kind, and using its integral equivalent, we obtain

$$\begin{aligned}
h_i(n; \psi') &= \rho_i \sqrt{\frac{\pi}{2 \left( \frac{4\pi f_i d \cos(\omega_o n - \varphi_o)}{c} \right)}} J_{1/2} \left( \frac{4\pi f_i d \cos(\omega_o n - \varphi_o)}{c} \right) \\
&= \frac{\rho_i \sqrt{\pi}}{\Gamma(1)\Gamma(1/2)} \int_0^1 \cos \left( \frac{4\pi f_i d \cos(\omega_o n - \varphi_o)}{c} y \right) dy
\end{aligned} \tag{28}$$

where  $\Gamma(\cdot)$  denotes the gamma function. The integrand in (28) can be simplified further using the Jacobi-Anger series [21],

$$\cos \left( \frac{4\pi f_i d \cos(\omega_o n - \varphi_o)}{c} y \right) = J_0 \left( \frac{4\pi f_i d}{c} y \right) + 2 \sum_{m=1}^{\infty} (-1)^m J_{2m} \left( \frac{4\pi f_i d}{c} y \right) \cos(m(2\omega_o n - 2\varphi_o)) \tag{29}$$

Using (29) in (28), and then applying the Fourier transform, we obtain

$$H_i(\omega, \psi') = \frac{2\pi\rho_i\sqrt{\pi}}{\Gamma(1)\Gamma(1/2)} \int_0^1 \left[ J_0 \left( \frac{4\pi f_i d}{c} y \right) \delta(0) + \sum_{m=1}^{\infty} (-1)^m J_{2m} \left( \frac{4\pi f_i d}{c} y \right) (\delta(\omega - 2m\omega_o) e^{-2mj\varphi_o} + \delta(\omega + 2m\omega_o) e^{2mj\varphi_o}) \right] dy \tag{30}$$

Using the identity  $\int_0^a J_\nu(x) dx = 2 \sum_{r=1}^{\infty} J_{\nu+2r+1}(a)$ , in (30), we obtain

$$H_i(\omega, \psi') = \frac{\rho_i \sqrt{\pi}}{\Gamma(1)\Gamma(1/2)} \times \frac{c}{f_i d} \left[ \sum_{r=1}^{\infty} J_{0+2r+1} \left( \frac{4\pi f_i d}{c} \right) \delta(0) + \sum_{m=1}^{\infty} (-1)^m \left( \delta(\omega - 2m\omega_o) e^{-2mj\varphi_o} + \delta(\omega + 2m\omega_o) e^{2mj\varphi_o} \right) \sum_{r=1}^{\infty} J_{2m+2r+1} \left( \frac{4\pi f_i d}{c} \right) \right] \tag{31}$$

Interestingly, the function in (31) has harmonics at  $0, \pm 2\omega_o, \pm 4\omega_o, \dots$ , where amplitudes are scaled by a complex combination of Bessel functions. From (26) and using the result in (31), it can be readily seen that the resulting expression after convolution retains the original harmonic structure, i.e., the spectrum  $X_i(\omega)$  has peaks at  $0, \pm \omega_o, \pm 2\omega_o, \dots, \infty$ , akin to the vibrational MD spectrum. Likewise, it can be shown that, for  $Q$  identical blades, the Fourier spectrum of has harmonics at  $0, \pm Q\omega_o, \pm 2Q\omega_o, \dots, \infty$ . In practice, similar to the vibrational MD case, there exist only a finite number of dominant harmonics for rotational MD. In essence, the suboptimal estimator, designed for the vibrational MD, can be also used for rotational

MD to estimate  $Q\omega_o$ , from which the suboptimal estimate of the rotational frequency denoted as  $\hat{\omega}_{oi,subopt}, i=1,2$  is readily obtained.

Unlike the vibrational MD case, it is not straightforward to use the amplitude of the peaks in the return signal spectrum to obtain suboptimal estimates of  $d$  and  $\varphi_o$  for rotational MD. This is due to the complicated structure of (31) and (26) involving Bessel functions and convolution. Instead, we use the grid search technique for estimating  $d$  and  $\varphi_o$ . The suboptimal estimates for  $d$  and  $\varphi_o$  at each of the carrier frequencies are readily obtained as,

$$(\hat{d}_{i,subopt}, \hat{\varphi}_{oi,subopt}) = \arg \max_{d, \varphi_o} G_i(\hat{\omega}_{oi,subopt}, d, \varphi_o)$$

$$G_i(\omega_o d, \varphi_o) = \frac{\left| \sum_{n=0}^{N-1} x_i(n) e^{-j4\pi f_i d \cos(\omega_o n - \varphi_o)/c} \right|^2}{\sum_{n=0}^{N-1} \gamma_i^2(n; \psi)} \quad (32)$$

The cost function  $G_i(\omega_o d, \varphi_o)$  is easily recognized as the ML cost function operating individually on the returns at the carrier  $f_i$ . Although (32) is designed for a single blade, it can be used directly when multiple blades are present. In fact, the presence of  $Q$  blades will reveal itself as  $Q$  dominant peaks in the cost function (32), provided that  $Q$  is finite.

The grid search on (32) is appealing because of two main reasons. Firstly, as opposed to traditional targets, rotating fans do not assume very high displacements. Thus, we can safely assume  $d \in (0, 1m]$ . Further,  $\varphi_o \in [0, 2\pi)$ . The entire parameter space can then be evaluated using a small and finite grid. For example, we can evaluate (32) for every 0.01m in the  $d$ -domain, and similarly for every  $0.01\pi$  in the  $\varphi_o$ -domain, which makes the grid search extremely feasible. Secondly, the visualization of the cost function using the grid search would indicate the global optimum corresponding to one blade, or several maxima corresponding to multiple blades in the radar returns. In other words, knowledge of the number of blades can be readily obtained, if it is not known *a priori*. For a reasonable SNR, the cost function in (32) will fail to reveal multiple peaks when  $Q \rightarrow \infty$ , which is quite unlikely for fans, or when the grid size is too



large to accommodate the support of all the peaks in the  $(d, \varphi_o)$  plane, in which case a single continuous peak is seen along the  $\varphi_o$ -axis.

Note that the suboptimal techniques for vibrational and to some extent rotational MD use the discrete Fourier transform, and thus, can be implemented using the FFT efficiently. It is now assumed that these suboptimal techniques give rise to estimates close to the true parameters so that the IRNLS-ML iterations converge to the optimal ML estimate.

## 1.5 Cramér-Rao Bounds

The vibrational MD CRBs were derived in [14]. In this section, we derive the multi-component rotational MD CRBs. Let  $\mathbf{F}$  be the Fisher information matrix and  $\boldsymbol{\theta} = [\boldsymbol{\psi}^T, \sigma_1^2, \sigma_2^2]^T$  be the complete parameter vector, where the MD parameter vector is defined as  $\boldsymbol{\psi} = [R_o, \omega_o, d, \varphi_o, \rho_1, \rho_2]^T$ . The FIM elements can be derived in a compact manner for the complex Gaussian pdf due to the Slepian-Bangs formula, which is given by [15],[25],

$$F_{\theta_r, \theta_s} = \text{Tr} \left\{ \mathbf{C}^{-1} \frac{\partial \mathbf{C}}{\partial \theta_r} \mathbf{C}^{-1} \frac{\partial \mathbf{C}}{\partial \theta_s} \right\} + 2 \text{Re} \left\{ \left[ \frac{\partial \boldsymbol{\mu}}{\partial \theta_r} \right]^H \mathbf{C}^{-1} \frac{\partial \boldsymbol{\mu}}{\partial \theta_s} \right\}, \quad (r, s) \in (1, 2, \dots, 8) \quad (33)$$

where  $\boldsymbol{\mu}$  and  $\mathbf{C}$  are the mean and the covariance matrix of the PDF, respectively. For the problem at hand, and using (33), it can be readily shown that

$$\begin{aligned} F_{\psi_r, \psi_s} &= 2 \text{Re} \left\{ \mathbf{1}^T \mathbf{E}_{\psi_r}^H \mathbf{C}^{-1} \mathbf{E}_{\psi_s} \mathbf{1} \right\}, \quad (r, s) \in (1, 2, \dots, 6) \\ \mathbf{E}_{\psi_r} &= \begin{bmatrix} \mathbf{E}_{1, \psi_r} \\ \mathbf{E}_{2, \psi_r} \end{bmatrix} \in \mathfrak{Z}^{2N \times Q}, \quad \mathbf{E}_{i, \psi_r} = [\mathbf{e}_{i1}^{\psi_r}, \mathbf{e}_{i2}^{\psi_r}, \dots, \mathbf{e}_{iQ}^{\psi_r}] \\ \mathbf{e}_{iq}^{\psi_r} &:= \frac{\partial}{\partial \psi_r} \boldsymbol{\beta}_{iq}(\boldsymbol{\psi}) = \frac{\partial}{\partial \psi_r} (\rho_i e^{j4\pi f_i R_o/c} \times \gamma_{iq}(\boldsymbol{\psi}') \square \mathbf{g}_{iq}(\boldsymbol{\psi}')) \end{aligned} \quad (34)$$

where  $\gamma_{iq}(\boldsymbol{\psi}')$  and  $\mathbf{g}_{iq}(\boldsymbol{\psi}')$  have been defined in (18). The derivatives with respect to the parameters are required. The partial derivatives of  $\boldsymbol{\beta}_{iq}(\boldsymbol{\psi})$  with respect to  $\psi_r, r = 1, 2, \dots, 6$  are given by,

$$\frac{\partial}{\partial R_o} \boldsymbol{\beta}_{iq}(\boldsymbol{\psi}) = \frac{j4\pi f_i}{c} \boldsymbol{\beta}_{iq}(\boldsymbol{\psi}), \quad \frac{\partial}{\partial \rho_i} \boldsymbol{\beta}_{iq}(\boldsymbol{\psi}) = \rho_i^{-1} \boldsymbol{\beta}_{iq}(\boldsymbol{\psi}) \quad (35)$$

$$\begin{aligned}
\frac{\partial}{\partial \omega_o} \mathbf{b}_{iq}(\boldsymbol{\psi}) &= \rho_i e^{j4\pi f_i R_o / c} \left( \frac{\partial \gamma_{iq}(\boldsymbol{\psi}')}{\partial \omega_o} \square \mathbf{g}_{iq}(\boldsymbol{\psi}') + \gamma_{iq}(\boldsymbol{\psi}') \square \mathbf{g}_{iq}(\boldsymbol{\psi}') \square \mathbf{n} \square \text{Im}\{\xi_q\} \times \frac{-j4\pi f_i d}{c} \right) \\
\xi_q &:= [1, e^{j\omega_o}, e^{2j\omega_o}, \dots, e^{j(N-1)\omega_o}]^T \times e^{-j\varphi_q}, \mathbf{n} := [0, 1, 2, \dots, N-1]^T \\
\frac{\partial \gamma_{iq}(\boldsymbol{\psi}')}{\partial \omega_o} &:= \begin{pmatrix} \text{Re}\{\mathbf{g}_{iq}(\boldsymbol{\psi}')\} \square \frac{-4\pi f_i d}{c} \mathbf{n} \square \text{Im}\{\xi_q\} \square \frac{4\pi f_i d}{c} \text{Re}\{\xi_q\} \\ -\text{Im}\{\mathbf{g}_{iq}(\boldsymbol{\psi}')\} \square \frac{-4\pi f_i d}{c} \mathbf{n} \square \text{Im}\{\xi_q\} \end{pmatrix} \square (\mathbf{v}^{\square -2}) \\
\mathbf{v} &:= \frac{4\pi f_i d}{c} \text{Re}\{\xi_q\}
\end{aligned} \tag{36}$$

where we define  $(\cdot)^{\square -k}$  as the element-wise division of a vector or a matrix raised to  $k$ -th power, i.e., if  $\mathbf{x} = [x_1, x_2, \dots, x_N]^T$ ,  $\mathbf{x}^{\square -k} = [1/x_1^k, 1/x_2^k, \dots, 1/x_N^k]^T$ . Using the same convention, the other derivatives which are required for evaluating the FIM are provided below.

$$\begin{aligned}
\frac{\partial}{\partial d} \mathbf{b}_{iq}(\boldsymbol{\psi}) &= \rho_i e^{j4\pi f_i R_o / c} \left( \frac{\partial \gamma_{iq}(\boldsymbol{\psi}')}{\partial d} \square \mathbf{g}_{iq}(\boldsymbol{\psi}') + \gamma_{iq}(\boldsymbol{\psi}') \square \mathbf{g}_{iq}(\boldsymbol{\psi}') \square \text{Re}\{\xi_q\} \times \frac{j4\pi f_i}{c} \right) \\
\frac{\partial \gamma_{iq}(\boldsymbol{\psi}')}{\partial d} &:= \begin{pmatrix} \text{Re}\{\mathbf{g}_{iq}(\boldsymbol{\psi}')\} \square \frac{4\pi f_i}{c} \text{Re}\{\xi_q\} \square \frac{4\pi f_i d}{c} \text{Re}\{\xi_q\} \\ -\text{Im}\{\mathbf{g}_{iq}(\boldsymbol{\psi}')\} \square \frac{4\pi f_i}{c} \text{Re}\{\xi_q\} \end{pmatrix} \square (\mathbf{v}^{\square -2})
\end{aligned} \tag{37}$$

$$\begin{aligned}
\frac{\partial}{\partial \varphi_o} \mathbf{b}_{iq}(\boldsymbol{\psi}) &= \rho_i e^{j4\pi f_i R_o / c} \left( \frac{\partial \gamma_{iq}(\boldsymbol{\psi}')}{\partial \varphi_o} \square \mathbf{g}_{iq}(\boldsymbol{\psi}') + \gamma_{iq}(\boldsymbol{\psi}') \square \mathbf{g}_{iq}(\boldsymbol{\psi}') \square \text{Im}\{\xi_q\} \times \frac{j4\pi f_i d}{c} \right) \\
\frac{\partial \gamma_{iq}(\boldsymbol{\psi}')}{\partial \varphi_o} &:= \begin{pmatrix} \text{Re}\{\mathbf{g}_{iq}(\boldsymbol{\psi}')\} \square \frac{4\pi f_i d}{c} \text{Im}\{\xi_q\} \square \frac{4\pi f_i d}{c} \text{Re}\{\xi_q\} \\ -\text{Im}\{\mathbf{g}_{iq}(\boldsymbol{\psi}')\} \square \frac{4\pi f_i d}{c} \text{Im}\{\xi_q\} \end{pmatrix} \square (\mathbf{v}^{\square -2})
\end{aligned} \tag{38}$$

From (33), two important observations are in order. First, the cross FIM elements with respect to  $\rho_i$  and the parameter  $R_o$  are zero for a single fan blade, and are in general non-zero when multiple blades are present, i.e.,

$$F_{\rho_i R_o} = 0, i = 1, 2, Q = 1 \tag{39}$$

This is because the amplitude,  $\rho_i$ ,  $i = 1, 2$  is not embedded in the phase of the signal, and similarly the range parameter  $R_o$  is not a function of  $h_i(n; \boldsymbol{\psi}')$ . The more important second observation arises from the



fact that since the covariance matrix is not a function of the parameters in  $\boldsymbol{\psi}$ , the cross FIM elements with respect to  $\sigma_i^2$  and all the parameters in  $\boldsymbol{\psi}$  are zero, i.e.,

$$F_{\sigma_i^2 \boldsymbol{\psi}_r} = 0, \quad r \in (1, \dots, 6), \quad i = 1, 2, \quad \forall Q \quad (40)$$

Eq. (40) implies that, regardless of the knowledge (or no knowledge) of the parameters,  $\sigma_i^2$ , the CRBs depend only on the inverted FIM of the MD parameters, including the range. Further simplifications of the FIM elements are tedious to derive. The above equations can be used to numerically evaluate the FIM and the CRBs.

## 1.6 Simulations and Experimental Results

### 1.6.1 Simulations

The carrier frequencies for the dual frequency operation are set to  $f_1 = 903 \text{ MHz}$  and  $f_2 = 921 \text{ MHz}$ . Also, we average the suboptimal estimates of parameters, such as  $\omega_o, d$ , and  $\varphi_o$ , corresponding to the two carrier frequencies, and use the averaged values for IRNLS initialization.

We first consider the vibrational MD. For simplicity we assume  $\rho_i = \rho$ . The SNRs for this case are defined as  $SNR_i = \|\mathbf{s}_i\|^2 / \sigma_i^2 N, \forall i = 1, 2$ . We force  $SNR_1 = 10 \text{ dB}$  and vary  $SNR_2$  from  $-10 \text{ dB}$  onwards, in increments of  $5 \text{ dB}$ . Figures 2(a)-(d) demonstrate the MSE for the IRNLS and the suboptimal estimation schemes. The number of Monte Carlo trials was 250 and the maximum number of allowed iterations,  $k_{\max}$ , was chosen as 10. The number of data samples  $N = 1024$ , and the parameters of the MD signal used were  $\boldsymbol{\psi} = [R_o = 1.3 \text{ m}, d = 0.07 \text{ m}, \omega_o = 0.123\pi, \varphi_o = \pi/3]^T$ . The received signal is wideband for the aforementioned carrier frequencies. In the suboptimal estimation scheme, we forced  $m = K = 1$  which makes  $\mathbf{K} = [-1, 0, 1]^T$  in eqs. (21), (23), and (25). This choice of  $K$  provides satisfactory results, and amounts to using the first harmonic and DC for estimation, i.e., the suboptimal scheme operates in a narrowband framework. The estimates after the first iteration of the IRNLS correspond to optimizing the

NLS cost function  $\sum_{i=1}^2 \|\mathbf{x}_i - \mathbf{s}_i(\boldsymbol{\psi})\|^2 / N$ , and are also provided in Fig. 2 for comparison. It is clear from

Fig. 2(a)-(d) that the IRNLS gives better MSE than the NLS and of course the suboptimal schemes. The corresponding CRBs for single frequency and dual frequency operations are also shown. It is clear that the single frequency CRBs guide the ML behavior for the dual frequency operations. The estimates are clearly above the dual-frequency CRBs. The IRNLS offers superior performance than the NLS for all parameters except  $R_o$  for which both the NLS and IRNLS give similar MSE. It is noted that when  $SNR_1 = SNR_2 \Rightarrow \sigma_1^2 = \sigma_2^2$ , the IRNLS and NLS MSE are the same for all parameters. It is clear that the MSE of the parameters decreases with the SNR, specifically  $SNR_2$  as predicted by the CRBs.

Next, we consider a rotating fan with multiple blades. Figs. 3 and 4 shows the corresponding CRBs with respect to  $SNR_2$  and the data record length,  $N$ , respectively. The parameters used in generating these figures were  $\boldsymbol{\psi} = [R_o = 1.4m, d = 0.253m, \omega_o = 0.02\pi, \phi_o = \pi/8]^T$ . The number of blades vary from one to four. From Fig. 3, it is evident that multiple blades yield better estimates for all the parameters. However, from Fig. 4, we observe that, for a fixed SNR and varying  $N$ , the CRBs corresponding to multiple blades are more or less similar to those for a single. In general, for the case of multiple identical blades, greater confidence in the estimates can be obtained which implies better estimation of the parameters. Consider, for example, the time-frequency distribution of a four blade return. The instantaneous frequency (IF) for the blades is identical in structure but differs in the phase parameter  $\phi_p$ . It is clear that, for example, the rotational frequency can be estimated with a greater confidence since four different IF curves in the TF plane can be used jointly to estimate the rotational frequency, rather than a single IF curve when a single blade is present, provided that the IF curves are mostly non-overlapping in the TF plane. The performance of the NLS and IRNLS and suboptimal estimators for the rotational MD corresponding to a fan with three blades is shown in Fig. 5. Parameters identical to those for Figs. 3 and 4 were used in Fig. 5. For generating the MSE, the number of Monte Carlo trials was set to 200, and the maximum number of allowed iterations,  $k_{\max}$ , was chosen as 10. A coarse grid search was used as in (32) to

suboptimally estimate the parameters  $d$  and  $\varphi_o$ . In the rotational MD simulations, we used the root-MUSIC algorithm to estimate the harmonics instead of peak picking in order to compute the MSE for SNR values less than 0dB. In Fig. 6(a), we show the LLcost as given in (8a), as well as the norm of the difference in parameter estimates for various iterations in the IRNLS in Fig. 6(b). Parameters identical to the rotational MD simulation of Fig. 5 were used to generate Fig. 6, except that we show one Monte Carlo simulation, and  $(SNR_1, SNR_2) = (10, 5)$  dB. It is clear from Fig. 6(b) that after six iterations of the IRNLS, the norm becomes zero. In essence, there exists a cluster or accumulation point as shown in Fig. (6b). The discussion in Appendix-A gives more details on the cluster point with respect to the IRNLS.

### 1.6.2 Experimental Results

In this section, we present results of IRNLS applied to various MD signal returns measured using a dual-frequency radar in a laboratory setting. First, a 12in conducting sphere was tied to the ceiling with a nylon string, and excited to oscillate in a simple harmonic fashion. This experiment corresponds to the vibrational MD scenario. The approximate range to the target was 16.4ft or 4.99m, the carrier frequencies were chosen to be 906.3 and 919.6 MHz, and the sampling frequency was 100Hz. More details on the experiment can be found in [26]. We processed only the first seven seconds of data, comprising 700 samples, in order to avoid damped oscillations. Figure 7 shows the IRNLS, NLS, and suboptimal instantaneous frequency (IF) trajectories overlaid on the spectrogram of the data. Clearly, the IRNLS yields better estimates when compared to the NLS, and agrees with the IF of the data for both carrier frequencies. The range estimates for IRNLS and NLS were 4.89m and 4.83m, respectively.

Second, the IRNLS is applied to measured returns from a table-top fan with 4-metallic blades. The carrier frequencies are chosen as 903.6 MHz and 921 MHz. The distance from the center of the fan to the radar was 3 m, and the sampling frequency was chosen to be 5 kHz to avoid aliasing. Two datasets, one for azimuth equal to  $0^\circ$ , and the other for  $60^\circ$  azimuth, were used for the ML analysis. Fig. 8(a) shows the spectrogram of the raw data for  $0^\circ$  azimuthal aspect, using a rectangular window of 101 samples which corresponds to around 130 % of the period of the rotation. For subsequent ML analysis, the data was

decimated by a factor of 5. The 2D grid search cost function, as given in (32) was used, and the cost function is shown in Fig. 8(b) for the second carrier. The grid was initialized with the rotational frequency estimate obtained from the Fourier spectrum. We can clearly see 4 dominant peaks corresponding to the 4 blades. The suboptimal estimates were used to initialize the ML algorithm. The range estimates and final LL costs are provided in Table I. The results in Table I indicate that both the NLS and IRNLS perform exceptionally well for this dataset. Fig. 9(a) shows the spectrogram of the raw data (not resampled), corresponding to 60° azimuthal aspect, using the same window length as in Fig. 8(a). The 2D grid search cost function corresponding to the second carrier frequency is shown in Fig. 9(b). Similar to Fig. 8(b), the 2D grid in Fig. 9(b) clearly shows 4 dominant peaks. The corresponding ML estimates for the range are shown in Table II, which shows that the IRNLS performs better than the NLS.

## 1.7 Conclusions

In this chapter, we considered dual frequency Doppler radars for range estimation of moving targets with application to urban sensing. The ML estimator was derived for the micro-Doppler motion profile, which is commonly exhibited by indoor moving targets. It was shown that the ML estimator, although not solvable in closed form, can be provided using a step-wise iterative algorithm termed as the IRNLS. The algorithm's solution and procedure depends on the motion profile model. The initial conditions are provided using suboptimal values which rely on the harmonic nature of the radar returns. For simulated data, the algorithm was shown to be superior in terms of the MSE when compared to suboptimal estimators. The iterative ML was also applied to data measurements corresponding to indoor moving targets, yielding superior IF estimates and good estimates of the range.



## Appendix-A: Convergence of the IRNLS algorithm

In this appendix, we do not assume any specific motion profile. The results are general and applicable to

$\theta = [\psi^T, \sigma_1^2, \sigma_2^2]^T$ ,  $\psi = [\psi_1, \psi_2, \psi_3, \dots, \psi_p]^T$  for the IRNLS.

**Proposition 1:** The FIM for the dual frequency radar can be expressed as

$$\mathbf{F}(\theta) = \begin{bmatrix} \mathbf{F}(\psi) & 0 & 0 \\ 0 & N / \sigma_1^4 & 0 \\ 0 & 0 & N / \sigma_2^4 \end{bmatrix}$$

(A.1)

**Proof:** The proof of the above proposition is standard and can be easily obtained using the Slepian-Bangs formula [15],[25].

**Proposition 2:** If the minimization in (10) is carried out using the method of Fisher scoring, with step size equal to unity, then the IRNLS algorithm becomes the Fisher scoring technique for the ML problem.

**Proof:** We first note that for a fixed arbitrary covariance matrix, the gradient vector with respect to the desired parameter vector  $\psi$  of the negative LL is identical to the gradient vector of the cost function in (10). Hence, the Fisher scoring technique for the  $k^{th}$  iteration for estimating  $\psi_k$  is then given as [27]

$$\hat{\psi}_k = \hat{\psi}_{k-1} - \lambda_k \mathbf{F}^{-1}(\hat{\psi}_{k-1})(-\nabla \mathbf{J}(\hat{\psi}_{k-1})) \quad (\text{A.2})$$

where  $\mathbf{F}^{-1}(\hat{\psi}_{k-1})$  and  $-\nabla \mathbf{J}(\hat{\psi}_{k-1})$  are the FIM, and the gradient vector of the cost function in (10), obtained using the previous estimate, and  $\lambda_k$  is the step size parameter. The negative sign in (A.2) preceding the second term indicates the minimization of the cost function (10), or equivalently minimization of the negative LL<sup>2</sup>. The Fisher scoring applied to the negative LL for the entire parameter vector  $\theta$ , takes the following form.

$$\hat{\theta}_k = \hat{\theta}_{k-1} - \lambda_k \begin{bmatrix} \mathbf{F}^{-1}(\hat{\psi}_{k-1}) & 0 & 0 \\ 0 & \hat{\sigma}_{1(k-1)}^4 / N & 0 \\ 0 & 0 & \hat{\sigma}_{2(k-1)}^4 / N \end{bmatrix} \begin{bmatrix} -\nabla \mathbf{J}(\psi) \\ -\partial \ln(p(\mathbf{x}; \psi) / \partial \sigma_1^2) \\ -\partial \ln(p(\mathbf{x}; \psi) / \partial \sigma_2^2) \end{bmatrix}_{\psi = \hat{\psi}_{k-1}, \sigma_i^2 = \hat{\sigma}_{i(k-1)}^2, i=1,2} \quad (\text{A.3})$$

---

<sup>2</sup> The sign is flipped for the conventional Fisher scoring technique which is applied to the maximizing the LL [27].



The term  $-\partial \ln(p(\mathbf{x}; \boldsymbol{\psi})) / \partial \sigma_i^2$ ,  $\forall i=1,2$  was an intermediate step in deriving (7). Using this intermediate step with  $\lambda_k = 1$ , and multiplying the matrix and the gradient vector in (A.3), we obtain (A.2) with  $\lambda_k = 1$ , and

$$\hat{\sigma}_{ik}^2 = \|\mathbf{x}_i - \mathbf{s}_i(\hat{\boldsymbol{\psi}}_{k-1})\|^2 / N, \quad \forall i=1,2 \quad (\text{A.4})$$

Equation (A.4) is the remaining key equation in the IRNLS for updating in (10). Q. E. D.

The special case of  $\lambda_k = 1$  is oftentimes used in the literature (see [15], and also [27]). The above proposition implies that the IRNLS is a special case of Fisher scoring algorithm. However, as well known, the Fisher scoring converges if the suboptimal estimates used to initialize it are close to the optimal ML solution. In [27, remark 4.1 and remark 4.2], under certain conditions it was shown that the Fisher scoring method converges to at least a local minimum of the negative LL as  $N \rightarrow \infty$ , i.e., asymptotically. The same follows from proposition 2 for the IRNLS, more details can be seen in [27]. If the negative LL objective is convex, which is a standard assumption for ML techniques, then the Fisher scoring converges surely to the global minimum [28]. Convergence is also attained if the initialization is contained within a set including the optimal solution, where the objective is locally convex [28]. For step-wise iterative ML schemes, an interesting result is provided in [29, lemma-1], where the authors prove the existence of a cluster point or an accumulation point, denoted as  $\boldsymbol{\theta}'$ , for the sequence of parameter iterates given by  $\{\boldsymbol{\theta}_k\}$  if the negative LL is bounded below, which is definitely satisfied by the Gaussian pdf. We can, thus, deduce that the IRNLS iterates also exhibit similar behavior. Essentially, if there exists a unique cluster point  $\boldsymbol{\theta}'$  for any sequence  $\{\boldsymbol{\theta}_k\}$ , then  $\boldsymbol{\theta}'$  is the ML solution  $\hat{\boldsymbol{\theta}}(\mathbf{x})$ . This directly implies that  $\lim_{k \rightarrow \infty} \|\boldsymbol{\theta}_{k+1} - \boldsymbol{\theta}_k\| = 0$ . The existence of the cluster point was also proven in [28] for the constrained Fisher scoring technique. We now prove that the Fisher scoring and hence the IRNLS increases the LL for every iteration monotonically.

**Proposition 3:** Under certain assumptions, the Fisher scoring and hence the IRNLS increases the LL for every  $k$ , until convergence as  $N \rightarrow \infty$ .

*Proof:* It is required to prove  $\ln(p(\mathbf{x}; \boldsymbol{\theta}_{k+1})) - \ln(p(\mathbf{x}; \boldsymbol{\theta}_k)) > 0$ . Expanding the pdf about the arbitrary point  $\lambda_k \mathbf{F}^{-1}(\boldsymbol{\theta}_k) \nabla \mathbf{J}(\boldsymbol{\theta}_k)$ , where  $\nabla \mathbf{J}(\boldsymbol{\theta}_k)$  is the gradient of the LL evaluated at the previous  $\boldsymbol{\theta}_k$ , using the Taylor series expansion.

$$\begin{aligned} \ln(\mathbf{x}; \boldsymbol{\theta}_{k+1}) - \ln(\mathbf{x}; \boldsymbol{\theta}_k) &= \lambda_k \nabla^T \mathbf{J}(\boldsymbol{\theta}_k) \mathbf{F}^{-1}(\boldsymbol{\theta}_k) \nabla \mathbf{J}(\boldsymbol{\theta}_k) \\ &+ \frac{\lambda_k^2}{2} \nabla^T \mathbf{J}(\boldsymbol{\theta}_k) (\mathbf{F}^T(\boldsymbol{\theta}_k))^{-1} [\nabla(\nabla^T \mathbf{J}(\boldsymbol{\theta}_k))] \nabla \mathbf{J}(\boldsymbol{\theta}_k) \mathbf{F}^{-1}(\boldsymbol{\theta}_k) \\ &+ O(\|\mathbf{F}^{-1}(\boldsymbol{\theta}_k) \nabla \mathbf{J}(\boldsymbol{\theta}_k)\|) \end{aligned}$$

(A.5)

where  $[\nabla(\nabla^T \mathbf{J}(\boldsymbol{\theta}_k))]$  is the Hessian matrix evaluated at  $\boldsymbol{\theta}_k$ . Now using the results in [30], i.e., as  $N \rightarrow \infty$  the negative Hessian matrix converges to the FIM with probability 1, we can replace the negative Hessian matrix with the FIM,  $\mathbf{F}(\boldsymbol{\theta}_k)$  in (A.5), further assuming that the LL can be approximated as a quadratic, i.e., ignoring the higher order terms, we get

$$\begin{aligned} \ln(\mathbf{x}; \boldsymbol{\theta}_{k+1}) - \ln(\mathbf{x}; \boldsymbol{\theta}_k) &= \lambda_k \nabla^T \mathbf{J}(\boldsymbol{\theta}_k) \mathbf{F}^{-1}(\boldsymbol{\theta}_k) \nabla \mathbf{J}(\boldsymbol{\theta}_k) - \frac{\lambda_k^2}{2} \nabla^T \mathbf{J}(\boldsymbol{\theta}_k) \mathbf{F}^{-1}(\boldsymbol{\theta}_k) \nabla \mathbf{J}(\boldsymbol{\theta}_k) \\ &= (\lambda_k - \lambda_k^2 / 2) \nabla^T \mathbf{J}(\boldsymbol{\theta}_k) \mathbf{F}^{-1}(\boldsymbol{\theta}_k) \nabla \mathbf{J}(\boldsymbol{\theta}_k) \end{aligned} \quad (\text{A.6})$$

Since the FIM is nonsingular and positive definite  $\forall \boldsymbol{\theta}_k$ , with  $\lambda_k \in (0, 1]$ , we have (A.6) is always positive, and becomes zero at the local optimum solution. This proves the proposition for the Fisher scoring approach. Likewise, substituting  $\lambda_k = 1, \forall k$  it is readily seen that (A.6) is always positive. This proves the proposition for the IRNLS. Q. E.D.

In this Appendix, we have proved that the IRNLS is a special case of Fisher scoring. Therefore, some of the results for Fisher scoring directly follow through to the IRNLS. In the simulations, we demonstrate the existence of the cluster point and the monotonic increase in the LL objective for every iteration.

## References

- [1] Journal of the Franklin Institute, Special Issue on 'Advances in Indoor Radar Imaging,' Sept. 2008, 345, (6)
- [2] Proceedings of the 2008 IEEE International Conference on Acoustics, Speech, and Signal Processing, Special Session on 'Through-the-Wall Radar Imaging,' Las Vegas, USA, Apr. 2008, pp. 5173-5196
- [3] Borek, S. E.: 'An overview of through the wall surveillance for homeland security', Proc. 34<sup>th</sup> Applied Imagery and Pattern Recognition Workshop, Washington D.C., USA, Oct. 2005
- [4] Proceedings of the 2005 IEEE AP-S International Symposium, Special Session on 'Through-Wall Imaging and Sensing', Washington D.C., USA, Jul. 2005, 3B, pp. 317-341
- [5] Skolnik, M. I.: 'Introduction to Radar Systems' (McGraw-Hill, New York, 3rd edn. 2002)
- [6] Amin, M., Zeman, P. D., Setlur, P., and Ahmad, F.: 'Moving target localization for indoor imaging using dual frequency CW radars', Proc. IEEE Workshop on Sensor Array and Multi-channel Processing, Waltham, Massachusetts, USA, Jul. 12-14, 2006, pp. 367-371
- [7] Ridenour, L. N.: 'Radar System Engineering', Vol. 1 of MIT Radiation Laboratory Series (McGraw-Hill, NY, 1947)
- [8] Boyer, W. D.: 'A duplex, Doppler, phase comparison radar', IEEE Trans. Aerosp. Navig. Electron., 1963, ANE-10, (3), pp. 27-33
- [9] Chen, V. C., Li, F., Ho, S. -S., and Wechsler, H.: 'Analysis of micro-Doppler signatures', IEE Proceedings Radar, Sonar and Navigation, Aug. 2003, (4), 150, pp. 271-276
- [10] Thayaparan, T., Abrol, S., Riseborough, E., Stankovic, L., Lamothe, D., and Duff, G.: 'Analysis of radar micro-Doppler signatures from experimental helicopter and human data', IET Radar Sonar and Navig., Aug. 2007, 1, (4), pp. 289-299

- [11] Smith, G., Woodbridge, K., Baker, C. J., and Griffiths, H.: 'Multistatic micro-Doppler radar signatures of personnel targets', IET Signal Processing, Special Issue on Time-Frequency Approach to Radar Detection, Imaging, and Classification, In press.
- [12] Rife, D., and Boorstyn, R.: 'Single tone parameter estimation from discrete-time observations', IEEE Trans. Inf. Theory, Sept. 1974, 20, (5), pp. 581-598
- [13] Saha, S., and Kay, S. M.: 'Maximum likelihood parameter estimation of superimposed chirps using Monte Carlo importance sampling', IEEE Trans. Sig. Proc., Feb. 2002, 50, (2), pp. 224-230
- [14] Setlur, P., Amin, M., and Ahmad, F.: 'Dual frequency Doppler radar for indoor range estimation: Cramér-Rao bound analysis', IET Signal Processing, Special Issue on Time-Frequency Approach to Radar Detection, Imaging, and Classification, In press.
- [15] Kay, S. M.: 'Fundamentals of Statistical Signal Processing, Volume: I, Estimation Theory' (Prentice Hall, Englewood Cliffs, NJ, 1993)
- [16] Green, P. J.: 'Iteratively reweighted least squares for maximum likelihood estimation, and some robust and resistant alternatives', Journal of the Royal statistical society, 1984, 46, (2), pp. 149-192
- [17] Huber, P. J.: 'Robust Statistics' (John Wiley, New York, 1981)
- [18] Chen, V. C, and Ling, H.: 'Time-Frequency Transforms for Radar Imaging and Signal Analysis' (Artech House, Boston, 2002)
- [19] Martin, J., and Mulgrew, B.: 'Analysis of the theoretical radar return signal from aircraft propeller blades', Proc. IEEE Radar Conf., Arlington, VA, USA, May 7-10, 1990, pp. 569-572
- [20] Schneider, H.: 'Application of an autoregressive reflection model for the signal analysis of radar echoes from rotating objects,' Proc. Int. Conf. Acoust., Speech, Signal Process., New York, NY, Apr. 11-14, 1988, pp. 1236-1239
- [21] Abramowitz, M. and Stegun, I. A.: 'Handbook of Mathematical Functions with Formulas, Graphs, and Mathematical tables' (Dover Publications, New York, 1972)

- [22] Gini, F., and Giannakis, G. B.: 'Hybrid FM-polynomial phase signal modeling: parameter estimation and Cramér-Rao bounds', IEEE Trans. Signal Process., Feb. 1999, 47, (2), pp. 363-377
- [23] Huang, S.-R, Lerner, R. M., and Parker, K. J.: 'On estimating the amplitude of harmonic vibration from the Doppler spectrum of reflected signals', Journal Acou. Soc. of Amer., Dec. 1990, 88, (6), pp. 2702-2712
- [24] Zhou, G., and Giannakis, G. B.: 'Parameter estimation of FM signals using cyclic statistics', Proc. IEEE Int. Symp. Time-Freq. Time-Scale Analysis., Philadelphia, PA, Oct. 25-28, 1994, pp. 248-251
- [25] Stoica, P., and Moses, R.: 'Introduction to Spectral Analysis' (Prentice-Hall, New Jersey, 1997)
- [26] Setlur, P., Amin, M., Ahmad, F., and Zeman, P. D.: 'Experiments on through-the-wall detection and ranging', Proc. SPIE Symposium on Defense and Security, Orlando, FL., Apr. 2007
- [27] Osbourne, M. R.: 'Fisher's method of scoring', International Statistical Review, Apr. 1992, 60, (1), pp. 99-117
- [28] Moore, T. J., Sadler, B. M., and Kozick, R. J.: 'Maximum-likelihood estimation, the Cramér-Rao bound, and the method of scoring with parameter constraints', IEEE Trans. Signal Process., Mar. 2008, 56, (3), pp. 895-907
- [29] Oberhoffer, W., and Kmenta, J.: 'A general procedure for obtaining the maximum likelihood estimates in generalized regression methods', Econometrica, May 1974, 42, (3), pp. 579-590
- [30] Serfling, R. J.: 'Approximation Theorems of Mathematical Statistics' (John Wiley, New York, 1980)



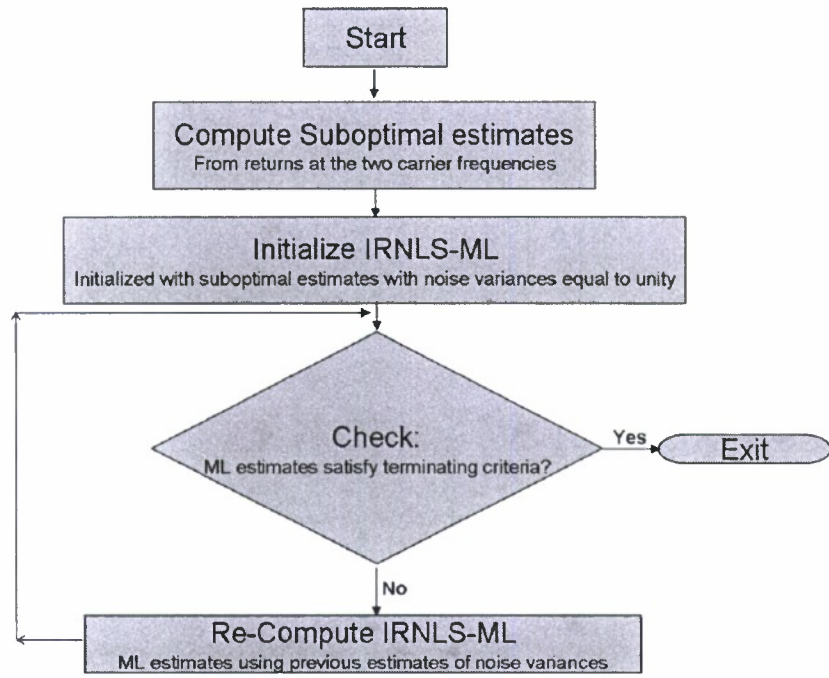
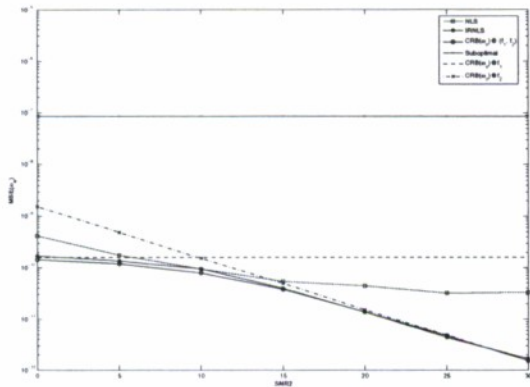
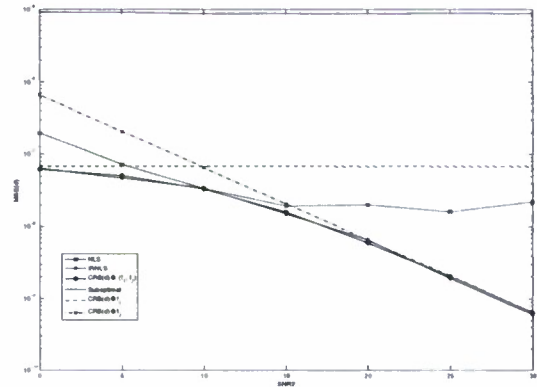


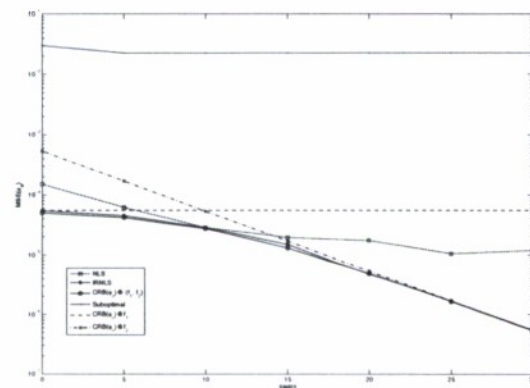
**Fig. 1** Flowchart of IRNLS ML.



(a)



(b)



(d)

(c)

Fig. 2 MSE of vibrational MD parameters. IRNLS Comparson wrt CRBs and NLS.

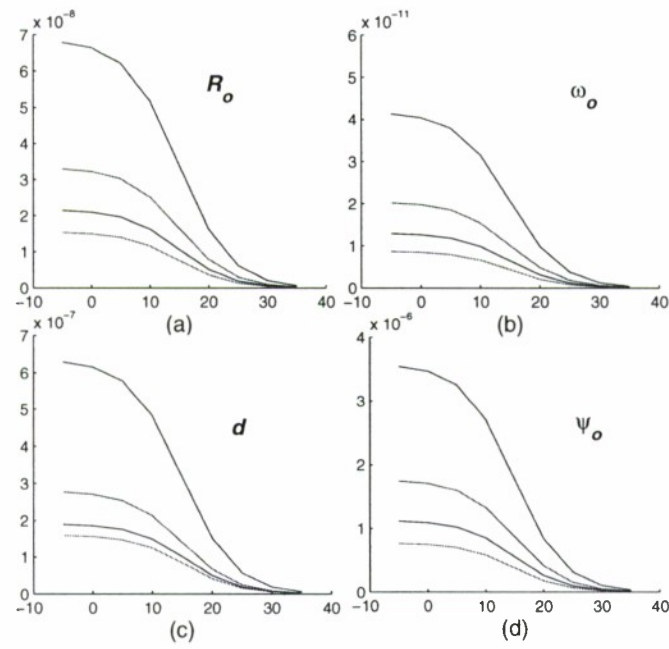


Fig. 3 CRBs for multiple blades,  $N=512$ ,  $\text{SNR}_1=15\text{dB}$ , x-axis  $\text{SNR}_2$  dBs, y-axis CRBs, blue ( 1blade), red (2 blades), black (3 blades), magenta (4 blades).

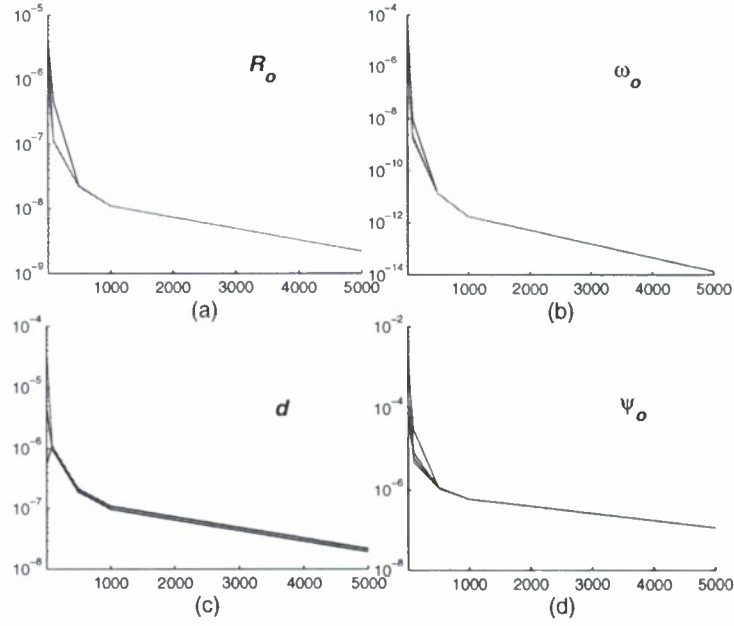


Fig. 4 CRBs for multiple blades,  $\text{SNR}_1=15\text{dB}$ ,  $\text{SNR}_2=-10\text{dB}$ , x-axis  $N$ , data record length, y-axis CRBs, blue ( 1blade), red ( 2 blades), black ( 3 blades), magenta ( 4 blades).

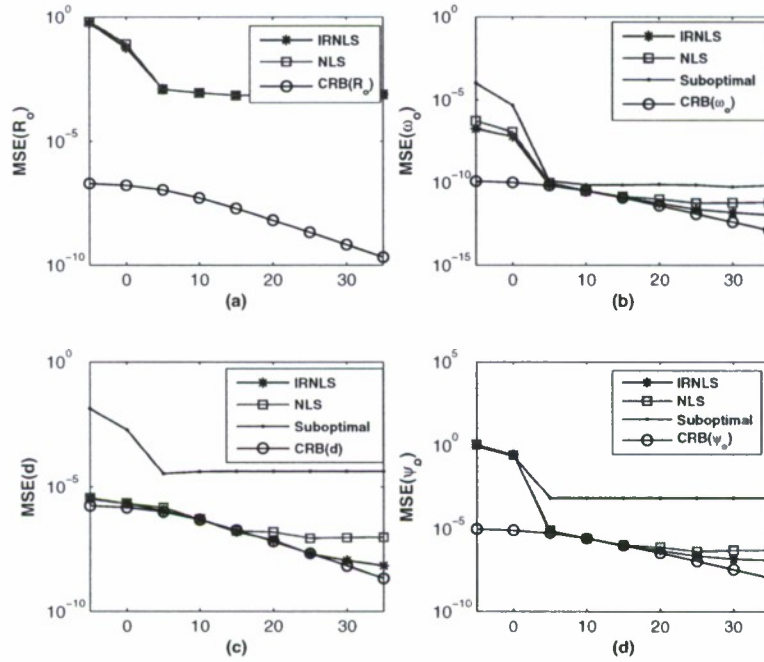


Fig. 5 MSE performance of rotational MD parameters,  $\text{SNR}_1=5\text{dB}$ ,  $\text{SNR}_2$  is varied.

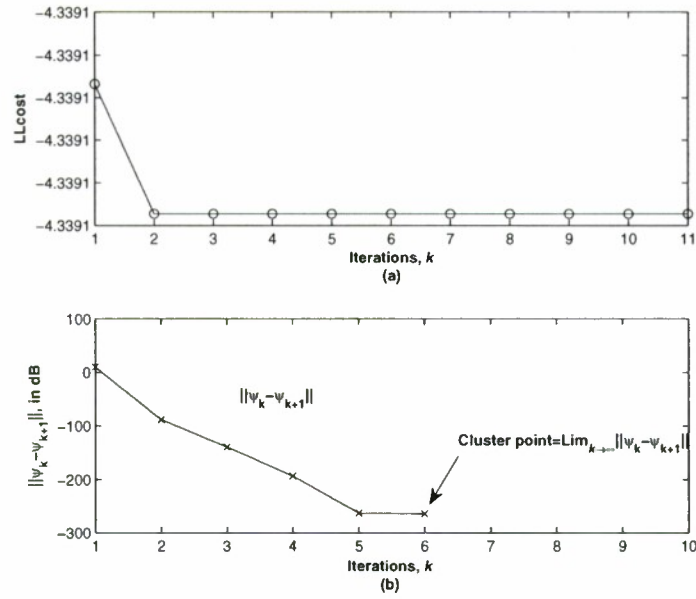


Fig. 6 Figures showing the (a) LL cost, (b) cluster point.

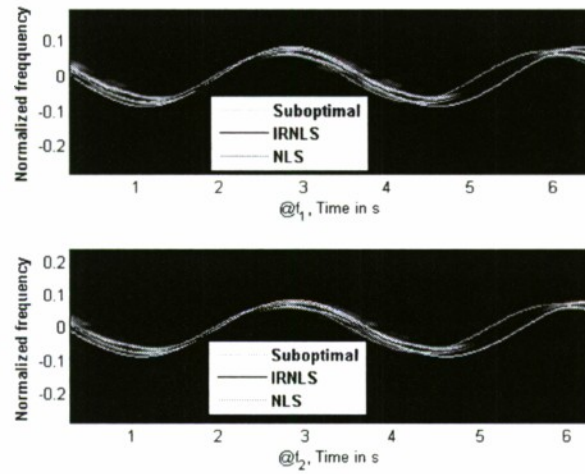


Fig. 7 Spectrogram of measured radar returns for vibrational MD, along with the final IF fits.

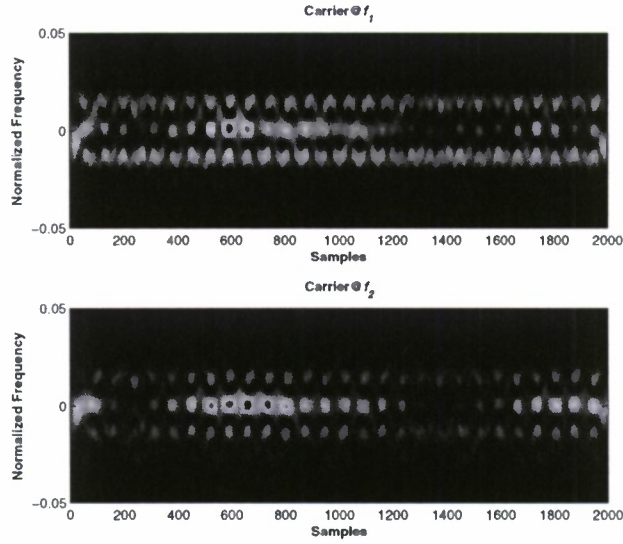


Fig. 8(a) Spectrograms of the measured returns at  $0^\circ$  azimuth at the two carriers.

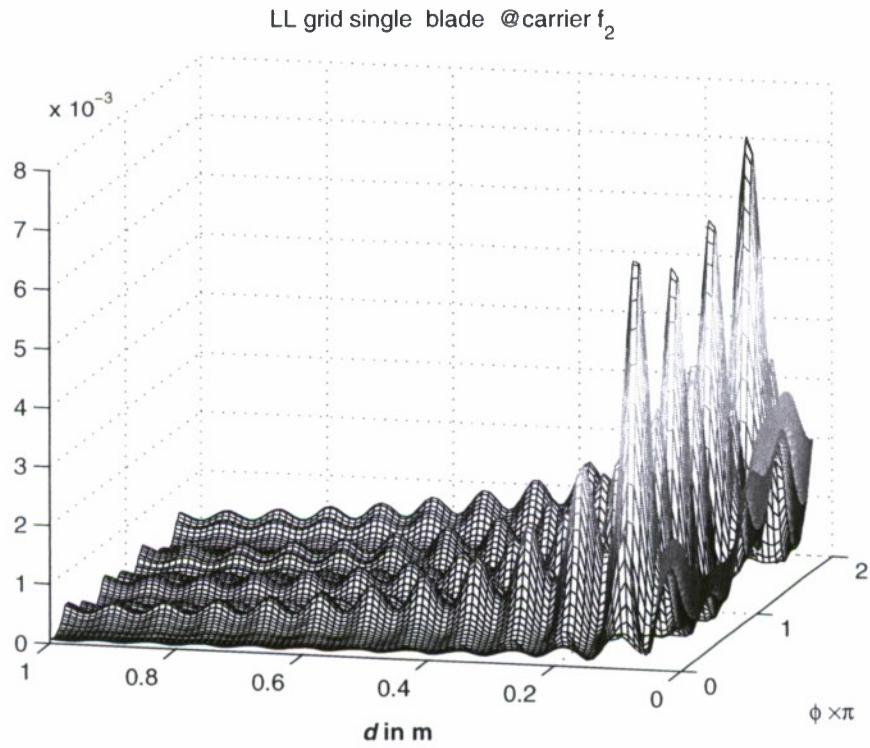


Fig. 8(b) LL grid ( $0^\circ$  azimuth) using single blade cost function, for carrier  $f_2$ . Four blades are clearly seen. Number of samples used is 1200.

Table I. Range estimates at  $0^\circ$  azimuth. True range is 3m.

Data chunks	Minimized	Minimized	Range estimate	Range esti-
-------------	-----------	-----------	----------------	-------------



<b>comprising of 500 samples.</b>	<b>LLcost (NLS) from 8(a)</b>	<b>LLcost (IRNLS) from 8(a)</b>	<b>(NLS) in meters</b>	<b>mate (IRNLS) in meters</b>
<b>100<sup>th</sup> sample onwards</b>	-28.7104	-28.9614	3.0046	2.9977
<b>700<sup>th</sup> Sample onwards</b>	-28.5853	-28.9000	3.0052	2.9985
<b>1400<sup>th</sup> Sample onwards</b>	-29.6069	-30.0953	3.0132	3.0051

**Table II.** Range estimates at 60° azimuth. True range is 3m.

<b>Data chunks comprising of 500 samples.</b>	<b>Minimized LLcost (NLS) from (8a)</b>	<b>Minimized LLcost (IRNLS) from 8(a)</b>	<b>Range estimate (NLS) in meters</b>	<b>Range esti- mate (IRNLS) in meters</b>
<b>100<sup>th</sup> sample onwards</b>	-31.8872	-31.9728	3.2449	3.2336
<b>700<sup>th</sup> Sample onwards</b>	-31.9589	-32.1712	3.1552	2.9286
<b>1400<sup>th</sup> Sample onwards</b>	-31.7151	-31.7550	3.0900	3.087

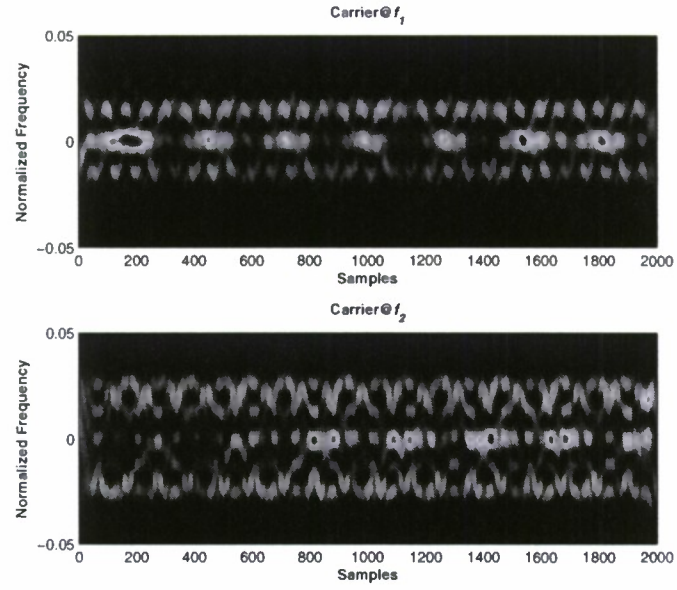


Fig. 9(a) Spectrograms of the measured returns at  $60^\circ$  azimuth at the two carriers.

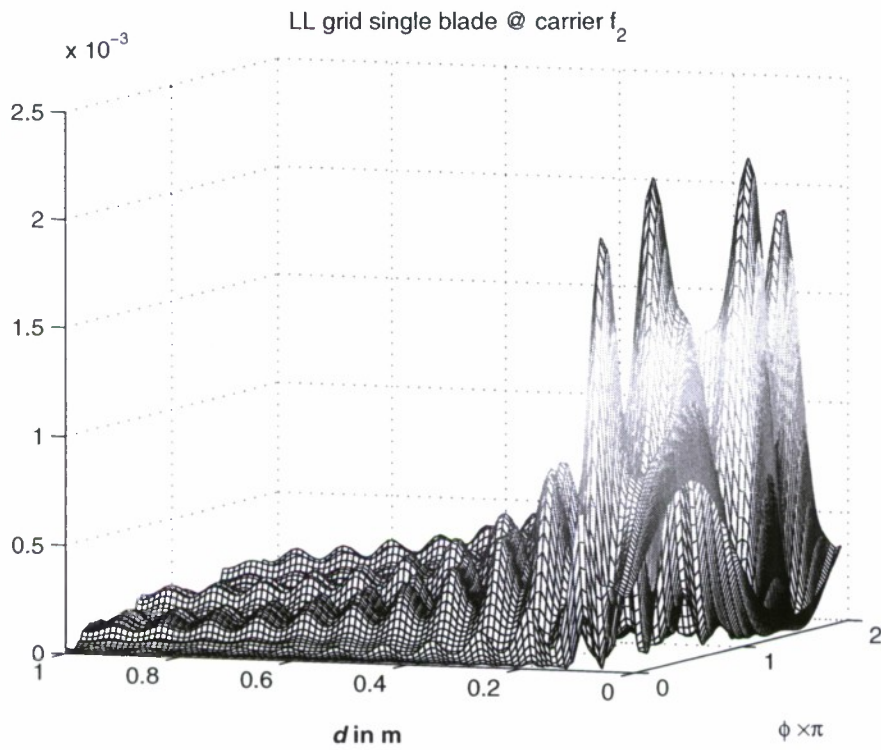


Fig. 9(b) LL grid ( $60^\circ$  azimuth) using single blade cost function, for carrier  $f_2$ . Four blades are clearly seen. Number of samples used is 1200.



## 2. Dual Frequency Doppler Radars for Indoor Range Estimation: Cramér-Rao Bound Analysis

### *Abstract*

Single frequency Doppler radars are effective in distinguishing moving targets from stationary targets, but suffer from inherent range ambiguity. With a dual-frequency operation, a second carrier frequency is utilized to overcome the range ambiguity problem. In urban sensing applications, the dual-frequency approach offers the benefit of reduced complexity, fast computation time, and real time target tracking. We consider a single moving target with three commonly exhibited indoor motion profiles, namely, constant velocity motion, accelerating target motion, and micro-Doppler motion. RF signatures of indoor inanimate objects, such as fans, vibrating machineries, and clock pendulums, are characterized by micro-Doppler motion, whereas animate translation movements produce linear FM Doppler. In this chapter, we derive Cramér-Rao bounds (CRB) for the parameters defining indoor target motions under dual-frequency implementations. Experimental data is used to estimate micro-Doppler parameters and to validate the CRBs.

## 2.1 Introduction

The emerging area of through-the-wall sensing addresses the desire to see inside enclosed structures and behind walls in order to determine building layouts, scene contents, and occupant locations. This capability has merits in a variety of civilian and military applications, as it provides vision into otherwise obscured areas, thereby, facilitating information-gathering and intelligent decision-making [1-4].

Motion detection is a highly desirable feature in many through-the-wall applications, such as fire-fighters searching for survivors or law-enforcement officers involved in hostage rescue missions. Doppler discrimination of movement from stationary background clutter can be readily used in these applications. Such systems can be classified into zero, one, two, or three dimensional systems [1]. A 0-D system simply provides a go/no-go motion detection capability and, as such, can employ single frequency continuous wave (CW) waveforms for scene interrogation. A 1-D system can provide range to moving targets by employing modulated or pulsed signals. A 2-D system provides both target range and azimuth information, whereas a 3-D system adds the dimension of height to the offerings of a 2-D system. However, the higher level of situational awareness offered by 2-D and 3-D systems is obtained at the expense of increased hardware and software complexity and higher computational load. A 1-D system provides a good compromise between level of situational awareness and cost versus size and weight. This is specifically the case when localizing moving targets is of primary interest.

In this chapter, we consider a 1-D system for range-to-motion estimation based on Doppler radars. Single frequency CW radars suffer from range ambiguity [5]. This problem is more pronounced for through-the-wall applications since the carrier frequencies are in the few GHz range due to antenna size and frequency allocation management issues. An additional carrier frequency can be introduced to resolve the uncertainty in range. The two carrier frequencies can be chosen such that the maximum unambiguous range is either equal to or greater than the spatial extent of the urban structure. In this case, the true solution is the one which corresponds to the target inside the enclosed structure. It is noted that other radar techniques, such as the swept frequency, pulse compression etc., can be used to reduce the uncertainty in range [5]. However, the operational logistics and system requirements for through-the-wall



operations, such as cost, hardware complexity, and portability, may prohibit the use of such techniques. The dual-frequency approach, although not new, meets all of the above requirements and is likely to emerge as a leading forerunner in modern urban sensing systems [6-9].

We focus on three target motion and range profiles, namely, linear translation, acceleration, and the micro-Doppler (MD) motions that are commonly encountered in urban sensing applications. For example, the swinging of the arms and the legs of a person during walking can be modeled as micro-Doppler, whereas the gross motion of the torso can be represented by translation. We develop Cramér-Rao bounds (CRBs) for the parameters corresponding to the aforementioned three indoor motion profiles. We provide the CRB for the range estimate in addition to motion speed, harmonic frequency, and chirp parameters. Specifically, we show that the dual frequency approach increases the Fisher information compared to a single frequency operation and, therefore, lowers the CRBs [10]. In the analysis, the radar aspect angle  $\theta$  is incorporated into the general CRB derivations. When the aspect angle is assumed unknown, the FIM becomes singular, rendering the parameters non-identifiable. It is noted that the main contribution of the chapter is the derivation of the CRBs, and no estimation technique is advocated here. For MD motion, we use experimental data to estimate micro-Doppler parameters and to validate the CRBs. We employ suboptimal techniques that make use of the inherent impulsive structure of the spectrum of the returns to estimate some of the parameters in the MD model [10]. Maximum Likelihood optimal estimator for MD motion profile is presented in [10].

A brief outline of the chapter is as follows. In Section 2.2, the signal model is introduced along with the governing range equations for the three motion profiles. In Section 2.3, a generic derivation of the CRB is presented, incorporating the nuisance parameters, and subsequently the CRBs of the three motion profiles are derived. Supporting simulation and experimental results are provided in Section 2.4. Section 2.5 contains the conclusions.

## 2.2 General Signal Model

Below, we briefly discuss the range ambiguity problem, and introduce the motivation for adopting carrier frequency diversity in CW radar for range estimation.

### 2.2.1 Range ambiguity in dual-frequency radar

For a dual frequency radar employing two known carrier frequencies  $f_1$  and  $f_2$ , the baseband signal returns due to a single moving target are expressed as,

$$\phi_1(nT_s) = 4\pi f_1 R(nT_s) / c, \quad \phi_2(nT_s) = 4\pi f_2 R(nT_s) / c \quad (1)$$

where  $T_s$  is the sampling period,  $R(nT_s)$  is the range of the target at sample  $n$ , and  $c$  is the speed of light in free space. Dropping  $T_s$  in the phase and range notations for convenience, and without considering phase wrapping, the range of the target is given by [6]

$$R(n) = \frac{c(\phi_2(n) - \phi_1(n))}{4\pi(f_2 - f_1)} \quad (2)$$

In reality, however, phase observations are wrapped within the  $[0, 2\pi)$  range. Therefore, the true phase can be expressed as

$$\phi^{(true)}(n) = \phi_2(n) - \phi_1(n) + 2m\pi, \quad (3a)$$

where  $m$  is an unknown integer. Accordingly, the range estimate is subject to range ambiguity [7], i.e.,

$$R(n) = \frac{c[\phi_2(n) - \phi_1(n)]}{4\pi(f_2 - f_1)} + \frac{cm}{2(f_2 - f_1)}. \quad (3b)$$

The second term in the above equation induces ambiguity in range. For the same phase difference, the range can assume infinite values separated by

$$R_u = c / (2(f_2 - f_1)) \quad (3c)$$

which is referred to as the maximum unambiguous range. From the above equation,  $R_u$  is inversely proportional to the difference of the carrier frequencies. Consider a single frequency Doppler radar operating at  $f_1 = 1$  GHz. In this case,  $R_u = c / 2f_1 = 15$  cm. For dual frequency operation at  $f_1 = 1$  GHz,

and  $f_2 = 1.01$  GHz,  $R_u = 15$  m, according to (3a). The increase in  $R_u$  from 15 cm to 15 m is sufficient for target location in rooms and small buildings. The other multiple range solutions given by (2), and (3b) are simply rejected since they do not fall within the spatial extent of the urban structure. In the following sections, we, therefore, assume  $m = 0$ , for simplicity. By choosing closely separated carrier frequencies, any maximum unambiguous range can be achieved. Coherent phase estimation may, however, be compromised if the frequency difference is too small to overcome noise effects and frequency drifts in down conversions [11]. Performance analysis of the dual-frequency radar in the presence of noise and frequency drifts is provided in [12]-[13].

It is noted that in the presence of multiple moving targets, the phase extracted from the radar returns cannot be used for range estimation of each target separately. This is because the phase terms corresponding to different targets are superimposed and cannot be separated in the time domain. This drawback of the dual-frequency scheme can be overcome provided that the target Doppler signatures are separable in the frequency or the time-frequency (TF) domain [14]. With the extraction of the phase of the individual targets in the Doppler domain, (2) can then be used to obtain the corresponding target range. Likewise for multipath which is similar to multiple targets the same procedure can be applied, provided they are separable in the frequency or time-frequency domain.

### 2.2.2 Signal model for CRB derivation

For a dual frequency radar employing two known carrier frequencies  $f_1$  and  $f_2$ , the baseband signal returns due to a single moving target are expressed as,

$$\begin{aligned} x_1(n) &= x_1(nT_s) = (\rho_1 + h_1(n; \psi)) \exp\left(j \frac{4\pi f_1 R(n)}{c}\right) + v_1(n) = s_1(n) + v_1(n) \\ x_2(n) &= x_2(nT_s) = (\rho_2 + h_2(n; \psi)) \exp\left(j \frac{4\pi f_2 R(n)}{c}\right) + v_2(n) = s_2(n) + v_2(n) \end{aligned} \quad (4)$$

$$\{n \mid n \in \mathbb{Z}^+, n = 0, 1, 2, 3, \dots, N-1\}$$

where  $\rho_i$  is the amplitude of the return at frequency  $f_i, i = 1, 2$ . The scalar function  $h_i(n; \psi)$ , dependent on both the sample index  $n$  and a vector  $\psi$  of desired parameters, is added to represent possible cyclic

amplitude fluctuations for the MD model. It is noted that for the case of constant Doppler and accelerating target motion profiles,  $h_i(n; \psi) = 0$ , since for these targets the radar cross section (RCS) can be assumed constant for a relatively small time on target.  $Z^+$  is the domain of positive integers. The two noise sequences, corresponding to the two frequencies of operation, over the observation period  $N$ , are complex additive white Gaussian noise (AWGN) and uncorrelated, i.e.,  $v_1(n) = v_1(nT_s) \sim CN(0, \sigma_1^2)$ ,  $v_2(n) = v_2(nT_s) \sim CN(0, \sigma_2^2)$ ,  $E\{v_1(n)v_2^*(n)\} = 0$ , where  $\sigma_1^2$  and  $\sigma_2^2$  represent the noise variance for the two frequencies, respectively and '\*' is the complex conjugate operator. To aid in the derivation, we vectorize the observations and describe the signal returns by a joint probability density function (pdf). The received signals at the two frequencies are appended to form a long vector,

$$\mathbf{x} = \mathbf{s} + \mathbf{v} = [x_1(0), x_1(1), x_1(2) \dots x_1(N-1), x_2(0), x_2(1) \dots x_2(N-1)]^T = [\mathbf{x}_1 \quad \mathbf{x}_2]^T \quad (5)$$

where

$$\begin{aligned} \mathbf{s} &= [s_1(0), s_1(1), s_1(2) \dots s_1(N-1), s_2(0), s_2(1) \dots s_2(N-1)]^T = [\mathbf{s}_1 \quad \mathbf{s}_2]^T \\ \mathbf{v} &= [v_1(0), v_1(1), v_1(2) \dots v_1(N-1), v_2(0), v_2(1) \dots v_2(N-1)]^T = [\mathbf{v}_1 \quad \mathbf{v}_2]^T \end{aligned} \quad (6)$$

The mean and covariance matrix of  $\mathbf{x}$  are given by

$$E\{\mathbf{x}\} = \boldsymbol{\mu} = [\mathbf{s}_1 \quad \mathbf{s}_2]^T, \quad E\{(\mathbf{x} - \boldsymbol{\mu})(\mathbf{x} - \boldsymbol{\mu})^H\} = \mathbf{C} = \begin{bmatrix} \sigma_1^2 \mathbf{I} & \mathbf{0}_{N \times N} \\ \mathbf{0}_{N \times N} & \sigma_2^2 \mathbf{I} \end{bmatrix} \quad (7)$$

The joint pdf of the data, assuming a multivariate complex Gaussian distribution, is

$$p(\mathbf{x}; \mathbf{s}) = \frac{1}{\pi^{2N} \det(\mathbf{C})} \exp(-(\mathbf{x} - \boldsymbol{\mu})^H \mathbf{C}^{-1} (\mathbf{x} - \boldsymbol{\mu})) \quad (8)$$

### 1) Constant Doppler Frequency

For the constant Doppler frequency model, the target range is parameterized as,

$$R(n) = R_o + v \cos(\theta)n, \quad \theta \in (-\pi/2, \pi/2) \quad (9)$$

where  $R_o$  is the initial range of the target at time  $n = 0$ . The discrete velocity  $v$  of the target is its actual velocity multiplied by the sampling period. The parameter  $\theta$  is the viewing, or aspect, angle of the radar

with respect to the target. In other words, the component  $v\cos(\theta)$  is the identifiable Doppler component registered by the radar system. Inserting (9) into (4), it is clear that the constant Doppler model is analogous to the sinusoidal parameter estimation [15, 16]. Hence, the identifiability criteria of the parameters are similar to the traditional single frequency estimation problem. However, some details must be added. The identifiability criteria are developed by putting  $\theta=0$  in (9) because for any other value of  $\theta$  in the defined range, the criteria are valid. The terms  $2f_1v/c$  and  $2f_2v/c$  in the phase of the signal returns are the Doppler frequencies, analogous to the frequencies (radian/s) in the sinusoidal parameter estimation problem. Hence, for  $v$  to be identifiable,  $-0.5 \leq 2f_1v/c < 0.5$  and  $-0.5 \leq 2f_2v/c < 0.5$  [15]. Since we have assumed  $f_2 > f_1$  implicitly,  $-c/4f_2 \leq v < c/4f_2$  represents the bounds on the positive and negative Doppler, respectively. For example, if  $f_2 = 1$  GHz, then the discrete velocity is constrained to a maximum of 0.075, assuming a nominal sampling frequency of 100Hz and the analog velocity is 7.5 m/s. It is noted that indoor animate moving targets such as humans and pets, do not assume such high velocities. Typically, in indoor settings, we expect analog velocities below 1m/s which allows the sampling frequency to be reduced to approximately 15 Hz. The terms  $4\pi f_1 R_o/c$  and  $4\pi f_2 R_o/c$  represent the phase in the sinusoidal parameter estimation model. Clearly,  $R_o$  can be uniquely estimated if the maximum unambiguous range is larger than the building extent, as determined by (3c). For this motion profile, as mentioned earlier, we use  $h_t(n; \psi) = 0$ , since the RCS is assumed to be constant.

## 2) Micro-Doppler (MD)

The range for this motion profile is parameterized as [17],

$$R(n) = R_o + d \cos(\theta) \cos(\omega_o n - \phi_o), \quad (d, \omega_o) \neq 0, \quad \theta \in (-\pi/2, \pi/2) \quad (10)$$

In the above equation, the parameter  $\omega_o$  is the discrete version of the rotational or the vibrational frequency. The parameter  $d \cos(\theta)$  is the maximum displacement from the initial range  $R_o$  along the radar's line of sight (LOS). For the specific case of rotation,  $2d \cos(\theta)$  represents the diameter of the circular trajectory in the direction of the LOS. The parameter  $\phi_o$  denotes the initial phase of the MD motion. The



MD signal returns represent the traditional sinusoidal FM model [10, 11], and are obtained by substituting (10) in (4). It is noted that the sinusoidal FM model is a good fit for motion profiles of indoor inanimate objects, such as fans, vibrating machineries, and clock pendulums. For the more complicated human motion, the sinusoidal FM model is a rough approximation to the swinging of the arms and the legs during walking.

The MD model can be further decomposed into vibration and rotation models based on the scalar function  $h_i(n; \psi)$ . For typical indoor targets undergoing pure vibration (i.e. the target moves back and forth), the displacements are small relative to the target range, especially for longer radar standoff distances from the wall, and the RCS is considered to be constant, i.e.,  $h_i(n; \psi) = 0$ . On the other hand, for a rotating target, a fixed-location radar observes different elevation aspects of the target, thereby inducing a cyclic amplitude modulation in the radar returns. These amplitude fluctuations are indeed dependent on the target geometry. In this case, the scalar function  $h_i(n; \psi)$  can be modeled as

$$h_i(n; \psi) = \Delta \rho_i \cos(\omega_o n - \phi_i) \quad (11)$$

where the parameter  $\Delta \rho_i$  represents the maximum deviation from the nominal amplitude  $\rho_i$ , whereas the parameter  $\phi_i \in [0, 2\pi)$  represents the phase at time  $n = 0$ . As an example, consider a rotating fan with one blade, at one extreme instant of time the tip of the blade is seen representing a near zero RCS, whereas at another extreme time instant, the entire length of the blade is seen by the radar representing a maximum RCS. The cyclic amplitude modulations will be demonstrated experimentally in the simulations section and are in agreement with the model in (11).

The identifiability criteria for MD signals are developed by substituting  $\theta = 0$  in (10). For the variable  $R_o$ , this case is identical to the case of constant Doppler. However, it is not straightforward to derive the parameter identifiability criteria for the rest of the parameters using the time domain model alone, as was the case in the constant Doppler model. We use the Fourier transform to aid in the derivation and to shed more light on the identifiability bounds and the discrete parameterization in the MD model. The noise free MD returns are given by,

$$s_i(n) = (\rho_i + h_i(n; \Psi)) \exp\left(j \frac{4\pi f_i R_o}{c} + j \frac{4\pi f_i d \cos(\omega_o n - \varphi_o)}{c}\right), \forall i = 1, 2 \quad (12)$$

Let  $J_k(\cdot)$  be the  $k^{\text{th}}$  order Bessel function of the first kind. Accordingly [18, 19],

$$\exp\left(j \frac{4\pi f_i d}{c} \cos(\omega_o n - \varphi_o)\right) = \sum_{k=-\infty}^{\infty} j^k \exp(jk(\omega_o n - \varphi_o)) J_k\left(\frac{4\pi f_i d}{c}\right) \quad (13)$$

Using (12) and the Fourier representation of (13), and ignoring  $h_i(n; \Psi)$ , as it does not affect identifiability, we obtain

$$S_i(e^{j\omega}) = \rho_i \exp\left(j \frac{4\pi f_i R_o}{c}\right) \sum_{k=-\infty}^{\infty} j^k \delta(\omega - k\omega_o) \exp(-jk\varphi_o) J_k\left(\frac{4\pi f_i d}{c}\right), \forall i = 1, 2 \quad (14)$$

As in traditional multiple sinusoidal parameter estimation, for the frequencies to be identifiable, they must lie in the interval  $[-\pi, \pi)$ . This condition, which translates in the underlying case to  $-\pi \leq k\omega_o < \pi$ ,  $\forall k$ ,  $k \in \mathbb{Z}$ , cannot be imposed, since there is an infinite number of harmonics. Moreover, it is clear from (14) that the signal is not analytic due to the presence of harmonics in the negative frequencies. However, it is well known that the Bessel functions decrease rapidly with  $k$ . Therefore, we impose the following two assumptions to derive the identifiability constraints: 1) Most of the energy in the signal can be represented by a finite number of harmonics; say  $K \in \mathbb{Z}$ , 2) The Nyquist theorem is satisfied. Assumption 1 implies that the Fourier transform in (14) can be replaced by

$$S_i(e^{j\omega}) = \rho_i \exp\left(j \frac{4\pi f_i R_o}{c}\right) \sum_{k=-K}^K j^k \delta(\omega - k\omega_o) \exp(-jk\varphi_o) J_k\left(\frac{4\pi f_i d}{c}\right), \forall i = 1, 2 \quad (15)$$

Assumption 2 then implies that  $-\pi \leq k\omega_o < \pi$ ,  $\forall k$ ,  $-K \leq k \leq K$  in order to avoid aliasing of the  $K$  harmonics. Since negative vibrational and rotational frequencies have no physical meaning, it is straightforward to note that from the above assumptions  $\omega_o \in (0, \pi)$ . Furthermore, since the harmonics are symmetric about DC, and knowing *a priori* that an MD target is present, it is sufficient to identify the first harmonic corresponding to  $k = \pm 1$ , i.e.,  $|\omega_o| < \pi$ . The criterion  $0 \leq \varphi_o < 2\pi$  is chosen for identifying  $\varphi_o$ . Surprisingly, the identifiability criteria are similar, although not identical, to the case of sinusoidal

parameter estimation. However, the bounds on  $\omega_o$  and  $\varphi_o$  are carrier independent, unlike the constant Doppler case, where the velocity bound was constrained by the higher carrier frequency,  $f_2$ .

The Bessel functions take arguments  $4\pi f_i d/c$ . Therefore, any real argument, excluding zero, is valid because  $J_k(0)=0, \forall k \neq 0$ . Since negative values of the maximum displacement,  $d$ , have no physical meaning, then  $d > 0$ . Moreover, in traditional sinusoidal FM, the argument  $4\pi f_i d/c$  is analogous to the modulation index [11], which is strictly real and positive. Therefore,  $0 < d < \infty$ . It is important to note, however, that it is impractical to constrain the initial range of the target to be within the maximum unambiguous range, while allowing the maximum displacement to be infinite. Therefore, to be consistent, we impose the criterion for  $d$  as  $0 < d \leq c/4(f_2 - f_1) = R_u/2$ .

It is noted that typical indoor MD targets, such as rotating fans, pendulums, etc, are essentially narrowband FM (NBFM). For example, consider the motion of a human, the maximum displacement of either the arm or the leg is much less than a meter, and for a carrier in the low GHz range, the bandwidth is typically a few Hz. In the case of an indoor rotating fan, the received signal bandwidth is proportional to the length of the fan's blade, and is clearly a few Hz for such carrier frequencies.

### 3) Accelerating Target

The range for this motion profile is given by,

$$R(n) = R_o + \cos(\theta)(\alpha n + \beta n^2), \quad \theta \in (-\pi/2, \pi/2) \quad (16)$$

where the parameters  $\alpha$  and  $\beta$  represent the initial velocity and half the acceleration (or deceleration) of the target, respectively. As before,  $R_o$  is the initial range of the target and its identifiability is identical to the constant Doppler case. Substituting (16) in (4), we obtain the desired signal returns for the accelerating target. It is clear that an accelerating target represents a linear chirp, or a second order Polynomial-phase signal (PPS) [20]. The identifiability criteria are developed by putting  $\theta=0$  in (16). The model is similar to the chirp parameter estimation model, albeit a few differences in identifiability [21]. The terms  $4\pi f_i \alpha/c$  and  $4\pi f_i \beta/c \quad \forall i, i=1,2$  represent the frequency and chirp rate in the chirp parameter estima-

tion model, respectively. Hence for identifiability, along with the fact that  $f_2 > f_1$ , we must have  $-c/4f_2 \leq \alpha < c/4f_2$  and  $-c/8f_2 \leq \beta < c/8f_2$ , which are carrier frequency dependent. It is noted that the bounds are for the discretized versions of the parameters. For this motion profile,  $h_i(n; \psi) = 0$ .

We note that in indoor environments, the above three motion profiles can occur individually or in combination. While a rotating fan or a clock pendulum will exhibit purely MD motion, the motion profile of a human walking can be predominantly modeled as a combination of translational and MD components. In this chapter, however, we focus on three “stand-alone” motion profiles, namely, translation, MD and acceleration individually. Combinations of these motions are not considered.

### 2.3 Cramér-Rao Bounds

In this section, we derive the CRB for the three motion profiles discussed previously. The parameter  $\theta$  is assumed known. In Appendix-A, we show that if  $\theta$  is unknown, then the FIM becomes singular. We begin with the generalized CRB derivation, taking into account the effect of the nuisance parameters. The parameter vector including the nuisance parameters is denoted by  $\boldsymbol{\eta} = [\boldsymbol{\psi}^T, \rho_1, \rho_2, \sigma_1^2, \sigma_2^2]^T_{(p+4) \times 1}$ , where  $\boldsymbol{\psi} = [\psi_1, \psi_2, \psi_3, \dots, \psi_p]^T$ . The parameters  $\psi_k$ ,  $1 \leq k \leq p$  are the  $p$  desired parameters, some of which are present purely in the phase of the signal returns. In general, the range is a function of both  $n$  and  $\boldsymbol{\psi}$ , i.e.  $R(n) = R(n; \boldsymbol{\psi})$ . For a complex Gaussian vector  $\mathbf{x}$ , with a covariance matrix  $\mathbf{C}$ , defined in (7), the Fisher information elements are expressed as [22],

$$[\mathbf{F}]_{qr} = \text{Tr} \left[ \mathbf{C}^{-1} \frac{\partial \mathbf{C}}{\partial \eta_q} \mathbf{C}^{-1} \frac{\partial \mathbf{C}}{\partial \eta_r} \right] + 2 \text{Re} \left\{ \left[ \frac{\partial \mathbf{s}}{\partial \eta_q} \right]^H \mathbf{C}^{-1} \left[ \frac{\partial \mathbf{s}}{\partial \eta_r} \right] \right\}, \quad 1 \leq (q, r) \leq p+4 \quad (17)$$

where  $\mathbf{s} = [\mathbf{s}_1 \quad \mathbf{s}_2]^T = \left[ (\boldsymbol{\rho}_1 + \mathbf{h}_1(\boldsymbol{\psi})) \circ \exp \left( j \frac{4\pi f_1}{c} \mathbf{R}(\boldsymbol{\psi}) \right) \quad (\boldsymbol{\rho}_2 + \mathbf{h}_2(\boldsymbol{\psi})) \circ \exp \left( j \frac{4\pi f_2}{c} \mathbf{R}(\boldsymbol{\psi}) \right) \right]^T$  with

the exponential taken elementwise,  $\mathbf{R}(\boldsymbol{\psi})$  and  $\boldsymbol{\rho}_i + \mathbf{h}_i(\boldsymbol{\psi})$  are  $1 \times N$  row vectors, whose  $n^{\text{th}}$  elements are  $R(n; \boldsymbol{\psi})$  and  $\rho_i + h_i(n; \boldsymbol{\psi})$ ,  $i=1,2$  respectively. That is, the dependency on  $n$  is suppressed. The operator

‘ $\circ$ ’ denotes the Hadamard product or element wise multiplication. Following the work of [23], and using the vector differential operator, we obtain

$$\begin{aligned}
\frac{\partial \mathbf{s}}{\partial \boldsymbol{\eta}^T} &= \begin{bmatrix} s_1 \\ s_2 \end{bmatrix} \begin{bmatrix} \frac{\partial}{\partial \boldsymbol{\psi}^T} & \frac{\partial}{\partial \rho_1} & \frac{\partial}{\partial \rho_2} & \frac{\partial}{\partial \sigma_1^2} & \frac{\partial}{\partial \sigma_2^2} \end{bmatrix} \\
&= \begin{bmatrix} \left[ \frac{\partial \mathbf{h}_1(\boldsymbol{\psi})}{\partial \boldsymbol{\psi}^T} \right] \\ \left[ \frac{\partial \mathbf{h}_2(\boldsymbol{\psi})}{\partial \boldsymbol{\psi}^T} \right] \end{bmatrix} \bullet \begin{bmatrix} \exp\left(\frac{j4\pi f_1 \mathbf{R}(\boldsymbol{\psi})}{c}\right) \\ \exp\left(\frac{j4\pi f_2 \mathbf{R}(\boldsymbol{\psi})}{c}\right) \end{bmatrix} + \begin{bmatrix} \frac{4\pi f_1}{c} \frac{\partial \mathbf{R}(\boldsymbol{\psi})}{\partial \boldsymbol{\psi}^T} \\ \frac{4\pi f_2}{c} \frac{\partial \mathbf{R}(\boldsymbol{\psi})}{\partial \boldsymbol{\psi}^T} \end{bmatrix} \bullet j\mathbf{s} \begin{bmatrix} \frac{\partial \mathbf{s}}{\partial \eta_2} & \frac{\partial \mathbf{s}}{\partial \eta_3} \end{bmatrix} \begin{bmatrix} \mathbf{0}_{2N \times 1} & \mathbf{0}_{2N \times 1} \end{bmatrix} \quad (18) \\
&\quad \left. \begin{bmatrix} \frac{\partial \mathbf{s}}{\partial \eta_2} \\ \frac{\partial \mathbf{s}}{\partial \eta_3} \end{bmatrix} \right]_{2N \times (p+4)} \\
\frac{\partial \mathbf{s}}{\partial \eta_2} &:= \begin{bmatrix} (\boldsymbol{\rho}_1 + \mathbf{h}_1(\boldsymbol{\psi}))^{T \circ -1} \\ \mathbf{0}_{N \times 1} \end{bmatrix} \circ \mathbf{s}, \quad \frac{\partial \mathbf{s}}{\partial \eta_3} := \begin{bmatrix} \mathbf{0}_{N \times 1} \\ (\boldsymbol{\rho}_2 + \mathbf{h}_2(\boldsymbol{\psi}))^{T \circ -1} \end{bmatrix} \circ \mathbf{s}
\end{aligned}$$

where ‘ $\bullet$ ’ denotes the generalized Hadamard product<sup>3</sup>, and ‘ $(\cdot)^{\circ -1}$ ’ denotes the Hadamard division of a vector or a matrix, i.e. if  $\mathbf{x} = [x_1, x_2, \dots, x_N]$ ,  $\mathbf{x}^{\circ -1} = [1/x_1, 1/x_2, \dots, 1/x_N]$ . In (17), the argument of the trace operator is zero except that which corresponds to the Fisher information of the noise nuisance parameters namely,  $\sigma_i^2$ ,  $i = 1, 2$ . Partitioning the FIM,

$$\mathbf{F} = \begin{bmatrix} \mathbf{F}_{11} & \mathbf{F}_{12} \\ \mathbf{F}_{21} & \mathbf{F}_{22} \end{bmatrix} \quad (19)$$

The desired CRBs reside on the diagonal of the inverse Schur complement of  $\mathbf{F}$ , with respect to  $\mathbf{F}_{22}$ ,

$$CRB(\boldsymbol{\psi}) = [(\mathbf{F}_{11} - \mathbf{F}_{12} \mathbf{F}_{22}^{-1} \mathbf{F}_{21})^{-1}]_{qq} \quad (20)$$

Using (18)-(20), it can be readily shown that

$$\begin{aligned}
\mathbf{F}_{11} &= 2 \sum_{i=1}^2 \frac{1}{\sigma_i^2} \left( \frac{\partial \mathbf{h}_i(\boldsymbol{\psi})}{\partial \boldsymbol{\psi}^T} \right)^T \frac{\partial \mathbf{h}_i(\boldsymbol{\psi})}{\partial \boldsymbol{\psi}^T} \\
&+ \frac{32\pi^2}{c^2} \sum_{i=1}^2 \frac{f_i^2}{\sigma_i^2} \left( (\boldsymbol{\rho}_i + \mathbf{h}_i(\boldsymbol{\psi})) \bullet \frac{\partial \mathbf{R}(\boldsymbol{\psi})}{\partial \boldsymbol{\psi}^T} \right)^T \left( (\boldsymbol{\rho}_i + \mathbf{h}_i(\boldsymbol{\psi})) \bullet \frac{\partial \mathbf{R}(\boldsymbol{\psi})}{\partial \boldsymbol{\psi}^T} \right) \quad (21) \\
\mathbf{F}_{12} &= \mathbf{F}_{21}^T = [\mathbf{0}_p \quad \mathbf{0}_p \quad \mathbf{0}_p \quad \mathbf{0}_p] \\
\mathbf{F}_{22} &= \text{Diag} \left[ 2N / \sigma_1^2 \quad 2N / \sigma_2^2 \quad N / \sigma_1^4 \quad N / \sigma_2^4 \right]
\end{aligned}$$

<sup>3</sup> For a matrix  $\mathbf{A} \in \mathbb{C}^{M \times N} = [\mathbf{a}_1 \mathbf{a}_2 \dots \mathbf{a}_N]$  and vector  $\mathbf{x} \in \mathbb{C}^{M \times 1}$   $\mathbf{A} \bullet \mathbf{x} \in \mathbb{C}^{M \times N} := [\mathbf{a}_1 \circ \mathbf{x} \quad \mathbf{a}_2 \circ \mathbf{x} \dots \mathbf{a}_N \circ \mathbf{x}] := \mathbf{x} \bullet \mathbf{A}$



where  $\text{Diag}[\cdot]$  is a diagonal matrix with entries as given in the brackets and the vector  $\mathbf{1}_{N \times 1}$  is the row vector of size  $N$  having entries all equal to one. Similarly, the vector  $\mathbf{0}_p$  is the column vector of size  $p$ , having all zero entries. The CRB of the desired parameters is then expressed in a compact form as

$$\text{CRB}([\boldsymbol{\psi}]_q) = [\mathbf{F}_{11}^{-1}]_{qq} \quad (22)$$

From (22), the CRBs for the desired parameters are completely decoupled from those of the nuisance parameters. The decoupling in (22) indicates that the variance of the range parameters are insensitive to the knowledge, or the information brought in by the estimation of the nuisance parameters, i.e. they are unaffected whether the nuisance parameters are known or unknown [22]. From matrix  $\mathbf{F}_{11}$  in (21), we observe that the scalar multiplier terms arise as a result of the carrier diversity, implied by the dual frequency operation, and therefore have an additive effect on the net Fisher information. It yields lower CRBs, when compared to the no diversity (single carrier frequency) case. In fact, the scalar term  $32\pi^2(f_1^2/\sigma_1^2 + f_2^2/\sigma_2^2)/c^2$  indicates that the CRBs are the lowest when  $f_1 = f_2 = 0$ , in which case,  $R_u = \infty$ . However, this is a trivial case, as diversity ceases to exist. In general, since the FIM elements are a function of the squared values of  $f_1$  and  $f_2$ , lower CRBs are achieved when higher carrier frequencies are chosen. The effect of the SNRs on the CRBs is straightforward to analyze. The addition of Fisher information is explored in greater detail in the following subsections. In the ensuing analysis, we derive the FIM elements for the desired parameters.

### 2.3.1 Constant Doppler CRB

In this case, the parameter vector is  $\boldsymbol{\psi} = [R_o \quad v]^T$ . Substituting (9) in (21) for the constant Doppler range profile, we obtain the corresponding FIM. In order to make the CRB analysis more generic, we introduce the parameters,  $\chi := f_2 / f_1$ , and  $\psi' := \sigma_1^2 / \sigma_2^2$ . It can be readily shown that for a single frequency radar employing carrier  $f_1$ , the FIM,  $\mathbf{F}_{f_1}$ , and its inverse are, respectively, given by [10]

$$\mathbf{F}_{f_1} = \frac{32\pi^2 \rho_1^2 f_1^2}{c^2 \sigma_1^2} \begin{bmatrix} N & \frac{N(N-1)\cos(\theta)}{2} \\ \frac{N(N-1)\cos(\theta)}{2} & \frac{N(N-1)(2N-1)\cos^2(\theta)}{6} \end{bmatrix} \quad (23)$$

$$\mathbf{F}_{f_1}^{-1} = \frac{c^2 \sigma_1^2}{K f_1^2 \rho_1^2} \begin{bmatrix} \frac{2(2N-1)}{N(N+1)} & \frac{-6}{\cos(\theta)N(N+1)} \\ \frac{-6}{\cos(\theta)N(N+1)} & \frac{12}{\cos^2(\theta)N(N^2-1)} \end{bmatrix} \quad (24)$$

where  $K = 32\pi^2$  is a constant. However, for the proposed dual frequency scheme, the FIM is given by

$$\mathbf{F} = \frac{32\pi^2 f_1^2}{c^2 \sigma_1^2} (\rho_1^2 + \rho_2^2 \chi^2 \psi') \begin{bmatrix} N & \frac{N(N-1)\cos(\theta)}{2} \\ \frac{N(N-1)\cos(\theta)}{2} & \frac{\cos^2(\theta)N(N-1)(2N-1)}{6} \end{bmatrix} \quad (25)$$

$$\mathbf{F}^{-1} = \frac{c^2 \sigma_1^2}{K(\rho_1^2 + \rho_2^2 \chi^2 \psi')} \begin{bmatrix} \frac{2(2N-1)}{N(N+1)} & \frac{-6}{\cos(\theta)N(N+1)} \\ \frac{-6}{\cos(\theta)N(N+1)} & \frac{12}{\cos^2(\theta)N(N^2-1)} \end{bmatrix} \quad (26)$$

It is clear from (23) and (25) that the Fisher information for the dual frequency scheme can be written as,

$$\mathbf{F} = \mathbf{F}_{f_1} + \mathbf{F}_{f_2} \quad (27)$$

The diagonal elements in (26) represent the CRBs for the initial range and velocity, respectively. It is evident from the scalar matrix multiplicative factor in (24) and (26) that the CRBs for both the initial range and velocity for the dual frequency case consistently assume smaller values as compared to their counterparts in single frequency operation. Hence, carrier frequency diversity lowers the CRBs for the range parameters. In (26), the matrix elements containing  $N$  characterize the temporal diversity in the Fisher information, whereas the scalar multiplier, containing the SNR terms and carriers, represents the carrier diversity in the Fisher information. Hence, the temporal diversity factor is identical for both frequencies, whereas the diversity induced by the carriers is different. If  $\chi \approx 1$ , and  $\psi' = 1$ , with  $\rho_i \approx \rho, i=1,2$ , then the carrier frequencies are closely separated and the SNR corresponding to the two frequencies are equal. In this case, the net Fisher information is simply  $2\mathbf{F}_{f_1}$  and the CRB are then

$0.5CRB(\boldsymbol{\psi})_{f_1}$ , where  $CRB(\boldsymbol{\psi})_{f_1}$  is the CRB of the parameter vector  $\boldsymbol{\psi}$ , associated with the single frequency  $f_1$ .

### 2.3.2 Micro-Doppler CRB

The derivation of the CRBs for the MD motion profile is different from that presented in [24], which uses a hybrid combination of PPS and MD signals. The results on the FIM elements presented in [24] are a special case of those presented here and do not provide closed form expressions of the FIM elements for MD signals, neither do they include the aspect angle and range parameters in the employed radar model. Since the frequency diversity appends the individual fisher information regardless of the motion profile, as shown in (27), we can simplify notation by suppressing the terms involving the carrier frequencies and

noise variances, i.e.,  $\epsilon_{1i} = 2 / \sigma_i^2, \forall i = 1, 2$  and  $\epsilon_{2i} = 16\pi^2 f_i^2 \epsilon_{1i} / c^2$ .

#### 1) MD Fisher information

In this case, the parameter vector is  $\boldsymbol{\psi} = [R_o \quad d \quad \omega_o \quad \phi_o \quad \Delta\rho \quad \phi]^T$ . The FIM can be derived from the general expression (21) using the range equation (10). It is straightforward to show that

$$F_{R_o R_o} = \sum_{i=1}^2 \sum_{n=0}^{N-1} \epsilon_{2i} (\rho_i + \Delta\rho_i \cos(\omega_o n - \phi_i))^2 \quad (28)$$

$$F_{R_o d} = \cos(\theta) \sum_{i=1}^2 \sum_{n=0}^{N-1} \epsilon_{2i} (\rho_i + \Delta\rho_i \cos(\omega_o n - \phi_i))^2 \cos(\omega_o n - \phi_o) \quad (29)$$

$$F_{R_o \omega_o} = -\cos(\theta) \sum_{i=1}^2 \sum_{n=0}^{N-1} \epsilon_{2i} (\rho_i + \Delta\rho_i \cos(\omega_o n - \phi_i))^2 \sin(\omega_o n - \phi_o) \quad (30)$$

$$F_{R_o \phi_o} = \cos(\theta) \sum_{i=1}^2 \sum_{n=0}^{N-1} \epsilon_{2i} (\rho_i + \Delta\rho_i \cos(\omega_o n - \phi_i))^2 d \sin(\omega_o n - \phi_o) \quad (31)$$

$$F_{R_o \Delta\rho_i} = 0, F_{R_o \phi_i} = 0, F_{d \Delta\rho_i} = 0, F_{d \phi_i} = 0 \quad (32)$$

$$F_{dd} = \cos^2(\theta) \sum_{i=1}^2 \sum_{n=0}^{N-1} \epsilon_{2i} (\rho_i + \Delta\rho_i \cos(\omega_o n - \phi_i))^2 \cos^2(\omega_o n - \phi_o) \quad (33)$$

$$F_{d\omega_o} = -\cos^2(\theta) \sum_{i=1}^2 \sum_{n=0}^{N-1} \varepsilon_{2i} (\rho_i + \Delta\rho_i \cos(\omega_o n - \phi_i))^2 dn \sin(\omega_o n - \varphi_o) \cos(\omega_o n - \varphi_o) \quad (34)$$

$$F_{d\varphi_o} = \cos^2(\theta) \sum_{i=1}^2 \sum_{n=0}^{N-1} \varepsilon_{2i} (\rho_i + \Delta\rho_i \cos(\omega_o n - \phi_i))^2 d \sin(\omega_o n - \varphi_o) \cos(\omega_o n - \varphi_o) \quad (35)$$

$$F_{\omega_o\omega_o} = \sum_{i=1}^2 \sum_{n=0}^{N-1} \varepsilon_{1i} \Delta\rho_i^2 n^2 \sin^2(\omega_o n - \phi_i) + \cos^2(\theta) \sum_{i=1}^2 \sum_{n=0}^{N-1} \varepsilon_{2i} (\rho_i + \Delta\rho_i \cos(\omega_o n - \phi_i))^2 d^2 n^2 \sin^2(\omega_o n - \varphi_o) \quad (36)$$

$$F_{\omega_o\varphi_o} = -\cos^2(\theta) \sum_{i=1}^2 \sum_{n=0}^{N-1} \varepsilon_{2i} (\rho_i + \Delta\rho_i \cos(\omega_o n - \phi_i))^2 d^2 n \sin^2(\omega_o n - \varphi_o) \quad (37)$$

$$F_{\omega_o\Delta\rho_i} = -\sum_{n=0}^{N-1} \varepsilon_{1i} \Delta\rho_i n \sin(\omega_o n - \phi_i) \cos(\omega_o n - \phi_i), \quad F_{\varphi_o\Delta\rho_i} = 0, \quad F_{\varphi_o\phi_i} = 0 \quad (38)$$

$$F_{\omega_o\phi_i} = -\sum_{n=0}^{N-1} \varepsilon_{1i} \Delta\rho_i^2 n \sin^2(\omega_o n - \phi_i), \quad F_{\Delta\rho_i\phi_i} = \sum_{n=0}^{N-1} \varepsilon_{1i} \Delta\rho_i \cos(\omega_o n - \phi_i) \sin(\omega_o n - \phi_i) \quad (39)$$

$$F_{\varphi_o\varphi_o} = \cos^2(\theta) \sum_{i=1}^2 \sum_{n=0}^{N-1} \varepsilon_{2i} (\rho_i + \Delta\rho_i \cos(\omega_o n - \phi_i))^2 d^2 \sin^2(\omega_o n - \varphi_o) \quad (40)$$

$$F_{\Delta\rho_i\Delta\rho_i} = \sum_{n=0}^{N-1} \varepsilon_{1i} \cos^2(\omega_o n - \phi_i), \quad F_{\phi_i\phi_i} = \sum_{n=0}^{N-1} \varepsilon_{1i} \Delta\rho_i^2 \sin^2(\omega_o n - \phi_i) \quad (41)$$

Since  $h_i(n; \psi)$  depends only on  $\omega_o$  and not on  $R_o$ ,  $d$ , and  $\varphi_o$ , the FIM elements in (32) are zero. In fact the FIM elements for  $\Delta\rho_i$  and  $\phi_i$  depend on  $\omega_o$  only and not on the rest of the parameters. The effect of  $h_i(n; \psi)$  and hence  $\Delta\rho_i$  is explained in the simulations section. Further simplifications of the FIM elements in eqs. (28-41) are shown in Appendix-B. For the special case of  $h_i(n; \psi) = 0, \Rightarrow \Delta\rho_i = 0, \forall i = 1, 2$  corresponding to a vibrating target, the FIM is a function of the aspect angle  $\theta$ , and the desired parameters are  $\psi = [R_o \quad d \quad \omega_o \quad \varphi_o]^T$ . In order to simplify notation, the terms with  $\theta$  are separated. We, therefore, obtain the final FIM as a Hadamard product of two matrices, the matrix  $\mathbf{A}$  containing the terms in  $\theta$  and the FIM,  $\mathbf{F}$ , corresponding to  $\theta = 0$ .

$$\mathbf{F}(\theta) = \mathbf{A} \circ \mathbf{F} = \begin{bmatrix} \mathbf{F}_1 & \mathbf{F}_3 \\ \mathbf{F}_3^T & \mathbf{F}_2 \end{bmatrix} \quad (42)$$

where

$$\mathbf{A} = \begin{bmatrix} 1 & \cos(\theta) & \cos(\theta) & \cos(\theta) \\ \cos(\theta) & \cos^2(\theta) & \cos^2(\theta) & \cos^2(\theta) \\ \cos(\theta) & \cos^2(\theta) & \cos^2(\theta) & \cos^2(\theta) \\ \cos(\theta) & \cos^2(\theta) & \cos^2(\theta) & \cos^2(\theta) \end{bmatrix}, \quad \mathbf{F} = \begin{bmatrix} F_{R_o R_o} & F_{R_o d} & F_{R_o \omega_o} & F_{R_o \varphi_o} \\ F_{d R_o} & F_{dd} & F_{d \omega_o} & F_{d \varphi_o} \\ F_{\omega_o R_o} & F_{\omega_o d} & F_{\omega_o \omega_o} & F_{\omega_o \varphi_o} \\ F_{\varphi_o R_o} & F_{\varphi_o d} & F_{\varphi_o \omega_o} & F_{\varphi_o \varphi_o} \end{bmatrix} \quad (43)$$

Using numerical inversion it can be verified that  $\mathbf{F}$  is positive definite (PD). However, from (43),  $\mathbf{A}$  is rank one with one positive eigenvalue,  $1+3\cos^2(\theta)$ . Thus,  $\mathbf{A}$  is positive semi-definite (PSD). Indeed, the Hadamard product of a PSD and a PD matrix is a cause for alarm, and prompts us to verify the non-singularity of  $\mathbf{F}(\theta)$ , without which the CRBs are unobtainable. Moreover, since  $\mathbf{F}(\theta)$  represents a Fisher information matrix, it must at least be PSD, in which case the CRBs are infinite. The positive definiteness of  $\mathbf{F}(\theta)$  can be proven using *Lemma-1*, implying non-singularity of the FIM [25]. In *Lemma-1*, the matrices are assumed complex, however the results can be generalized to real matrices. In [25], the authors have provided the complete definiteness characteristics of the Hadamard product of two matrices. However, in our case, it is sufficient to prove that  $\mathbf{F}(\theta)$  is PD.

*Lemma 1:* Consider matrices  $\mathbf{A}, \mathbf{B} \in \mathbb{C}^{N \times N}$ , where  $\mathbf{A}$  is Hermitian PSD and  $\mathbf{B}$  is Hermitian PD. Then,  $\mathbf{A} \circ \mathbf{B}$  is PD if all the diagonal elements of  $\mathbf{A}$  are not equal to zero.

*Proof:* This lemma is proved in [25, pg. 309, theorem 5.2.1]. The proof uses the Sylvester's law of inertia extensively.

The CRBs are present along the diagonal of  $\mathbf{F}(\theta)^{-1}$ . From *Lemma-1*,  $\mathbf{F}(\theta)$  is invertible, we can simplify  $\mathbf{F}(\theta)^{-1}$  as



$$\mathbf{F}(\theta)^{-1} = \begin{bmatrix} 1 & 1/\cos(\theta) & 1/\cos(\theta) & 1/\cos(\theta) \\ 1/\cos(\theta) & 1/\cos^2(\theta) & 1/\cos^2(\theta) & 1/\cos^2(\theta) \\ 1/\cos(\theta) & 1/\cos^2(\theta) & 1/\cos^2(\theta) & 1/\cos^2(\theta) \\ 1/\cos(\theta) & 1/\cos^2(\theta) & 1/\cos^2(\theta) & 1/\cos^2(\theta) \end{bmatrix} \circ \begin{bmatrix} F_{R_o R_o} & F_{R_o d} & F_{R_o \omega_o} & F_{R_o \varphi_o} \\ F_{d R_o} & F_{dd} & F_{d \omega_o} & F_{d \varphi_o} \\ F_{\omega_o R_o} & F_{\omega_o d} & F_{\omega_o \omega_o} & F_{\omega_o \varphi_o} \\ F_{\varphi_o R_o} & F_{\varphi_o d} & F_{\varphi_o \omega_o} & F_{\varphi_o \varphi_o} \end{bmatrix}^{-1} \quad (44)$$

For deriving (44), the theorem in Appendix-C was used. The inverse of the second matrix in (44) is tedious and, therefore, is computed using numerical techniques. It is evident from (44) that the parameter  $R_o$  is insensitive to  $\theta$ , whereas the other parameters are sensitive to  $\theta$ , depending on  $\cos^2(\theta)$ .

### 2.3.3 Accelerating Target CRB

In this case, the parameter vector is defined by  $\boldsymbol{\psi} = [R_o \quad \alpha \quad \beta]^T$ . The FIM can be derived from the general expression (21) using the range equation (16). Proceeding in the same fashion as before, i.e., using the Hadamard product approach, we obtain

$$\mathbf{F}(\theta) = \begin{bmatrix} 1 & \cos(\theta) & \cos(\theta) \\ \cos(\theta) & \cos^2(\theta) & \cos^2(\theta) \\ \cos(\theta) & \cos^2(\theta) & \cos^2(\theta) \end{bmatrix} \circ \begin{bmatrix} F_{R_o R_o} & F_{R_o \alpha} & F_{R_o \beta} \\ F_{\alpha R_o} & F_{\alpha \alpha} & F_{\alpha \beta} \\ F_{\beta R_o} & F_{\beta \alpha} & F_{\beta \beta} \end{bmatrix} \quad (45)$$

where

$$F_{R_o R_o} = \sum_{i=1}^2 \rho_i^2 \varepsilon_{2i} N, \quad F_{R_o \alpha} = \sum_{i=1}^2 \sum_{n=0}^{N-1} \rho_i^2 \varepsilon_{2i} n = \frac{N(N-1)}{2} \sum_{i=1}^2 \rho_i^2 \varepsilon_{2i} \quad (46a)$$

$$F_{R_o \beta} = \sum_{i=1}^2 \sum_{n=0}^{N-1} \rho_i^2 \varepsilon_{2i} n^2 = \frac{N(N-1)(2N-1)}{6} \sum_{i=1}^2 \rho_i^2 \varepsilon_{2i} \quad (46b)$$

$$F_{\alpha \alpha} = \sum_{i=1}^2 \sum_{n=0}^{N-1} \rho_i^2 \varepsilon_{2i} n^2 = \frac{N(N-1)(2N-1)}{6} \sum_{i=1}^2 \rho_i^2 \varepsilon_{2i} \quad (47a)$$

$$F_{\alpha \beta} = \sum_{i=1}^2 \sum_{n=0}^{N-1} \rho_i^2 \varepsilon_{2i} n^3 = \frac{N^2(N-1)^2}{4} \sum_{i=1}^2 \rho_i^2 \varepsilon_{2i} \quad (47b)$$

$$F_{\beta \beta} = \sum_{i=1}^2 \sum_{n=0}^{N-1} \rho_i^2 \varepsilon_{2i} n^4 = \left( \frac{N^5}{5} - \frac{N^4}{2} + \frac{N^3}{3} - \frac{N}{30} \right) \sum_{i=1}^2 \rho_i^2 \varepsilon_{2i} \quad (48)$$

The CRB's after inverting the FIM, are given by

$$CRB(R_o) = \frac{3}{(\rho_1^2 \varepsilon_{21} + \rho_2^2 \varepsilon_{22})} \times \frac{3N^2 - 3N + 2}{N(N^2 + 3N + 2)} \quad (49)$$

$$CRB(\alpha) = \frac{12}{\cos^2(\theta)(\rho_1^2 \varepsilon_{21} + \rho_2^2 \varepsilon_{22})} \times \frac{16N^2 - 30N + 11}{N(N^4 - 5N^2 + 4)} \quad (50)$$

$$CRB(\beta) = \frac{1}{\cos^2(\theta)(\rho_1^2 \varepsilon_{21} + \rho_2^2 \varepsilon_{22})} \times \frac{180}{N(N^4 - 5N^2 + 4)} \quad (51)$$

where  $\varepsilon_{2i}$  is defined before and includes both carrier frequency and noise variance terms.

## 2.4 Simulations and Quasi-Experimental Results

### 2.4.1 Numerical simulations

We begin by examining the effect of  $\theta$  on the CRBs. The term  $1/\cos^2(\theta)$  in the CRBs will simply increase the CRBs for increased value of  $\theta$ . The CRB's become infinite when  $\theta = \pm\pi/2$ . Moreover,  $\theta = \pm\pi/2$  yields a singular FIM. The minimum CRB is achieved when  $\theta = 0$ , i.e., when the target is moving along the LOS of the radar system. Without loss of generality, in the simulations we assume,  $\rho_i = \rho$ , and  $h_i(n; \psi) = h(n; \psi), \forall i = 1, 2$ . This then implies  $\Delta\rho_i = \Delta\rho$  and  $\phi_i = \phi$ . The SNR for constant Doppler and accelerating target motion profiles, are denoted by  $SNR_i = \rho^2 / \sigma_i^2, i = 1, 2$  for the two carriers respectively. Fig 1 illustrates the sensitivity of the CRBs for the constant Doppler and accelerating target motion profiles, the carrier frequencies were chosen to be  $f_1 = 906$  MHz and  $f_2 = 919$  MHz. Fig. 2 shows the CRBs for the MD motion profile for the vibration model ( $\Delta\rho = 0$ ), and the rotation model. We define SNR for MD as  $SNR_i = (\rho + \Delta\rho)^2 / \sigma_i^2, i = 1, 2$ . In order to be fair in our comparison, the SNR for both the vibration and rotation models was assumed identical in Fig. 2, and the parameters for vibration and rotation model are subscripted by 'v' and 'r' respectively. Fig. 2 clearly shows that the CRBs for the rotation model are higher than those of the vibration model for the same SNRs. It is well known that the CRBs of the phase parameters increase with the bandwidth of the signal amplitude [22,

26]. The bandwidth of the amplitude for the vibration model is zero (DC), whereas, bandwidth of the amplitude for the rotation model is  $\omega_o$ . Indeed, the scalar function  $h(n; \psi)$  in the rotation model smears the exponential part of the returns and makes parameter estimation more difficult. In Fig. 1 we observe that  $\nu$  has higher sensitivity than  $R_o$ , since it has a lower CRB for increasing  $N$  [22]. Similarly, from Fig. 1, the chirp, or the accelerating target parameter  $\beta$ , is the most sensitive, whereas  $R_o$  is the least sensitive. From Fig. 2, for data record length  $N > 50$ , the parameter  $\omega_o$  is the most sensitive. It is noteworthy that the CRB for  $R_o$  is much lower than the CRB for parameter  $d$ , both of which have the same units of measurement and represent a distance and displacement, respectively. Sensitivity of the parameters, as evidenced by the CRBs, are an indication of some order of estimation of the parameters. For example, we have seen that  $\nu$  is the most sensitive parameter for the constant Doppler motion and it represents the frequency in the sinusoidal parameter estimation problem, whereas  $R_o$  represents the phase in the sinusoidal parameter estimation model. It is well known that the maximum likelihood estimator (MLE) for the sinusoidal parameter model estimates the frequency first, and then the phase [15]. Similarly, for the PPS signal model, the highest order PPS coefficient is estimated first, and the lower orders are estimated subsequently [23, 26-28]. In our case, this agrees with  $\beta$  being the most sensitive for a second order PPS signal, i.e. the accelerating target returns. For the case of MD, we have a suboptimal estimator already in place in eqs. (13-14). Clearly, taking the Fourier transform of the MD returns, using the DC as a reference, and selecting the two nearest peaks around 0 Hz is the quickest way to estimate  $\omega_o$ .

#### 2.4.2 Quasi-Experimental results

In urban sensing applications, the rotational or the vibrational frequency is an important parameter for differentiating animate from inanimate targets. An indoor rotating fan with three plastic blades was used as the target for the real-data collection experiment. In order to obtain strong single component returns, one of the blades was wrapped in aluminum foil. The carrier frequencies of the dual-frequency radar were chosen to be  $f_1 = 906.3$  MHz, and  $f_2 = 919.8$  MHz, and the sampling frequency was set to 1 kHz. The

radar returns at the two frequencies were simultaneously collected for a total duration of 1s. The center of rotation of the fan was at a distance of 1.22m from the antenna feed point along the LOS. The rotation speed of the fan was measured to be 780 rpm, which is in agreement with the technical specifications of the fan, and is considered to be the true value of the parameter  $\omega_o$ . The objective is to estimate the rotational frequency of the fan for varying SNRs, and compute its variance for comparison with the CRB. The data is at a high SNR and is virtually noise free. In order to vary the SNR, we add complex white Gaussian noise. Hence the term quasi-experimental is used. Since no estimation technique has been advocated in this chapter, we use the Fourier domain analysis, as given by eqs. (13-14) and extract the frequency of the first harmonic. This procedure is definitely suboptimal, the optimal method of maximum likelihood is not pursued here due to its associated computational complexity [24]. Extracting the first harmonic frequency is sufficient to obtain the estimate of the rotational frequency, since typically indoor inanimate targets are NBFM, see [24] for more details on estimating harmonics of NBFM. The FIM for MD is a function of the parameters  $d$  and  $\varphi_o$ , which are unknown. Furthermore, the amplitudes of the returns are also unknown. We employ some suboptimal schemes to estimate these and use these in our FIM calculations. The estimation of the unknown parameters is performed using the real data without adding artificial noise, these estimates are then considered as the true parameters. In particular, since the amplitudes of the returns are unknown, and, in general, are time-varying, the amplitudes can be efficiently estimated using the second order cyclic moment, see [28] and references therein. On the other hand, the time-frequency (TF) distribution is particularly useful in extracting the parameter  $d$ . The maximum and minimum instantaneous frequencies of the MD signal are given by  $\pm 2f_i d \omega_o / c$  corresponding to the two carrier frequencies, respectively. The bandwidth of the MD signal can then be defined as  $4f_i d \omega_o / c$ . The bandwidth is estimated from the original returns using the spectrogram, and since the rotational frequency is known, computation of  $d$  is straightforward, this value is then taken as the true parameter value. The return for the first carrier was used for calculating  $d$ . For estimating the phase  $\varphi_o$ , we use the least squares estimator as in [24], with  $K = 1$  using the returns corresponding to the first carrier frequency. For



this procedure, the returns were zero padded and an 8192 point FFT was computed. These parameters were then used in computing the CRBs. Fig. 3(a) shows the spectrogram of the original returns corresponding to the carrier  $f_1$ . It also shows the signature using the estimated  $d$  and  $\varphi_o$ , and the true rotational frequency  $\omega_o$  as a solid black line, which closely follows the TF signature of the returns. The maximum and minimum of instantaneous frequency are depicted with the dotted black lines. In Fig. 3(b), the raw FFT of the returns corresponding to the carrier  $f_1$  is shown, Fig. 3(c) shows the estimated second order cyclic moment for the carrier frequency  $f_1$ , and Fig. 3(d) shows the real part of the returns for the first carrier. From Fig. 3(c) it is clear that the second order cyclic moment shows harmonics at the rotational frequency  $\omega_o$ , indicating the cyclic RCS changes, and hence validating the cyclic amplitude modulation we have assumed for the MD rotational model. We are now in a position to compute the CRB and the simulated mean square error (MSE) using Monte Carlo simulations. Fig. 4 shows the CRB for the rotational frequency and the MSE of its estimates vs. SNRs, 100 Monte Carlo trials was used in the simulations. For each carrier frequency, the initial estimate was derived from a raw FFT search, and subsequently the chirp-z transform was used to compute the final estimate of the first harmonic around the coarse initial estimate from the FFT, the search span of the chirp-z transform was 8192 points. This estimation procedure is identical to that used in [24] with  $K=1$ . The final estimate of the rotational frequency was the average of these estimates for the two carrier frequencies. A strong and consistent bias of the order  $10^{-3}$  was observed in the raw MSE for  $\text{SNR} \geq 20$  dB, as shown in Fig. 4, the bias-corrected MSE is also shown and comes close to the CRB for the rotational model. The strong bias maybe due to the chirp-z transform, necessitating optimization methods to be employed for estimation, for example the non-linear least squares. For comparison, the CRB for the vibration model (the single frequency and dual frequency) are also shown, the simulated MSE is far away from the vibration model CRBs.



## 2.5 Conclusions

In this chapter, we considered dual frequency radar for range estimation with application to urban sensing. Three important and commonly encountered indoor range profiles were considered, namely, linear translation, micro-Doppler and accelerating target motion profiles. The CRBs were derived for the initial range and key target classification parameters, namely, velocity, acceleration and oscillatory frequency of targets respectively, encountering linear, accelerating, and simple harmonic motions. A parametric model specific to the dual frequency radar technique was developed for the range profiles, incorporating the target aspect angles. It was shown that if the aspect angle is unknown, then the FIM becomes singular, leading to unidentifiability of the parameters. Closed form expressions for CRBs were derived for the parameters associated with translational motion profiles. However, for the MD case, the CRBs were intractable in closed form, and numerical matrix inversion was pursued. It was also shown that the dual-frequency approach provides lower bounds as compared to the single frequency counterpart.

## APPENDIX-A

We demonstrate by example, when  $\theta$  is unknown and is a desired parameter, the FIM is singular. Specifically, the derivation is for the constant Doppler range profile, the derivation can be generalized to any other motion profile. For convenience, and without loss of generality, we assume  $\rho_i = \rho$ . The parameter vector sought after is  $\psi = [R_o \quad v \quad \theta]$ . Using (17) and (9), and skipping the trivial details

$$\mathbf{F}(\theta) = \begin{bmatrix} F_{R_o R_o} & F_{R_o v} & F_{R_o \theta} \\ F_{R_o v} & F_{vv} & F_{v\theta} \\ F_{R_o \theta} & F_{v\theta} & F_{\theta\theta} \end{bmatrix}$$

$$\begin{bmatrix} \varepsilon N & \frac{\varepsilon \cos(\theta) N(N-1)}{2} & \frac{-v\varepsilon \sin(\theta) N(N-1)}{2} \\ \frac{\varepsilon \cos(\theta) N(N-1)}{2} & \frac{\varepsilon \cos^2(\theta) N(N-1)(2N-1)}{6} & \frac{-v\varepsilon \sin(2\theta) N(N-1)(2N-1)}{12} \\ \frac{-v\varepsilon \sin(\theta) N(N-1)}{2} & \frac{-v\varepsilon \sin(2\theta) N(N-1)(2N-1)}{12} & \frac{\varepsilon v^2 \sin^2(\theta) N(N-1)(2N-1)}{6} \end{bmatrix} \quad (\text{A.1})$$

It can be shown that the FIM is singular, implying non-identifiable parameters for the chosen model [29]. This can, however, be overcome if an additional carrier diverse radar system, oriented differently from the original radar system, is used. This involves an additional angle diversity term in the Fisher information. Moreover, the orientation of the two radars with respect to each other must be known for identifiability.

## APPENDIX-B

In order to bring the FIM elements for MD in closed form, we need the following which can be derived easily using elementary trigonometry, and elementary calculus. The series are assumed to uniformly converge so that the differential and summation operators can be interchanged.

$$g_1(\omega, \psi) = \sum_{n=0}^{N-1} \cos(\omega n - \psi) = \operatorname{Re} \left\{ \sum_{n=0}^{N-1} e^{j(\omega n - \psi)} \right\} = \frac{\cos(\omega(N-1)/2 - \psi) \sin(\omega N/2)}{\sin(\omega/2)} \quad (\text{B.1})$$

$$g_2(\omega, \psi) = \sum_{n=0}^{N-1} \sin(\omega n - \psi) = \operatorname{Im} \left\{ \sum_{n=0}^{N-1} e^{j(\omega n - \psi)} \right\} = \frac{\sin(\omega(N-1)/2 - \psi) \sin(\omega N/2)}{\sin(\omega/2)} \quad (\text{B.2})$$

$$g_3(\omega, \psi) = \sum_{n=0}^{N-1} -n \sin(\omega n - \psi) = \frac{\partial g_1(\omega, \psi)}{\partial \omega} = \frac{1}{4 \sin^2\left(\frac{\omega}{2}\right)} \left( \begin{array}{l} (2N-1) \sin \frac{\omega}{2} \cos\left(\omega \frac{2N-1}{2} - \psi\right) \\ -\cos \frac{\omega}{2} \sin\left(\omega \frac{2N-1}{2} - \psi\right) - \sin(\psi) \end{array} \right) \quad (\text{B.3})$$

$$\begin{aligned} g_4(\omega, \psi) &= \sum_{n=0}^{N-1} n^2 \sin^2(\omega n - \psi) = \frac{1}{2} \sum_{n=0}^{N-1} (n^2 - n^2 \cos(2\omega n - 2\psi)) \\ &= \frac{1}{2} \left( \frac{N(N-1)(2N-1)}{6} + \frac{\partial g_3(\omega, \psi)}{\partial \omega} \Big|_{\omega=2\omega, \psi=2\psi} \right) \\ &= \frac{1}{2} \left( \frac{N(N-1)(2N-1)}{6} + \frac{1}{8 \sin^3(\omega)} \left( \begin{array}{l} 2 \cos^2(\omega) \sin(\omega(2N-1) - 2\psi) \\ + 2 \cos(\omega) \sin(2\psi) \\ - \left( (2N-1) \sin(2\omega) \right. \\ \times \cos(\omega(2N-1) - 2\psi) \right) \\ - \left( 4N(N-1) \sin^2(\omega) \right. \\ \times \sin(\omega(2N-1) - 2\psi) \end{array} \right) \right) \end{aligned} \quad (\text{B.5})$$

$$g_5(\omega, \psi) = \sum_{n=0}^{N-1} n^2 \cos^2(\omega n - \psi) = \frac{N(N-1)(2N-1)}{6} - g_4(\omega, \psi) \quad (\text{B.7})$$

$$g_6(\omega, \psi) = \sum_{n=0}^{N-1} n^2 \cos(\omega n - \psi) = \frac{-\partial g_3(\omega, \psi)}{\partial \omega} = \frac{N(N-1)(2N-1)}{6} - 2g_4(\omega/2, \psi/2) \quad (\text{B.8})$$

$$g_7(\omega, \psi) = \sum_{n=0}^{N-1} -n \cos(\omega n - \psi) = -\frac{\partial g_2(\omega n - \psi)}{\partial \omega}$$

$$= \frac{-1}{4 \sin^2(\omega/2)} \left( \begin{aligned} &(2N-1) \sin \frac{\omega}{2} \sin \left( \omega \frac{2N-1}{2} - \psi \right) \\ &+ \cos \frac{\omega}{2} \cos \left( \omega \frac{2N-1}{2} - \psi \right) - \cos(\psi) \end{aligned} \right) \quad (\text{B.10})$$

$$g_8(\omega, \psi) = \sum_{n=0}^{N-1} -n \sin^2(\omega n - \psi) = \frac{1}{2} (-N(N-1)/2 - g_7(2\omega, 2\psi)) \quad (\text{B.11})$$

We are now in a position to express the FIM elements in closed form. The following can be readily shown

$$F_{R_o R_o} = \sum_{i=1}^2 \varepsilon_{2i} \left( \rho_i^2 N + 2\rho_i \Delta \rho_i g_1(\omega_o, \phi_i) + \frac{\Delta \rho_i^2 (g_1(2\omega_o, 2\phi_i) + N)}{2} \right) \quad (\text{B.12})$$

$$F_{R_o d} = \cos(\theta) \sum_{i=1}^2 \varepsilon_{2i} \left( \begin{aligned} &(\rho_i^2 + \Delta \rho_i^2 / 2) g_1(\omega_o, \varphi_o) + \frac{\Delta \rho_i^2 (g_1(3\omega_o, \varphi_o + 2\phi_i) + g_1(\omega_o, 2\phi_i - \varphi_o))}{4} \\ &+ \rho_i \Delta \rho_i (g_1(2\omega_o, \varphi_o + \phi_i) + N \cos(\varphi_o - \phi_i)) \end{aligned} \right) \quad (\text{B.13})$$

$$F_{R_o \omega_o} = \cos(\theta) \sum_{i=1}^2 \varepsilon_{2i} \left( \begin{aligned} &(\rho_i^2 d + \Delta \rho_i^2 d / 2) g_3(\omega_o, \varphi_o) + \rho_i \Delta \rho_i d g_3(2\omega_o, \varphi_o + \phi_i) \\ &-\rho_i \Delta \rho_i d \sin(\phi_i - \varphi_o) N(N-1)/2 + \Delta \rho_i^2 d g_3(3\omega_o, \varphi_o + 2\phi_i)/4 \\ &-\Delta \rho_i^2 d g_3(\omega_o, \varphi_o - 2\phi_i)/4 \end{aligned} \right) \quad (\text{B.14})$$

$$F_{R_o \varphi_o} = \cos(\theta) \sum_{i=1}^2 \varepsilon_{2i} \left( \begin{aligned} &(\rho_i^2 d + \Delta \rho_i^2 d / 2) g_2(\omega_o, \varphi_o) + \rho_i \Delta \rho_i d g_2(2\omega_o, \varphi_o + \phi_i) - \rho_i \Delta \rho_i d \sin(\phi_i - \varphi_o) N \\ &+ \Delta \rho_i^2 d g_2(3\omega_o, \varphi_o + 2\phi_i)/4 - \Delta \rho_i^2 d g_2(\omega_o, \varphi_o - 2\phi_i)/4 \end{aligned} \right) \quad (\text{B.15})$$

$$F_{R_o \Delta \rho_i} = 0, F_{R_o \phi_i} = 0, F_{d \Delta \rho_i} = 0, F_{d \phi_i} = 0 \quad (\text{B.16})$$

$$F_{dd} = \cos^2(\theta) \sum_{i=1}^2 \varepsilon_{2i} \left( \begin{aligned} &\rho_i^2 (N + g_1(2\omega_o, 2\varphi_o)) / 2 + \rho_i \Delta \rho_i g_1(\omega_o, \phi_i) + \rho_i \Delta \rho_i g_1(3\omega_o, 2\varphi_o + \phi_i) / 2 \\ &+ \rho_i \Delta \rho_i g_1(\omega_o, 2\varphi_o - \phi_i) / 2 + \Delta \rho_i^2 (N + g_1(2\omega_o, 2\phi_i) + g_1(2\omega_o, 2\varphi_o)) / 4 \\ &+ \Delta \rho_i^2 (N + g_1(4\omega_o, 2\phi_i + 2\varphi_o) + N \cos(2\varphi_o - 2\phi_i)) / 8 \end{aligned} \right) \quad (\text{B.17})$$

$$F_{d \omega_o} = \cos^2(\theta) \sum_{i=1}^2 \varepsilon_{2i} \left( \begin{aligned} &\rho_i^2 d g_3(2\omega_o, 2\varphi_o) / 2 + \rho_i \Delta \rho_i d g_3(3\omega_o, 2\varphi_o + \phi_i) / 2 + \rho_i \Delta \rho_i d g_3(\omega_o, 2\varphi_o - \phi_i) / 2 \\ &+ \Delta \rho_i^2 d (g_3(4\omega_o, 2\varphi_o + 2\phi_i) - N(N-1) \sin(2\phi_i - 2\varphi_o) / 2) / 8 + \Delta \rho_i^2 d g_3(2\omega_o, 2\varphi_o) / 4 \end{aligned} \right) \quad (\text{B.18})$$

$$F_{d \varphi_o} = \cos^2(\theta) \sum_{i=1}^2 \varepsilon_{2i} \left( \begin{aligned} &\rho_i^2 d g_2(2\omega_o, 2\varphi_o) / 2 + \rho_i \Delta \rho_i d g_2(3\omega_o, 2\varphi_o + \phi_i) / 2 + \rho_i \Delta \rho_i d g_2(\omega_o, 2\varphi_o - \phi_i) / 2 \\ &+ \Delta \rho_i^2 d (g_2(4\omega_o, 2\varphi_o + 2\phi_i) + N \sin(2\phi_i - 2\varphi_o)) / 8 + \Delta \rho_i^2 d g_2(2\omega_o, 2\varphi_o) / 4 \end{aligned} \right)$$

(B.19)

$$F_{\omega_o\omega_o} = \sum_{i=1}^2 \varepsilon_{1i} \Delta \rho_i^2 g_4(\omega_o, \phi_i) + \cos^2(\theta) \sum_{i=1}^2 \varepsilon_{2i} \left( \begin{aligned} &\rho_i^2 d^2 g_4(\omega_o, \varphi_o) + \rho_i \Delta \rho_i g_5(\omega_o, \phi_i) \\ &- \rho_i \Delta \rho_i d^2 (g_6(3\omega_o, \phi_i + 2\varphi_o) + g_6(\omega_o, 2\varphi_o - \phi_i)) / 2 \\ &+ \Delta \rho_i^2 d^2 (N(N-1)(2N-1)/6) / 4 \\ &- \Delta \rho_i^2 d^2 (g_6(2\omega_o, 2\phi_i) - g_6(2\omega_o, 2\varphi_o)) / 4 \\ &- \Delta \rho_i^2 d^2 (g_6(4\omega_o, 2\phi_i + 2\varphi_o) + N(N-1)(2N-1)\cos(2\phi_i - 2\varphi_o)/6) / 8 \end{aligned} \right) \quad (B.20)$$

$$F_{\omega_o\varphi_o} = \cos^2(\theta) \sum_{i=1}^2 \varepsilon_{2i} \left( \begin{aligned} &\rho_i^2 d^2 g_8(\omega_o, \varphi_o) + \rho_i \Delta \rho_i d^2 g_7(\omega_o, \phi_i) \\ &- \rho_i \Delta \rho_i d^2 (g_7(3\omega_o, \phi_i + 2\varphi_o) + g_7(\omega_o, 2\varphi_o - \phi_i)) / 2 \\ &- \Delta \rho_i^2 d^2 N(N-1) / 8 \\ &+ \Delta \rho_i^2 d^2 (g_7(2\omega_o, 2\phi_i) - g_7(2\omega_o, 2\varphi_o)) / 4 \\ &+ \Delta \rho_i^2 d^2 (N(N-1)\cos(2\phi_i - 2\varphi_o) / 2 - g_7(4\omega_o, 2\phi_i + 2\varphi_o)) / 8 \end{aligned} \right) \quad (B.21)$$

$$F_{\omega_o\Delta\rho_i} = \varepsilon_{1i} \Delta \rho_i g_3(2\omega_o, 2\phi_i) / 2, \quad F_{\omega_o\phi_i} = \varepsilon_{1i} \Delta \rho_i^2 (-g_7(2\omega_o, 2\phi_i) - N) / 2 \quad (B.22)$$

$$F_{\varphi_o\varphi_o} = \cos^2(\theta) \sum_{i=1}^2 \varepsilon_{2i} \left( \begin{aligned} &\rho_i^2 d^2 (N - g_1(2\omega_o, 2\varphi_o)) / 2 + \rho_i \Delta \rho_i d^2 g_1(\omega_o, \phi_i) \\ &- \rho_i \Delta \rho_i d^2 (g_1(3\omega_o, 2\varphi_o + \phi_i) + g_1(\omega_o, 2\varphi_o - \phi_i)) / 2 \\ &+ \Delta \rho_i^2 d^2 (N - g_1(2\omega_o, 2\varphi_o) + g_1(2\omega_o, 2\phi_i)) / 4 \\ &- \Delta \rho_i^2 d^2 (N \cos(2\varphi_o - 2\phi_i) + g_1(4\omega_o, 2\varphi_o + 2\phi_i)) / 8 \end{aligned} \right) \quad (B.23)$$

$$F_{\varphi_o\Delta\rho_i} = 0, \quad F_{\varphi_o\phi_i} = 0, \quad F_{\Delta\rho_i\Delta\rho_i} = \varepsilon_{1i} (N + g_1(2\omega_o, 2\phi_i)) / 2 \quad (B.24)$$

$$F_{\Delta\rho_i\phi_i} = \varepsilon_{1i} \Delta \rho_i g_2(2\omega_o, 2\phi_i) / 2, \quad F_{\phi\phi} = \varepsilon_{1i} \Delta \rho_i (N - g_1(2\omega_o, 2\phi_i)) / 2 \quad (B.25)$$



## APPENDIX-C

*Theorem-1:* Let  $\mathbf{A}, \mathbf{B}$  be two complex matrices  $\in C^{N \times N}$ . The rank of  $\mathbf{A}$  is one with non-zero diagonal elements and the rank of  $\mathbf{B}$  is  $N$ . Then  $(\mathbf{A} \circ \mathbf{B})^{-1} = \mathbf{B}^{-1} \circ (\mathbf{A}^{\circ-1})^T = \mathbf{B}^{-1} \circ (\mathbf{A}^T)^{\circ-1}$ , where  $\mathbf{A}^{\circ-1} = [a_{ij}^{-1}]$ .

*Proof:* Since  $\mathbf{A}$  is rank one, it can be rewritten as an outer product, given by

$$\mathbf{A} = \mathbf{x}\mathbf{y}^H, \mathbf{A}^T = \mathbf{y}^* \mathbf{x}^T, \text{ with } \mathbf{x}, \mathbf{y} \in C^{N \times 1} \quad (\text{C.1})$$

The Hadamard product can then be expressed as

$$\mathbf{A} \circ \mathbf{B} = \mathbf{B} \circ \mathbf{x}\mathbf{y}^H = \mathbf{D}_\mathbf{x} \mathbf{B} \mathbf{D}_\mathbf{y}^H \quad (\text{C.2})$$

where

$$\mathbf{D}_\mathbf{x} = \text{Diag}[\mathbf{x}] = \begin{bmatrix} x_1 & & \\ & \ddots & \\ & & x_N \end{bmatrix}, \mathbf{D}_\mathbf{y} = \text{Diag}[\mathbf{y}] = \begin{bmatrix} y_1 & & \\ & \ddots & \\ & & y_N \end{bmatrix} \quad (\text{C.3})$$

It is also clear from (C.2) that  $\mathbf{A} \circ \mathbf{B}$  is non-singular. At this stage it is instructive to note that if any diagonal element of  $\mathbf{A}$  is zero, which is tantamount to any element in (C.3) being zero, then the inverse of  $\mathbf{A} \circ \mathbf{B}$  does not exist. This is primarily the reason for imposing the condition, that none of the diagonal elements of  $\mathbf{A}$  are zero in the statement of the theorem. The proof is straightforward from hereon, from (C.2)

$$(\mathbf{A} \circ \mathbf{B})^{-1} = (\mathbf{D}_\mathbf{y}^H)^{-1} \mathbf{B}^{-1} \mathbf{D}_\mathbf{x}^{-1} \quad (\text{C.4})$$

Rewriting the diagonal matrices in terms of the Hadamard and the outer products as in (C.2), we get

$$(\mathbf{A} \circ \mathbf{B})^{-1} = \mathbf{B}^{-1} \circ \begin{bmatrix} 1/y_1^* \\ \vdots \\ 1/y_N^* \end{bmatrix} \begin{bmatrix} 1/x_1 & \dots & 1/x_N \end{bmatrix} = \mathbf{B}^{-1} \circ (\mathbf{y}^{\circ-1})^* (\mathbf{x}^{\circ-1})^T \quad (\text{C.5})$$

Expanding the outer product and rewriting the elements in terms of  $\mathbf{A}$ , we obtain

$$(\mathbf{A} \circ \mathbf{B})^{-1} = \mathbf{B}^{-1} \circ (\mathbf{A}^{\circ-1})^T = \mathbf{B}^{-1} \circ (\mathbf{A}^T)^{\circ-1} \quad (\text{C.6})$$

It must be noted that if  $\mathbf{A}$  has a rank greater than one, then the inverse of the Hadamard product is quite complicated to derive. Fortunately, such a situation does not arise in this chapter.

## References

- [1] Journal of the Franklin Institute, Special Issue on 'Advances in Indoor Radar Imaging,' Sept. 2008, 345, (6)
- [2] Proceedings of the 2008 IEEE International Conference on Acoustics, Speech, and Signal Processing, Special Session on 'Through-the-Wall Radar Imaging,' Las Vegas, USA, April 2008, pp. 5173-5196
- [3] Borek, S. E.: 'An overview of through the wall surveillance for homeland security', Proc. 34th Applied Imagery and Pattern Recognition Workshop, Washington D.C., USA, Oct. 2005
- [4] Proceedings of the 2005 IEEE AP-S International Symposium, Special Session on 'Through-Wall Imaging and Sensing', Washington D.C., USA, July 2005, 3B, pp. 317-341
- [5] Skolnik, M. I.: 'Introduction to Radar Systems' (McGraw-Hill, New York, 3rd edn. 2002)
- [6] Ridenour, L. N.: 'Radar System Engineering', Vol. 1 of MIT Radiation Laboratory Series (McGraw-Hill, NY, 1947)
- [7] Amin, M., Zeman, P., and Ahmad, F.: 'Moving target localization for indoor imaging using dual frequency CW radars', Proc. IEEE Workshop on Sensor Array and Multi-channel Processing, Waltham, Massachusetts, USA, Jul. 12-14, 2006, pp. 367-371
- [8] Boyer, W. D.: 'A duplex, Doppler, phase comparison radar', IEEE Trans. Aerosp. Navig. Electron., 1963, ANE-10, (3), pp. 27-33
- [9] Dingley, G., and Alabaster, C.: 'Radar based automatic target system', Proc. Fourth Int. Waveform Diversity and Design Conf., Orlando, FL, USA, Feb. 2009, pp. 22-25
- [10] Setlur, P., Amin, M., and Ahmad, F.: 'Cramer-Rao bounds for range and motion parameter estimations using dual frequency radars', Proc. Int. Conf. Acoust., Speech Signal Process., Honolulu, Hawaii, Apr. 15-20, 2007
- [11] Haykin, S.: 'Communication Systems' (John Wiley, New York, 4th edn. May 2000)
- [12] Ahmad, F., Amin, M. G., and Zeman, P. D.: 'Performance analysis of dual-frequency CW radars for motion detection and ranging in urban sensing applications', Proc. SPIE Defense and Security Symposium, Orlando FL, USA, April 2007
- [13] Ahmad, F., Amin, M. G., and Zeman, P. D.: 'Dual-frequency radars for target localization in urban sensing', IEEE Trans. on Aerospace and Electronic Systems, In Press.
- [14] Zhang, Y., Amin, M. G., and Ahmad, F.: 'Time-frequency analysis for the localization of multiple moving targets using dual-frequency radars', IEEE Signal Processing Letters, 2008, 15, pp. 777-780
- [15] Kay, S. M.: 'Modern Spectral Estimation: Theory and Application' (Prentice Hall, Englewood Cliffs, NJ, 1988)

- [16] Rife, D., and Boorstyn, R.: 'Single tone parameter estimation from discrete-time observations', IEEE Trans. Inf. Theory, Sep. 1974, 20, (5), pp. 581-598
- [17] Chen, V. C., Li, F., Ho, S. -S., and Wechsler, H.: 'Micro-Doppler effect in radar: phenomenon, model, and simulation study', IEEE Trans. Aerosp. Electron. Syst., January 2006, 42, (1), pp. 2-21
- [18] Abramowitz, M. and Stegun, I. A.: 'Handbook of Mathematical Functions with Formulas, Graphs, and Mathematical tables' (Dover Publications, New York, 1972)
- [19] Grewal, B. S.: 'Higher Engineering Mathematics', (Khanna Publishers, New Delhi, India, 2002)
- [20] Peleg, S., and Porat, B.: 'The Cramér-Rao lower bound for signals with constant amplitude and polynomial phase', IEEE Trans. Signal Process., Mar. 1991, 39, (3), pp. 749-752
- [21] Zoubir, A. M. and Taleb, A.: 'The Cramer-Rao bound for the estimation of noisy phase signals', Proc. Int. Conf. Acoust., Speech Signal Process., Salt Lake City, Utah, USA, May 2001
- [22] Kay, S. M.: 'Fundamentals of Statistical Signal Processing, Volume: I, Estimation Theory' (Prentice Hall, Englewood Cliffs, NJ, 1993)
- [23] Cirillo, L., Zoubir, A., and Amin, M.: 'Parameter estimation for locally linear FM signals using a time-frequency Hough transform', IEEE Trans. Signal Process., September 2008, 56, (9), pp. 4162-4175
- [24] Gini, F., and Giannakis, G. B.: 'Hybrid FM-polynomial phase signal modeling: parameter estimation and Cramér-Rao bounds', IEEE Trans. Signal Process., February 1999, 47, (2), pp. 363-377
- [25] Horn, R. A., and Johnson, C. R.: 'Topics in Matrix Analysis' (Cambridge University Press, Cambridge, UK, 1991)
- [26] Ghogho, M., Swami, A., and Nandi, A. K.: 'Cramér-Rao bounds and maximum likelihood estimation for random amplitude phase modulated signals', IEEE Trans. Signal Process., Nov. 1999, 47, (11), pp. 2905-2916
- [27] Barbarossa, S., Scaglione, A., and Giannakis, G. B.: 'Product high-order ambiguity function for multicomponent polynomial-phase signal modeling', IEEE Trans. Signal Process., March 1998, 46, (3), pp. 691-708
- [28] Ghogho, M., Swami, A., and Garel, B.: 'Performance analysis of cyclic statistics for the estimation of harmonics in multiplicative and additive noise', IEEE Trans. Signal Process., December 1999, 47, (12), pp. 3235-3249
- [29] Stoica, P., and Marzetta, T. L.: 'Parameter estimation problems with singular information matrices', IEEE Trans. Signal Process., Jan. 2001, 49, (1), pp. 87-90

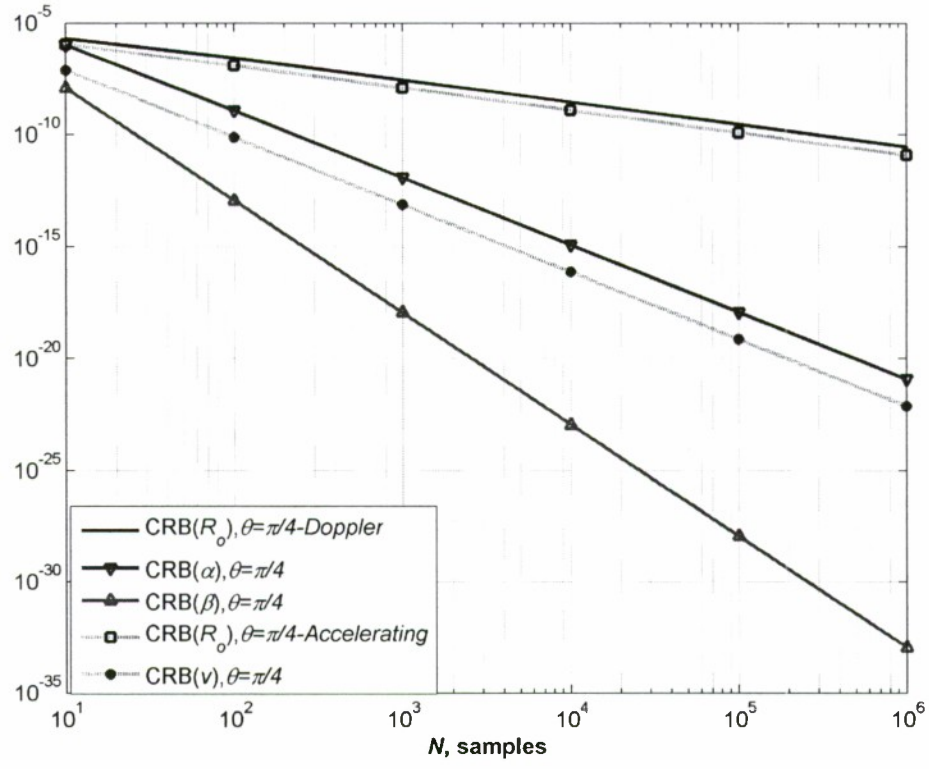


**Fig. 1** Constant Doppler and accelerating target CRB's for  $(SNR1, SNR2) = (10, 20)$  dB.



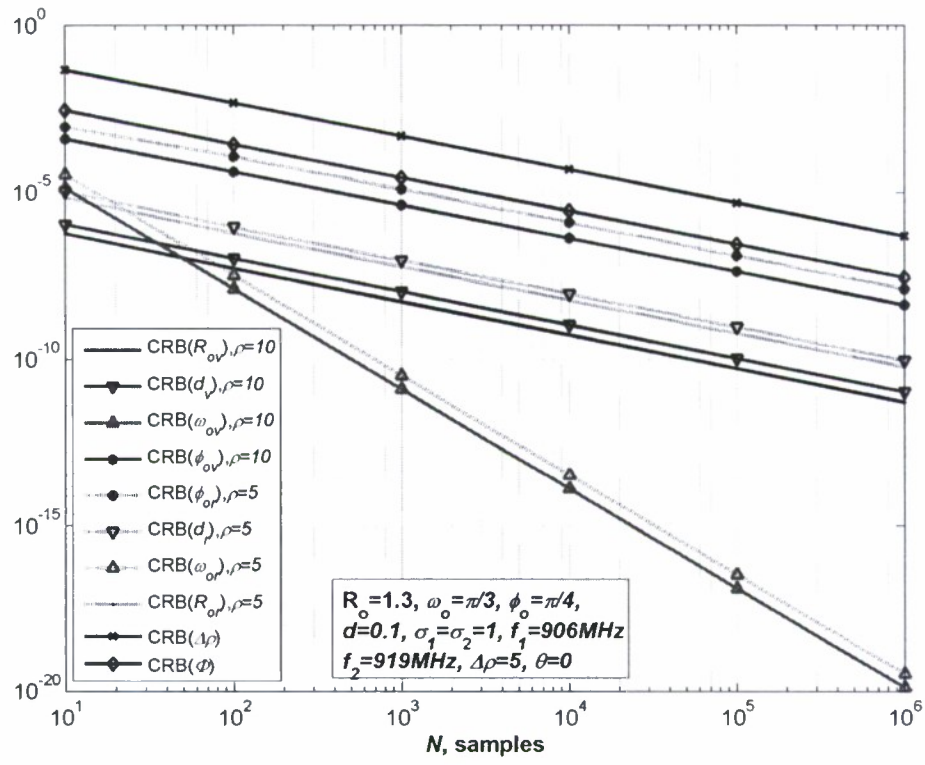
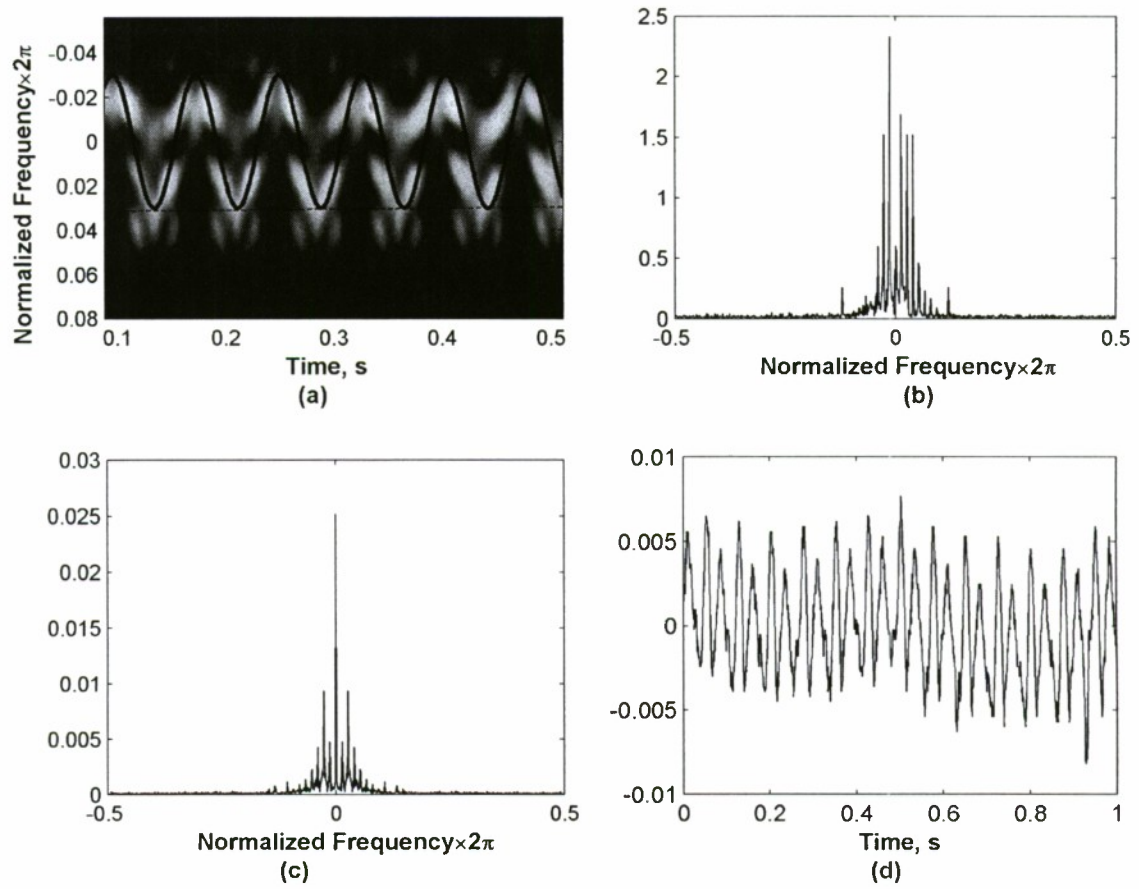
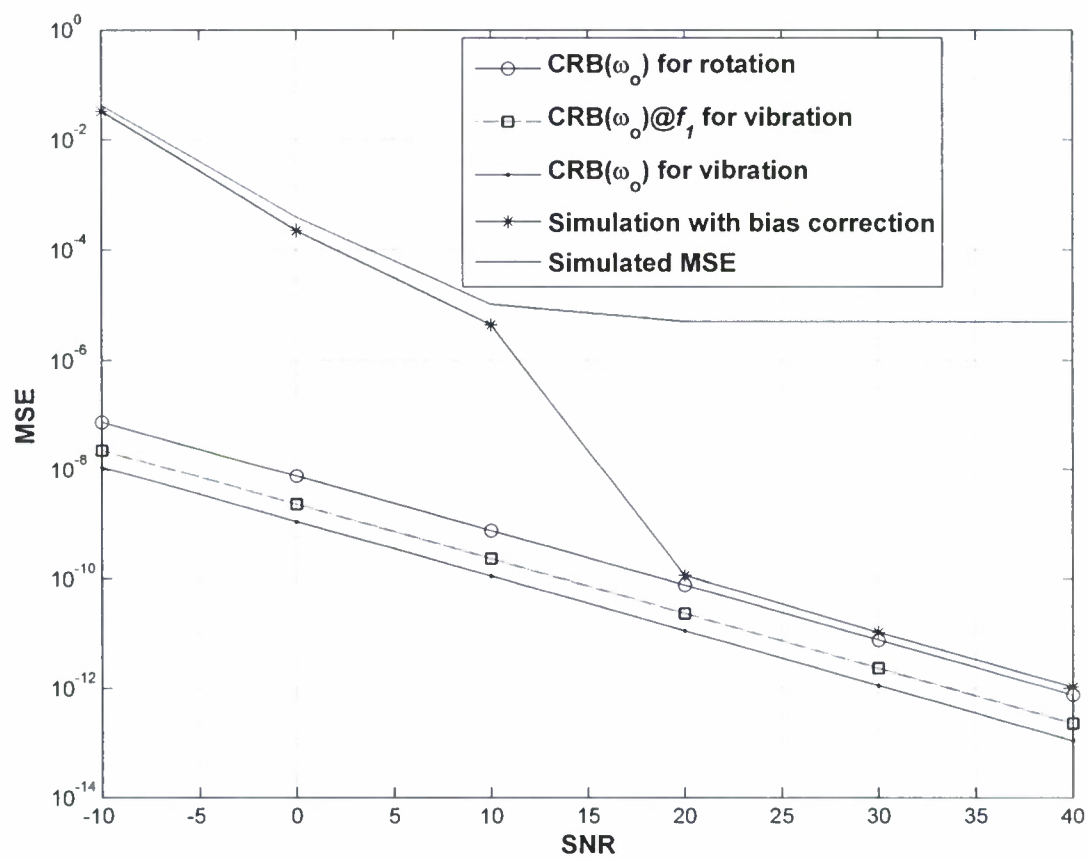


Fig. 2 MD CRBs.



**Fig. 3** (a) Spectrogram of the returns, (b) FFT of raw returns, (c) Second order cyclic moment.

(d) Real part of the returns.



**Fig. 4** Simulation results with respect to SNR.

### 3. Optimal Waveform Design for Improved Indoor Target Detection in Sensing Through-the-Wall Applications

#### *Abstract*

This chapter deals with waveform design for improved detection and classification of targets behind walls and enclosed structures. The target impulse response is incorporated in an optimum design of the transmitted waveform which aims at maximizing the signal to interference and noise ratio (SINR) at the receiver output. The interference represents signal-dependent clutter which along with the wall degrades the receiver performance compared to the free-space and zero-clutter case. Computer simulations show sensitivity of the optimum waveform to target orientation, but depict an SINR enhancement over chirped waveform radar emissions at all aspect angles. Numerical electromagnetic modeling is used to provide the impulse response of typical indoor stationary targets, namely tables, chairs, and humans.

### 3.1 Introduction

Waveform diversity and design has been recently investigated in many applications of Radar and Communications [1]-[4]. In particular, the advances in adaptive radar transmitters have permitted the use of sophisticated pulse shaping techniques in order to improve the detection of point and extended targets [5], [6]. However, waveform design has not been properly addressed in the context of through-the-wall radar imaging (TWRI) [7]. TWRI is an emerging area of research and development with numerous civilian and military applications [37]-[10]. The ultimate TWRI system objective is to detect and classify animate and inanimate objects behind walls. This is achieved by transmitting, receiving, and processing radio frequency signals over the frequency range of [900 MHz– 5 GHz]. Based on extensive experimental and modeling results, it has been decided that this frequency band provides desirable tradeoff between wall signal attenuation, scene resolutions, and antenna size [9].

TWRI applications have specific properties and challenges [10]-[15]. Primarily, the presence of walls distorts the signal and causes significant attenuation and time dispersion. This dispersion may present itself in the form of reverberations and creates constructive and destructive interference in the time-domain which subsequently obscures the EM signatures of targets behind walls. Further, an indoor scene, in addition to humans, is populated by few typical objects, for example, chairs and tables of different possible sizes and shapes.

Considering waveform design in TWRI is motivated by the fact that in target detection and identification, an appropriate choice of the radar waveform has a considerable effect on the amount of information obtained about the target, especially in the case of spatially extended targets. As such, the design of appropriate waveforms is important for improving the performance of TWRI systems [16]. Indoor targets exhibit different frequency responses when illuminated by a wideband signal.

The concept of matched illumination theory introduced in [17], [21] considers designing the transmitter-receiver pair that maximizes the signal-to-interference and noise ratio (SINR) at the output of the receiver matched filter for optimal detection of targets with known impulse responses. It is shown that optimum waveform design produces a waveform that places most of its energy into the frequency band at



which the frequency response of the target of interest or the combined target-wall frequency response exhibits the highest peaks, while suppressing the energy in the frequency bands in which most of the clutter and noise power reside.

For target identification and classification, the criterion is to design a transmitter-receiver pair that maximizes the square of the Mahalanobis distance between the echoes from two targets followed by a bank of matched filters. The filter with the highest output classifies the target.

In this chapter, we extend the matched illumination concept to detection and classification of targets behind walls and inside enclosed structures. We formulate the problem for generic targets, but focus on human as well as two commonly used indoor items, namely, a table and a chair. We address two different cases for optimum waveform design in through wall sensing. In the first case, we account for the wall transmission impulse response, whereas in the second case, the wall presence is totally ignored and is not incorporated in the design. The latter represents what is referred to as free-space waveform design. We demonstrate the improvement in SINR and Mahalanobis distance when using the optimum waveform over a chirp signal of the same energy and time duration, for both the free-space and through-the-wall cases. We also consider waveform design in clutter and under range resolution requirements. Waveform design process with uncertainty in target orientation is also examined.

This chapter considers only a single antenna monostatic operation. Consideration of multi-antenna including bistatic, multi-static, MIMO operations is important for the purpose of target localization and imaging, but is beyond the scope of this chapter.

In Section 3.2, we provide a brief background on applying the linear-time-invariant model to the radar scattering problem as suggested in [16]. We also present an overview of the matched illumination for free-space, and propose a modification to matched illumination, where the wall's impulse response is incorporated into the optimum waveform design process. Section 3.3 deals with the effects of adding a range resolution constraint to the optimization process and illustrates the trade off between improving the range resolution and enhancing the SINR. Section 3.4 addresses the issue of designing the optimal

waveform for detection and classification under uncertainty in target orientations. Various FDTD based simulations are presented in Section 3.5, and finally the conclusions are given in Section 3.6.

### 3.2 Radar Scattering Model and Target Impulse Response

The point target model can reasonably describe the radar returns when employing narrowband pulses. In an idealized point target model, it is assumed that the echo is a scaled and delayed version of the transmitted waveform. In this case, the output of the receiver filter matched to the transmitted waveform produced an SINR that only depends on the total energy of the transmitted waveform. With large signal bandwidth, the returned signal can be considered as that scattered from several points in an extended region in space. In this case, the received echo is a function of the transmitted waveform temporal characteristics as well as the target's impulse response [16].

A common way to model an extended target is to consider the target as a linear system and, thus, examine the input/output relationship of the respective linear model. Since indoor targets (except humans) are usually stationary, we assume linear time-invariant systems over the observation period. The corresponding system model is shown in Fig.1.

If  $z(t)$  represents the electromagnetic field illuminating the target, and  $s(t)$  is the scattered field at an arbitrarily point in the far field, then

$$s(t) = z(t) * q(t) \quad (1)$$

where  $q(t)$  is the target impulse response and  $(*)$  is the convolution operation. The same waveform convolved with the clutter response  $W_c(t)$  yields the signal dependent clutter return  $c(t) = z(t) * W_c(t)$ .

The receiver waveform is then,

$$r(t) = s(t) + x(t) \quad (2)$$

where  $x(t) = c(t) + n(t)$  represents the total undesired contribution of clutter and noise. The receiver applies the matched filter,  $b_{match}(t)$ , to produce the output,

$$y(t) = b_{match}(t) * r(t) \quad (3)$$

The concept of optimum matched illumination waveform design was originally developed to improve the detection of low observable aircrafts [21]. Here, this technique is applied for target detection and classification in TWRI applications. When the target of interest is present, the received signal consists of the reflection of the transmitted waveform from the target, the signal dependent clutter, and additive thermal noise. In the no-target case, the receiver signal has only a thermal noise component and clutter, and exhibits less energy compared to the target case. Thus, in a Gaussian noise and clutter environment, in order to improve target detection, we need to enhance the receiver signal-to-interference and noise ratio (SINR).

The target response to an UWB signal is obtained by full-wave numerical simulations using the commercial software package XFDTD based on the Finite-Difference Time-Domain method (FDTD). Once the scattered field is calculated, an approximation of the impulse response of a target can be obtained by deconvolving the incident waveform from the backscattered field [22].

For convenience of mathematical representations, we use matrix-vector formulations. The transmitted signal  $z(t)$  is given by  $N$  equally spaced time samples separated by an interval  $\Delta t$ , i.e.,  $\mathbf{z} \equiv [z_0, z_1, \dots, z_{N-1}]$ . In a similar way, the received signal  $s(t)$  is represented by  $M$  temporal samples, where  $M > N$ ,  $\mathbf{s} \equiv [s_0, s_1, \dots, s_{M-1}]$ . A matrix representation of this model is,

$$\underbrace{\begin{bmatrix} z_0 & 0 & 0 & \cdots & 0 \\ z_1 & z_0 & 0 & \cdots & 0 \\ \vdots & \vdots & \vdots & \ddots & \vdots \\ z_{N-1} & z_{N-2} & \cdots & \cdots & z_0 \\ z_N & z_{N-1} & \cdots & \cdots & z_1 \\ \vdots & \vdots & \ddots & \ddots & \vdots \\ z_{M-1} & z_{M-2} & \cdots & \cdots & z_{M-N} \end{bmatrix}}_{\mathbf{Z}} \underbrace{\begin{bmatrix} q_0 \\ q_1 \\ q_2 \\ \vdots \\ \vdots \\ \vdots \\ q_{N-1} \end{bmatrix}}_{\mathbf{q}} = \underbrace{\begin{bmatrix} s_0 \\ s_1 \\ s_2 \\ \vdots \\ \vdots \\ \vdots \\ s_{M-1} \end{bmatrix}}_{\mathbf{s}} \quad (4)$$

where  $\mathbf{Z}$  is  $M$ -by- $N$  convolution matrix containing the incident waveform,  $\mathbf{q}$  is the unknown target's impulse response, and  $\mathbf{s}$  is  $M$ -dimensional vector of the scattered field. The target impulse response  $\mathbf{q}$  can be obtained as the least squares solution,

$$\mathbf{q} = (\mathbf{Z}^H \mathbf{Z})^{-1} \mathbf{Z}^H \mathbf{s} \quad (5)$$

where  $[\cdot]^H$  represents the Hermitian operator.

Once the target impulse response is determined, its samples are arranged in an  $M \times N$  convolution matrix  $\mathbf{Q}$  identical in structure to  $\mathbf{Z}$ . The clutter-free received signal can be obtained by the multiplication of the convolution matrix  $\mathbf{Q}$  with the transmitted waveform  $\mathbf{z}$ , i.e.,  $\mathbf{s} = \mathbf{Q}\mathbf{z}$ . Accordingly, the system output, after matched filtering, is given by,

$$\mathbf{y} = \mathbf{b}_{match}^H \mathbf{r} = \mathbf{b}_{match}^H \mathbf{s} + \mathbf{b}_{match}^H \mathbf{x} \quad (6)$$

where  $\mathbf{b}_{match}^H$  is the matched filter of length  $M-1$ . In the sequel, we assume that the target's impulse response is known and deterministic, while the clutter  $W_c$  and the noise  $n$ , are assumed to be independent wide sense stationary stochastic processes.

The autocorrelation matrix of the received signal is  $\mathbf{R}_r \equiv E[\mathbf{r}\mathbf{r}^H] = \mathbf{R}_s + \mathbf{R}_x$ , where  $E[\cdot]$  is the expected value operator and  $\mathbf{R}_s \equiv E[\mathbf{s}\mathbf{s}^H] = \mathbf{s}\mathbf{s}^H$ ,  $\mathbf{R}_x \equiv E[\mathbf{x}\mathbf{x}^H]$  are the autocorrelation matrices of the signal and the noise plus clutter, respectively. Here,  $\mathbf{R}_x$  is the Hermitian Toeplitz matrix with its  $l$ -th element given by

$$r_l = \int_{-\pi}^{+\pi} \left\{ G_n(\omega) + G_c(\omega) |Z(\omega)|^2 \right\} e^{jl\omega} d\omega \quad (7)$$

where  $G_n(\omega)$ ,  $G_c(\omega)$ , and  $|Z(\omega)|^2$  are the power spectral density functions of the noise, clutter, and the transmitted waveforms, respectively. For the case when noise is stationary and white  $G_n(\omega) = N_0$ , and in

absence of clutter,  $G_c(\omega) = 0$ , matrix  $\mathbf{R}_r$  becomes diagonal, with diagonal elements equal to the noise power. The filter output SINR can be expressed as [5],

$$\gamma = \frac{\mathbf{b}_{match}^H \mathbf{R}_s \mathbf{b}_{match}}{\mathbf{b}_{match}^H \mathbf{R}_x \mathbf{b}_{match}} \quad (8)$$

The optimum matched receiver filter  $\mathbf{b}_{match}$  can be written as the Weiner-Hopf equation,

$$\mathbf{b}_{match} = \mathbf{R}_x^{-1} \mathbf{s} = \mathbf{R}_x^{-1} \mathbf{Q} \mathbf{z} \quad (9)$$

Substituting **Error! Reference source not found.** into **Error! Reference source not found.**, the SINR of the matched filter becomes,

$$\gamma_{match} = \max_{\mathbf{b}_{match}} \gamma = \mathbf{s}^H \mathbf{R}_x^{-1} \mathbf{s} \quad (10)$$

Since the optimization is for the purpose of obtaining the optimal transmitted waveform  $\mathbf{z}$ , Eq.

**Error! Reference source not found.** can be rewritten in terms of the transmitted waveform  $\mathbf{z}$ ,

$$\gamma_{opt} \equiv \max_{\mathbf{z}} \gamma_{match} \equiv \max_{\mathbf{z}} \mathbf{z}^H \mathbf{\Omega} \mathbf{z} \quad (11)$$

where  $\mathbf{\Omega} = \mathbf{Q}^H \mathbf{R}_x^{-1} \mathbf{Q}$ .

The optimum transmitted waveform is of finite-duration and finite energy. When the clutter is present, this waveform can be obtained by using an iterative procedure described in [21]. In the case of zero clutter  $G_c(\omega) = 0$ , as shown in [17], [21], the SINR  $\gamma_{opt}$  is optimized if  $\mathbf{z}$  is proportional to the eigenvector of the autocorrelation matrix of the target  $\mathbf{\Omega}$  corresponding to the largest eigenvalue.

In TWRI applications, typical indoor targets can be a priori defined and modeled. Subsequently, the target optimum waveform may be designed off-line and be ready for emission with system deployment.

The model of Fig. 1 can be extended to account for the walls, as described in Fig. 2. The type of wall significantly impacts the ability to detect, resolve, and image the targets behind it [9]. In this chapter, we apply computational electromagnetics to find the impulse responses of both homogeneous walls and simple targets. These responses are then used to design the optimum waveforms, leading to improved target detection.



The free-space matrix formulation in Section 3.2 can be modified to incorporate the wall's impulse response into the optimization process. In this case, the received echo is expressed as,

$$s(t) = z(t) * w(t) * q(t) * w(-t) \quad (12)$$

where  $w(t)$  is the wall's impulse response. Let  $u(t) = w(t) * q(t) * w(-t)$  be the combined wall/target impulse response. Note that for symmetric walls such as homogeneous ones,  $w(t) = w(-t)$ . This combined response can be arranged in a convolution matrix  $U$  having the same form as  $Z$  in Eq. **Error! Reference source not found.**. In this case, the combined wall/target autocorrelation matrix is  $\Omega_w = U^H R_x^{-1} U$ . Accordingly, and similar to free-space, the optimal waveform is proportional to the eigenvector with the highest eigenvalue of  $\Omega_w$ , when there is no clutter, otherwise, the optimum waveform can be obtained using an iterative procedure described in [17].

In the above discussion, we have assumed the wall characteristics to be known, or a priori estimated, and we only considered the wall transmission impulse response in designing the target optimum waveforms. The estimate of the wall electric characteristics and EM signatures has been a subject of many recent publications, e.g., [18], where the wall parameters, thickness and dielectric constant, are estimated and used to model the wall returns, which are then subtracted from the data. This is an effective way to mitigate the wall reflections and separate them from those which depend on the target. The approaches in [19], [20], on the other hand, do not estimate the wall parameters, but they rather remove wall reflections by relying on similarity of wall returns measured from different antenna positions parallel to the wall. Differential SAR or spatial filtering methods can be applied for this purpose.

### 3.3 Range Resolution Considerations

Optimum waveform design may be subject to other constraints, in addition to maximizing the receiver SINR. The length, or time extent, of the optimum waveform can be subject to imaging resolution requirements. For point targets, the range resolution is given by,

$$\Delta R = c\tau/2 \quad (13)$$

where  $\tau$  is the emitted pulse duration and  $c$  is the speed of light. If the extended target has an impulse response of  $L$  samples, then two targets are resolved if they are separated by  $M/2$  samples, since the convolution forces the echo to extend over an interval of  $M = L + N - 1$  samples, where  $M > N$ . The parameter  $\tau$  in Eq. **Error! Reference source not found.** becomes

$$\tau_e = \frac{1}{f_s}(L + N - 1) \quad (14)$$

where  $f_s$  is the sampling frequency of the output signal. Therefore, the range resolution is determined by both the emitted pulse duration and the target's impulse response duration.

The presence of a wall with an impulse response of length  $K$  samples will further degrade the range resolution, since the two-way signal propagation through the wall must now be accounted for. In this case, the temporal interval in Eq. **Error! Reference source not found.** is given by,

$$\tau_w = \tau_e + \frac{2}{f_s}(K - 1) = \frac{1}{f_s}[(N + L - 1) + 2(K - 1)] \quad (15)$$

Since the impulse responses of the wall and the target depend on different factors, most of which are not under the waveform designer or system operator control, the only parameter that can be varied to achieve a certain range resolution is the length of the transmitted waveform  $N$ . It is clear from Eq. **Error! Reference source not found.** that the minimum bound on the range resolution value, i.e.,  $\Delta R_{\min}$  is achieved when  $N = 1$ . In this case,

$$\Delta R_{\min} = \frac{c}{2f_s}(L + 2K - 2) \quad (16)$$

For any other value of range resolution,  $\Delta R > \Delta R_{\min}$ , the corresponding pulse width  $N$  should at most be,

$$N = \frac{2f_s\Delta R}{c} - L - 2(K + 1) \quad (17)$$

This value, which represents the constrained length of the optimum waveform, should define the number of columns in the matrix in eq. **Error! Reference source not found.**

### 3.4 Application of Matched Illumination Technique for Target Identification

The design of the optimized waveform that maximizes the probability of correct target classification is developed in [17], [21] and is similar to those design techniques used for optimized detection. Maximizing the probability of correct classification is equivalent to the maximization of the Mahalanobis distance between the two target echoes,

$$\eta^2 = (s_\alpha - s_\beta)^H R_x^{-1} (s_\alpha - s_\beta) \quad (18)$$

where  $s_\alpha$  and  $s_\beta$  are the vectors corresponding to the echoes from targets  $\alpha$  and  $\beta$ , respectively. The Hermitian Toeplitz matrix  $R_x$  is the autocorrelation matrix of the noise and clutter. Eq. (8) can be presented in terms of the targets' impulse responses,

$$\eta^2 = \mathbf{z}^H \mathbf{\Omega} \mathbf{z} \quad (19)$$

where  $\mathbf{\Omega} = (\mathbf{Q}_\alpha - \mathbf{Q}_\beta)^H R_x^{-1} (\mathbf{Q}_\alpha - \mathbf{Q}_\beta)$ . Similar to the no-clutter case, the optimum discriminating waveform is proportional to the eigenvector corresponding to the highest eigenvalue of  $\mathbf{\Omega}$ . When the clutter is present in the scene, the optimal waveform is obtained via an iterative solution (see e.g., [5], [21]). In the presence of the wall,  $\mathbf{Q}_a$  and  $\mathbf{Q}_b$  are replaced by the combined wall/target convolution matrix presented in Eq. **Error! Reference source not found.**

### 3.5 Target Detection and Classification with Target Orientation Uncertainties

The optimal waveforms are aspect angle dependent since radar targets have different impulse responses for different orientations. So, in order to achieve optimal detection or classification for a specific target, one needs to know the target's orientation with respect to the radar's antenna a priori. This information is not always available for the radar, especially when the target is behind walls. One simple way to over-

come this problem is to cycle through all possible waveforms for the given target of interest. This may be justified by the stationary nature of the objects and the feasibility of using a large number of pulses over a long observation period. In this case, the transmitted waveform corresponding to the actual target orientation will provide the highest matched filter's output SINR.

If the above scheme is not possible due the additional processing and delay in acquisition time, and if only a single waveform can be transmitted from the radar for a given known target, then two different approaches based on statistical characterization or subspace decomposition can be pursued as an extension or alternative to the work presented in this chapter. In both cases, only a single waveform is designed for each given target. In the former approach, the waveform design is based on the target average radar cross-section (RCS) behavior, characterized by the target frequency spectrum, over angle, rather than its frequency response. This approach can benefit from the analyses in [27, 28]. In the subspace approach, eigendecomposition can be applied to the target impulse response matrix to reveal the dominant eigenvectors that capture the main target impulse response variations over angle. A combination of these eigenvectors can then be used as an equivalent target's impulse response. In the above two approaches, we can proceed with the waveform design based on the average impulse response and continue with the same steps described earlier.

We have examined the performance of designing a single waveform by just averaging the target's impulse responses over angles (orientations). We compare, in the Simulation section, the performance of the averaged waveform and the optimal waveform. Indeed, the waveform obtained through the use of the new averaged target's impulse response is suboptimal and will not provide the same SINR or Mahalanobis distance improvement compared to the case where the target's orientation is known, or properly estimated, and the waveform corresponding to that angle is transmitted.

### 3.6 Numerical Simulations

As a proof of concept, the optimum waveforms were constructed for the human as well as for the two simple stationary targets that are commonly found in an indoor environment, namely, a wooden chair and



a wooden table. The geometry and dimensions of the table and the chair targets are shown in Fig. 3. All targets were probed by a vertically polarized modulated Gaussian pulse (see Fig. 4). The pulse is of 1–8 GHz extent, with almost uniform energy over the band of 1–3 GHz, which is a common band used for TWRI applications. It is assumed that both transmitter and receiver are located in the far zones of the targets.

For the numerical modeling, a commercial EM simulator XFDTD by REMCOM was used. For each target, we performed a series of monostatic simulations, computing the scattering field for all azimuth angles (from  $0^\circ$  to  $180^\circ$  with a  $1^\circ$  increment) in the horizontal plane. The target is located in  $xy$  of the coordinate system, and the zero degree angle corresponded to the  $x$  axis. The azimuthal angle  $\varphi$  was measured from the positive  $x$  axis in a counter clockwise direction and the elevation angle  $\theta$  from the positive  $z$  direction towards the  $xy$  plane, respectively. In all cases presented below, we used  $\theta = 90^\circ$ . Thus, for each target, the scattered field for 180 aspect angles was collected. The scattered fields for the chair and the table targets obtained at the position of the transmitter-receiver pair at  $\varphi = 0^\circ$  are shown in Fig. 5. The corresponding impulse responses, obtained according to Section 3.2, are depicted in Fig. 6. Parts (z) to (f) below deal with the two inanimate objects whereas part (g) focuses on human target.

### 3.6.1 Free-space illumination

The matched illumination concept was applied to a series of impulse responses, and the optimal waveforms were obtained for each aspect angle for the targets considered. A comparison between the frequency response of the target and the optimum waveform's frequency response for the same aspect angle is presented in Fig. 7. This figure shows that most of the energy in the optimal waveform is concentrated in one or two narrow frequency bands, corresponding to the target's resonant frequencies or to those of the highest frequency response.

In order to compare the performance of different waveforms, we fix the input SNR to the matched filter in all cases. The noise variance may be obtained as,



$$\sigma^2 = \frac{P_{\max}}{10^{SNR_{in}/10}} \quad (20)$$

where  $P_{\max}$  is the highest power of the received signal and  $SNR_{in} = 10 \text{ dB}$ . The output SINRs corresponding to the transmitted optimum waveforms were compared to those of a chirp waveform of the same duration and energy. The SINR, computed for every aspect angle for the chair target using the optimum signal and the chirped signal, is shown in Fig. 8. It is evident that the optimum waveform provides a significant improvement (more than 10 dB) over the chirp signal. The matched filter is matched to the expected echo rather than the transmitted waveform. We observe that the symmetry of the target is reflected in Fig. 8.

### 3.6.2 Behind the wall illumination

The same targets of part (a) are now placed behind a homogeneous concrete wall of 8 inches thick. The permittivity of concrete was  $\epsilon = 6\epsilon_0$ . We find the SINRs at the output of the receiver's matched filter due to a chirp, due to the optimum free-space waveform, and due to the optimum waveform for the target behind the wall. The results for this part are shown for the table target. The optimum waveform, in the case of the wall places most of its energy into the frequency bins where both the wall and the target's frequency responses exhibit peaks (see Fig. 9). It is also clear from Fig. 9, that the optimum waveform designed with the wall accounted for performs better than the two other waveforms, except at two angles, namely  $60^\circ$  and  $90^\circ$ , where its performance is comparable to the free-space optimal waveform. It is interesting to note that at these angles a common peak exists between the table frequency response and the wall frequency response, which is shown in Fig. 10 for  $\varphi = 60^\circ$ . In this case, the optimum free-space waveform, in essence, has the same spectrum as the one optimized for the wall case. At other angles, the optimum waveform for the wall case exhibits a different spectrum than its free-space counterpart. The plots of the table frequency response, the frequency response of the optimal free-space waveform, and the frequency response of the optimal wall/target waveform for  $\varphi = 30^\circ$  are shown in Fig. 11. It is clear

from that figure that the optimal wall/target waveform's frequency response places its energy into the frequency that jointly resonates the wall and the target, while the optimum free-space waveform has its energy concentrated at a lower frequency, where the target only resonates.

### 3.6.3 Target discrimination

In order to evaluate the performance of optimal waveforms for the discrimination between different targets of interest, i.e., the table and the chair, we examined the Mahalanobis distances between the target's echoes for different transmitted signals. We compare the optimal discrimination waveforms, a chirp waveform, and the optimal detection waveforms for the chair and the table. The result, depicted in Fig. 12, clearly shows the advantages of using the optimal discrimination waveform.

### 3.6.4 Target resolution and constrained design

As described in Section 3.3, the minimum range resolution is a function of the target's impulse response and the pulse duration. The target impulse response itself is a function of the dimensions of the target and its dielectric properties. For proof of concept, we computed the impulse responses for a metal chair and a metal table of the same dimensions as those of the wooden targets. The impulse responses of the metal chair and table are presented in Fig. 13. It is clear from these figures, that the impulse responses of metal targets are shorter as compared to those of the wooden targets (compare Fig. 6 and Fig. 13). Therefore, the minimum range resolution for the metal targets is also smaller. The minimum range resolutions for different targets both in the free-space ( $K=0$ ) and behind the wall calculated from Eq. Error! Reference source not found., are summarized in Table I.

A tradeoff between SINR performance and range resolution for a wooden table in the free-space and incorporating the wall is illustrated in Fig. 14 and Fig. 15, respectively. One may notice that as the range resolution improves, the SINR corresponding to the optimal waveforms decreases. The spectra of three different optimal waveforms for the table at  $\varphi=0^\circ$  with different range resolution constraints are presented in Fig. 16. In this case, the three range resolutions exceeding the minimum achievable resolu-

tion (Table 1) were used, namely 2, 3, and 5 meters. The energy of optimal waveforms is concentrated around the resonant frequency of the target (Fig. 16). The smaller is the range resolution, the broader is the optimal waveform's frequency response. This leads to degradation in the SINR, since the energy is no longer confined within the narrowband around the resonance frequency of the target.

The proposed matched illumination waveform design technique can be extended to handle targets separated in cross-range. This is simply achieved by using spatial selectivity and beamforming [27] at the transmit and/or at the receive, depending whether a physical or synthesized aperture is employed. In this respect, for each increment in the aspect angle, optimum waveform based designed detector can be applied. The beamforming, in addition to separating targets in cross-range, can also lower multipath which are incident on the sidelobes. Within the same beam, constrained range resolution design, discussed above, can be applied to enable resolving range multipaths due to the target. The problem then becomes similar to typical radar operations with two distinctions 1) The transmitted waveform is target dependent, 2) the range resolution is relatively relaxed to account for the narrowband property of the waveform and to utilize full prior detailed description of the target under consideration.

It is noted that the concept of matched illumination considers the detection of a given target with known size, shape, and material, i.e, impulse response. In this respect, once the presence of the target is declared by the detector based on the use of the optimally designed waveform, the target information is readily available and no additional information concerning the nature of the target may be obtained via high resolution imaging.

### 3.6.5 Target orientation uncertainty

In the case of target uncertainty, we design an average waveform, as discussed in Section 3.5. It is noted that the Swerling I distribution of human RCS was already shown in [23]. In order to evaluate the performance when using the average waveform, we compare the waveform detection capability with that of a chirp. The result is shown in see Fig. 17, which underscores the fact that the average waveform is “suboptimal” and, indeed, for some aspect angles, it loses performance against the chirp waveform. We

have also implemented the stochastic-based approach for waveform design which computes the autocorrelation matrix from the target power spectrum density [27]. The latter was obtained by averaging the magnitude square of the frequency response of the target with various orientations. The results were almost identical, up to numerical errors, to the average waveform shown in Fig. 17.

### 3.6.6 Effects of clutter

Since in TWRI applications, we always deal with a non-zero clutter, we have numerically simulated the presence of clutter for the wooden table using the iterative algorithm [21]. The clutter and the noise are of independent samples and the clutter-to-noise ratio (CNR) was set to 10 dB. In Fig. 18, the SINR at the output of the receiver filter due to the optimum transmitted waveform for the clutter, was compared with the SINR corresponding to the optimum waveform for no-clutter case (CNR=0) and a chirp waveform, providing all transmitted waveforms have the same duration and energy. We observe from Fig. 18 that the optimized waveform obtained via the iterative technique provides better detection in the presence of clutter, though the overall SINR improvement degrades as the CNR increases. It is noted that we only considered clutter that is modeled by equation (2). Clutter arises from target-to-target or target-to-wall interactions and multipath should be included for a full representation of all clutter sources in the scene.

It is clear from Fig. 9, that even with the optimum waveform, the table has a different SNR in the echo for different aspect angles. We chose two aspect angles, one with a relatively low SNR ( $15^\circ$  aspect angle) and another with a higher SNR in the echo ( $90^\circ$  aspect angle). Figure 19 shows the ROC curves corresponding to each of the two aspect angles using three different waveforms at each angle. The first waveform is the optimal waveform for the table behind a concrete wall, whereas the second waveform is the optimal waveform for the table in free space, and finally there is a chirp waveform. We can see from the ROC curves that the optimal waveform for the table behind the wall has a better probability of detection, for a given probability of false alarm, than the other two suboptimal waveforms.



### 3.6.7 Human behind wall

We have also employed XFDTD for modeling a human behind a cinder block wall. The human model used in FDTD simulations is the High Fidelity Frozen Male Body shown in Fig 20. The body consists of 5 mm cubical FDTD mesh cells and constitutes of 23 different tissue types, each with its own dielectric properties. An overall mesh size is  $136 \times 87 \times 397$  cells. Although the entire mesh has about 4 million cells, it occupies only 128 MB of RAM and highly optimized for numerical computations. Cinder block wall contains 72 cinderblocks ( $6 \times 12$ ). Each cinder block is  $40.62 \times 20.32 \times 20.3$  cm made of cement with  $\epsilon=7.66 \epsilon_0$  and  $\sigma=0.06$  S/m. The XFDTD cell size was selected as 4.5mm as directed by dielectric parameter of the object under investigation. The computational domain is surrounded by 8 perfectly match layers (PMLs). The padding between the computational domain and the PML was 50 spatial cells which is more than half wavelengths away and provides the sufficient convergence of the solution.

The scene is excited by a Gaussian pulse with the positive gain over the bandwidth of about 0.7-3.5GHz. The temporal duration of the pulse is 251 temporal steps. The scattered field is collected in plane parallel to the surface of the wall with the stand-off distance of 1m. Such distance ensures that the diffraction from the walls edges does not have a significant impact on the scattered field. The temporal interval for the collection of the scattered field was sufficient to have all the secondary reflections and multiple path effect taken into account.

Table II shows the SNR of the echo from the human behind the concrete wall scenario. It can be clearly seen from the results that the optimal through the wall waveform gives the highest SNR, followed by the optimal human in the free space waveform and finally the chirp, has the lowest SNR.

### 3.6.8 Effect of wall errors

Optimal through-the-wall target detection or classification requires perfect knowledge of the wall transmission response. In practical situations, the wall characteristics may not be known *a priori*, and need to be estimated. We evaluate the performance of the optimal detection waveforms for the wooden table in terms of the SINR in the presence of ambiguities in wall knowledge. The same wall and target parameters



of Fig. 9 are used. Figure 21 shows the difference in SNR between the exact wall and ambiguous wall cases as a function of target aspect angle (0-60 degrees) under various error conditions. Indeed, the SNR is lowered when wall errors are present. For the example presented, an average of 2dB drop in SNR is observed for 10% wall parameter error.

### 3.7 Conclusions

In this chapter, the concept of matched illumination was considered for through the wall radar imaging applications. An optimal waveform design technique was applied for stationary target detection and classification. The algorithm was tested on the two sample targets commonly found in an indoor environment, namely, wooden table and chair, and on a simulated human model behind a concrete wall. The performance of the optimum waveform was compared to a conventionally used chirp waveform. The result showed significant improvement when using the optimum waveform in the SINR for both cases in which the targets of interest were in free-space and behind the wall. The proposed technique was tested in no-clutter and simulated clutter scenarios. In both cases, the optimized waveform outperforms the chirp waveform. The sensitivity of the optimum waveform and the corresponding receiver performance due to uncertainty in target orientation was also examined.

The optimum waveform derived in this chapter was for a single antenna monostatic operation. The work can be extended to deal with an imaging system with physical or synthesized aperture, and for bistatic and multi-static operations [24-26]. For these schemes, the variation of the target RCS and its correlations over different aspect angles and at long standoff distances should be carefully examined prior to waveform design.

This chapter has dealt with known targets and, as such, considered the deterministic-based approach for waveform design using the concept of matched illumination. The corresponding stochastic-based approach for waveform design based on matched illumination, discussed in [27, 28], is a welcomed and important extension of the deterministic-based approach, in which the target impulse response correlation matrix is replaced by the autocorrelation matrix that is derived from the known target power spectrum. In

this case, different target sizes within the same class of targets, such as chairs, tables, or humans, give rise to different realizations of the impulse response, and can be captured in a single waveform based on average statistical characterization. Future work in matched illumination waveform design in TWRI should consider the stochastic-based approach for different categories or classes of targets, and assess the improvement in signal to noise and clutter ratio as compared to conventional waveforms.

## References

- [1] Y. Yang, R. Blum, "Waveform design for MIMO radar based on mutual information and minimum mean-square error estimation," Proc. 40th Annual Conference on Information Sciences and Systems, pp. 111-116, March 2006.
- [2] L. S. Riggs, M. A. Richards, T. H. Shumpert, C. R. Smith, "On waveform design for optimal target discrimination," International Journal of Imaging Systems and Technology, Vol. 4, No. 4, pp. 327-335, 1992.
- [3] S. Blunt and P. Yatham, "Waveform Design for Radar-Embedded Communications," Proceedings of the International Waveform Diversity and Design Conference, pp. 214-218, Pisa, Italy, June 2008.
- [4] G. Frazer, B. Johnson, and Y. Abramovich, "Orthogonal Waveform Support in MIMO HF OTH Radars," Proceedings of the International Waveform Diversity and Design Conference, pp. 423-427, Pisa, Italy, June 2008.
- [5] S. U. Pillai, H. S. Oh, D. C. Youla, J. R. Guerci, "Optimum transmit-receiver design in the presence of signal-dependent interference and channel noise," IEEE Trans. on Information Theory, Vol. 46, No. 2, pp. 577-584, March 2000.
- [6] S. Kay, "Optimal signal design for detection of Gaussian point targets in stationary Gaussian clutter/reverberation," IEEE Journal on Selected Topics in Signal Processing, Vol. 1, No. 1, pp. 31-41, June 2007.
- [7] H. Estephan, M. Amin, K. Yemelyanov, and A. Hoorfar, "Waveform design for through-the-wall radar imaging applications," Proceedings of the SPIE Symposium on Defense and Security, (C31), volume 6943, pp. 69430S-69430S-11, Orlando, Florida, March 2008.
- [8] Proceedings of the 2008 IEEE International Conference on Acoustics, Speech, and Signal Processing, Special Session on 'Through-the-Wall Radar Imaging,' Las Vegas, Nevada, April 2008.
- [9] M. Farwell et al, "Sense Through the wall system development and design considerations," Journal of Franklin Institute, Special Issue on 'Advances in Indoor Radar Imaging,' vol. 345, No. 6, pp. 570-591, September 2008.
- [10] E. Baranoski, "Through-wall sensing; radar signal processing; model-based reasoning; propagation effects," Journal of Franklin Institute, Special Issue on "Advances in Indoor Radar Imaging," vol. 345, No. 6, pp. 556-569, September 2008.
- [11] P. Withington, H. Fluhler, S. Nag, "Enhancing homeland security with advanced UWB sensors," IEEE Microwave Magazine, Vol. 4, No. 3, pp. 51-58, 2003.

- [12] F. Ahmad, M. G. Amin, S. A. Kassam, "Synthetic aperture beamformer for imaging through a dielectric wall," *IEEE Trans. on Aerospace and Electronic Systems*, Vol. 41, No. 1, pp. 271-283, January 2005.
- [13] F. Ahmad, Y. Zhang, M. G. Amin, "Three-dimensional wideband beamforming for imaging through a single wall," *IEEE Geoscience and Remote Sensing Letters*, Vol. 5, No. 2, pp. 176-179, April 2008.
- [14] R. M. Narayanan, "Through Wall Radar Imaging Using UWB Noise Waveforms", *Journal of the Franklin Institute*, vol. 345, No. 6, pp. 659-678, September 2008.
- [15] V.C. Chen and H. Ling, *Time Frequency Transforms for Radar Imaging and Signal Analysis*, Artech House, Boston, MA, 2002.
- [16] M. R. Bell, "Information theory and radar waveform design," *IEEE Trans. on Information Theory*, Vol. 39, pp. 1578-1597, September 1993.
- [17] D. A. Garren, A. C. Odom, M. K. Osborn, J. S. Goldstein, S. U. Pillai, J. R. Guerci, "Full-polarization matched-illumination for target detection and identification," *IEEE Trans. on Aerospace and Electronic Systems*, Vol. 38, No. 3, pp. 824-837, July 2002.
- [18] M. Dehmollaian and K. Sarabandi, "Refocusing through building walls using synthetic aperture radar," *IEEE Trans. Geosci. Remote Sensing*, vol. 46, no. 6, pp. 1589-1599, Jun. 2008
- [19] M. Dehmollaian and K. Sarabandi, "Analytical, numerical, and experimental methods for through-the-wall radar imaging," in *IEEE Int. Conf. Acoustics, Speech, and Signal Processing*, Apr. 2008, pp. 5181-5184.
- [20] Y. Yoon and M. G. Amin, "Spatial Filtering for Wall-Clutter Mitigation in Through-the-Wall Radar Imaging," *IEEE Transactions on Geosciences and Remote Sensing*, Under Review.
- [21] D. A. Garren, A. C. Odom, M. K. Osborn, J. S. Goldstein, S. U. Pillai, J. R. Guerci, "Enhanced target detection and identification via optimized radar transmission pulse shape," *IEE Proc. on Radar, Sonar and Navigation*, Vol. 148, No. 3, pp. 130-138, June 2001.
- [22] E. J. Rothwell, W. Sun, "Time domain deconvolution of transient radar data," *IEEE Trans. on Antennas and Propagation*, Vol. 38, No. 4, pp. 470-475, April 1990.
- [23] T. Dogaru, L. Nguyen, and C. Le, "Computer models of the human body signature for sensing through the wall radar applications," *Army Research Lab Technical Report No. ARL-TR-4290*, September 2007. Available: <http://www.arl.army.mil/arlreports/2007/ARL-TR-4290.pdf>. [Accessed Jan. 13, 2009].
- [24] F. Ahmad and M. Amin, "Optimal Waveform Design for Through-the-Wall Radar Imaging," *Proceedings of the SPIE Symposium on Defense, Security, and Sensing, Radar Sensor Technology XIII Conference*, Orlando, FL, April 2009.

- [25] J. R. Guerci, M. C. Wicks, J. S. Bergin, P. M. Techau, and S. U. Pillai, " Theory and Application of Optimum and Adaptive MIMO Radar," Proceedings of the IEEE Radar Conference, pp. 2146-2151, Rome, Italy, May 2008.
- [26] I. Bradaric, G. Caparo, M. Wicks, and P. Zulch, "Signal Processing and waveform Selection Strategies in Multistatic Radar Systems," Proceedings of the International Waveform Diversity and Design Conference, pp. 307-311, Pisa, Italy, June 2008.
- [27] R. Romero and N. Goodman, "Information-Theoretic Matched Waveform in Signal Dependent Interference," in Proc. IEEE 2008 Radar Conf., Rome, Italy, May 26-30, 2008.
- [28] J. Hyeong-Bae and N. Goodman, "Adaptive Waveforms for Target Class Discrimination," in Proc. 2007 Int. Waveform Div. and Des. Conf, pp. 395-399, Jun. 2007.

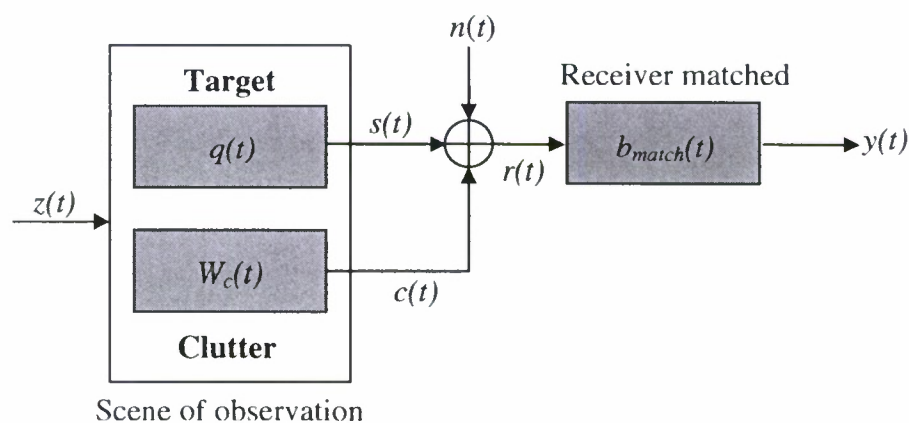


**Fig. 1** Block diagram of system.



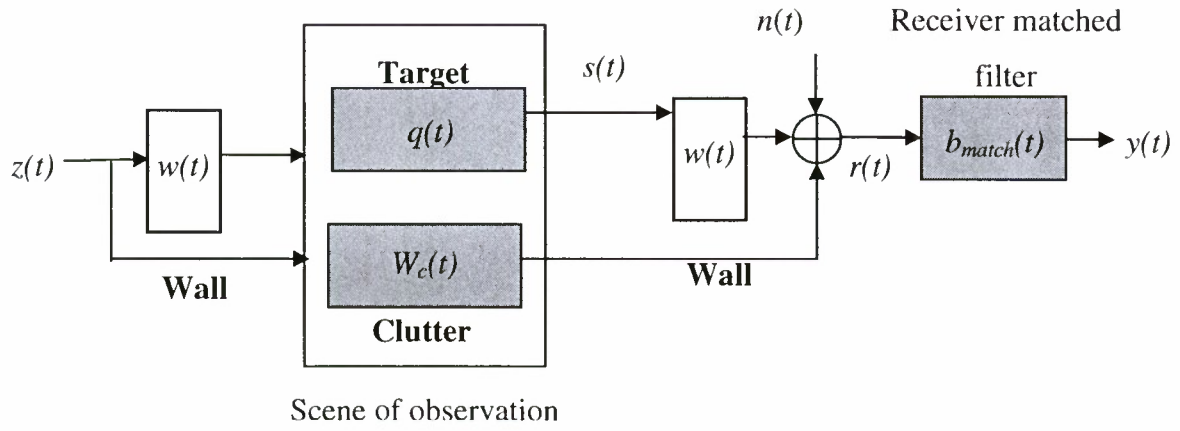
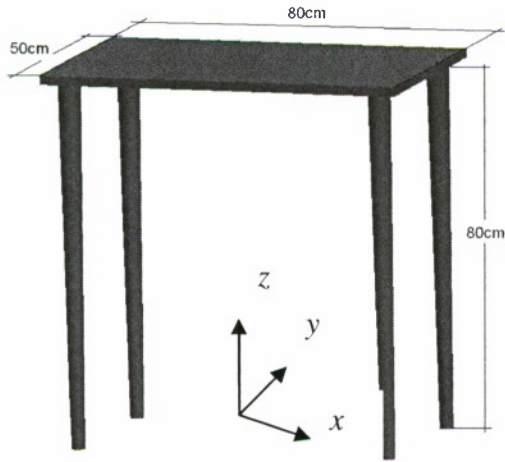
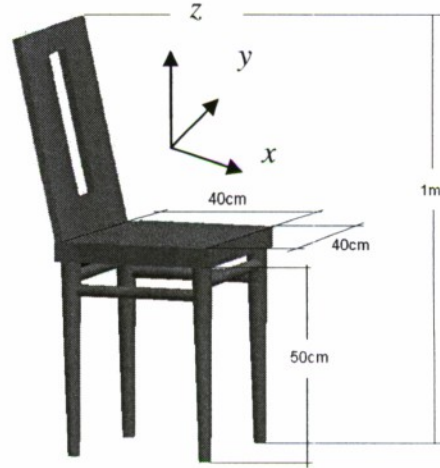


**Fig. 2** Block diagram of the system in the presence of a wall.

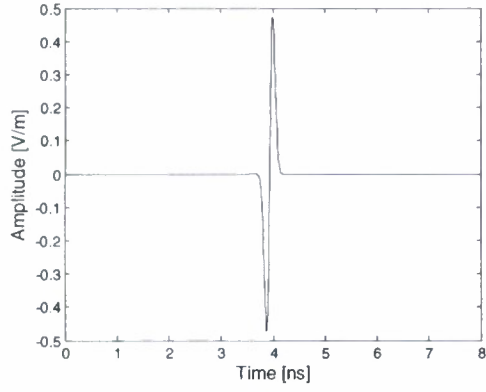


(a) Wooden table

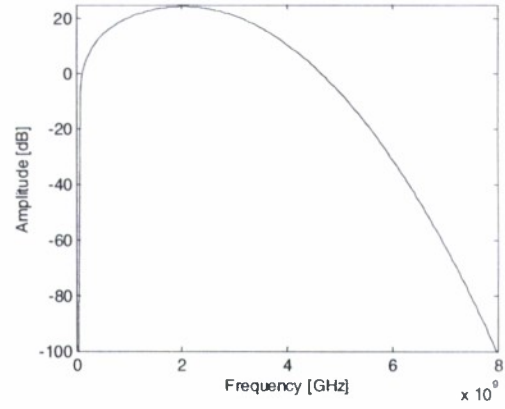


(b) Wooden chair

**Fig. 3** 3-D models of indoor targets used in simulations. The reference point, “zero-degree angle” was chosen at the direction of  $x$  axis.

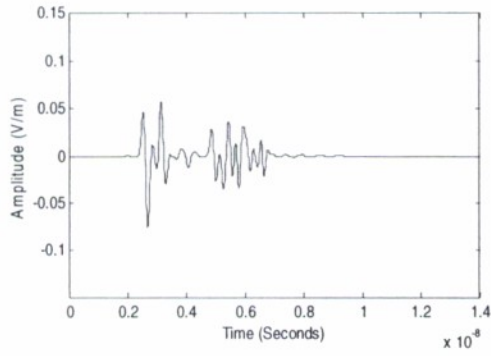


(a)

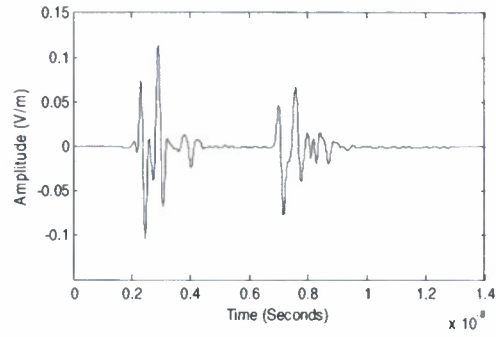


(b)

**Fig. 4** Incident Gaussian pulse (a) Time-domain, (b) Frequency-domain.

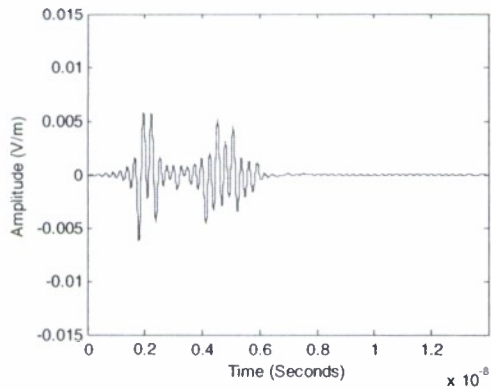


(a) Chair

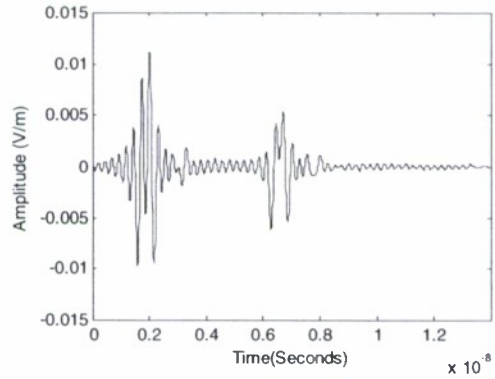


(b) Table

**Fig. 5** EM field scattered by the targets for transmitter-receiver pair located at  $\varphi = 0^\circ$ .

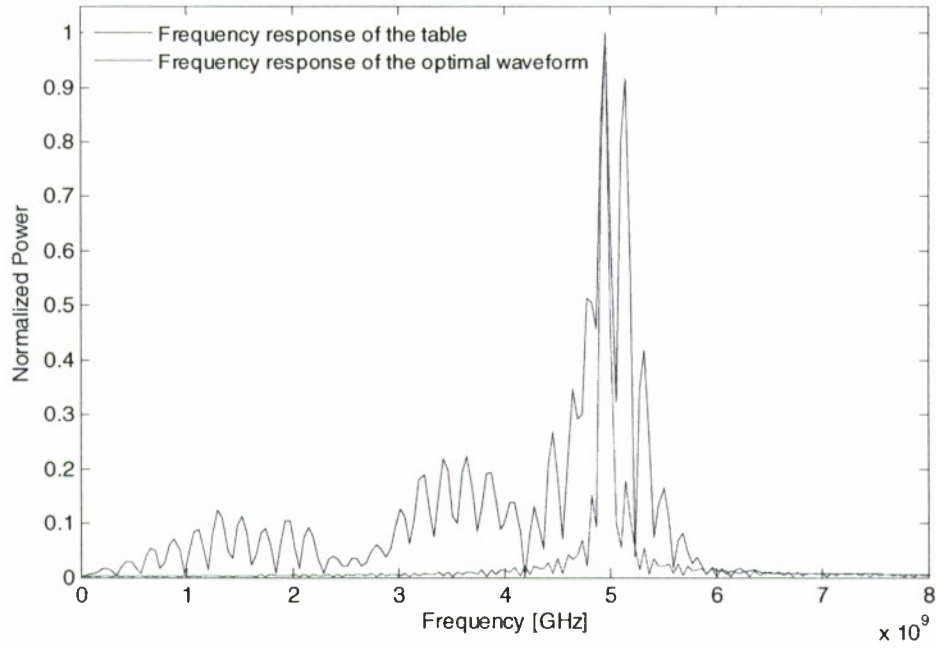


(a) Chair

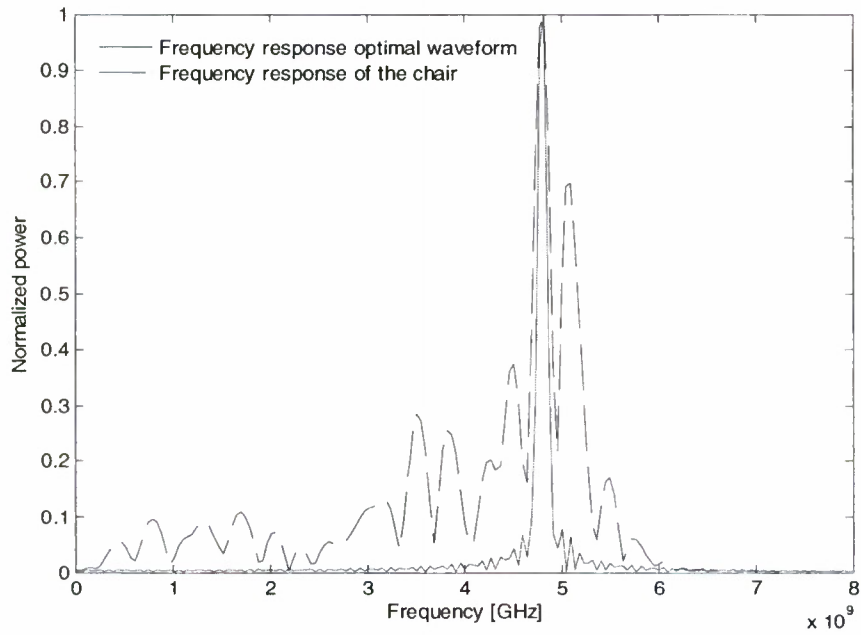


(b) Table

**Fig. 6** Impulse responses for the sample targets when transmitter-receiver pair is located at  $\varphi = 0^\circ$ .



(a)



(b)

**Fig. 7** frequency responses of the optimal waveform capturing the targets frequency band with the highest energy at  $\varphi = 0^\circ$ , (a) Chair, (b) Table.

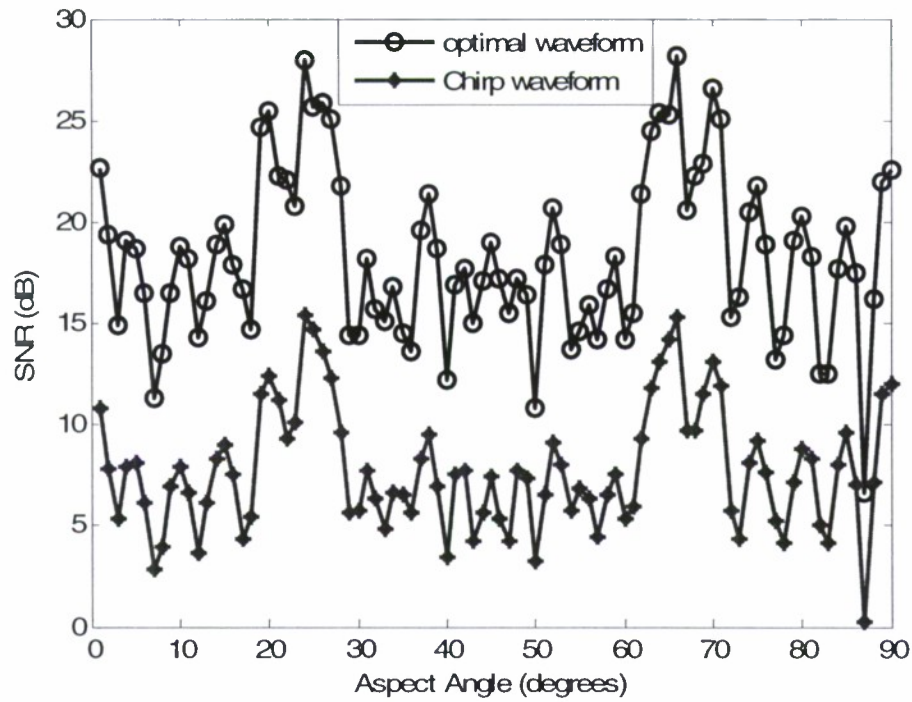


**Fig. 8** SINR improvement, for the chair target, resulting from transmitting the optimum waveform at each aspect angle versus a chirp waveform of the same duration and energy for all aspect angles.

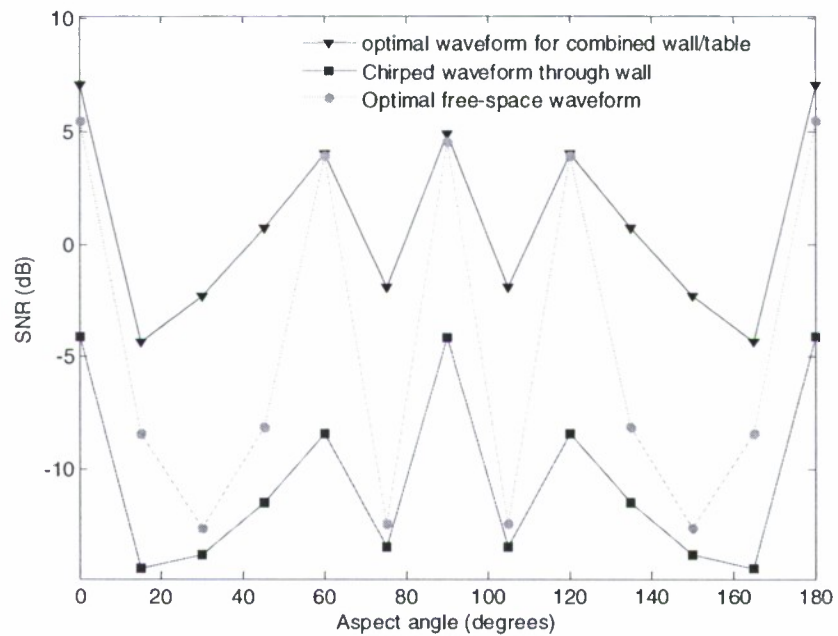


**Fig. 9** SINR resulting from transmitting the optimum through the wall waveform at each aspect angle for the table, the optimum free-space waveform when the target is behind the wall and finally a chirp.

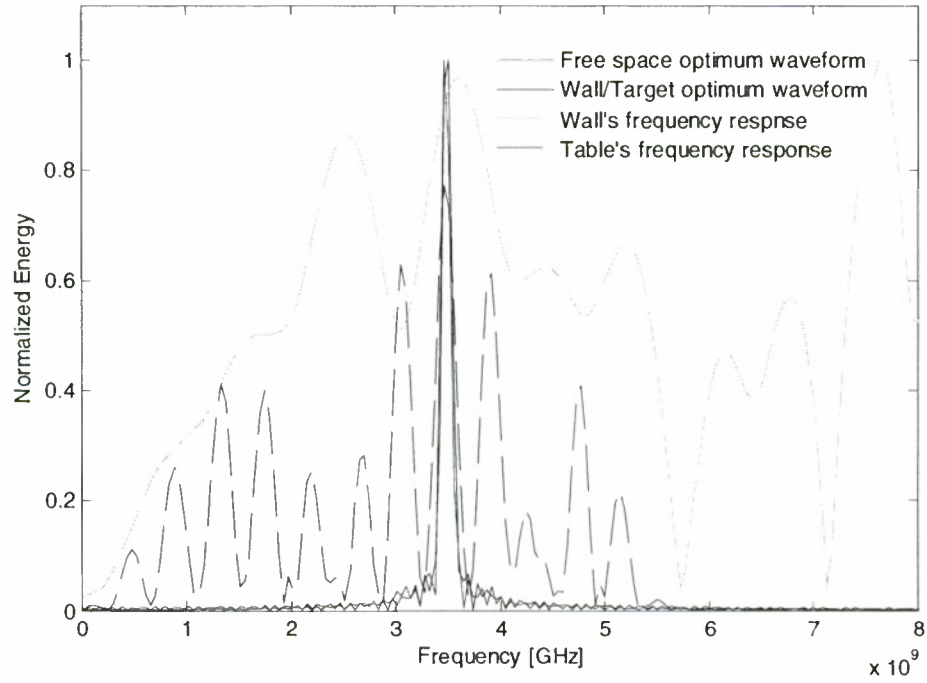


**Fig. 10** Spectra of optimum free-space waveform, through the wall optimum waveform, wall's impulse response, and table's impulse response at  $\varphi = 60^\circ$ .

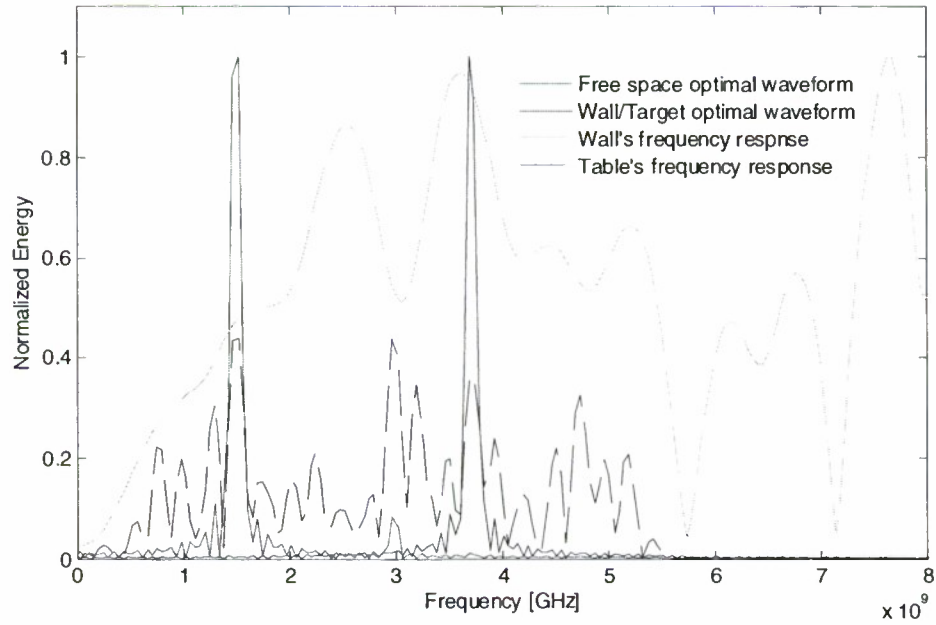


**Fig. 11** Free-space optimal waveform, through-the-wall optimal waveform, wall's frequency response, and table's frequency response at  $\varphi = 30^\circ$ .



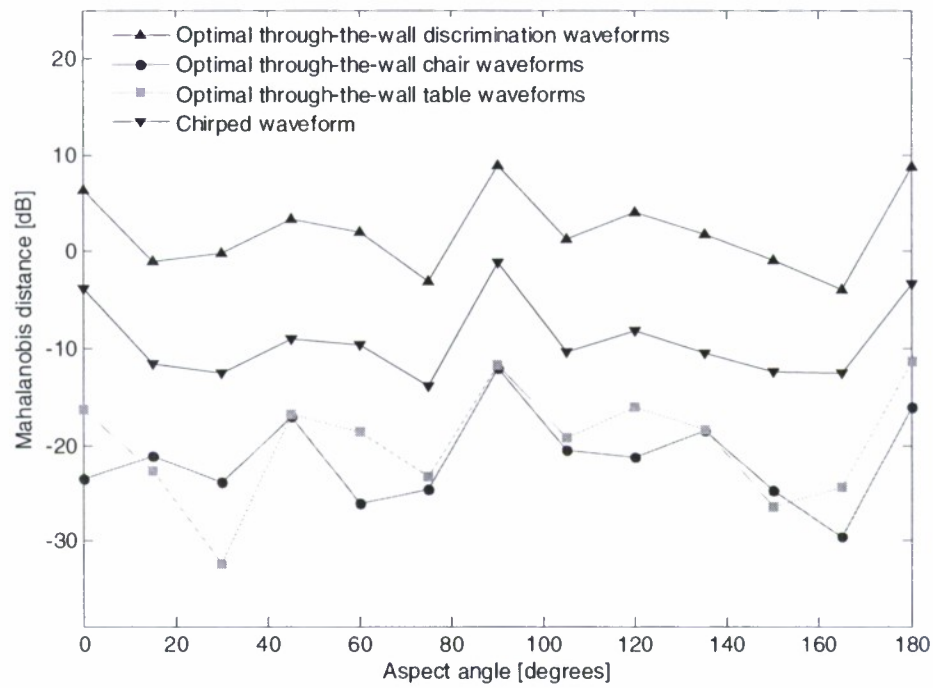
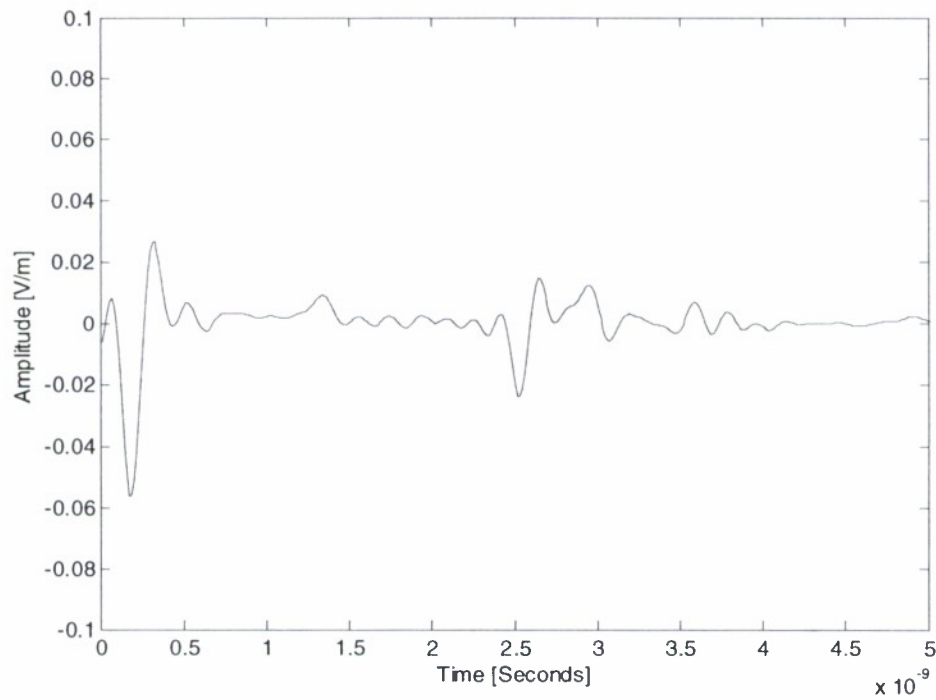
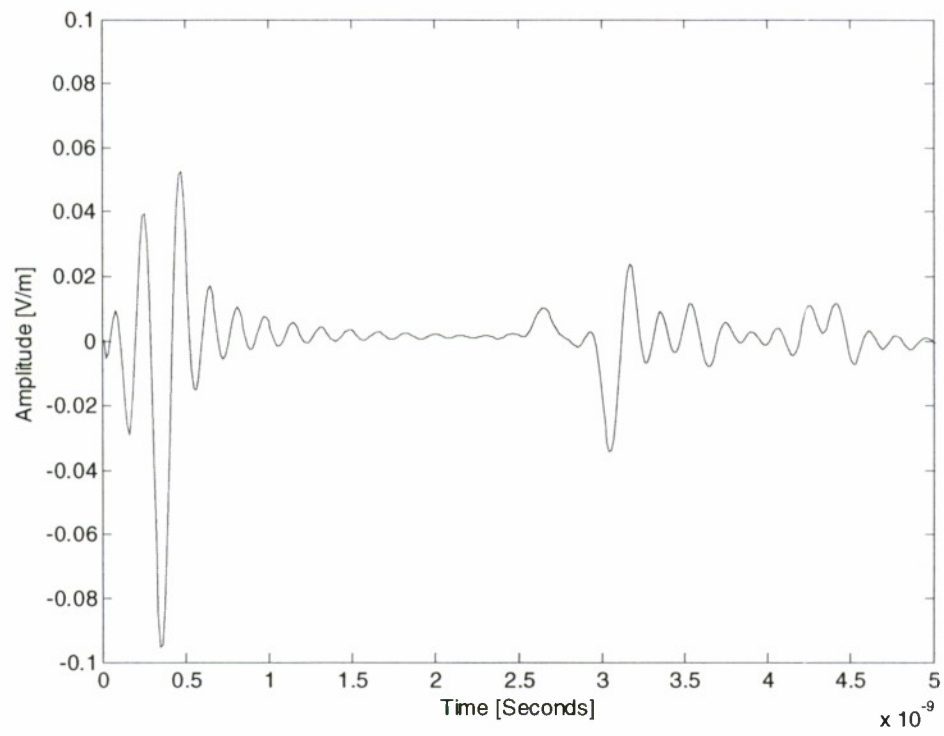


**Fig. 12** Mahalanobis distances due to the optimum through-the-wall discriminant waveforms, optimal table detection waveforms, optimal chair detection waveforms, and a chirped waveform.



(a)



(b)

**Fig. 13** Impulse responses for  $\varphi = 0^\circ$ , (a) for metal table, (b) metal chair.

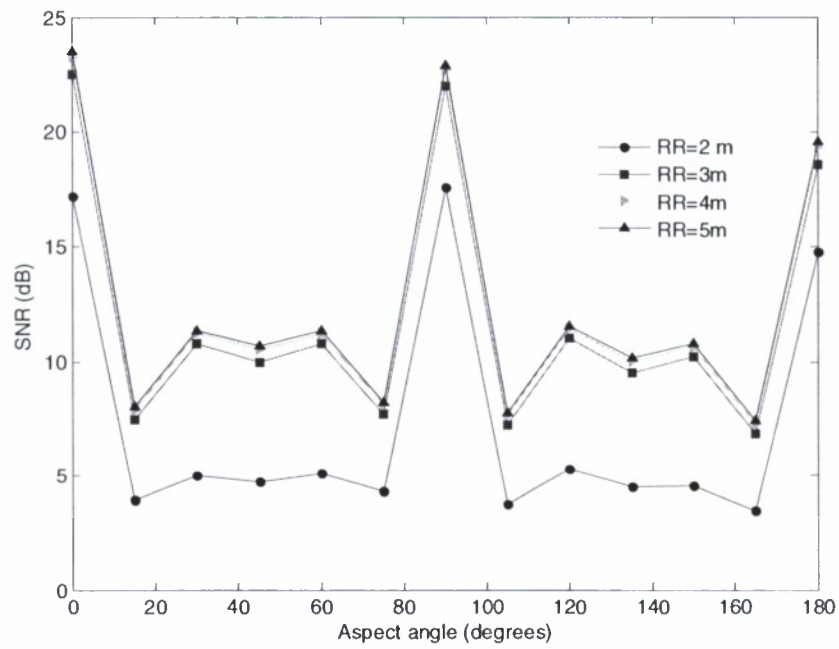


**Fig. 14** Degradation in SINR as we vary the range resolution constraint of the transmitted waveform, in free space.

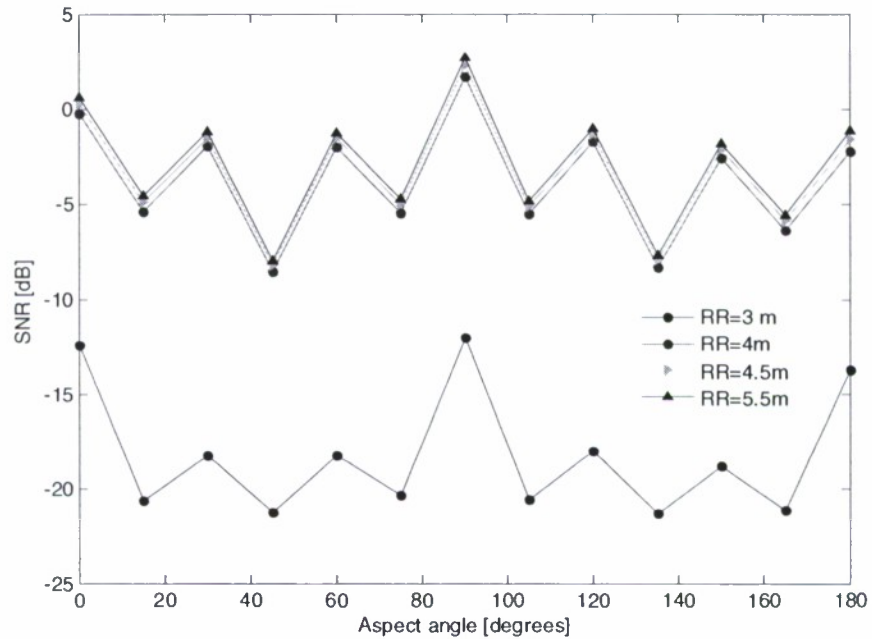


**Fig. 15** Degradation in SINR as we vary the range resolution constraint of the transmitted waveform, when target is behind the wall.

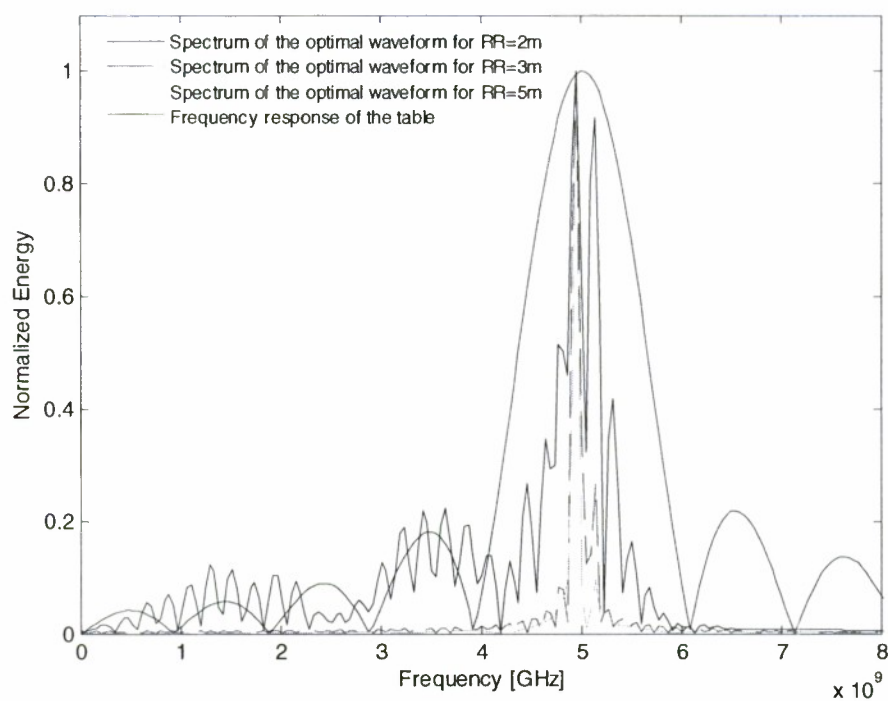


**Fig. 16** Spectra of three different optimum waveforms with different range resolution constraint plotted on top of the table frequency response.

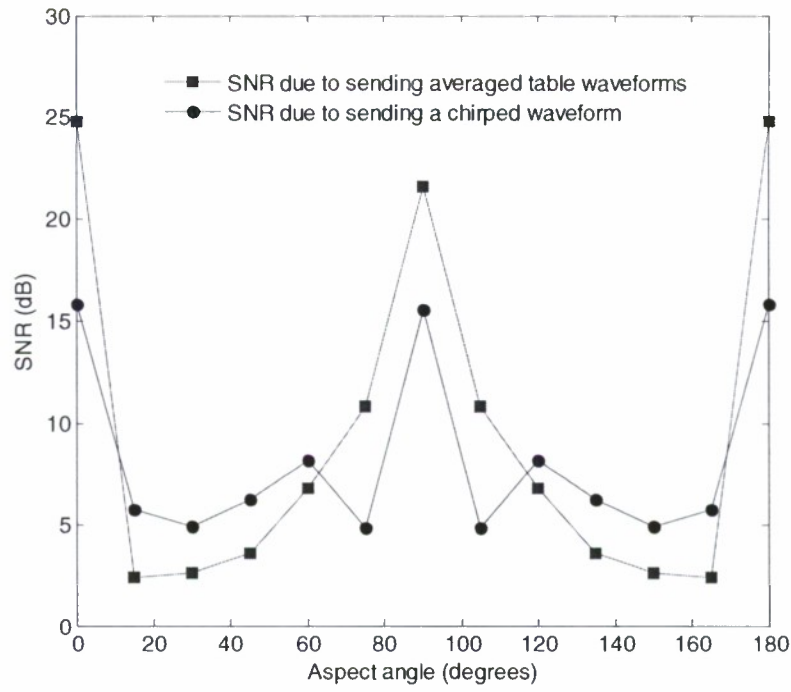


**Fig. 17** SINR due to the average waveform in case of aspect angle uncertainty versus the SINR from using a chirp.

**Table I.** Minimum required separation in range to resolve two targets.

Target	$\Delta R_{\min}$ in the free-space (meters)	$\Delta R_{\min}$ behind the wall (meters)
Wooden table	1.86	2.9
Wooden Chair	1.86	2.9
Metal Table	0.6	1.73
Metal Chair	0.6	1.73



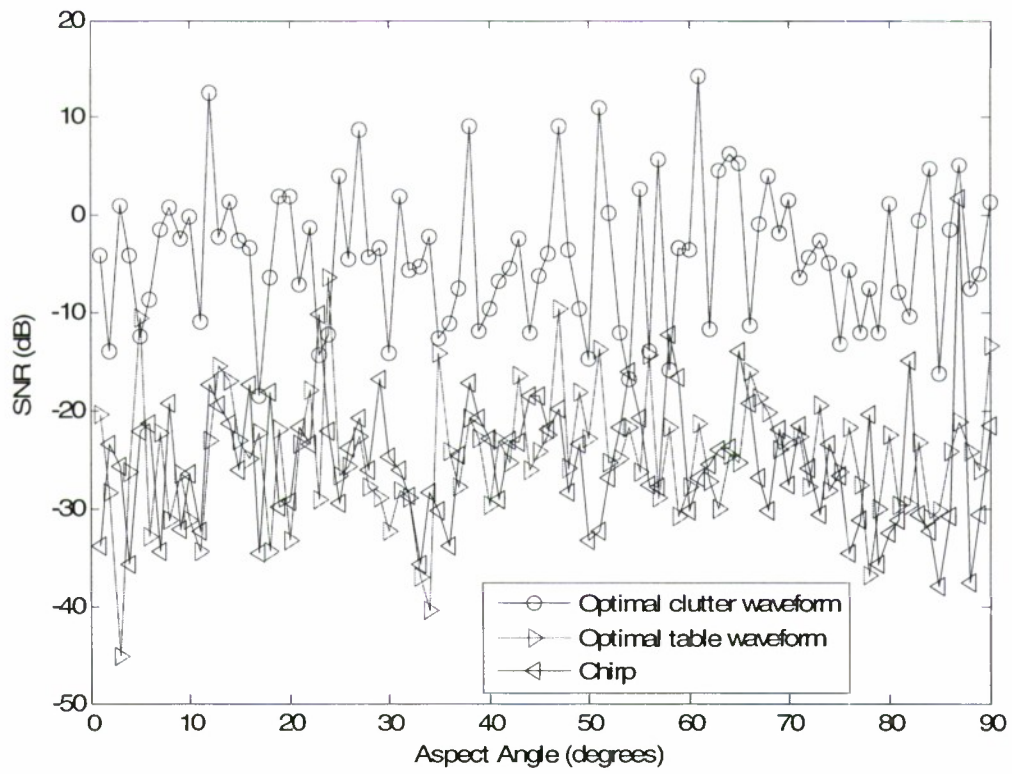


**Fig. 18** SINR at the output of the receiver filter in the case of the chair being the clutter while the table is the target of interest.

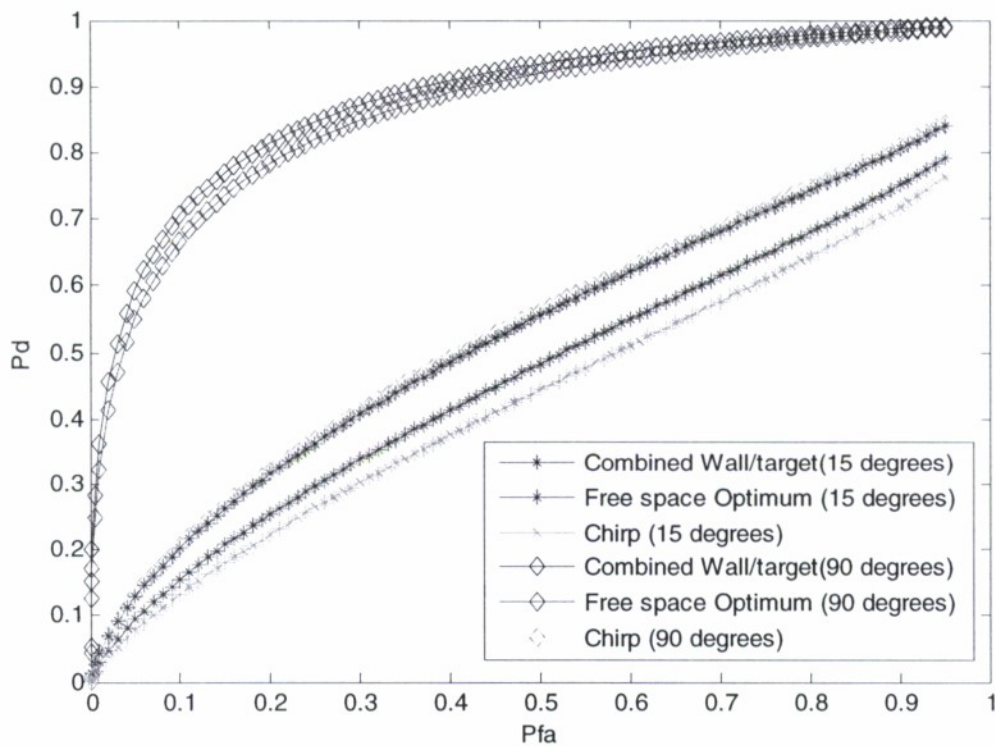


**Fig. 19** ROC curves when the wooden table is behind a concrete wall and is illuminated by the through-the-wall optimum waveform, free space optimum waveform and the chirp, respectively, and at two different target aspects, 15° and 90°.

**Table II.** SNR of the received signal from a real human model behind a concrete wall, using three different waveforms.

Human Behind the wall	
SNR using Optimum Free space waveform	24.01 dB
SNR using Optimum behind the wall waveform	26.44 dB
SNR using a chirp	20.76 dB

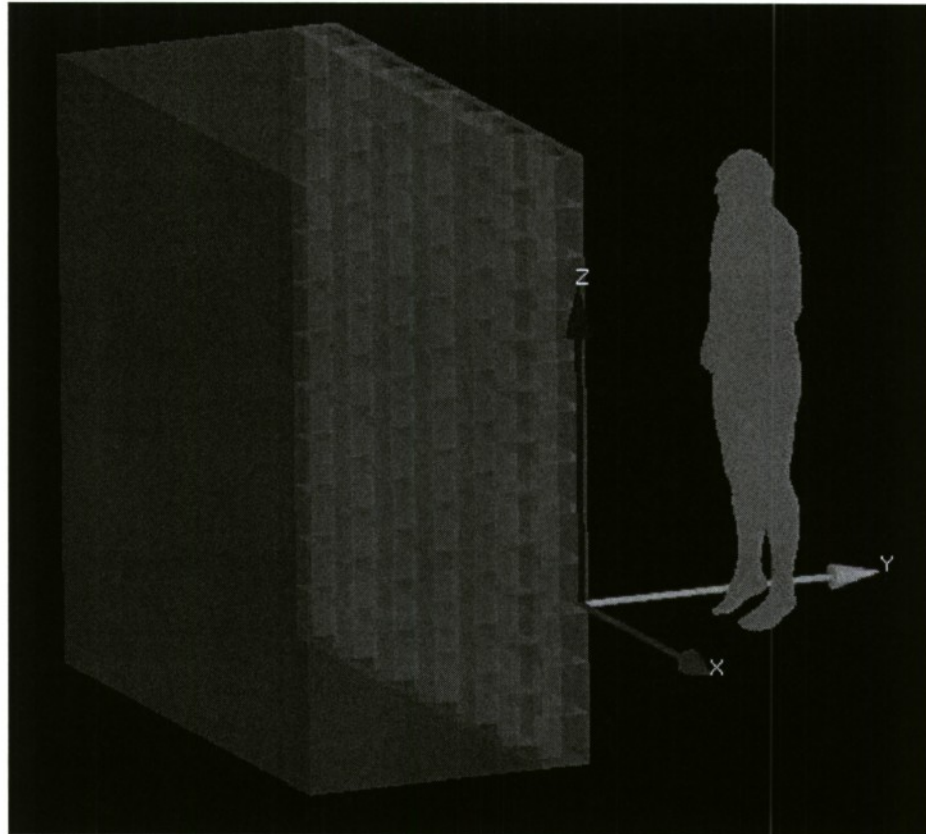


**Fig. 20** Geometry of the frozen human model used in the simulation.

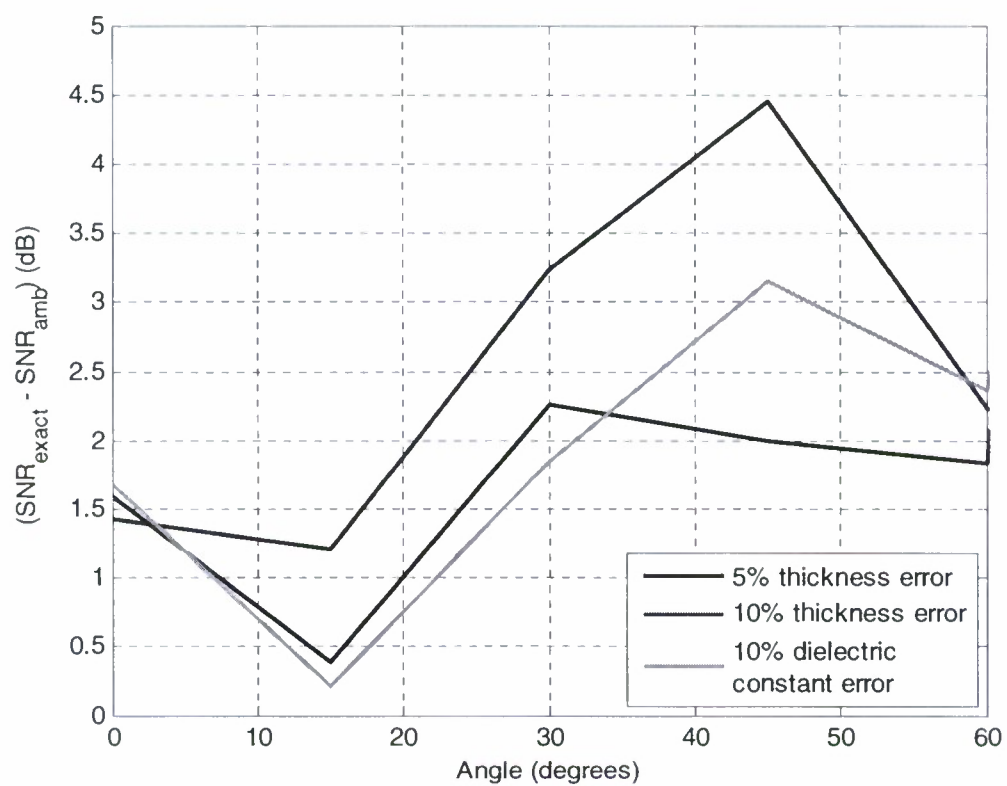


**Fig. 21** Difference in SNR between exact wall and ambiguous wall cases.

## 4. Matched-Illumination Waveform Design for a Multistatic Through-the-Wall Radar System

### *Abstract*

We present the matched illumination waveform design for improved target detection in through-the-wall radar imaging and sensing applications. We consider a multistatic radar system for detection of stationary targets with known impulse responses behind walls. The stationary and slowly moving nature of typical indoor targets relaxes the orthogonality requirement on the waveforms, thereby allowing sequential transmissions from each transmitter with simultaneous reception at multiple receivers. The generalization of the matched illumination waveform design concept from a monostatic to a multistatic setting casts the indoor radar sensing problem in terms of multiple-input multiple-output (MIMO) operations and puts in context the offering of MIMO to urban sensing and imaging of targets in enclosed structures. Numerical electromagnetic modeling is used to provide the impulse response of typical behind-the-wall stationary targets, namely tables and humans, for different target orientations and at various incident and reflection angles. Simulation results depict an improvement in the signal-to-clutter-and-noise-ratio (SCNR) at the output of the matched filter receiver for multistatic radar as compared to monostatic operation.



## 4.1 Introduction

Design and implementation of signature exploitation systems is an important area of current research [1]-[6]. The fundamental philosophy behind such systems is as follows. In typical radar operational environments, the possible targets considered in the scene of interest are known in advance. Sufficient *a priori* information about the properties and characteristics of these targets, such as the target shape, size, and composition, is available. The goal of the sensor system is to detect the presence of the target of interest and to determine its location. Signature exploitation systems make use of the *a priori* information for improved target detection and classification.

Utilization of target signature for design of transmission waveforms for optimum detection and classification has been recently investigated in many applications of radar, such as air-to-air and air-to-ground radar systems [1], [4]-[6]. However, it has not been utilized in the context of urban sensing and through-the-wall radar imaging (TWRI). This new emerging field of research and development involves the process of remotely detecting, classifying, and locating targets inside buildings or other structures. With recent advances in both algorithm and component technologies, TWRI is emerging as an affordable sensor technology in both civil and military settings [7]-[10]. It has been successfully sought out for surveillance and reconnaissance in urban environments, requiring not only the layout of the building, including types and locations of walls, but also detection and localization of both moving and stationary targets within enclosed structures [11], [12]. This technology can also be used in rescue missions, searching for fire, earthquakes, and avalanche victims and survivors, and behind-the-wall detection and surveillance of suspected criminals and outlaws [13]-[14]. For through-the-wall radar applications, in addition to humans, there are only a finite number of objects that are commonly found inside rooms and behind walls, for example, chairs and tables of a few different sizes and possible shapes. As such, the underlying application provides ideal premises for considering waveform design based on signature exploitation.

Target matched illumination theory is a signature exploitation concept that considers design of the optimum detection system, comprising matched transmission waveform and ‘matched filter’ receiver, for

targets with known impulse responses [5]-[6], [15]. More explicitly, it designs the transmitter-receiver pair that maximizes the signal-to-clutter-and-noise-ratio (SCNR) at the output of the receiver matched filter. Matched illumination was considered for the detection of targets behind walls and in enclosed structures in [16] for single antenna monostatic operation. In this chapter, we develop matched-illumination waveform design for through-the-wall applications using a multistatic radar system in which the system transmitters and receivers are spatially distributed over a wide area rather than being housed on the same physical platform. This generalization of matched illumination waveform design from a monostatic to a multistatic setting puts into context the offerings of multiple-input multiple-output (MIMO) operations to indoor radar imaging and sensing [17]-[19].

It is noted that the process of sensing targets behind walls typically consists of two stages, namely, the detection stage and the classification stage. The latter is more complex and requires processing off-line. This chapter treats the detection aspect of the problem. We focus on widely separated transmitters and receivers, and exploit the variations in the target impulse response as a function of the transmitter-to-target aspect angle and the transmitter-receiver bistatic angle for improved through-the-wall target detection. The targets of interest are either stationary or moving at very low speed, thereby allowing sequential use of the transmitters with simultaneous reception at multiple receivers. We, therefore, develop the matched illumination detection system for the multistatic radar employing a signal model based on single active transmitters and under the assumption of coherent processing of the target returns at the different receivers. The waveform for each transmitter is optimally designed. We analyze the performance of the proposed multistatic system under both no-clutter and clutter-plus-noise scenarios and compare it to that of single antenna monostatic systems employing, respectively, an optimal matched illumination and a conventionally used chirp waveform.

The chapter is organized as follows. In Section 4.2, we develop the signal model for the multistatic through-the-wall radar system. The test statistic, the probabilities of detection and false alarm, and the receiver operating characteristic (ROC) curves are provided in Section 4.3. In Section 4.4, we extend the matched illumination waveform design technique for multistatic through-the-wall operation. Simulations

results based on finite-difference time-domain (FDTD) modeling of typical indoor targets are presented in Section 4.5, and Conclusions are provided in Section 4.6.

## 4.2 Problem Statement and Signal Model

We consider the detection of a single stationary extended target inside a room with homogenous walls using a through-the-wall radar system that employs multiple spatially distributed transmitters and receivers. The target could be an animate or inanimate object. The former includes a human, whereas the latter encompasses cache of weapons. The proposed system, unlike the monostatic radar operations, exploits the variations in the target impulse response as a function of the transmitter-to-target aspect angle and the transmitter-receiver bistatic angle for improved performance [18]. Indoor targets, depending on their orientations, may render monostatic-only radar systems ineffective in revealing the target presence. Curvatures and edges can cause weak monostatic target radar cross section (RCS) when viewed from specific angles.

For through-the-wall application, the targets of interest are either physically stationary or moving at very low speeds such that they remain within the same range gate and assume the same impulse response. Therefore, the set of transmitted waveforms need not be orthogonal to facilitate separation between waveforms arriving simultaneously at each receiver. We leverage the target invariance property to propose a matched illumination multistatic approach in which a sequential multiplexing of the transmitters with simultaneous reception at multiple receivers is used [19]. As such, a signal model can be developed based on single active transmitters.

### 4.2.1 Single Active Transmitter

Let the active transmitter be located at  $\mathbf{x}_t = (x_t, y_t)$  and the  $M$  receivers be positioned at  $\mathbf{x}_m = (x_m, y_m)$ ,  $m = 1, 2, \dots, M$ , as shown in Fig. 1. If  $z(t)$  is the energy-limited transmitted signal and  $s_m(t)$  is the target return at the  $m$ -th receiver, then

$$s_m(t) = q_m(t) * z(t) \quad (1)$$

where ‘\*’ denotes convolution and  $q_m(t)$  is the combined wall/target impulse response corresponding to the  $m$ -th transmitter-receiver pair, and is given by

$$q_m(t) = u(t) * \xi_m(t) * u(-t) * \delta(t - \eta_m). \quad (2)$$

In the above equation,  $u(t)$  is the transmission impulse response of the wall, which is assumed to be known and independent of the transmitter and receiver locations. This is a reasonable assumption since, in general, the wall thickness is small compared to the typical antenna stand-off distance, which could be 10m or more from the wall. In this case, the differences in the path lengths through the wall as a function of antenna position are negligible. The deterministic function  $\xi_m(t)$  is the impulse response of the target corresponding to the  $m$ -th transmitter-receiver pair, and is presumed known. The discussion on how to address the case when the target impulse responses corresponding to the various transmitter-receiver pairs are not exactly known is deferred to a later section. The quantity  $\eta_m$  in eq. (2) is the propagation delay measured from the transmitter to the target and then back to the  $m$ -th receiver. It has contributions both from the propagation delays through the air and through the wall [20]. Since the target location is not known beforehand, the propagation delay and hence the combined wall-target impulse response  $q_m(t)$  should be assumed unknown. However, exact knowledge of the combined wall-target impulse response is required to implement matched illumination waveform design techniques. In order to overcome this issue, range gating is employed and the matched illumination waveform will be designed separately for each range gate within which the target could be present. That is, the optimum waveform depends not only on the target and wall impulse responses, but also on the target location.

Let  $w_{c,m}(t)$  represent the clutter response for the  $m$ -th transmitter-receiver pair and  $n_m(t)$  be additive noise. Both the clutter and the noise are assumed to be stationary stochastic processes, which are independent of each other. The  $m$ -th received signal  $r_m(t)$  is given by,

$$r_m(t) = s_m(t) + c_m(t) + n_m(t), \quad c_m(t) = w_{c,m}(t) * z(t) \quad (3)$$

where  $c_m(t)$  is the signal dependent clutter return.



It is noted that in the above model, we have only considered the wall transmission impulse response. The radar return from the wall itself arrives earlier than the return from the target. The wall reflections are assumed to have been either resolved from that of the target or mitigated using effective wall return removal techniques such as those recently proposed in [21]-[23]. In [21], the wall parameters are estimated and used to model the wall returns, which are then subtracted from the target scene data. The approach in [23], similar to the work in [22], does not estimate the wall parameters and instead preprocesses the data by applying a filter in the spatial domain to notch the zero spatial frequency which corresponds to the approximately invariant signal returns from the wall at different antenna locations. This preprocessing scheme is analogous, in its objective, to the moving target indicator (MTI) clutter filter operation in the time-domain where signal return invariance is over time, not space.

To facilitate simulation on a computer, we use a discrete-time formulation of the signal model. The transmitted signal  $z(t)$  is given by  $N_z$  equally spaced time samples separated by an interval  $\Delta t$ , i.e., the transmitted signal vector is defined as  $\mathbf{z} = [z_1, z_2, \dots, z_{N_z}]^T$ . Target impulse responses  $\xi_m(t)$ ,  $m=1, 2, \dots, M$ , can extend over different finite time durations. However, for simplicity of presentation, they are assumed to be of the same finite length. The combined wall/target impulse response  $q_m(t)$  is sampled at the same rate as the transmitted signal to produce an  $N_q \times 1$  impulse response vector  $\mathbf{q}_m = [q_{m1}, q_{m2}, \dots, q_{mN_q}]^T$  and the  $m$ -th received target return  $s_m(t)$  is represented by the return signal vector,  $\mathbf{s}_m = [s_1, s_2, \dots, s_{N_s}]^T$ , where  $N_s = N_z + N_q - 1$ . A convenient matrix representation of the  $m$ -th target return, free of noise and clutter, can be obtained following a similar formulation in [15] as

$$\mathbf{s}_m = \mathbf{Q}_m \mathbf{z} \quad (4)$$

where the  $N_s \times N_z$  combined wall/target convolution matrix  $\mathbf{Q}_m$  is given by



$$\mathbf{Q}_m = \begin{bmatrix} q_{m1} & 0 & 0 & \cdots & 0 \\ q_{m2} & q_{m1} & 0 & \cdots & 0 \\ \vdots & \vdots & \vdots & \ddots & \vdots \\ q_{mN_q} & q_{m(N_q-1)} & \cdots & \cdots & q_{m(N_q-N_z)} \\ 0 & q_{mN_q} & \cdots & \cdots & q_{m(N_q-N_z+1)} \\ \vdots & & & & \\ 0 & 0 & \cdots & \cdots & q_{m(N_q-1)} \end{bmatrix} \quad (5)$$

Likewise, by representing the clutter return and the noise by vectors of their respective temporal samples, the  $m$ -th received signal can be expressed in vector form as

$$\mathbf{r}_m = \mathbf{s}_m + \mathbf{c}_m + \mathbf{n}_m \quad (6)$$

where

$$\mathbf{r}_m = [r_{m1}, r_{m2}, \dots, r_{mN_s}]^T, \quad \mathbf{c}_m = [c_{m1}, c_{m2}, \dots, c_{mN_s}]^T, \quad \mathbf{n}_m = [n_{m1}, n_{m2}, \dots, n_{mN_s}]^T \quad (7)$$

We collect the received signals from the  $M$  receivers in an  $MN_s \times 1$  vector  $\mathbf{r}$

$$\mathbf{r} = \mathbf{Q}\mathbf{z} + \mathbf{c} + \mathbf{n} = \mathbf{s} + \mathbf{c} + \mathbf{n} \quad (8)$$

$$\mathbf{r} = \begin{bmatrix} \mathbf{r}_1 \\ \mathbf{r}_2 \\ \vdots \\ \mathbf{r}_M \end{bmatrix}, \quad \mathbf{s} = \begin{bmatrix} \mathbf{s}_1 \\ \mathbf{s}_2 \\ \vdots \\ \mathbf{s}_M \end{bmatrix}, \quad \mathbf{n} = \begin{bmatrix} \mathbf{n}_1 \\ \mathbf{n}_2 \\ \vdots \\ \mathbf{n}_M \end{bmatrix}, \quad \mathbf{c} = \begin{bmatrix} \mathbf{c}_1 \\ \mathbf{c}_2 \\ \vdots \\ \mathbf{c}_M \end{bmatrix}, \quad \mathbf{Q} = \begin{bmatrix} \mathbf{Q}_1 \\ \mathbf{Q}_2 \\ \vdots \\ \mathbf{Q}_M \end{bmatrix}$$

#### 4.2.2 A note on range resolution and range gate

As mentioned above, the convolution of the transmitted pulse of length  $N_z$  samples with the combined wall/target impulse response of length  $N_q$  samples forces the return to extend over an interval of  $N_s = N_z + N_q - 1$  samples. For free-space propagations, two point targets can be resolved in range if the target returns are separated by

$$\tau = (N_z - 1)\Delta t \quad (9)$$

where  $\tau$  is the received echo duration (same as the emitted pulse duration). Accordingly, for the case of extended targets behind the wall, the separation between the target returns should be

$$\tau = (N_s - 1)\Delta t = (N_z + N_q - 2)\Delta t, \quad (10)$$

In the signal model of eq. (8), we assume that the range gate is determined by eq. (10).

### 4.2.3 Multiple transmitters

Consider a multistatic through-the-wall radar system with  $L$  transmitters. When the  $l$ -th transmitter is active and emits the signal  $\mathbf{z}_l$ , the  $MN_s \times 1$  received signal vector  $\mathbf{r}_{t_l}$  is given by eq. (8), reproduced below with the introduction of the subscript  $l$ .

$$\mathbf{r}_{t_l} = \mathbf{Q}_{t_l} \mathbf{z}_l + \mathbf{c}_{t_l} + \mathbf{n}_{t_l} = \mathbf{s}_{t_l} + \mathbf{c}_{t_l} + \mathbf{n}_{t_l}, \quad l = 1, 2, \dots, L \quad (11)$$

$$\mathbf{r}_{t_l} = \begin{bmatrix} \mathbf{r}_{l1} \\ \mathbf{r}_{l2} \\ \vdots \\ \mathbf{r}_{lM} \end{bmatrix}, \quad \mathbf{s}_{t_l} = \begin{bmatrix} \mathbf{s}_{l1} \\ \mathbf{s}_{l2} \\ \vdots \\ \mathbf{s}_{lM} \end{bmatrix}, \quad \mathbf{n}_{t_l} = \begin{bmatrix} \mathbf{n}_{l1} \\ \mathbf{n}_{l2} \\ \vdots \\ \mathbf{n}_{lM} \end{bmatrix}, \quad \mathbf{c}_{t_l} = \begin{bmatrix} \mathbf{c}_{l1} \\ \mathbf{c}_{l2} \\ \vdots \\ \mathbf{c}_{lM} \end{bmatrix}, \quad \mathbf{Q}_{t_l} = \begin{bmatrix} \mathbf{Q}_{l1} \\ \mathbf{Q}_{l2} \\ \vdots \\ \mathbf{Q}_{lM} \end{bmatrix}$$

Note that we have assumed that each of the  $L$  transmitted signals has the same length  $N_z$  and the target impulse responses apparent to the  $LM$  transmitter-receiver pairs are all of length  $N_q$ . The values of  $N_z$  and  $N_q$  can be chosen based on their possible maximum values, consistent with system and target specifications and properties.

We combine the  $L$  received signals, obtained from the sequential use of the  $L$  transmitters, to form a tall vector  $\mathbf{r}_{tot}$  of length  $LMN_s$ , given by

$$\mathbf{r}_{tot} = \mathbf{Q}_{tot} \mathbf{z}_{tot} + \mathbf{c}_{tot} + \mathbf{n}_{tot} = \mathbf{s}_{tot} + \mathbf{c}_{tot} + \mathbf{n}_{tot}$$

$$\mathbf{r}_{tot} = \begin{bmatrix} \mathbf{r}_{t_1} \\ \mathbf{r}_{t_2} \\ \vdots \\ \mathbf{r}_{t_L} \end{bmatrix}, \quad \mathbf{s}_{tot} = \begin{bmatrix} \mathbf{s}_{t_1} \\ \mathbf{s}_{t_2} \\ \vdots \\ \mathbf{s}_{t_L} \end{bmatrix}, \quad \mathbf{n}_{tot} = \begin{bmatrix} \mathbf{n}_{t_1} \\ \mathbf{n}_{t_2} \\ \vdots \\ \mathbf{n}_{t_L} \end{bmatrix}, \quad \mathbf{c}_{tot} = \begin{bmatrix} \mathbf{c}_{t_1} \\ \mathbf{c}_{t_2} \\ \vdots \\ \mathbf{c}_{t_L} \end{bmatrix}, \quad \mathbf{Q}_{tot} = \begin{bmatrix} \mathbf{Q}_{t_1} & \mathbf{0} & \dots & \mathbf{0} \\ \mathbf{0} & \mathbf{Q}_{t_2} & \dots & \mathbf{0} \\ \vdots & \vdots & \ddots & \vdots \\ \mathbf{0} & \mathbf{0} & \dots & \mathbf{Q}_{t_L} \end{bmatrix} \quad (12)$$

### 4.3 Detection Statistic

In this section, we formulate the through-the-wall detection problem for the multistatic radar using the proposed sequential multiplexing approach. We assume that both the noise  $\mathbf{n}_{tot}$  and the signal-dependent clutter return  $\mathbf{c}_{tot}$  in eq. (12) are independent zero-mean multivariate real Gaussian processes with known covariance matrices,

$$\mathbf{R}_n = E\{\mathbf{n}_{tot}\mathbf{n}_{tot}^T\} = \sigma^2 \mathbf{I}_{LMN_s}, \quad \mathbf{R}_c = E\{\mathbf{c}_{tot}\mathbf{c}_{tot}^T\} \quad (13)$$

where  $\sigma^2$  is the noise variance and  $\mathbf{I}_{LMN_s}$  is an identity matrix of dimensions  $LMN_s \times LMN_s$ . More explicitly, the noise is independent across the receivers from one transmission to the next and is identically distributed. Also, the signal-dependent clutter is assumed to be uncorrelated across the widely separated transmitters and receivers in which case the matrix  $\mathbf{R}_c$  takes the block diagonal form

$$\mathbf{R}_c = \text{diag}(\mathbf{R}_{c,1,1}, \mathbf{R}_{c,1,2}, \dots, \mathbf{R}_{c,L,M}) = \begin{bmatrix} \mathbf{R}_{c,1,1} & \mathbf{0} & \cdots & \mathbf{0} \\ \mathbf{0} & \mathbf{R}_{c,1,2} & \cdots & \mathbf{0} \\ \vdots & \vdots & \ddots & \vdots \\ \mathbf{0} & \mathbf{0} & \cdots & \mathbf{R}_{c,L,M} \end{bmatrix} \quad (14)$$

where  $\mathbf{R}_{c,l,m} = E\{\mathbf{c}_{lm}\mathbf{c}_{lm}^T\}$  is the  $N_s \times N_s$  clutter covariance matrix corresponding to the  $m$ -th receiver for the  $l$ -th transmission and it depends on the transmitted signal  $\mathbf{z}_l$ .

With respect to a given range gate, we define the null and alternative hypotheses as

$$\begin{aligned} H_0 : & \quad \text{Clutter and noise only} \\ H_1 : & \quad \text{Target plus clutter and noise} \end{aligned} \quad (15)$$

The log-likelihood ratio test is given by

$$\begin{aligned} \Lambda(\mathbf{r}_{tot}) \geq \ln \gamma & \Rightarrow H_1 \text{ is true} \\ \Lambda(\mathbf{r}_{tot}) < \ln \gamma & \Rightarrow H_0 \text{ is true} \end{aligned}, \quad \Lambda(\mathbf{r}_{tot}) = \ln \frac{p(\mathbf{r}_{tot} / H_1)}{p(\mathbf{r}_{tot} / H_0)} \quad (16)$$

where  $p(\mathbf{r}_{tot} / H_0)$  and  $p(\mathbf{r}_{tot} / H_1)$  are the conditional probability density functions (pdfs) of the received signal  $\mathbf{r}_{tot}$ , given the null and alternative hypothesis, respectively. The parameter  $\gamma$  is the threshold which maximizes the probability of detection, while controlling the probability of false-alarm. Given the

signal model of eq. (12) and under the assumption of Gaussian distributed clutter and noise, the probability density functions for the null and alternative hypotheses are

$$\begin{aligned} p(\mathbf{r}_{tot} / H_0) &= \frac{1}{(2\pi)^{LMN_s/2} |\mathbf{R}_c + \sigma^2 \mathbf{I}_{LMN_s}|^{1/2}} \exp(-\mathbf{r}_{tot}^T (\mathbf{R}_c + \sigma^2 \mathbf{I}_{LMN_s})^{-1} \mathbf{r}_{tot}) \\ p(\mathbf{r}_{tot} / H_1) &= \frac{1}{(2\pi)^{LMN_s/2} |\mathbf{R}_c + \sigma^2 \mathbf{I}_{LMN_s}|^{1/2}} \exp(-(\mathbf{r}_{tot} - \mathbf{s}_{tot})^T (\mathbf{R}_c + \sigma^2 \mathbf{I}_{LMN_s})^{-1} (\mathbf{r}_{tot} - \mathbf{s}_{tot})) \end{aligned} \quad (17)$$

Using the expressions for  $p(\mathbf{r}_{tot} / H_0)$  and  $p(\mathbf{r}_{tot} / H_1)$  in eq. (16) and absorbing the term independent of  $\mathbf{r}_{tot}$  into the detection threshold, the log-likelihood ratio test takes the form

$$\begin{aligned} \Lambda(\mathbf{r}_{tot}) \geq \gamma' &\Rightarrow H_1 \text{ is true} \\ \Lambda(\mathbf{r}_{tot}) < \gamma' &\Rightarrow H_0 \text{ is true}, \quad \Lambda(\mathbf{r}_{tot}) = \mathbf{s}_{tot}^T (\mathbf{R}_c + \sigma^2 \mathbf{I}_{LMN_s})^{-1} \mathbf{r}_{tot} \end{aligned} \quad (18)$$

with  $\gamma' = \ln \gamma + \mathbf{s}_{tot}^T (\mathbf{R}_c + \sigma^2 \mathbf{I}_{LMN_s})^{-1} \mathbf{s}_{tot}$ . Thus, the optimal detector is a matched filter whose impulse response  $\mathbf{b}_{match}$  is given by,

$$\mathbf{b}_{match} = (\mathbf{R}_c + \sigma^2 \mathbf{I}_{LMN_s})^{-1} \mathbf{s}_{tot} \quad (19)$$

Using eqs. (13) and (14), the matched filter of eq. (19) can be expressed as,

$$\mathbf{b}_{match} = \begin{bmatrix} (\mathbf{R}_{c,1,1} + \sigma^2 \mathbf{I}_{N_s})^{-1} \mathbf{s}_{11} \\ (\mathbf{R}_{c,1,2} + \sigma^2 \mathbf{I}_{N_s})^{-1} \mathbf{s}_{12} \\ \vdots \\ (\mathbf{R}_{c,L,M} + \sigma^2 \mathbf{I}_{N_s})^{-1} \mathbf{s}_{LM} \end{bmatrix} \equiv \begin{bmatrix} \mathbf{b}_{match,1,1} \\ \mathbf{b}_{match,1,2} \\ \vdots \\ \mathbf{b}_{match,L,M} \end{bmatrix}, \quad (20)$$

and the output  $y_{out}$  of the matched filter detector is given by,

$$y_{out} = \sum_{l=1}^L \sum_{m=1}^M \mathbf{b}_{match,l,m}^T \mathbf{r}_{lm} = \sum_{l=1}^L \sum_{m=1}^M \mathbf{s}_{lm}^T (\mathbf{R}_{c,l,m} + \sigma^2 \mathbf{I}_{N_s})^{-1} \mathbf{r}_{lm} \quad (21)$$

It is noted that, due to the block diagonal nature of the matrix  $(\mathbf{R}_c + \sigma^2 \mathbf{I}_{LMN_s})$ , the processing of the LM received signals corresponding to the L sequential transmissions becomes decoupled. With the l-th transmitter active, the corresponding m-th received signal is passed through a matched filter whose impulse response entails the clutter statistics and the target echo for the (l, m)-th transmitter-receiver

pair only. The LM matched filter outputs corresponding to the L sequential transmissions are coherently combined to obtain the output of the overall multistatic optimal detector.

#### 4.3.1 Receiver operating characteristic

The probabilities of detection and false alarm for the matched filter detector of eq. (18) are given by

$$P_d = \int_{\gamma'}^{\infty} f_{\Lambda}(\Lambda / H_1) d\Lambda, \quad P_{fa} = \int_{\gamma'}^{\infty} f_{\Lambda}(\Lambda / H_0) d\Lambda \quad (22)$$

where  $f_{\Lambda}(\Lambda / H_1)$  and  $f_{\Lambda}(\Lambda / H_0)$  are the likelihood ratio distributions under the alternate and null hypothesis, respectively. Since matched filtering is a linear operation on the Gaussian vector  $\mathbf{r}_{tot}$ ,  $\Lambda$  is also Gaussian distributed with respective means equal to zero and  $\mathbf{b}_{match}^T \mathbf{s}_{tot}$  under  $H_0$  and  $H_1$ , and covariance  $\mathbf{b}_{match}^T (\mathbf{R}_c + \sigma^2 \mathbf{I}_{LMN_s}) \mathbf{b}_{match}$  under both hypotheses. Therefore,  $P_d$  and  $P_{fa}$  take the form [24]

$$\begin{aligned} P_d &= \left[ 1 - \Phi \left( \frac{\gamma' - \mathbf{b}_{match}^T \mathbf{s}_{tot}}{\sqrt{(\mathbf{b}_{match}^T (\mathbf{R}_c + \sigma^2 \mathbf{I}_{LMN_s}) \mathbf{b}_{match})}} \right) \right] \\ P_{fa} &= \left[ 1 - \Phi \left( \frac{\gamma'}{\sqrt{(\mathbf{b}_{match}^T (\mathbf{R}_c + \sigma^2 \mathbf{I}_{LMN_s}) \mathbf{b}_{match})}} \right) \right] \end{aligned} \quad (23)$$

where  $\Phi(u) = \frac{1}{2} + \frac{1}{2} \text{erf} \left( \frac{u}{\sqrt{2}} \right)$  is the cumulative distribution function of a Gaussian random variable with

zero mean and unit variance and  $\text{erf}(x) = \frac{2}{\sqrt{\pi}} \int_0^x e^{-t^2} dt$  denotes the error function [25].

The corresponding receiver operating characteristics curve is given by [24],

$$\begin{aligned} P_d &= (1 - \Phi(\Phi^{-1}(1 - P_{fa}) - d)) \\ d^2 &= \frac{\mathbf{b}_{match}^T \mathbf{s}_{tot} \mathbf{s}_{tot}^T \mathbf{b}_{match}}{(\mathbf{b}_{match}^T (\mathbf{R}_c + \sigma^2 \mathbf{I}_{LMN_s}) \mathbf{b}_{match})} \end{aligned} \quad (24)$$

where  $d^2$  can be readily identified as the SCNR at the output of the matched filter.



### 4.3.2 Coherent vs. combining

Since the optimal detector requires coherent combining of the received signals resulting from  $L$  sequential transmissions, phase synchronization across the spatially separated transmitters and receivers is required. This requirement is not too stringent for through-the-wall applications in urban environments. For illustration, consider a typical urban data acquisition scenario shown in Fig. 2(a). Assuming access to only the front of a 10m-by-10m building of interest, the urban setting permits a maximum viewing angle of  $53^\circ$  [26]. For a standoff distance of 10m, this translates to a maximum distance of 19.94m between the sensors.

However, in the case when access is available to multiple sides of a building in an urban setting or for sensing in a suburban environment where the buildings along a street are widely separated (see Fig. 2(b)), the maximum distance between the sensors could be relatively large. In such situations, it may be still feasible to distribute the transmitters in such a way that only phase synchronization across the receivers is required, enabling coherent processing, while the matched filtered outputs corresponding to the  $L$  sequential transmissions are noncoherently combined. In this case, the test statistic is given by,

$$y_{out} = \sum_{l=1}^L y_{out,l}^2, \quad y_{out,l} = \mathbf{b}_{match,l}^T \mathbf{r}_{t_l} \quad (25)$$

where  $\mathbf{b}_{match,l} = [\mathbf{b}_{match,l,1} \quad \mathbf{b}_{match,l,2} \quad \dots \quad \mathbf{b}_{match,l,M}]^T$ . Since  $\mathbf{r}_{t_l}$  is Gaussian distributed with means equal to zero and  $\mathbf{b}_{match,l}^T \mathbf{s}_{t_l}$ , respectively, under the null and the alternative hypothesis, and covariance  $\mathbf{b}_{match,l}^T (\mathbf{R}_{c,l} + \sigma^2 \mathbf{I}_{MN_s}) \mathbf{b}_{match,l}$  with  $\mathbf{R}_{c,l} = \text{diag}(\mathbf{R}_{c,l,1}, \mathbf{R}_{c,l,2}, \dots, \mathbf{R}_{c,l,M})$  under both hypotheses, then each  $y_{out,l}$  has a central  $\chi^2$  distribution under  $H_0$ , and a noncentral  $\chi^2$  distribution under  $H_1$ . However, as the variance of the pdfs of  $\mathbf{r}_{t_l}$  depends on the transmitted signal through  $\mathbf{s}_{t_l}$ , a different pdf applies to each  $y_{out,l}$ . Therefore, the derivation of the distributions of the test statistic of eq. (25) under  $H_0$  and  $H_1$  and the corresponding probabilities of detection and false-alarm becomes much more involved and is beyond the scope of this work.

#### 4.4 Matched Illumination Waveform Design

The objective of the matched illumination waveform design is to find the transmitted signal vector  $\mathbf{z}_{tot}$  that maximizes the signal-to-clutter-and-noise ratio at the output of the matched filter detector of eq. (18).

Using eqs. (19) and (24), the waveform design problem can be formulated mathematically as,

$$\begin{aligned} \max_{\mathbf{z}_{tot}} \text{SCNR} &= \max_{\mathbf{z}_{tot}} \frac{\mathbf{b}_{match}^T \mathbf{s}_{tot} \mathbf{s}_{tot}^T \mathbf{b}_{match}}{\mathbf{b}_{match}^T (\mathbf{R}_c + \sigma^2 \mathbf{I}_{LMN_s}) \mathbf{b}_{match}} \\ &= \max_{\mathbf{z}_{tot}} \mathbf{s}_{tot}^T (\mathbf{R}_c + \sigma^2 \mathbf{I}_{LMN_s})^{-1} \mathbf{s}_{tot} \end{aligned} \quad (26)$$

Exploiting the block diagonal nature of  $(\mathbf{R}_c + \sigma^2 \mathbf{I}_{LMN_s})$  and  $\mathbf{Q}_{tot}$ , the SCNR simplifies to

$$\begin{aligned} \text{SCNR} &= \sum_{l=1}^L \mathbf{z}_l^T \left( \sum_{m=1}^M \mathbf{Q}_{lm}^T (\mathbf{R}_{c,l,m} + \sigma^2 \mathbf{I}_{N_s})^{-1} \mathbf{Q}_{lm} \right) \mathbf{z}_l \\ &= \sum_{l=1}^L \mathbf{z}_l^T \mathbf{Q}_{t_l}^T (\mathbf{R}_{c,l} + \sigma^2 \mathbf{I}_{MN_s})^{-1} \mathbf{Q}_{t_l} \mathbf{z}_l \end{aligned} \quad (27)$$

Since the  $l$ -th term in the summation on the right hand side of SCNR in eq. (27) depends only on the  $l$ -th transmission, it is clear that the original waveform design problem of eq. (26) is equivalent to designing  $L$  individual waveforms  $\mathbf{z}_1, \mathbf{z}_2, \dots, \mathbf{z}_L$ , such that

$$\max_{\mathbf{z}_l} \mathbf{z}_l^T \mathbf{Q}_{t_l}^T (\mathbf{R}_{c,l} + \sigma^2 \mathbf{I}_{MN_s})^{-1} \mathbf{Q}_{t_l} \mathbf{z}_l, \quad l=1, 2, \dots, L \quad (28)$$

In the case of zero or negligible clutter, the solution  $\mathbf{z}_l$  to the design problem of eq. (28) is proportional to the eigenvector corresponding to the largest eigenvalue of  $\mathbf{\Omega}_l = \frac{1}{\sigma^2} \mathbf{Q}_{t_l}^T \mathbf{Q}_{t_l}$  [15], [16]. On the other hand, when both signal-dependent clutter and noise are present and significant, the optimal waveforms  $\mathbf{z}_1, \mathbf{z}_2, \dots, \mathbf{z}_L$  can be obtained iteratively, as discussed in [15].

The above analysis was carried out under the assumption of known impulse responses of the target corresponding to the various transmitter-receiver pairs. Note that for a given range gate, the target impulse response at each receiver is a function of the incident angle, the reflected angle, and the transmitter-to-target aspect angle, which may not always be available when the target is behind walls. One simple way to overcome this problem is to cycle through all possible optimal matched-illumination waveforms

for the target of interest given the multistatic sensor geometry. The SCNR varies as a function of the target orientation, the incident and reflected angles, even when a corresponding optimal pulse is used for each orientation. Therefore, the transmitted waveform corresponding to the actual target orientation and angles of incidence and reflection will provide the highest SCNR. It is noted that the symmetry of the target can be utilized to reduce the number of optimal waveforms used to interrogate the scene.

## 4.5 Simulation Results

A multistatic radar system, consisting of three sensors, was considered. Two different sensor functionalities, listed in Table I, were simulated. In the first case (Case I), sensor S1 acts as a receiver, S2 is a transceiver, and S3 is a transmitter, whereas in Case II, the roles of sensors S2 and S3 are reversed. The sensors are placed at a standoff distance of 10m from a 0.2in thick solid concrete wall with a dielectric constant of 7.66 and conductivity of 0.06 S/m, as depicted in Fig. 3. A single stationary target is located 1.3m behind the wall. For the first set of simulations, a wooden table, shown in Fig. 4(a), was used as the target, with its long side parallel to the wall. For the second dataset, the model of a standing human facing the wall was employed. The particular human model used, shown in Fig. 4(b), is the “High Fidelity Frozen Male Body” by Remcom Inc. The human's phantom consists of 23 different tissue types, each with its own dielectric properties. The model is optimized for numerical computations and occupies only 128 MB of RAM [27].

Since the optimal waveform design involves target impulse responses, free-space simulations were first carried out using a commercial electromagnetic (EM) simulator XFDTD<sup>®</sup> by Remcom for computing the impulse responses of both the table and the human apparent to each transmitter/receiver pair. It was assumed that both the transmitter and the receiver are located in the far-field of the target. Each target was probed by a vertically polarized modulated Gaussian pulse, covering the 1-8 GHz frequency band with almost uniform energy over 1-3 GHz, as shown in Fig. 5. Dual-polarized target detection and imaging systems for through-the-wall radar applications prove very effective, but their consideration in the underlying multistatic waveform design problem has not yet been investigated and it is outside the scope

of this chapter. For each transmitter/receiver bistatic angle, the corresponding target impulse response  $\xi$  was obtained as the least squares solution [16],

$$\xi = (\mathbf{Z}^T \mathbf{Z})^{-1} \mathbf{Z}^T \mathbf{s} \quad (29)$$

where  $\mathbf{Z}$  is a convolution matrix, identical in structure to eq. (5), containing the incident modulated Gaussian waveform, and  $\mathbf{s}$  is the target return vector. The transmission impulse response of the wall was similarly computed. Since XFDTD<sup>®</sup> produced results for a far-field scenario with plane wave excitation, the combined wall/table and wall/human impulse responses were preprocessed to reflect the multistatic radar functional modes for Cases I and II.

Optimal matched illumination waveforms were first constructed for the wooden table for the zero clutter case. A range gate of 19.93 ns, centered at the target, was used. The target orientation was also assumed to be known. The SCNR corresponding to the multistatic radar system using the optimal waveforms are provided in Table II. For comparison, the optimal matched illumination waveform corresponding to monostatic operation from the transceiver, was also obtained and the corresponding SCNR are given in Table II. In order to compare the performance of the different waveforms, we used the same total transmit power and identical noise variance of 0.001 in all cases. From Table II, we note that the multistatic operation provides a significant increase in the SCNR over the monostatic case, more so for sensor functionality mode I, and subsequently, a significant improvement in the ROC behavior, as shown in Fig. 6. The difference in improvement over the monostatic operation for the two modes can be attributed to the difference in the monostatic RCS of the table corresponding to the aspect angle apparent to the transceivers in each mode.

In order to gain insights into the characteristics of the optimum waveform relative to those of the wall and the target, we plot in Fig. 7 the two-way wall frequency response, the table frequency responses apparent to the two receivers with transmitter 1 active, and the frequency response of the optimal waveform transmitted from transmitter 1, all for multistatic sensor mode I. It is clear from the figure that the optimal waveform places its energy in a narrow frequency band that jointly resonates the wall and the



target. However, we note that the energy of the optimal pulse is concentrated only where the wall and the target frequency response corresponding to receiver 2 exhibit peaks. The reason for this is two-fold. Firstly, as clear from Fig. 7, the peaks of the target frequency response corresponding to receiver 1 do not align very well with the peaks of the wall response. Secondly, the impulse response of the table corresponding to receiver 2 has a relatively small amplitude than that corresponding to receiver 1, as shown in Fig. 8.

Next, we constructed the optimal matched illumination waveforms for the human for the zero clutter case. A range gate of 18.5 ns, centered at the target, was used. The SCNR corresponding to both multistatic and monostatic operations using the optimal waveforms are provided in Table III. Again, the multistatic system outperforms the monostatic operation for both sensor functionality modes. The optimal waveform corresponding to transmitter 1 for mode I is plotted in Fig. 9.

For both the human and the wooden table in the presence of noise only, the output SCNRs corresponding to the optimal transmitted waveforms for monostatic and multistatic operations were also compared to those of chirp waveforms of the same energy and respective durations. Similar to the optimal waveforms, the matched filter for the chirp waveform was matched to the expected target echo, as given by eq. (19), rather than the transmitted waveform. The SCNRs corresponding to the chirp waveforms for the table and human are, respectively, provided in Tables II and III. It is evident that the optimal waveforms significantly outperform the chirp signal for both monostatic and multistatic operations.

For the case of non-zero clutter, we have designed the optimum multistatic waveforms for the human for sensor functionality mode I using the iterative algorithm presented in [15]. The clutter and the noise are assumed to be of independent samples. The clutter-to-noise ratio (CNR) was first set to -10 dB and then to 10dB. Table IV provides the SCNR at the output of the matched filter due to three different waveforms, namely, the optimum transmitted waveform for clutter and noise, the optimum waveform for noise only case, and a chirp waveform, all of the same duration and energy. For CNR of -10 dB, we observe that the optimized waveform obtained via the iterative technique provides better detection in the presence of clutter, though the overall SCNR improvement compared to the noise only case has degraded.



On the other hand, when the CNR is 10 dB, all transmission waveforms yield similar SCNR. This is in compliance with the degenerate case of significant clutter, described in [15], wherein all transmission waveforms yield identical SCNR. The optimal waveform corresponding to transmitter 1 for CNR=-10 dB is plotted in Fig. 10.

## 4.6 Conclusions

In this chapter, we presented a generalization of the matched illumination based waveform design for through-the-wall radar operation using a multistatic radar system for improved detection of stationary targets. The slowly moving and stationary nature of the indoor targets permits sequential use of the transmitters, rendering the use of orthogonal waveforms unnecessary. Proof of concept was provided using EM modeled data for both a human and a typical indoor inanimate object, namely, a wooden table, behind a solid concrete wall. The two cases of noise-only and clutter-plus-noise were analyzed. It was assumed that the target signal returns to a transmitted waveform can be coherently processed at the different receivers. Performance of the optimal multistatic waveform was compared to that of the optimum waveform for single antenna monostatic operation as well as a conventionally used chirp waveform. It was shown that, for the targets considered and in the clutter-free radar returns, the optimal multistatic waveform provided a superior performance and outperformed the others in terms of the SCNR at the output of the matched filter. In the presence of clutter, the optimal multistatic waveform provided improvements over the other waveforms. However, more extensive simulations need to be performed in order to properly assess the performance of the optimal multistatic waveform for cluttered scenes.

## References

- [31] J. A. Malas and K. M. Pasala, "Radar signature analysis using information theory," in *IEEE Radar Conf.*, May 2008.
- [32] N. A. Goodman, P. R. Venkata, and M. A. Neifeld, "Adaptive waveform design and sequential hypothesis testing for target recognition with active sensors," *IEEE J. Sel. Topics Signal Process.*, vol. 1, issue 1, pp.105 – 113, June 2007.
- [33] Y. Yang and R. Blum, "Waveform design for MIMO radar based on mutual information and minimum mean-square error estimation," *Proc. 40th Annual Conference on Information Sciences and Systems*, pp. 111-116, March 2006.
- [34] A. K. Mitra, "Position-adaptive UAV radar for urban environments," in *IEEE Int. Radar Conf.*, pp. 303 – 308, September 2003.
- [35] S. U. Pillai, H. S. Oh, D. C. Youla, and J. R. Guerci, "Optimum transmit-receiver design in the presence of signal-dependent interference and channel noise," *IEEE Trans. Inf. Theory*, vol. 46, no. 2, pp. 577-584, March 2000.
- [36] D. T. Gjessing, *Target adaptive matched illumination RADAR: Principles and applications*, IEE Electromagnetic Waves Series 22, Peter Peregrinus Ltd., London, UK, 1986.
- [37] *Journal of the Franklin Institute*, Special Issue on 'Advances in Indoor Radar Imaging,' vol. 345, no. 6, September 2008.
- [38] *Proceedings of the 2008 IEEE International Conference on Acoustics, Speech, and Signal Processing*, Special Session on 'Through-the-Wall Radar Imaging,' Las Vegas, Nevada, April 2008.
- [39] P. Withington, H. Fluhler, and S. Nag, "Enhancing homeland security with advanced UWB sensors," *IEEE Microw. Mag.*, vol. 4, no. 3, pp. 51-58, 2003.
- [40] S. E. Borek, "An overview of through the wall surveillance for homeland security," in *Proceedings of the 34<sup>th</sup> Applied Imagery and Pattern Recognition Workshop*, Washington, DC, October 2005.

- [41] E. Baranoski, "Through-wall imaging: Historical perspective and future directions," *Journal of Franklin Institute*, vol. 345, no. 6, pp. 556-569, September 2008.
- [42] M. Farwell, J. Ross, R. Luttrell, D. Cohen, W. Chin, and T. Dogaru, "Sense through the wall system development and design considerations," *Journal of Franklin Institute*, vol. 345, no. 6, pp. 570-591, September 2008.
- [43] E. F. Greneker, "RADAR flashlight for through-the-wall detection of humans", in *Proceedings of the SPIE*, vol. 3375, April 1998, pp. 280-285.
- [44] M. Pieraccini, G. Luzi, D. Dei, L. Pieri, and C. Atzeni, "Detection of Breathing and Heartbeat Through Snow Using a Microwave Transceiver," *IEEE Geosci. Remote Sens. Lett.*, vol. 5, no. 1, pp. 57-59, 2008.
- [45] D. A. Garren, M. K. Osborn, A. C. Odom, J. S. Goldstein, S. U. Pillai, and J. R. Guerci, "Enhanced target detection and identification via optimised radar transmission pulse shape," *IEE Proc.-Radar, Sonar Navig.*, vol. 148, No. 3, pp. 130-138, June 2001.
- [46] H. Estephan, M. Amin, and K. Yemelyanov, "Waveform design for through-the-wall radar imaging applications," in *Proc. of the SPIE Defense and Security Symposium*, vol. 6943, Orlando, FL, March 2008.
- [47] J. Li and P. Stoica, "MIMO Radar with Colocated Antennas," *IEEE Signal Process. Mag.*, pp. 106-114, September 2007.
- [48] A. M. Haimovich, R. S. Blum, and L. J. Cimini, Jr., "MIMO Radar with widely separated antennas," *IEEE Signal Process. Mag.*, pp. 116-129, January 2008.
- [49] J. R. Guerci, M. C. Wicks, J. S. Bergin, P. M. Techau, and S. U. Pillai, "Theory and application of optimum and adaptive MIMO Radar," in *IEEE Int. Radar Conf.*, May 2008, pp. 2146-2151.
- [50] F. Ahmad and M. G. Amin, "Noncoherent approach to through-the-wall target localization," *IEEE Trans. Aerosp. Electron. Syst.*, vol. 42, issue 4, pp. 1405-1419, October 2006.

- [51] M. Dehmollaian and K. Sarabandi, "Refocusing through building walls using synthetic aperture radar," *IEEE Trans. Geosci. Remote Sens.*, vol. 46, no. 6, pp. 1589–1599, June 2008.
- [52] M. Dehmollaian and K. Sarabandi, "Analytical, numerical, and experimental methods for through-the-wall radar imaging," in *IEEE Int. Conf. Acoustics, Speech, and Signal Processing*, April 2008, pp. 5181–5184.
- [53] Y. Yoon and M. Amin, "Spatial filtering for wall-clutter mitigation in through-the-wall radar imaging," *IEEE Trans. Geosci. Remote Sens.*, vol. 47, no. 9, pp. 3192 – 3208, Sept. 2009.
- [54] V. H. Poor, *An Introduction To Signal Detection And Estimation*, 2<sup>nd</sup> Edition, Springer-Verlag, 1994.
- [55] M. Abramowitz and I. Stegun, *Handbook of Mathematical Functions with Formulas, Graphs, and Mathematical Tables*, New York, Dover Publications, 1972.
- [56] E. J. Baranoski, "VisiBuilding: Sensing through Walls," in *Fourth IEEE Workshop on Sensor Array and Multichannel Processing*, July 2006.
- [57] Available: <http://www.remcom.com/xfdtd/optional-modules/biological-meshes.html>.

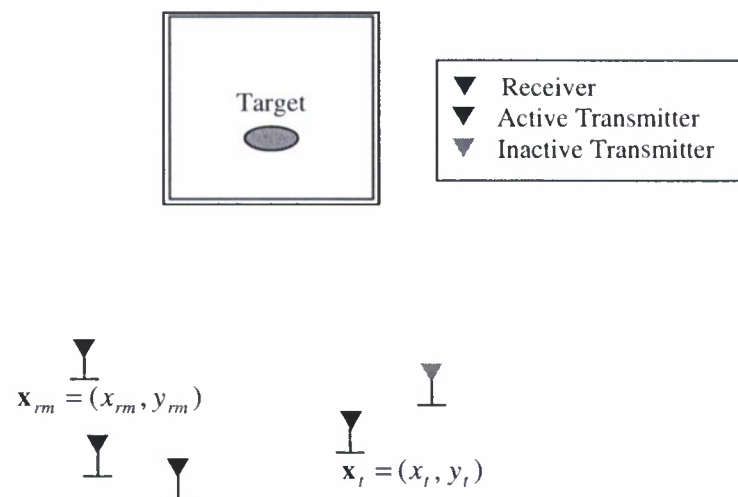


**Fig. 1** Through-the-wall multistatic sensing scenario with a single active transmitter.

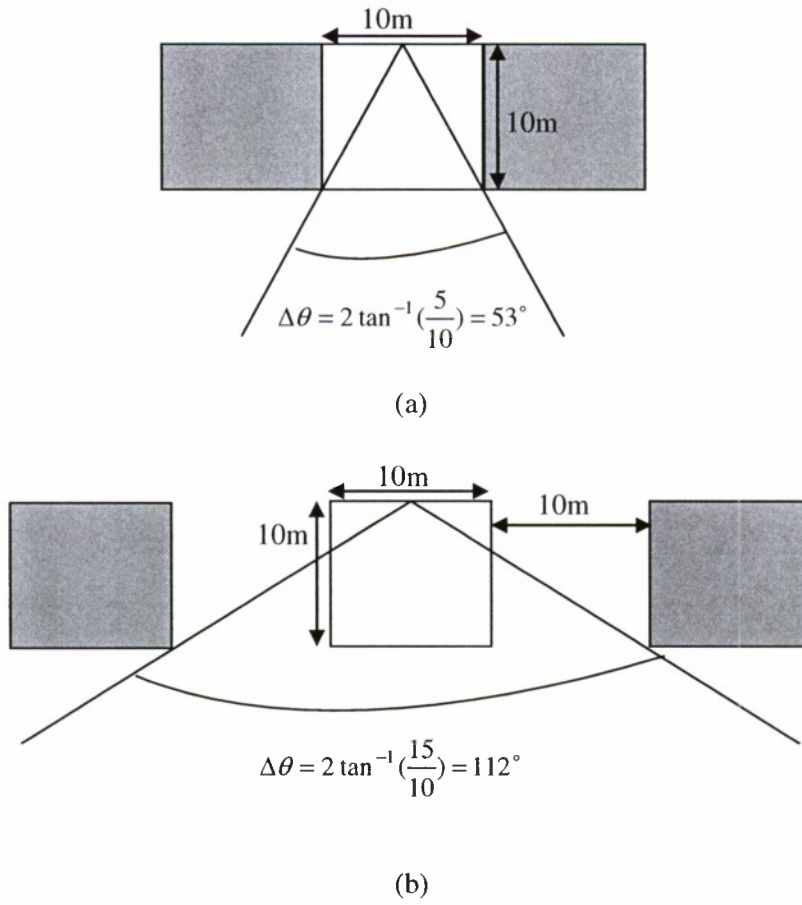


**Fig. 2** Through-the-wall sensing scenarios in (a) urban environment, (b) suburban environment. (Adapted from [26]).

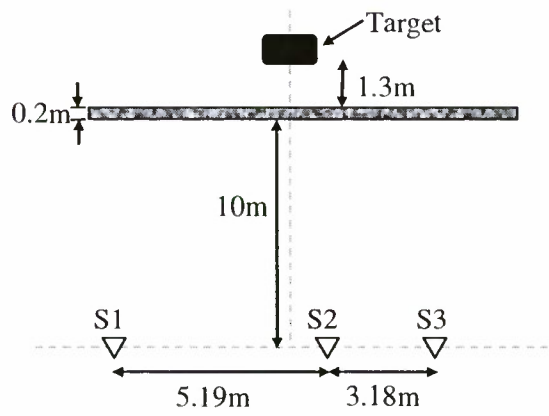


**Fig. 3** Layout of the simulated scene.



**Table I.** Functionality of the sensors.

Operational Mode	Transmitter 1	Transmitter 2	Receiver 1	Receiver 2
Case I	S3	S2	S2	S1
Case II	S3	S2	S3	S1



(a)

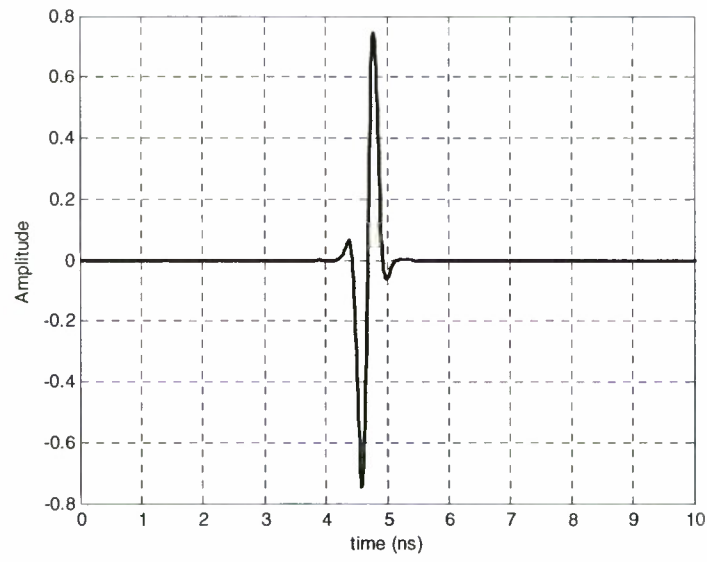


(b)

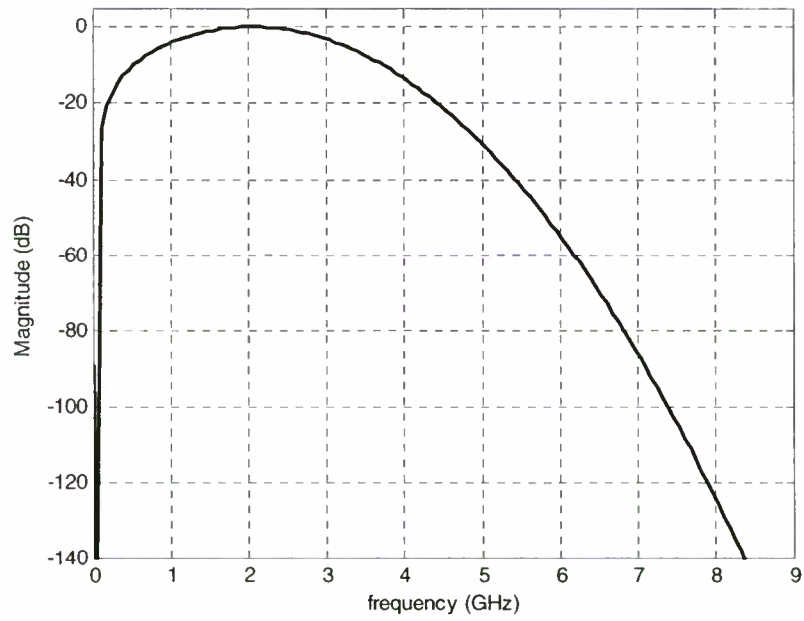
Fig. 4 (a) 3-D model of a wooden table, (b) High Fidelity Frozen Human Model.

Table II. SCNR at the output of the matched filter for the table.

Target	Functional Mode	Waveform	SCNR (dB)	
			Monostatic Operation	Multistatic Operation
Wooden Table	I	Optimal	1.2617	9.6067
		Chirp	-7.2687	-0.4066
	II	Optimal	8.2217	10.8628
		Chirp	-3.9222	0.0437



(a)



(b)

**Fig. 5** (a) Modulated Gaussian Pulse, (b) Corresponding spectrum.

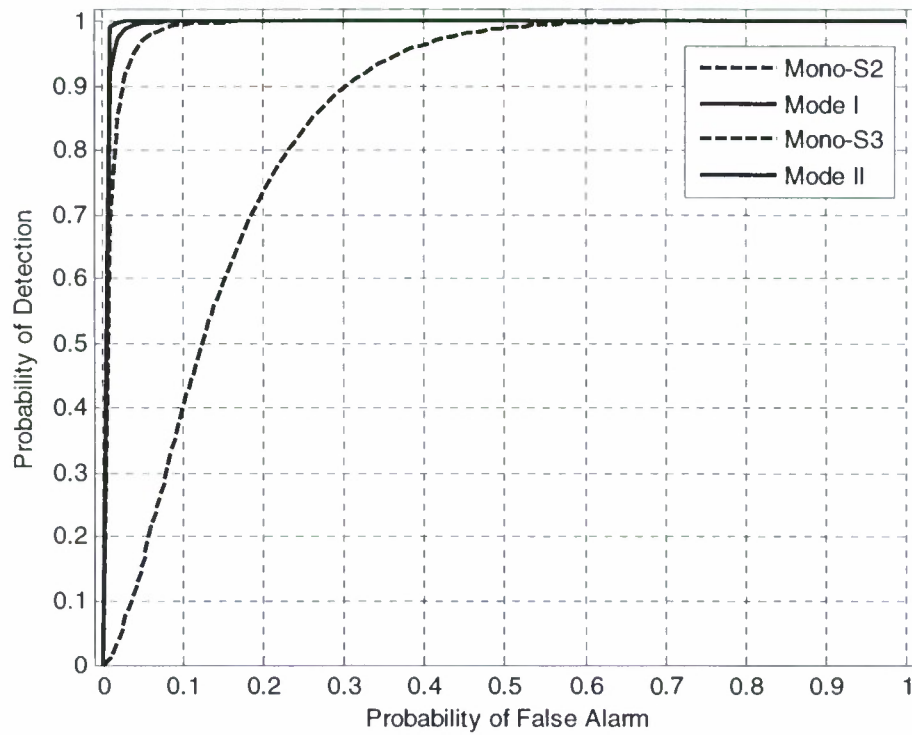


**Fig. 6** ROC curves corresponding to the optimal waveforms for the wooden table for multistatic and monostatic operation under sensor functionality modes I and II.

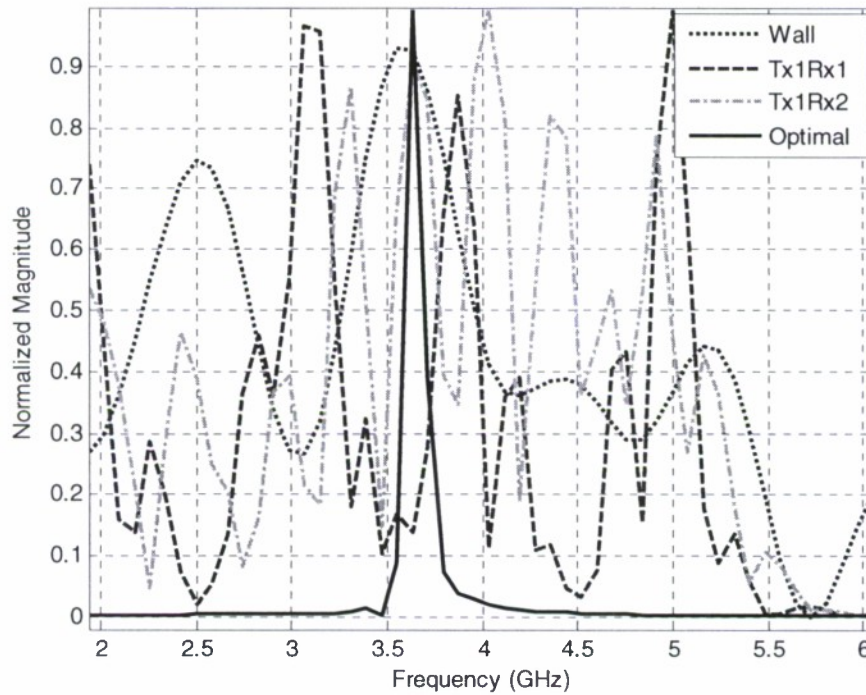


**Fig. 7** Normalized Magnitude Spectra of the two-way wall response, target impulse responses apparent to the receivers with transmitter 1 active, and the optimal waveform for transmitter 1, for sensor operational Mode I.

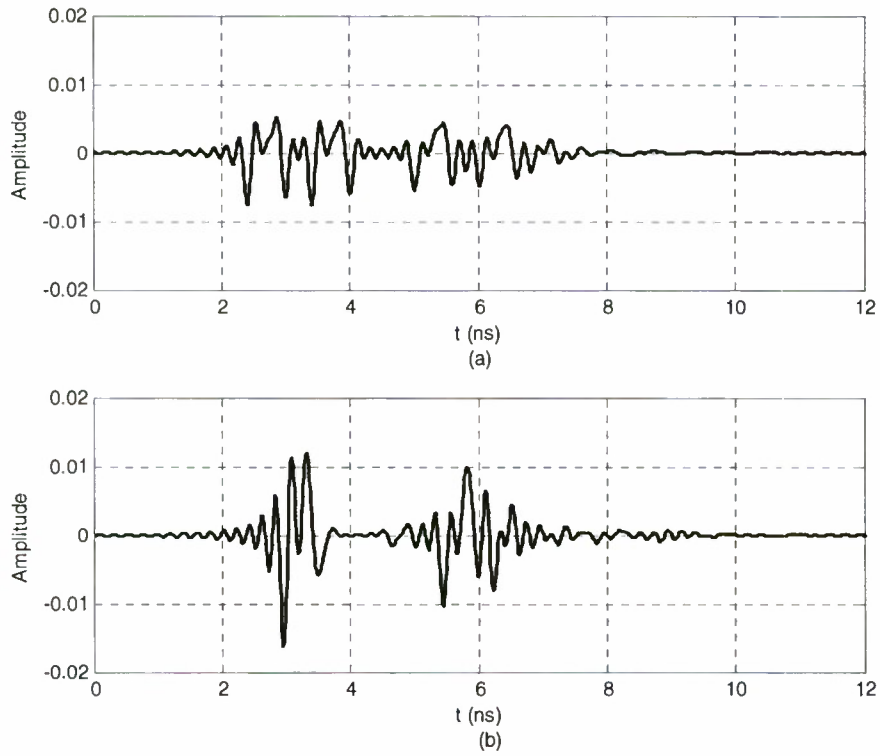


**Fig. 8** Target impulse response corresponding to (a) Transmitter 1/Receiver 1 (b) Transmitter 1/Receiver 2, for Mode I.

**Table III.** SCNR at the output of the matched filter for the human.

Target	Functional Mode	Waveform	SCNR (dB)	
			Monostatic Operation	Multistatic Operation
Standing Human	I	Optimal	-4.1907	1.0279
		Chirp	-14.8916	-10.6437
	II	Optimal	-7.7216	0.7260
		Chirp	-14.8094	-10.6277

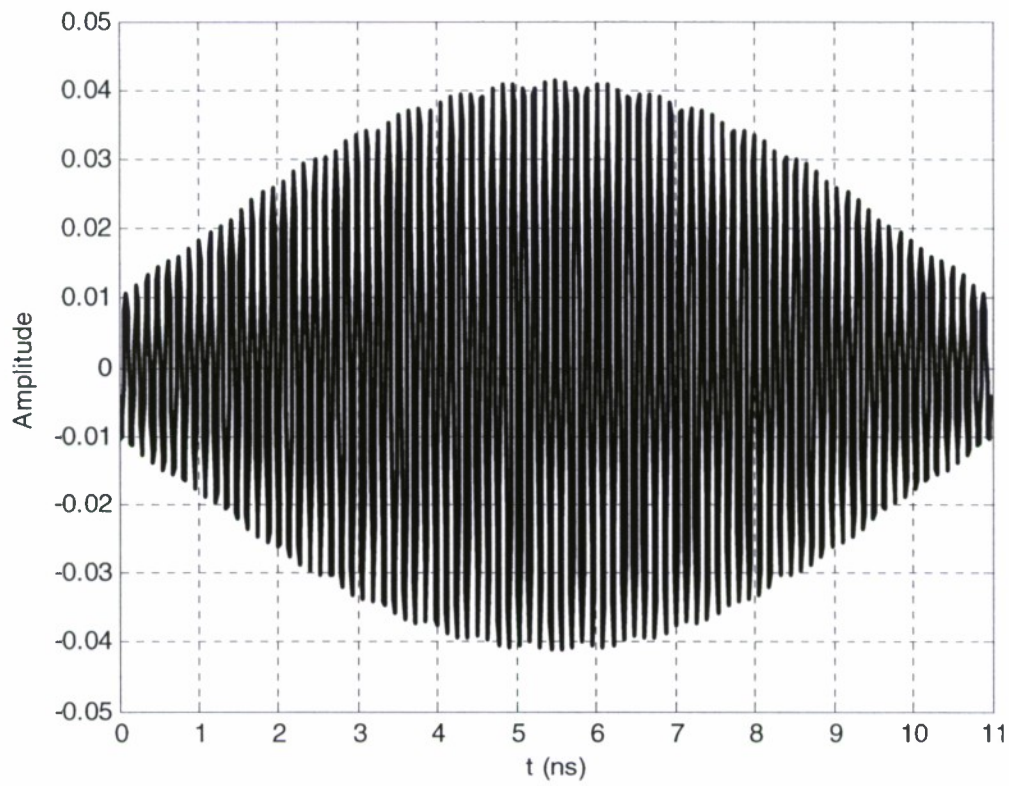


**Fig. 9** Optimal Waveform for Transmitter 1 in Mode I for no-clutter case. The standing human was used as the target.

**Table IV.** Multistatic SCNR at the output of the matched filter for the human in the presence of clutter and noise.

Target	Waveform	Multistatic SCNR (dB)	
		CNR= -10 dB	CNR=10 dB
Standing Human	Optimal – Clutter and Noise	-24.9107	-42.7754
	Optimal – Noise only	-25.9141	-43.2472
	Chirp	-29.6381	-42.1243



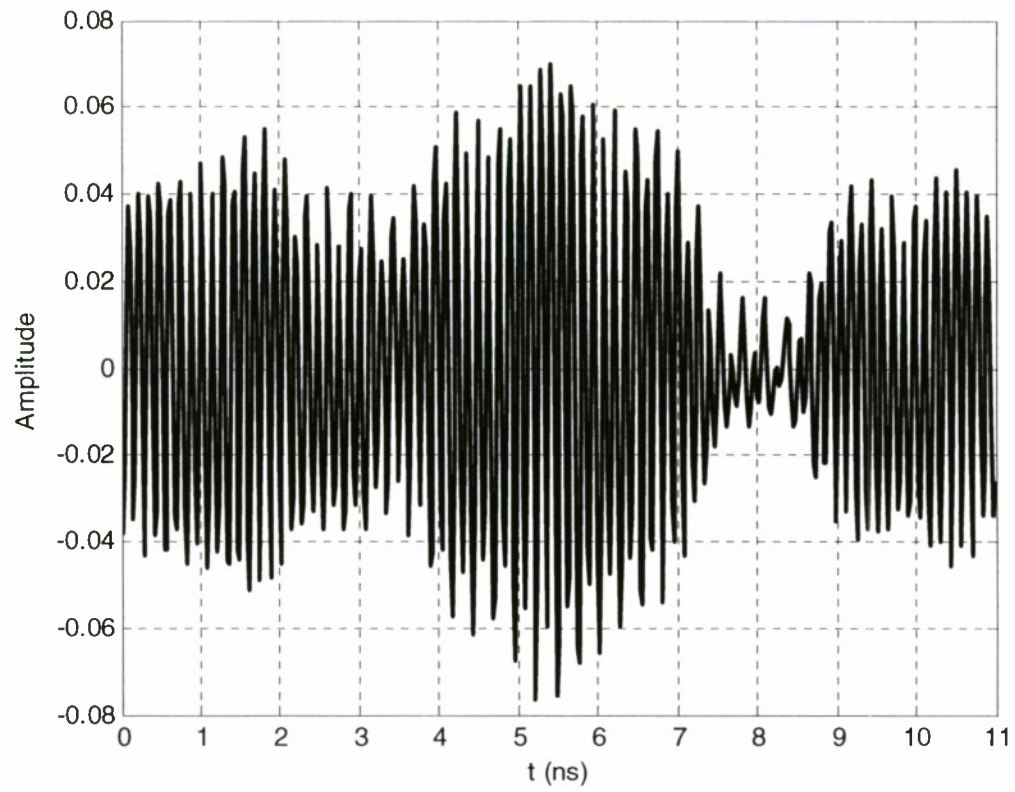


**Fig. 10** Optimal Waveform for Transmitter 1 in Mode I for non-zero clutter and noise. The standing human was used as the target.

## 5. High-Resolution Through-the-Wall Radar Imaging Using Beamspace MUSIC

### *Abstract*

The MUSIC algorithm is a high-resolution direction finding technique which has been successfully applied to enhance radar imaging in inverse synthetic aperture radar (ISAR). Although this signal subspace-based method has proven effective when dealing with point targets and high SNR, it may fail to work when directly applied to extended targets or target returns of low SNR. The Beamspace MUSIC (BS-MUSIC), in which the MUSIC algorithm is applied to multiple beams is capable of locating spatially extended targets in low SNR environments. We propose BS-MUSIC as an image formation method for indoor radar imaging problems and sensing through-the-wall applications. We compare BS-MUSIC performance to conventional beamforming and element-space MUSIC. Imaging results with both synthesized and real data demonstrate the advantages of the proposed algorithm in depicting targets behind walls.

## 5.1 Introduction

High resolution radar imaging has recently gained much attention, as its military and civilian application areas are broadening to include new challenges in urban sensing and homeland security. One application that has traditionally made use of high resolution radar imaging is the inverse synthetic aperture radar (ISAR) [1-2]. In ISAR, point targets are detected and located by examining the phase information induced from changes in the distance between the targets and the antenna. When targets are approximated by points in space, the two-dimensional spatial spectrum of the scene embeds sufficient information to uniquely determine the targets' location. As such, high-resolution spectrum estimation methods such as MUSIC [3], Capon [4], and ESPRIT [5] can be used as high-resolution image formation techniques [2, 6-8].

Most recently, "seeing" through obstacles such as walls, doors, and other visually opaque materials, using microwave signals has become a powerful tool for a variety of emerging applications in both military and commercial paradigms. Through-the-wall imaging (TWI) has been recently sought out in behind-the-wall target detection, surveillance and reconnaissance [9]. In addition to surveillance of adversaries, and detection and monitoring of suspected criminals and outlaws, TWI technology is used in rescue missions to search for earthquake and avalanche victims, and can also aid fire fighters searching for survivors. In comparison to ISAR application, through-the-wall radar imaging faces the challenges of counteracting the impairing effects of unknown multiple wall characteristics, and to deal with small enclosed scenes with a large variety of indoor targets. These targets may occupy several range and cross-range cells or may be confined to a single resolution cell. Similar to ISAR, the two-dimensional spatial spectrum of the scene using collected TWI data can be generated and signal subspace methods can be directly employed for resolution enhancement [10-11].

We apply the MUSIC algorithm to the outputs of spatial beams, rather than to raw sensor data. The latter is referred to as element-space MUSIC (ES-MUSIC). Although different in some ways from conventional one-dimensional beamspace MUSIC, we will refer to the proposed method as beamspace MUSIC (BS-MUSIC), so as to distinguish it from the ES-MUSIC. In the underlying indoor radar imaging

application, beamspace processing has three main advantages over element-space processing. First, BS-MUSIC outperforms ES-MUSIC in low signal-to-noise ratio (SNR) cases due to the processing gain offered by beamforming. The beamforming gain is equal to the number of sensors when a single narrow-band signal is used. This gain is important in view of significant signal power attenuations that can be caused by exterior as well as interior walls. Second, the ES-MUSIC relies on the basic assumption of point targets [1]. Extended targets violate the point-target assumption and cannot be properly processed, and furthermore, their presence prevents the ES-MUSIC from locating even point targets. With no assumptions on target characteristics, in terms of type and size, the BS-MUSIC is considered attractive since it can image both point targets and extended targets simultaneously. This capability is essential for indoor imaging where, due to small standoff distance and limited bandwidth and aperture, many targets behind walls classify as spatially extended targets. Third, the ES-MUSIC requires two dimensional interpolation to provide sampled data along a rectangular grid. In BS-MUSIC, the data sampled along a rectangular grid is obtained by beamforming, rather than interpolation. Avoiding interpolation is a welcomed step, given the fact that a single outlier in the data set can even result in large interpolation errors. It is noted that rectangular grid sampling in both algorithms is required to permit covariance matrix estimation from one set of measurements.

We examine in this write-up the BS-MUSIC performance with real data as well as synthesized data. The real data is collected by the series of experiments carried out in the Radar Imaging Lab at the Center for Advanced Communications, Villanova University. The test results show that the BS-MUSIC provides better imaging quality compared to the ES-MUSIC and conventional beamforming.

## 5.2 High-Resolution Imaging

### 5.2.1 Signal Modeling

A narrowband signal with frequency  $f_0$  transmitted and received at an antenna located at  $(x_a, y_a)$  can be modeled as,

$$z(f_0) = \sum_{p=0}^{P-1} \sigma_p \exp\{-j4\pi f_0 r_p / c\} \quad (1)$$

where  $\sigma_p$  is the reflection coefficient of the  $p$ -th target, or the target cross-section,  $c$  is the propagation speed,  $P$  is the number of targets in the scene, and  $r_p$  is the range from the antenna to the  $p$ -th target such that

$$r_p = \sqrt{(x_p - x_a)^2 + (y_p - y_a)^2}, \quad (2)$$

where  $(x_p, y_p)$  is the location of the  $p$ -th target. All targets assume fixed positions over the imaging interval. This interval includes data acquisition time over all frequencies, and in the case of synthetic aperture system, accounts for the time to move the antenna from one position to another. In equation (2), the range  $2r_p$  implies that both transmit antenna and receive antenna are located at the same position (monostatic radar). In order to obtain a high range resolution image, a wideband signal must be used. Suppose that  $S(f)$  is the Fourier transform of the wideband signal. Then,

$$s(t) = \int_{-\infty}^{\infty} S(f) \exp\{j2\pi ft\} df. \quad (3)$$

A stepped-frequency signal is an approximation of a wideband signal with finite number of narrowband signals whose center frequencies are uniformly spaced within the signal bandwidth. The stepped-frequency implementation of high resolution imaging is considered attractive due to its hardware simplicity, function reliability, and ability to control the signal power at different frequencies for counteracting wall signal dispersion [12]. Using  $N_f$  frequencies, the stepped-frequency signal is given by,

$$\hat{s}(t) = \sum_{m=0}^{N_f} S(f_m) \exp\{j2\pi f_m t\}, \quad (4)$$

with



$$\begin{aligned} f_m &= f_L + m\Delta f, \\ \Delta f &= \frac{f_H - f_0}{N_f - 1}, \end{aligned} \quad (5)$$

where the frequency band is bounded by  $f_L$  and  $f_H$ . In a monostatic radar system with  $N_a$  antennas, the received spatio-temporal signal assumes the two-dimensional form,

$$z(m, n) = \sum_{p=0}^{P-1} \sigma_p \exp\{-j4\pi f_m r_{p,n} / c\}. \quad (6)$$

In the above equation, the frequency index is  $m = 0, \dots, N_f - 1$  and the spatial index,  $r_{p,n}$ , is the distance between the  $p$ -th target and the  $n$ -th antenna for  $n = 0, \dots, N_a - 1$ .

For long standoff distances where the center of the scene is far from each antenna in the imaging system,  $r_{p,n}$  can be approximated by,

$$r_{p,n} = r_n + x'_p \cos \theta_n - y'_p \sin \theta_n \quad (7)$$

where  $r_n$  is the range from the  $n$ -th antenna to the center of the scene  $(x_c, y_c)$ ,  $(x'_p, y'_p)$  is the position of the  $p$ -th target in  $x' - y'$  plane. The center of the scene is at  $(0,0)$ , and  $\theta_n$  is the looking angle of the  $n$ -th antenna (see Fig.1). Accordingly, the range  $r_n$  assumes a fixed value, independent of target's location. We note that  $r_n$  can be easily determined if the scene represents an interior of an enclosed structure, such as a room or a building, whose dimensions are known from using ground-based monitoring or surveillance system. Aerial mapping, such as UAV, can also provide accurate 2-D extent of the structure and its center. If the phase term due to  $r_n$  is compensated for in each antenna, then equation (6) becomes,

$$z(m, n) = \sum_{p=0}^{P-1} \sigma_p \exp\{-j4\pi f_m (x'_p \cos \theta_n - y'_p \sin \theta_n) / c\}. \quad (8)$$

The above expression is exactly the same as the ISAR signal model [2]. Let  $Z(k_x, k_y)$  be the 2-D spatial spectrum,

$$Z(k_x, k_y) = \sum_{p=0}^{P-1} \sigma_p \exp\left\{-j\frac{4\pi}{c}(k_x x'_p - k_y y'_p)\right\}. \quad (9)$$

Then, equation (8) can be viewed as a sampled version of equation (9), i.e.,

$$z(m,n) = Z(k_x, k_y) \big|_{k_x = f_m \cos \theta_n, k_y = f_m \sin \theta_n} \quad (10)$$

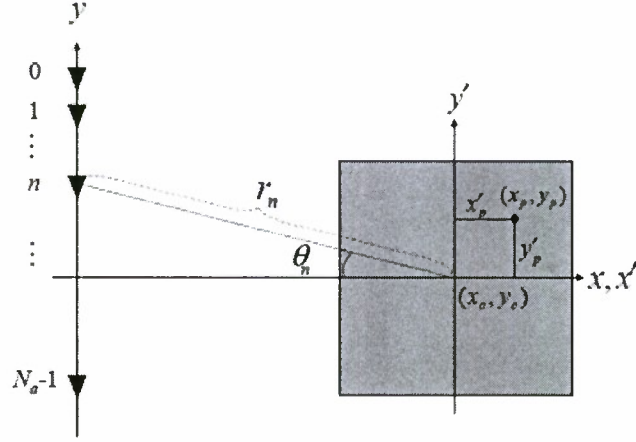


**Fig. 1** Geometry of the scene and the antennas. The  $x$ - $y$  plane represents global locations whereas the  $x'$ - $y'$  plane represents a scene with center at  $(0,0)$ .

### 5.2.2 MUSIC Based Imaging

Estimating the covariance matrix is necessary for performing the MUSIC algorithm. The eigen decomposition of the covariance matrix yields both the signal subspace and the noise subspace. The latter is used to define the projection operation for constructing the MUSIC spectrum, in which peak positions represent an estimate of target locations. In temporal processing, estimating the covariance matrix is achieved by time-averaging of the instantaneous correlation values. The main challenge in radar image applications is that correlation averaging is not applicable, as only a single snapshot (data set) is available. However, it is possible to estimate the covariance matrix from virtual snapshots generated from the data set [2, 6]. In order to obtain the virtual snapshots, the data in (10) should be uniformly sampled, which can be achieved through 2-D interpolation. Linear, polynomial, or spline interpolation methods can be applied. For simplicity, we used linear interpolation in the simulations in Section 5.4.

Let  $\hat{z}(m,n)$  be the uniformly sampled version of (10) for  $m = 0, \dots, M-1$  and  $n = 0, \dots, N-1$ . That is,

$$\hat{z}(m, n) = \sum_{p=0}^{P-1} \sigma_p \exp \left\{ -j \frac{4\pi}{c} (k_m x_p' - k_n y_p') \right\}. \quad (11)$$

where the sampled spatial frequencies are

$$k_m = k_{x,0} + m\Delta k_x, \quad (12)$$

$$k_n = k_{y,0} + n\Delta k_y. \quad (13)$$

The frequency steps  $\Delta k_x$  and  $\Delta k_y$  in equations (12) and (13) represent the interpolation intervals. Note that the spatial frequencies  $k_m$  and  $k_n$  are bounded by

$$\begin{aligned} f_0 \leq k_m \leq f_{N_f-1} \\ f_0 \sin \theta_0 \leq k_n \leq f_0 \sin \theta_{N_a-1}. \end{aligned} \quad (14)$$

In order to avoid aliasing, the following inequality should hold.

$$-1/2 < (M-1)\Delta k_x, (N-1)\Delta k_y < 1/2. \quad (15)$$

Define  $\mathbf{Z}$  as an  $M \times N$  matrix whose  $mn$ -th element is  $\hat{z}(m, n)$ . Let  $\mathbf{F}_{i,j}$  be the  $K \times L$  sub-matrix of  $\mathbf{Z}$  such that

$$\mathbf{F}_{i,j} = \begin{bmatrix} z_{i,j} & z_{i,j+1} & \cdots & z_{i,j+L-1} \\ z_{i+1,j} & z_{i+1,j+1} & \cdots & z_{i+1,j+L-1} \\ \vdots & \vdots & \ddots & \vdots \\ z_{i+K-1,j} & z_{i+K-1,j+1} & \cdots & z_{i+K-1,j+L-1} \end{bmatrix}$$

where  $z_{i,j}$  is the  $ij$ th element of the matrix  $\mathbf{Z}$ . Then, the *virtual snapshots*  $\mathbf{z}_i$  is defined as

$$\mathbf{z}_i = \text{vec}\{\mathbf{F}_{i,i}\} \quad (16)$$

where

$$\text{vec}\{[\mathbf{v}_1 \cdots \mathbf{v}_N]\} = [\mathbf{v}_1^H \cdots \mathbf{v}_N^H]^H. \quad (17)$$

Let  $\mathbf{u}_i(x_p', y_p')$  be the  $i$ -th *virtual snapshots* when a point target is located at  $(x_p', y_p')$ . Then,

$$\begin{aligned}
\mathbf{z}_i &= \sum_{p=0}^{P-1} \mathbf{u}_i(x'_p, y'_p) \\
&= \sum_{p=0}^{P-1} \exp\{-ji(\Delta k_x x'_p + \Delta k_y y'_p)\} \mathbf{u}_0(x'_p, y'_p)
\end{aligned} \tag{18}$$

which shows only a constant phase difference for each target between consecutive snapshots.

The covariance matrix estimate is provided by averaging the outer products,

$$\hat{\mathbf{R}} = \frac{1}{N_s} \sum_{i=0}^{N_s-1} \mathbf{z}_i \mathbf{z}_i^H, \tag{19}$$

where  $N_s = \min\{M - K + 1, N - L + 1\}$  is the number of virtual snapshots. Processing of the *virtual* snapshots according to (19) amounts to subarray and subband averaging, which utilizes the phase difference to restore the rank of the covariance matrix in coherent environments [6]. If forward-backward smoothing is used, the covariance matrix estimate becomes [6]

$$\hat{\mathbf{R}} = \frac{1}{2N_s} \sum_{i=0}^{N_s-1} (\mathbf{z}_i \mathbf{z}_i^H + \mathbf{J} \mathbf{z}_i^* \mathbf{z}_i^T \mathbf{J}), \tag{20}$$

where  $(\ )^*$  and  $(\ )^T$  denote complex conjugate and transpose, respectively, and  $\mathbf{J}$  is the exchange matrix, such as

$$\mathbf{J} = \begin{bmatrix} 0 & \cdots & 0 & 1 \\ 0 & \cdots & 1 & 0 \\ \vdots & \ddots & \vdots & \vdots \\ 1 & 0 & \cdots & 0 \end{bmatrix}$$

Rather than using diagonal sub-matrices, as implied by equation (20), it is possible to use all sub-matrices of  $\mathbf{Z}$  [13]. In this case,

$$\hat{\mathbf{R}}_{new} = \frac{1}{2(M - K + 1)(N - L + 1)} \sum_{i=0}^{M-K-L} \sum_{j=0}^{M-K-L} (\mathbf{z}_{i,j} \mathbf{z}_{i,j}^H + \mathbf{J} \mathbf{z}_{i,j}^* \mathbf{z}_{i,j}^T \mathbf{J}) \tag{21}$$

where  $\mathbf{z}_{i,j} = \text{vec}\{\mathbf{F}_{i,j}\}$ . Although there are some cases where the covariance matrix estimate in (21) is invalid, those cases are unlikely to occur in the applications where the number of targets  $P$  are typically much smaller than  $M$  and  $N$ . The sufficient condition for the covariance matrix estimate,  $\hat{\mathbf{R}}_{new}$ , to be

valid is  $L > p_x$  and  $K > p_y$  where  $p_x$  and  $p_y$  are the maximum multiplicity of the target position along x-axis and y-axis, respectively [14]. Multiplicity denotes the number of targets that have the same position along one axis. For example, if there are three targets that have the same x position, the multiplicity along x-axis becomes three.

The MUSIC algorithm based on the covariance matrix estimate in (21) has, in general, better performance than that associated with the estimate in (20). This is because the errors in the perturbation errors of the matrix elements are inversely proportional to the number of samples [15]. The latter is much larger in (21) than in (20). For example, for  $M = N = 2K = 2L$ , the number of snapshots associated with equation (20) is  $2(K+1)$  whereas the corresponding number in (21) is  $2(K+1)^2$ .

The MUSIC estimator of target locations relies on the eigendecomposition of the covariance matrix estimate and is given by,

$$I(x, y) = \frac{\mathbf{a}^H(x, y)\mathbf{a}(x, y)}{\mathbf{a}^H(x, y)\mathbf{W}\mathbf{W}^H\mathbf{a}(x, y)} \quad (22)$$

where the *virtual* array response vector  $\mathbf{a}(x, y)$  is of length  $KL$  and given by,

$$\begin{aligned} \mathbf{a}(x, y) &= \begin{bmatrix} 1 & \alpha & \cdots & \alpha^{K-1} & \beta & \alpha\beta & \cdots & \alpha^{K-1}\beta \\ & & & & \beta^2 & \alpha\beta^2 & \cdots & \alpha^{K-1}\beta^{L-1} \end{bmatrix} \\ \alpha &= \exp\{-j\frac{4\pi}{c}\Delta k_x x\} \\ \beta &= \exp\{j\frac{4\pi}{c}\Delta k_y y\} \end{aligned} \quad (23)$$

The matrix  $\mathbf{W}$  in equation (22) is the noise subspace,

$$\mathbf{W} = [\mathbf{u}_D \quad \mathbf{u}_{D+1} \quad \cdots \quad \mathbf{u}_{KL-1}] \quad (24)$$

where  $\mathbf{u}_0, \mathbf{u}_1, \dots, \mathbf{u}_{KL-1}$  are the ordered eigenvectors of  $\hat{\mathbf{R}}_{new}$  arranged from the largest corresponding eigenvalues to the smallest. The product  $\mathbf{W}\mathbf{W}^H$  is the projection operator that projects the array response vector onto the noise subspace.



### 5.2.3 Through-the-Wall Radar Data

In through-the-wall radar, the antennas are not typically placed against the wall, but rather at a standoff distance. This is mainly due safety and logistic operation reasons. In this case, and for a single wall, the signal travels, on transmission, in the air, through the wall, and then in the air, again. It propagates with the same order when traveling from the target back to the receiver. The signal propagation in the wall is different from that in the air [16]. Consider a homogeneous wall with known dielectric constant  $\epsilon$ . The signal path from the antenna to a position through the wall is shown in Fig. 2. Instead of following a straight-line direct path from the antenna to the target when no wall is present, the signal now propagates along  $g_1$ ,  $g_2$ , and  $g_3$ . From Snell's law, the angle  $\phi_i$  is

$$\phi_n = \sin^{-1} \left( \frac{\sin \theta'_n}{\sqrt{\epsilon}} \right). \quad (25)$$

If the targets are behind a wall, the angle  $\theta_n$  as well as the range to the center  $r_n$  in equation (7) should be replaced by  $\theta'_n$  and  $r'_n$  such as,

$$r'_n = g_1 + g_2 + g_3. \quad (26)$$

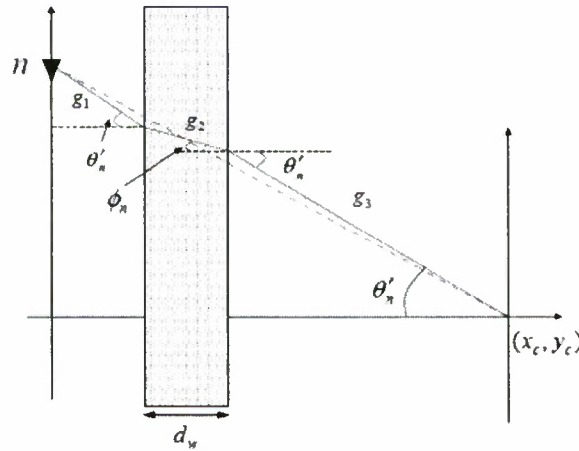


**Fig. 2** Geometry of through-the-wall radar. The dotted line represents direct path from the antenna to the center of the scene. However, signal travels through the solid line.

The parameters  $g_i$ ,  $i = 1, 2, 3$  and  $\theta'_n$  can be calculated from the following equations [17]

$$g_1 = -y_n^{(a)} / \cos \theta_n', \quad (27)$$

$$(x_c - (x_n^{(a)} - y_n^{(a)} \tan \theta_n'))^2 + y_c^2 = g_2^2 + g_3^2 - 2g_3g_2 \cos(\pi + \varphi_n - \theta_n'),$$

where  $(x_n^{(a)}, y_n^{(a)})$  is the position of the  $n$ -th antenna. The above equations can be solved numerically by the Newton method with reasonable initial values. Once  $r_n'$  is obtained for all  $n$ , the phase term can be compensated, resulting in equation (7) with  $\theta_n'$  in place of  $\theta_n$ . Extension of equation (27) can be developed in the case where the target is behind multiple walls.

### 5.3 Beamspace MUSIC for Imaging

#### 5.3.1 Beamspace

As stated in the previous section, the MUSIC algorithm can be applied upon generating the 2-D uniformly sampled spatial spectrum. An alternative to data interpolation can be provided through the use of beamforming. Consider the 2-D delay-and-sum (DS) spatial beams,

$$b(x, y) = \frac{1}{N_f N_s} \sum_{m=0}^{N_f-1} \sum_{n=0}^{N_s-1} w(m, n) z(m, n) \exp\{j4\pi f_m R_n / c\} \quad (28)$$

where  $R_n$  is the range between the  $n$ -th antenna and the beamforming point  $(x, y)$ , and  $w(m, n)$  is an optional window that can be used to shape the point spread function in terms of mainlobe and sidelobe characteristics. If a wall is present between targets and antennas, the range  $R_n$  should be calculated through equations (27-28). The beams, corresponding to uniformly spaced points along the x-axis and y-axis, produce a 2-D image that is same as the one produced by the backprojection method [18]. The  $M \times N$  equally spaced beams are constructed for  $x_l = X_0 + l\Delta x$  and  $y_k = Y_0 + k\Delta y$ , where  $\Delta x$  and  $\Delta y$  are the distances between beams along x-axis and y-axis, respectively. We can express the beams using simpler notations as,

$$b(l, k) := b(x_l, y_k) \quad (29)$$

for  $l = 0, \dots, M-1$  and  $k = 0, \dots, N-1$ . The two-dimensional discrete Fourier transform (DFT) of  $b(l, k)$  is,

$$\begin{aligned} B(m, n) &= \frac{1}{MN} \sum_{l=0}^{M-1} \sum_{k=0}^{N-1} b(l, k) \exp\{-j(mlk_x + nkk_y)\} \\ &= \frac{1}{MN} \sum_{p=0}^{P-1} b(l_p, k_p) \exp\{-j(ml_p k_x + nk_p k_y)\} \end{aligned} \quad (30)$$

for  $m = 0, \dots, M-1$  and  $n = 0, \dots, N-1$ . In the above equation,  $k_x = 2\pi / M$ ,  $k_y = 2\pi / N$ , and  $(l_p, k_p)$  is the pixel index of the  $p$ -th target. Note that  $b(l, k) = 0$  when there is no target at  $(l, k)$ . Since (30) has the same structure as (11), we can proceed with the MUSIC estimator, without the need for performing interpolations. In this case, the sub-matrix  $\mathbf{F}_{i,j}$  is redefined as

$$\mathbf{F}_{i,j} = \begin{bmatrix} B(i, j) & B(i, j+1) & \cdots & B(i, j+L-1) \\ B(i+1, j) & B(i+1, j+1) & \cdots & B(i+1, j+L-1) \\ \vdots & \vdots & \ddots & \vdots \\ B(i+K-1, j) & B(i+K-1, j+1) & \cdots & B(i+K-1, j+L-1) \end{bmatrix}$$

and the covariance matrix follows the same process described in Section 5.2.2.

### 5.3.2 Advantages

Although the BS-MUSIC requires additional computations due to DS beamforming, it has key advantages over the ES-MUSIC. First, it is robust to low SNR. The ES-MUSIC uses 2-D spectrum which is an interpolated data set  $\hat{z}(m, n)$  of the received signal. Since it employs raw data, the target returns will be highly corrupted by noise at low SNR, resulting in a compromised quality image. In contrast, the BS-MUSIC enjoys the processing gain of the beamforming. It is noted that the beamforming gain is up to  $N_x N_f$  when a target's location matches the beamforming point [19]. Second, the BS-MUSIC does not put any demands on target characteristics. The ES-MUSIC high-resolution image formation process begins with a very important assumption of point targets. Under this assumption, the signal model of (1) becomes valid. However, in practice, both extended targets and point targets could be present in the same

scene. For instance, interior walls, closets, bookshelves, large and small file cabinets, and tables of different sizes are typically encountered in through-the-wall radar imaging [20].

Consider an extended target located at  $(x_e, y_e)$ . The width and length of the target are denoted as  $d_x$  and  $d_y$ , respectively. Assume that the reflection coefficient  $\sigma$  is constant over the target 2-D extent. Then, the received signal becomes

$$\begin{aligned}
 z_{ext}(m, n) &= \sigma \int_{-d_x/2}^{d_x/2} \exp\left\{ \frac{4\pi f_m}{c} \cos \theta_n (x_e + x) \right\} dx \\
 &\quad \cdot \int_{-d_y/2}^{d_y/2} \exp\left\{ -\frac{4\pi f_m}{c} \sin \theta_n (y_e + y) \right\} dy \\
 &= \text{sinc}\left(\frac{2\pi f_m \cos \theta_n d_x}{c}\right) \text{sinc}\left(\frac{2\pi f_m \sin \theta_n d_y}{c}\right) \\
 &\quad \cdot \sigma 4d_x d_y \exp\left\{ -j \frac{4\pi f_m}{c} (x_e \cos \theta_n - y_e \sin \theta_n) \right\}
 \end{aligned} \tag{31}$$

where  $\text{sinc}(\cdot)$  is the Sinc function given by,

$$\text{sinc}(x) = \frac{\sin x}{x}.$$

The two multiplicative Sinc terms in (31), due to non-zero  $d_x$  and  $d_y$ , make the noise-free *virtual* snapshots  $\mathbf{z}_{i,j}$  independent of each other. The uniformly sampled version of  $z_{ext}(m, n)$  takes the form,

$$\begin{aligned}
 \hat{z}_{ext}(m, n) &= \text{sinc}\left(\frac{2\pi k_m d_x}{c}\right) \text{sinc}\left(\frac{2\pi k_n d_y}{c}\right) \\
 &\quad \cdot \sigma 4d_x d_y \exp\left\{ -j \frac{4\pi}{c} (k_m x_e - k_n y_e) \right\}.
 \end{aligned} \tag{32}$$

Let

$$u(m, n) = \text{sinc}\left(\frac{2\pi k_m d_x}{c}\right) \text{sinc}\left(\frac{2\pi k_n d_y}{c}\right). \tag{33}$$

Then,

$$\hat{z}_{ext}(m, n) = \sigma 4d_x d_y u(m, n) \exp\left\{ -j \frac{4\pi}{c} (k_m x_e - k_n y_e) \right\}. \tag{34}$$

Note that  $\hat{z}_{ext}(m, n) = \hat{z}(m, n)$  when  $d_x = d_y = 0$ . In order for the MUSIC estimator to work, the noise-free *virtual* snapshots should lie in the signal subspace and be similar in structure to the array manifold vector  $\mathbf{a}(x, y)$  in equation (23). However, in the underlying case,

$$\mathbf{z}_{i,j} = \mathbf{U}(i, j)\mathbf{a}(x_e, y_e), \quad (35)$$

where  $\mathbf{U}(i, j)$  is a  $KL \times KL$  diagonal matrix such that,

$$\text{diag}\{\mathbf{U}(i, j)\} = [u(i, j) u(i+1, j) \dots u(i+K-1, j+L-1)]^T \quad (36)$$

The values of  $u(i, j)$  are not given, as they are determined by the target unknown spatial extent. Furthermore, the *virtual* snapshots for the same target are different since the elements of  $\mathbf{U}(i, j)$  vary depending on the index  $i$  and  $j$ . This difference is more than just a phase change. This means that the *virtual* snapshots are all independent (or dissimilar), and subsequently, the rank of the noise-free covariance matrix estimate will exceed the number of targets. Accordingly, applying MUSIC estimator with the array manifold vector  $\mathbf{a}(x, y)$  fails and becomes inappropriate for extended targets.

For the BS-MUSIC, we consider the beam  $b(l, k)$  to be within the extended target. Then,

$$b(l, k) = \sigma \int_{-b_x/2}^{b_x/2} \int_{-b_y/2}^{b_y/2} f(x', y') dx' dy', \quad (37)$$

where  $f(x, y)$  represents the beam pattern of the beamformer, and  $b_x$  and  $b_y$  are the beamwidth along x-axis and y-axis, respectively. Suppose that an extended target encompasses the beams  $b(l_0 - m_0, k_0 - n_0), b(l_0 - m_0 + 1, k_0 - n_0), \dots, b(l_0 + m_0, k_0 + n_0)$ , as shown in Fig. 3. Note that the center location is now indexed as  $(l_0, k_0)$  and the size is  $2m_0 \times 2n_0$ . The corresponding 2-D discrete Fourier transform of the beamspace is,

$$B(m, n) = \sum_{l=l_0-m_0}^{l_0+m_0} \sum_{k=k_0-n_0}^{k_0+n_0} b(l, k) \exp\{-j(mk_x l + nk_y k)\}. \quad (38)$$

If  $b(l, k)$  is constant, the above equation becomes,



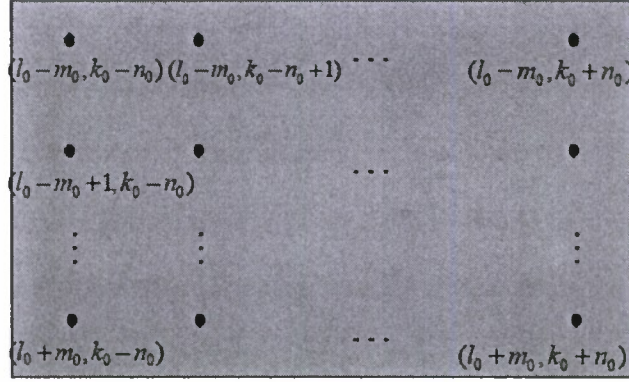


Fig. 3 Extended targets in BS-MUSIC.

$$\begin{aligned}
 B(m, n) &= b(l_0, k_0) \exp\{-j(mk_x l_0 - nk_y k_0)\} \\
 &\cdot \sum_{l=1}^{m_0} \sin\{mk_x(l_0 + l)\} \\
 &\cdot \sum_{k=1}^{n_0} \sin\{nk_y(k_0 + k)\},
 \end{aligned} \tag{39}$$

which has the same shortcoming as equation (34). However, the beampattern of an array  $f(x, y)$  changes, depending on the beamforming point. We note that the beamwidth varies as a function of standoff distance and the imaging point relative to the boresight direction. Therefore, if we redefine  $b(l, k)$  as,

$$b(l, k) = \sigma \iint f(x, y; l, k) dx dy, \tag{40}$$

then,

$$b(l, k) \neq b(l', k'), \tag{41}$$

for  $k \neq k'$  or  $l \neq l'$ . Therefore, the 2-D spectrum of beamspace remains as

$$B(m, n) = \sum_{l=l_0-m_0}^{l_0+m_0} \sum_{k=k_0-n_0}^{k_0+n_0} b(l, k) \exp\{-j(mk_x l + nk_y k)\}.$$

The above equation has the same structure as equation (30), since the phase terms from the targets do not collapse into the Sinc term. The extended target, in essence, is viewed as an aggregate of consecutive point targets, allowing the MUSIC estimator to function properly.

### 5.3.3 Forming Beamspace

#### 5.3.3.1 Number of Beams

It is assumed that all antennas of the imaging system have identical characteristics. The beamforming positions can be located anywhere within the antenna radiation pattern. Accordingly, the number of beams can be chosen arbitrary. However, since the beams must be uniformly spaced for DFT implementations, the number of beams is decided based on beam spacing. The resolution offered by the imaging array through the corresponding DS beamformer presents a good basis to form the different beam orientations. In order to ensure that all targets in the scene are illuminated, the beams should be separated by less than a beamwidth, which also defines target resolution. Target resolution includes the down-range resolution and the cross-range resolution. The down-range is the range perpendicular to the array plane, whereas the cross-range is parallel to the array plane. The down-range resolution of the DS beamformer is given by

$$\delta_r = \frac{c}{2B}, \quad (42)$$

where  $B$  is the signal bandwidth. The cross-range resolution is

$$\delta_a = \frac{r\lambda}{2L} \quad (43)$$

where  $r$  is the down-range,  $\lambda$  is the signal wavelength, and  $L$  is the array length [17]. If the beam spacing is chosen as the beamwidth, the targets positioned close to or at the middle of two consecutive beams will be illuminated with small SNR. Therefore, it would be better if the beams are formed more densely. In the simulations, we used half the cross-range resolution (one fourth of the beamwidth) as the beam separation (spacing).

### 5.3.3.2 Covariance Matrix Estimation

When the distance between beams are less than the beamwidth, the presence of a point target will be reflected in several consecutive beams, leading to broadening of the target extent and representation in the beamspace. In this case, the spatial frequency bandwidth of the target is reduced by the fixed time-bandwidth product. Consequently, the 2-D spectrum of the target has a narrowband-like representation. Therefore, only part of the DFT of the beams should be included in covariance matrix estimation. Let  $\tau_x$  be the beamwidth of the DS beamformer and  $\Delta t_x$  be the space between beams, both along the x-axis. Suppose that both parameters have the following relation.

$$\Delta t_x = \tau_x / q. \quad (44)$$

Then, the support of beams (spatial frequency bandwidth) will be  $1/(q\Delta t_x)$  and the number of rows of 2-D spectrum that can be used in the covariance matrix estimation is

$$M_{eff} = \min\{M, \lfloor M / q \rfloor\}, \quad (45)$$

where  $\lfloor \cdot \rfloor$  represents the maximum integer that does not exceed the number. By the same argument, when  $\Delta t_y = \tau_y / p$ , the number of columns that include spectrum of the point target is

$$N_{eff} = \min\{N, \lfloor N / p \rfloor\}, \quad (46)$$

where  $\tau_x$  and  $\Delta t_x$  are the beamwidth of the DS beamformer and beam spacing, respectively, both along the y-axis.

When  $q$  and  $p$  are larger than 1, implying that the distance between beams is smaller than the beamwidth, we can use only  $M_{eff}$  rows and  $N_{eff}$  columns in the covariance estimation (see Fig. 4). The location of the columns and rows can be anywhere, depending on the phase of the reflection coefficient of the target. In order to locate the spectrum of the target, we used the magnitude of the beams prior to DFT implementation.

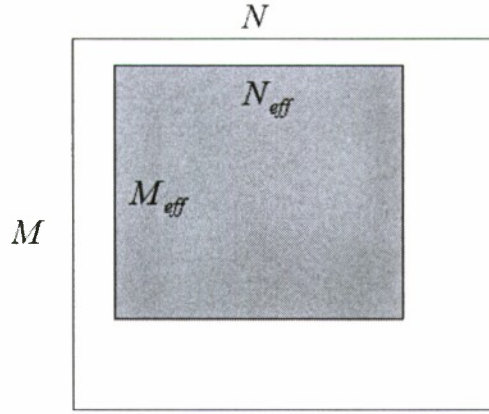


**Fig. 4** Effective elements in the 2-D spatial spectrum. Among  $M \times N$  2-D spectrum of the beams, only the shaded part has information on the targets.

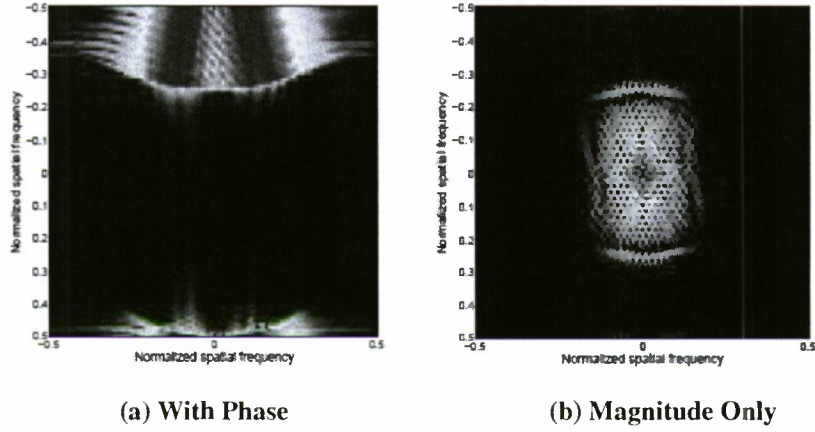


**Fig. 5** Spatial spectrum of the DS image (a) with phase information and (b) with magnitude only. The information on target location is partly present and it is located around the center when only magnitude of the image is used.

In some applications, such as target recognition, phase information from target may be necessary. However, in high-resolution image formations, the magnitudes of the beams are sufficient. After excluding the phase, the signal is located at the center of the 2-D spectrum, and the center part in the covariance estimation can be considered (See Fig. 5). Extensive simulations have shown that, depending on SNR, there could be significant difference in the BS-MUSIC performance when considering the entire extent of the 2-D spectrum vs. only using the region where most of the signal power is concentrated.

## 5.4 Simulations

The proposed algorithm is tested with real data as well as synthesized data.

### 5.4.1 Experiment

Through-the-wall data set is collected at the test site of the Center for Advanced Communications (CAC) at Villanova University, PA, USA [20]. The RF system, used for data collection, is housed in the Radar Imaging Lab of the CAC. It consists of off-the-shelf equipment, including the network analyzer (ENA5071B, Agilent, Santa Clara) and horn antennas (BAE-H1479, BAE Systems). The network analyzer, which has operational frequency range of 300kHz - 8.5 GHz, was used over the limited frequency band 2GHz - 3GHz. The transmission power was 5dBm. The wideband horn antenna, whose operation frequency range is 1 - 12.4 GHz, were used for both transmission and reception. In order to move the antenna and position it precisely over the  $P$  different locations, the Damaskos Inc. Field Probe Scanner model 7X7Y was used. Although the signals were transmitted and received on the 2-D vertical plane, only data collected at the horizontal linear position is used for the simulation. Fig. 6 shows the block diagram of the data collection system. A 12' x 8' typical interior residential wall stood between the antenna and the scene. The wall consists of exterior grade 3/4 -inch plywood on one side and 5/8 -inch gypsum wallboard was applied to the other. Between them, 2x4 wood studs placed.

Two scenes were used for data collection. In the first scene, trihedrals, dihedrals, cylinder and sphere are positioned as point targets in a 25' x 25' room (see Fig. 7). Reflections from interiors other than targets were minimized by absorbing wall modules utilizing 18" pyramidal foam absorber and laminated polyurethane foam sheet absorber. Step-frequency narrowband signals between 2 GHz and 3 GHz with 5 MHz interval are transmitted and received by the horn antenna at each location, and this is repeated at 57 uniformly spaced locations. The total array length is 1.2446 m. In the other scene, a 6-ft (1.82 m) long and 2.25 inch (5.7 cm) thick wall is used as an extended target. In this data set, the number of frequencies is 335 and the number of antenna locations is 81. The array length is 1.778 m.



In order to compare the performance, we processed synthesized data of similar settings where we can control SNR. Three point targets are considered in the synthesized data. Fig. 8 summarizes the specification of data sets.

### 5.4.2 Results

In all simulations, DS beamformer with a rectangular window is used. In DS beamforming, the space between beams is one fourth the down-range resolution ( $q, p = 4$ ). The center half of the 2-D spectrum is used in the covariance matrix estimation. The number of pixels in the final image rendered by the MUSIC estimator is same as the number of beams.

Fig. 9-12 are the log-scaled images obtained from the synthesized data. The true target locations are indicated by '+'. Three well-separated targets were considered. The targets locations in cross-range and down-range were  $(-0.9, 4.1)$ ,  $(-0.5, 4.5)$  and  $(0.3, 3.4)$  meter. The size of the 2-D spectrum and submatrices is set to  $160 \times 160$  and  $5 \times 5$ , respectively. The SNR for each antenna is -20 dB. The DS beamforming in Fig. 9 shows the three targets. However, it also shows many target-like objects due to high sidelobes

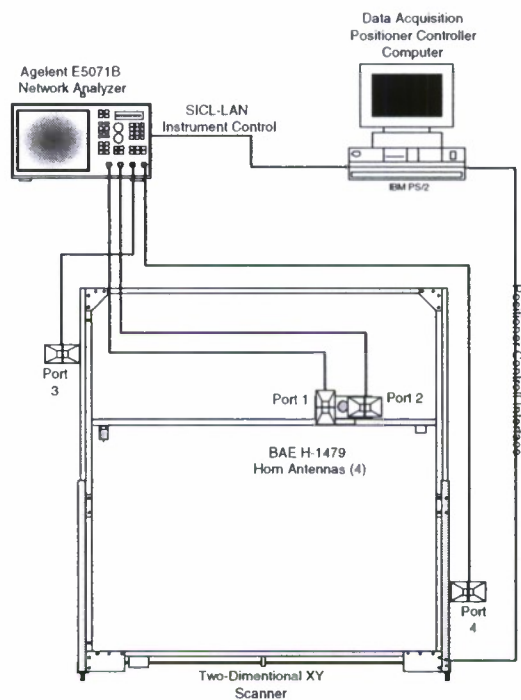


**Fig. 6** Block diagram of the data collection system.

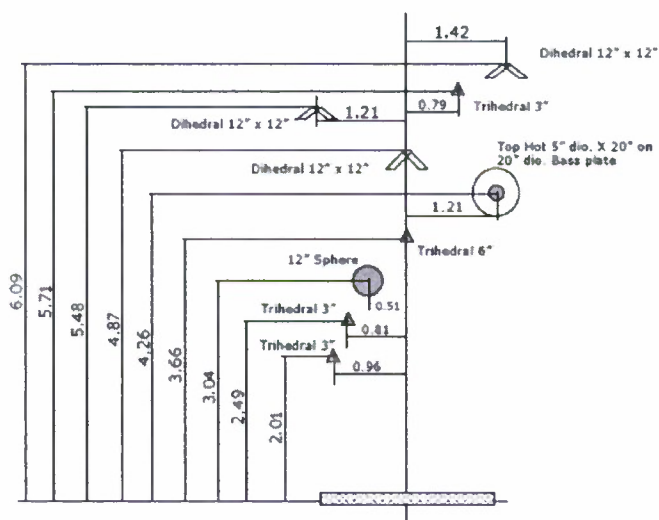


**Fig. 7** Ground truth of the targets in the point-target experiment all in meters. Note that the targets are not in the same x-y plane due to height differences.

Criterion	Experiment 1	Experiment 2	Synthesized
Bandwidth	1 GHz	1 GHz	1 GHz
Array length	1.2446 m	1.778 m	1.2 m
Freq. step	5 MHz	3 MHz	5 MHz
Antenna space	0.022 m	0.022 m	0.02 m

**Fig. 8** Data specification.

and noise. Because of low SNR, the ES-MUSIC estimator fails to identify the three point targets, whereas the BS-MUSIC estimator in Fig. 11 and Fig. 12 succeed in resolving them. The difference in performance between the ES-MUSIC and the BS-MUSIC underscores the advantage of the SNR gain provided by DS beamforming. Comparing the two BS-MUSIC images, Fig. 12 shows better result than that of Fig. 11. This is expected since the covariance estimate  $\hat{\mathbf{R}}_{new}$  in Fig. 12 is superior to  $\hat{\mathbf{R}}$  in Fig. 11.

Real data measurements consisting of point targets are also processed. In this case, the beamspace size is also  $160 \times 160$ , but the size of the sub-matrices is  $14 \times 14$  and the dimension of the signal subspace is 25. In the real data case, since the number of point targets is larger than the synthesized data, we used higher dimension sub-matrices and signal subspace. Once again, the output of BS-MUSIC (Fig. 15) shows a better image compared to the ES-MUSIC (Fig. 14). Note that there is bias in the MUSIC target location estimates. This is because the scene is a horizontal 2-D plane whose height is the same as the antenna, but the targets are located at different heights. The height difference results in bias in the image. In Fig. 14, only three targets are identifiable, while Fig. 15 shows seven out of nine targets.

Real wall data was collected and used to verify the advantage of the BS-MUSIC in dealing with an extended target. This time,  $8 \times 8$  sub-matrices are used and the dimension of the signal subspace is four. Fig. 16 is the output of DS beamformer. Figure 17 and Fig. 18 show the results of the ES-MUSIC and the BS-MUSIC, respectively. The image by the ES-MUSIC looks meaningless while the BS-MUSIC clearly

shows wall image. The experiment and imaging results support the aforementioned discussions which consider the ES-MUSIC as a good imaging approach for extended targets.

### **5.4.3 Conclusions**

High-resolution image formation is important for ISAR and TWI applications. The ES-MUSIC is commonly used to obtain high-resolution imaging. We propose the BS-MUSIC, which applies the MUSIC algorithm to the 2-D spatial spectrum in beamspace. The key advantages of the BS-MUSIC over the ES-MUSIC are its robustness to low SNR and ability to resolve extended targets. These two advantages make the BS-MUSIC more suitable for urban sensing applications, especially, TWI, where a typical scene is a mixture of both extended targets and point targets with several reflections from surrounding scatterers are present. The performance of the BS-MUSIC with both synthesized and real data was shown to be superior to the ES-MUSIC.

## References

- [1] R. Nuthalapati, "High resolution reconstruction of ISAR images," *IEEE Trans. Aerosp. Electron. Syst.*, vol. 28, no. 2, pp. 462–472, Apr. 1992.
- [2] A. Hua, F. Baqai, Y. Zhu, and D. Heilbronn, "Imaging of point scatterers from step-frequency ISAR data," *IEEE Trans. Aerosp. Electron. Syst.*, vol. 29, no. 1, pp. 195–205, Jan. 1993.
- [3] R. Schmidt, "Multiple emitter location and signal parameter estimation," *IEEE Trans. Antennas Propagat.*, vol. AP-34, no. 3, pp. 276–280, Mar. 1986.
- [4] J. Capon, "High-resolution frequency wavenumber spectrum analysis," *Proc. IEEE*, vol. 57, no. 8, pp. 1408–1411, 1969.
- [5] R. Roy and T. Kailath, "ESPRIT-estimation of signals parameters via rotational invariance techniques," *IEEE Trans. Acoust., Speech, Signal Processing*, vol. 37, no. 7, pp. 462–472, July 1989.
- [6] J. Odendaal, E. Barnard, and C. Pistorius, "Two-dimensional superresolution radar imaging using the MUSIC algorithm," *IEEE Trans. Antennas Propagat.*, vol. 42, pp. 1386–1391, Oct. 1994.
- [7] G. Benitz, "High-definition vector imaging," *Lincoln Lab Journal*, vol. 10, no. 2, 1997.
- [8] S. Rouquette and M. Najim, "Estimation of frequencies and damping factors by two-dimensional ESPRIT type methods," *IEEE Trans. Signal Processing*, vol. 49, no. 1, pp. 237–245, Jan. 2001.
- [9] D. Ferris, Jr. and N. Currie, "A survey of current technologies for through-the-wall surveillance (TWS)," *Proceedings of SPIE*, no. 3577, pp. 62–72, Nov. 1998.
- [10] F. Ahmad, M. Amin, and S. Kassam, "Synthetic aperture beamformer for imaging through a dielectric wall," *IEEE Trans. Aerosp. Electron. Syst.*, vol. 41, no. 1, pp. 271–283, Jan. 2005.
- [11] F. Ahmad and M. Amin, "High-resolution imaging using Capon beamformers for urban sensing applications," in *Proc. IEEE Int. Conf. Acoustics, Speech, Signal Process.*, Apr. 2007.
- [12] F. Ahmad, G. Frazer, S. Kassam, and M. Amin, "Design and implementation of near-field, wideband synthetic aperture beamformers," *IEEE Trans. Aerosp. Electron. Syst.*, vol. 40, no. 1, pp. 206–220, Jan. 2004.
- [13] Y. Hua, "Estimating two-dimensional frequencies by matrix enhancement and matrix pencil," *IEEE Trans. Signal Processing*, vol. 40, no. 9, pp. 2267–2280, Sept. 1992.
- [14] H. Hua and Y. Hua, "On rank of block hankel matrix for 2-d frequency detection and estimation," *IEEE Trans. Signal Processing*, vol. 44, no. 4, pp. 1046–1048, Apr. 1996.
- [15] P. Stoica and A. Nehorai, "MUSIC, maximum likelihood, and cramer-rao bound," *IEEE Trans. Acoust., Speech, Signal Processing*, vol. 37, no. 5, pp. 720–741, May 1989.
- [16] L. Frazier, "Radar surveillance through solid materials," in *Proceedings of SPIE, Command, Control, Communications, and Intelligence Systems for Law Enforcement*, vol. 2938, Nov. 1997, pp. 139–146.
- [17] F. Ahmad and M. Amin, "Noncoherent approach to through-the-wall radar localization," *IEEE Trans. Aerosp. Electron. Syst.*, vol. 42, no. 4, pp. 1405–1419, Oct. 2006.
- [18] R. Lewitt, "Reconstruction algorithms: Transform methods," *Proceedings of IEEE*, vol. 71, no. 3, 1983.
- [19] D. Johnson and D. Dudgeon, *Array Signal Processing: Concepts and techniques*. Englewood Cliffs, NJ: Prentice Hall, 1993.



- [20] R. Dilsavor, W. Ailes, P. Rush, F. Ahmad, W. Keichel, G. Titi, and M. Amin, "Experiments on wideband through-the-wall imaging," in *Proceedings of SPIE, Algorithm for Synthetic Aperture Radar Imagery XII Conference*, vol. 5808, 2005, pp. 196–209.

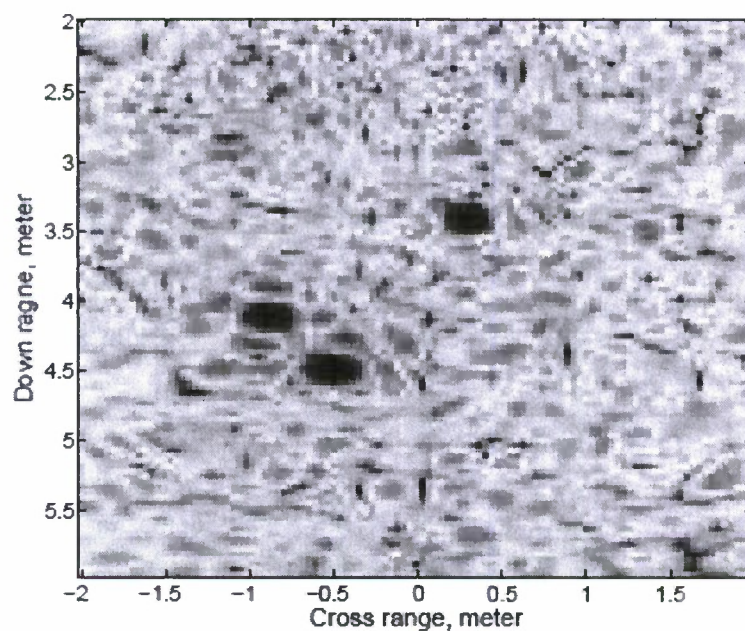


**Fig. 9** The target locations are marked by '+'. Although three targets are visible, many false small targets appear due to low SNR (-20 dB).

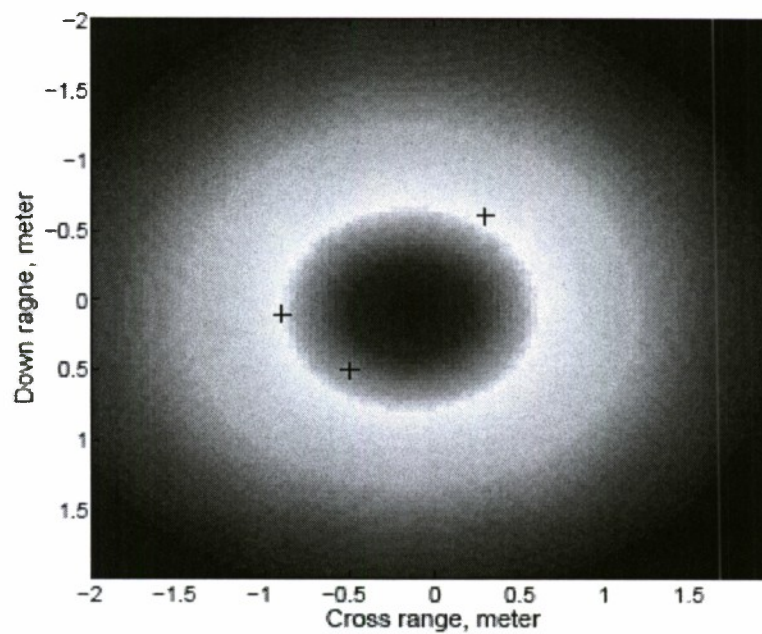


**Fig. 10** Poor imaging quality is due to the low SNR at each antenna.

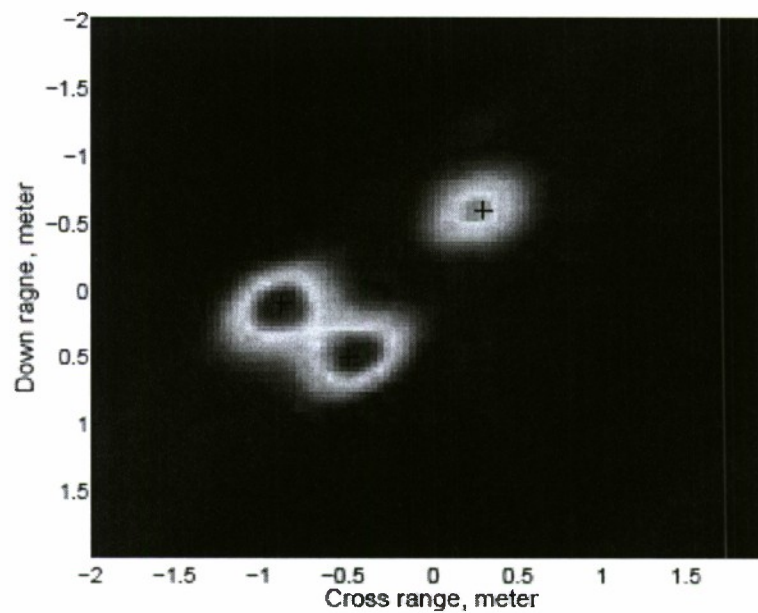


**Fig. 11** BS-MUSIC using the covariance matrix estimated with diagonal sub-matrices as in eq. (20).

Although three targets are identifiable, it shows artifacts and the point targets are blurred.

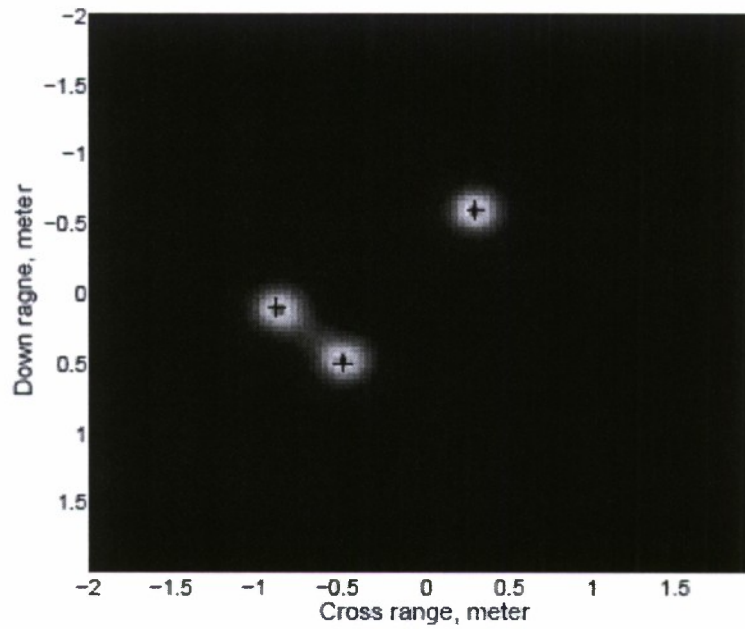


**Fig. 12** BS-MUSIC using the covariance matrix estimate in eq. (21). Note that sharper image is obtained compared to the DS image.

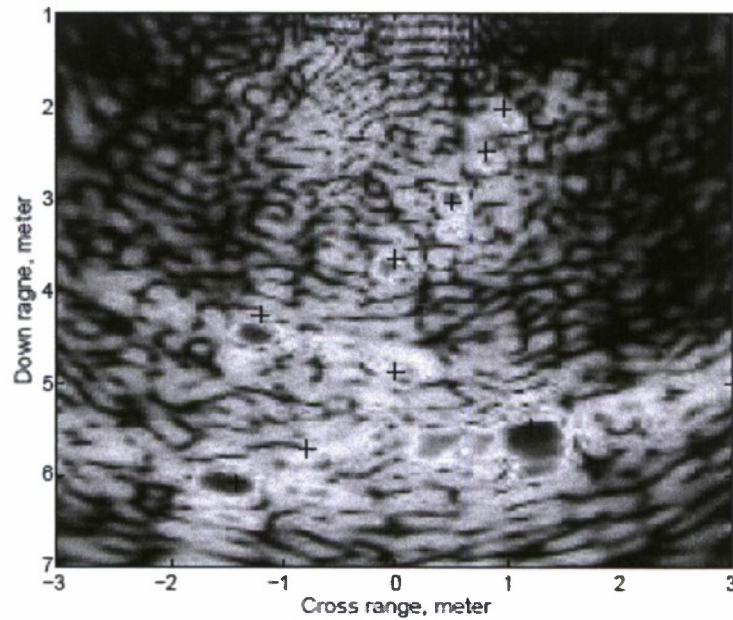


**Fig. 13** DS beamformer for the experimental data (point targets).

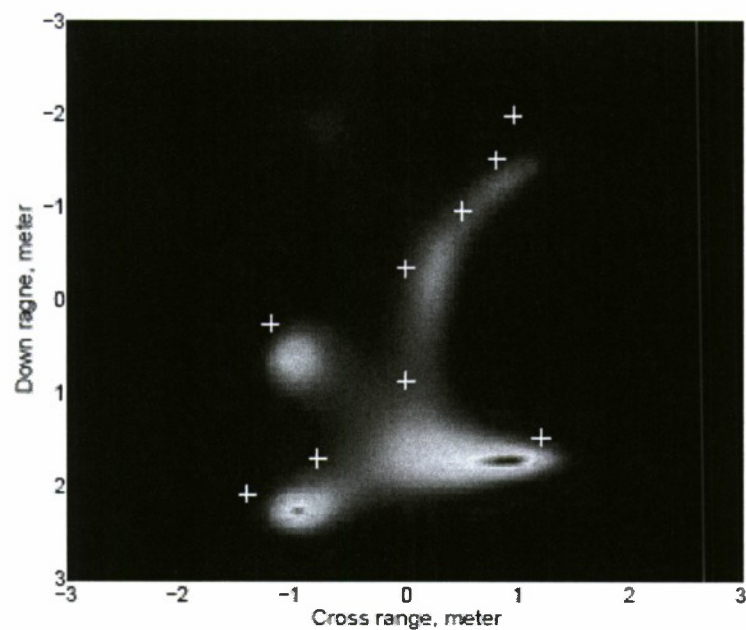


**Fig. 14** ES-MUSIC for experimental data. Only three targets out of nine targets are identifiable.

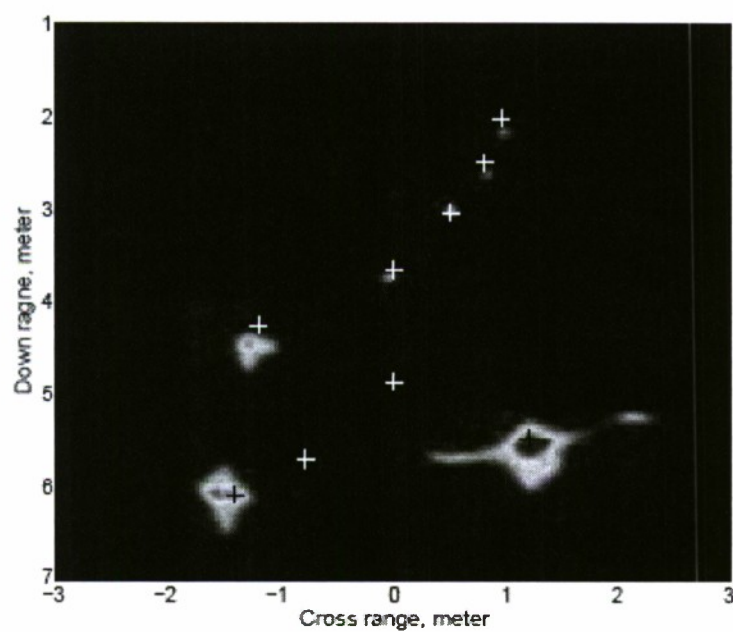


**Fig. 15** BS-MUSIC for the experimental data. Seven out of nine targets are identifiable. Note that the bias is due to the fact that the heights of imaged targets are different from the 2-D plane.



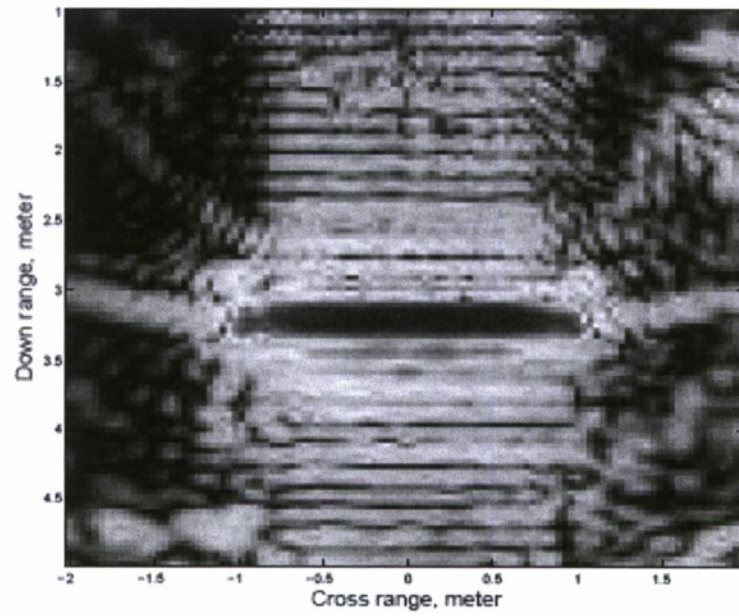


Fig. 16 DS beamformer for the experimental wall data.

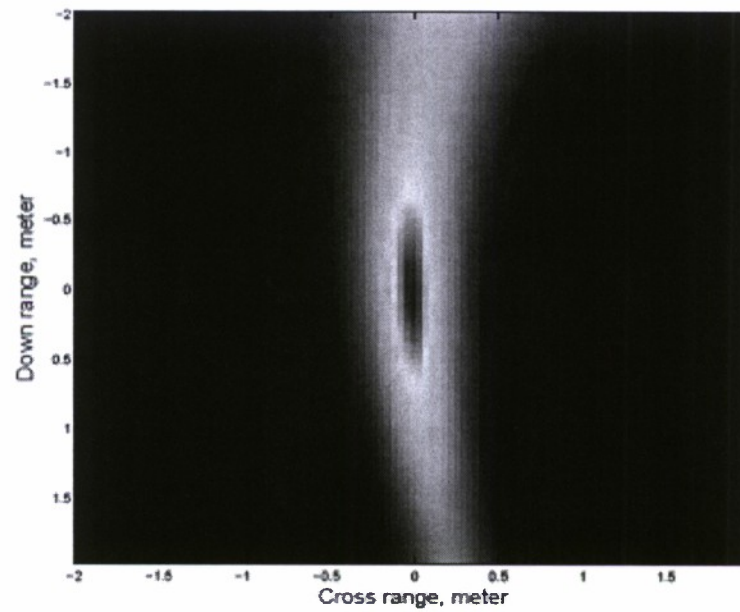
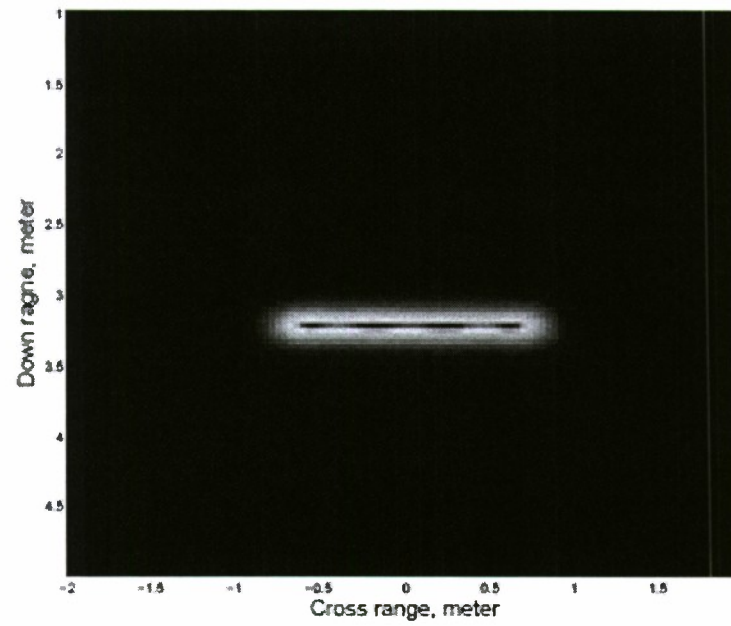


Fig. 17 BS-MUSIC for the experimental wall data. The BS-MUSIC fails to image the wall.





**Fig. 18** BS-MUSIC for experimental wall data. A wall is clearly seen in this image.

**REPORT DOCUMENTATION PAGE****Form Approved**  
**OMB No. 0704-0188**

Public reporting burden for this collection of information is estimated to average 1 hour per response, including the time for reviewing instructions, searching data sources, gathering and maintaining the data needed, and completing and reviewing the collection of information. Send comments regarding this burden estimate or any other aspect of this collection of information, including suggestions for reducing this burden to Washington Headquarters Service, Directorate for Information Operations and Reports, 1215 Jefferson Davis Highway, Suite 1204, Arlington, VA 22202-4302, and to the Office of Management and Budget, Paperwork Reduction Project (0704-0188) Washington, DC 20503.

**PLEASE DO NOT RETURN YOUR FORM TO THE ABOVE ADDRESS.**

<b>1. REPORT DATE (DD-MM-YYYY)</b> 30-04-2010		<b>2. REPORT TYPE</b> Final		<b>3. DATES COVERED (From - To)</b> February 2007 – January 2010	
<b>4. TITLE AND SUBTITLE</b> Radar Imaging for Urban Sensing				<b>5a. CONTRACT NUMBER</b>	
				<b>5b. GRANT NUMBER</b> N00014-07-1-0043	
				<b>5c. PROGRAM ELEMENT NUMBER</b>	
<b>6. AUTHOR(S)</b> Amin, Moeness, G.				<b>5d. PROJECT NUMBER</b>	
				<b>5e. TASK NUMBER</b>	
				<b>5f. WORK UNIT NUMBER</b>	
<b>7. PERFORMING ORGANIZATION NAME(S) AND ADDRESS(ES)</b> Villanova University 800 East Lancaster Avenue Villanova, Pa 19085				<b>8. PERFORMING ORGANIZATION REPORT NUMBER</b> Acct: 527793	
<b>9. SPONSORING/MONITORING AGENCY NAME(S) AND ADDRESS(ES)</b> Office of Naval Research 875 North Randolph Street Arlington VA 22203-1995				<b>10. SPONSOR/MONITOR'S ACRONYM(S)</b> ONR 311	
				<b>11. SPONSORING/MONITORING AGENCY REPORT NUMBER</b>	
<b>12. DISTRIBUTION AVAILABILITY STATEMENT</b> Approved for Public Release; Distribution is Unlimited					
<b>13. SUPPLEMENTARY NOTES</b>					
<b>14. ABSTRACT</b> The research efforts in this project focused on signal processing techniques and algorithms for urban sensing and through the wall radar imaging. We have considered both stationary and moving targets and animate and inanimate objects. Progress has been made on different fronts and dealt with target detection, classification, motion parameter estimation, and high resolution imaging. Target detection has been performed both in the data and in the image domains. We have developed 1) Maximum Likelihood and suboptimal schemes for Micro-Doppler estimation using Carrier diverse Doppler radars, 2) Cramér-Rao Bound Analysis of dual frequency Doppler radars for indoor range estimation, 3) Optimal waveform design for improved indoor target detection in sensing Through-the-Wall applications, 4) Matched-Illumination waveform design for a Multistatic Through-the-Wall radar systems, 5) Beam-space MUSIC for high resolution imaging in Through-the-Wall radar imaging applications, 6) Minimum variance distortionless response beamforming for Through-the-wall, 7) Adaptive target detection with application to Through-the-Wall Radar Imaging					
<b>15. SUBJECT TERMS</b> Waveform Design; MicroDoppler; High Resolution Imaging; Through the Wall Radar Imaging; Urban Sensing					
<b>16. SECURITY CLASSIFICATION OF:</b>			<b>17. LIMITATION OF ABSTRACT</b> UU	<b>18. NUMBER OF PAGES</b> 178	<b>19a. NAME OF RESPONSIBLE PERSON</b>
<b>a. REPORT</b> U	<b>b. ABSTRACT</b> U	<b>c. THIS PAGE</b> U			<b>19b. TELEPHONE NUMBER (Include area code)</b>